

Review of Survey activities 2017

Edited by

Adam A. Garde, Ole Bennike and W. Stuart Watt

Keywords

Geological Survey of Denmark and Greenland, survey organisations, current research, Denmark, Greenland.

Cover photographs from left to right

1. Hyperspectral analysis of inaccessible rock faces using land- or sea-based platforms has potential to become a powerful geological mapping tool, as individual mineral species can be identified with this method. Example from central West Greenland.
2. 3D imaging by hand-held digital photogrammetry is used in both current geological mapping and assessment of landslide risks in Greenland. Photograph: Jonas Petersen.
3. Potential storage sites for unwanted brine around the Lille Torup gas storage facility in Jylland, and seismic lines used in the location of suitable sites.
4. Studying intense glaciotectonic fracturing of Cretaceous chalk at Stevns Klint.

Frontispiece: facing page

The GEUS ice-sheet field camp photographed on 20 July, 2017 above the former Camp Century buried in the Greenland ice sheet near Thule Air Base.

Chief editor of this series: Adam A. Garde

Editorial board of this series: John A. Korstgård, Department of Geoscience, Aarhus University; Minik Rosing, Geological Museum, University of Copenhagen; Finn Surlyk, Department of Geosciences and Natural Resource Management, University of Copenhagen

Scientific editors: Adam A. Garde, Ole Bennike and W. Stuart Watt

Editorial secretary: Jane Holst

Referees (numbers refer to first page of reviewed article): Henrik Friis & Ida L. Fabricius, DK (9); Reinhard Kirsch, DE & Michael Engkilde, DK (13); Theis I. Sølling & Jan Audun, DK (17); Jakob Qvortrup Christensen & Lars Kristiansen, DK (21); Jakob Qvortrup Christensen & Jette Sørensen, DK (25); Jørgen C. Toft & Arne Thorshøj, DK (29); Nicolaj Krog Larsen & Anders Bjørk, DK (33); Andy Whitham, UK & John Korstgård, DK (39); Steve Piercey, CA & Hartwig Frimmel, DE (43); Christian Rogass, DE & Asger K. Pedersen, DK (47, 51); Chris Harrison & Kate Dickie, CA (57); Asger K. Pedersen, DK & Ken McCaffrey, UK (63); Louwrens Hacquebord, NL & Ole Humlum, NO (67); Niels Tvis Knudsen, DK & Kirsty Langley, GL (71); James H. Lever, US & Jacob Clement Yde, NO (75); Xavier Fettweis, BE & Horst Machguth, CH (79); Torben Schmidt, DK & Martin Miles, NO (83); Gang Lui & Michael Engkilde, DK (87); Andreas Møller & Peter Grønksjær, DK (91); Robert Tomas, CH (95); Birgir V. Óskarsson, IS & Max Strunk, SE (99).

Illustrations: Stefan Sølberg, Adam A. Garde, Ole Bennike and Susanne Rømer

Layout and graphic production: Jane Holst and Jacob Lind Bendtsen

Printer: Rosendahls-Schultz Grafisk A/S, Albertslund, Denmark

Manuscripts received: 1 February – 28 May 2018

Final versions approved: 20 February – 28 June 2018

Printed: 15 August 2018

Erratum: The repetition of Fig. 3 in Fig. 4's position on page 73 has been corrected to show Fig. 4 in the online version of this Bulletin.

ISSN (print) 1604-8156, ISBN (print) 978-87-7871-500-5

ISSN (online) 1904-4666, ISBN (online) 978-87-7871-501-2

Citation of the name of this series

It is recommended that the name of this series is cited in full, viz. *Geological Survey of Denmark and Greenland Bulletin*.

If abbreviation of this volume is necessary, the following form is suggested: *Geol. Surv. Den. Green. Bull.* 41, 104 pp.

Available from

Geological Survey of Denmark and Greenland, Øster Voldgade 10, DK-1350 Copenhagen K, Denmark

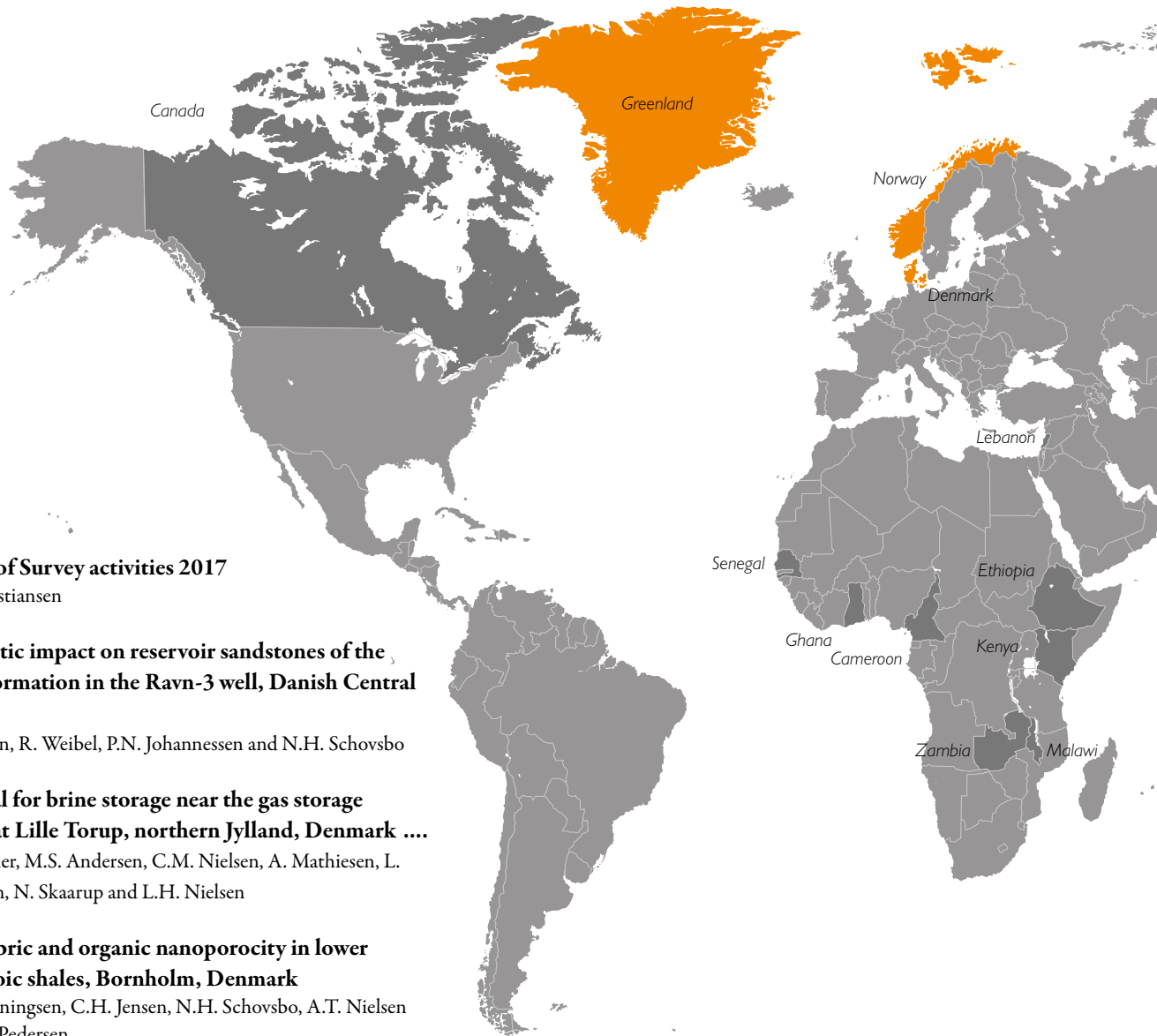
To buy bulletin in printed form please contact bogsalg@geus.dk

and at www.geus.dk/bulletin41 (open access)

© De Nationale Geologiske Undersøgelser for Danmark og Grønland (GEUS), 2018

For the full text of the GEUS copyright clause, please refer to www.geus.dk/bulletin





7 Review of Survey activities 2017

F.G. Christiansen

9 Diagenetic impact on reservoir sandstones of the Heno Formation in the Ravn-3 well, Danish Central Graben

S. Pedersen, R. Weibel, P.N. Johannessen and N.H. Schovsbo

13 Potential for brine storage near the gas storage facility at Lille Torup, northern Jylland, Denmark

M.L. Hjuler, M.S. Andersen, C.M. Nielsen, A. Mathiesen, L. Kristensen, N. Skaarup and L.H. Nielsen

17 Shale fabric and organic nanoporosity in lower Palaeozoic shales, Bornholm, Denmark

L.M. Henningsen, C.H. Jensen, N.H. Schovsbo, A.T. Nielsen and G.K. Pedersen

21 Chalk-glacitectonite, an important lithology in former glaciated terrains covering chalk and limestone bedrock

S.A.S. Pedersen, P. Gravesen and K. Hinsby

25 Sedimentological and glaciotectonic interpretation of georadar data from the margin of the Vig ice-push ridge, NW Sjælland, Denmark

C.S. Andersen & P.R. Jakobsen

29 Miocene oil-bearing diatom ooze from the North Sea

E. Sheldon, E.S. Rasmussen, K. Dybkjær, T.E. Eidvin, F. Riis and R. Weibel

33 Initial observations of the shallow geology in Tannis Bugt, Skagerrak, Denmark

M.J. Owen, N.H. Witt, Z. Al-Hamdani, N. Nørgaard-Pedersen, K.J. Andresen and J.O. Leth

39 Update of the seamless 1:500 000 scale geological map of Greenland based on recent field work in the Wandel Sea Basin, Eastern North Greenland.

K. Svennevig

43 Base-metal and REE anomalies in lower Palaeozoic sedimentary rocks of Amundsen Land, central North Greenland: implications for Zn-Pb potential

D. Rosa, J.F. Slack and H. Falck

47 Mineral mapping by hyperspectral remote sensing in West Greenland using airborne, ship-based and terrestrial platforms

S. Salehi and S.M. Thaarup

51 Hyperspectral analysis of lithologies in the Arctic areas with abundant lichen cover

S. Salehi



Dark grey indicates non-european countries where GEUS has ongoing or recently completed projects.

Orange indicates countries with GEUS projects described in this volume.

57 New subsurface mapping offshore southern West Greenland using geophysical and geological data

U. Gregersen, M.S. Andersen, H. Nøhr-Hansen, E. Sheldon, T.F. Kokfelt, M. Olivarius, C. Knudsen, K.G. Jakobsen and J.S. Adolphsen

63 Remote geological mapping using 3D photogrammetry: an example from Karrat, West Greenland

E.V. Sørensen and P. Guarnieri

67 European trading, whaling and climate history of West Greenland documented by historical records, drones and marine sediments

N.E. Mikkelsen, A. Kuijpers, S. Ribeiro, M. Myrup, I. Seiding and A.E. Lennert

71 The Greenland ice sheet – snowline elevations at the end of the melt seasons from 2000 to 2017

R.S. Fausto and the PROMICE team

75 Initial field activities of the Camp Century Climate Monitoring Programme in Greenland

W. Colgan, A. Pedersen, D. Binder, H. Machguth, J. Abermann and M. Jayred

79 Circum-Greenland, ice-thickness measurements collected during PROMICE airborne surveys in 2007, 2011 and 2015

L.S. Sørensen, S.B. Simonsen, R. Forsberg, L. Stenseng, H. Skourup, S.S. Kristensen and W. Colgan

83 Observationally constrained reconstruction of 19th to mid-20th century sea-ice extent off eastern Greenland

D.A.M. Hallé, N.B. Karlsson, A.M. Solgaard and C.S. Andresen

87 Examining the rare-earth elements (REE) supply-demand balance for future global wind power scenarios

P. Kalvig and E. Machacek

91 Analysis of cod otolith microchemistry by continuous line transects using LA-ICP-MS

S.H. Serre, K.E. Nielsen, P. Fink-Jensen, T.B. Thomsen and K. Hüseyin: Tulstrup and M. Pedersen

95 Towards a common geological data infrastructure for Europe

J. Tulstrup and M. Pedersen

99 Analytical procedures for 3D mapping at the Photogeological Laboratory of the Geological Survey of Denmark and Greenland

E.V. Sørensen and M. Dueholm

Review of Survey activities 2017

Flemming G. Christiansen

Deputy Director

2017 was a year where we all experienced how fatal geological forces can be for society. On June 17, a tragic natural disaster hit Greenland. Following a huge landslide into Karrat Fjord, major waves flooded the settlements of Nuugaatsiaq and Illorsuit. Four persons were lost and many houses in Nuugaatsiaq were destroyed. Due to the continued high risk for more landslides, the inhabitants of the two settlements have not returned and the Greenlandic authorities advise against visiting the risk area.

Such a natural disaster together with many extremes in weather and climate conditions around the World, also in Denmark and Greenland, directs our focus on the consequences of the changing climate. This requires regularly updated climate models and response with suggestions for adaptation to climate change and will have strong implications for GEUS' continued research and monitoring in many years to come, including further studies and monitoring of geohazards.

GEUS will have an important role in guiding society for better and safer living conditions in both Denmark and Greenland. It is necessary to work with such topics and provide society and authorities with transparent information. GEUS has presented a new website providing key information on many different research areas and with specific information and data from monitoring programmes like *www.promise.dk*, celebrating its 10 years anniversary in 2017 and *www.camppcenturyclimate.dk* that was established in 2017.

It is essential that such key information builds on results of a high scientific standard and that data are well documented in international publications, and in papers and maps in our own series. This issue of GEUS' Review of Survey activities includes 22 papers covering many different activities in Denmark, Greenland and internationally. Seven papers are on Denmark, 11 on Greenland and four on other themes.

Activities in Denmark

GEUS works with many different – and often closely related – topics in Denmark such as the use of water, energy and mineral resources, protection of nature when exploiting resources, and the impact of climate change. The economic

and political implications are very significant, and making up-to-date geological and geophysical data and information available for society, authorities and industry is of great value in this context.

One paper is on the diagenetic impact of Upper Jurassic sandstones in the Ravn-3 well in the Danish Central Graben. Understanding these processes is important for the production of oil from deeply buried oil fields. Another paper is on the thickness, depth and properties of reservoir rocks within the sedimentary succession close to the Lille Torup gas storage facility in northern Jylland. To increase the volume of caverns, saline brine from the salt structure must be stored elsewhere, and one of the options could be to re-inject the brine into the subsurface. A third paper deals with the controlling factors of porosity development in Palaeozoic shales and the implications for shale-gas plays in Denmark. An example from Bornholm, demonstrates that this is controlled by both shale fabric and organic nanoporosity, in contrast to conventional sandstone reservoirs.

Understanding rocks formed by glacial processes is important in Denmark, e.g. for flow modelling of ground water and for handling geotechnical problems when establishing new infrastructure. One paper describes the formation of chalk-glacioteconite with examples from former glaciated terrains covering chalk and limestone bedrock from localities on Møn, Sjælland and Jylland. A second paper presents sedimentological and glacioteconic interpretation of georadar data from NW Sjælland, where the interior structure of ridges has been characterised.

For cost-reduction reasons, there is a growing interest for oil exploration in the youngest and shallowest part of the sedimentary succession in the North Sea. A paper gives a detailed description of nanofossils, microfossils and palynomorphs in a Miocene oil-bearing diatom ooze from the Valhall field area in the Norwegian sector. A final paper is on the shallow geology of Tannis Bugt in Skagerak where habitat mapping has been carried out in a Natura2000 area. The geological history here is very complex with deformed units and possibility of pre-Quaternary bedrock being exposed on the sea bottom.

Activities in Greenland

As in previous years, there was a high level of geological and glaciological activities in Greenland in 2017: both traditional studies with focus on geological mapping, the mineral and petroleum potential and monitoring and research related to climate changes and their effects.

One paper discusses the implications of a new 1:100 000 map from Kilen in North Greenland for the seamless 1:500 000 regional map of Greenland. New procedures and documentation are necessary, as many geological maps from Greenland are likely to be updated in digital versions in the coming years. A second paper on North Greenland describes base-metal and rare-earth elements (REE) anomalies in lower Palaeozoic sedimentary rocks and discusses the implications for the zinc and lead potential.

Hyperspectral remote sensing has a great potential for geological mapping and exploration in Greenland. A paper from West Greenland provides details on mineralogical mapping of basement rocks in the Nagssugtoqidian Orogen using airborne, ship-based and terrestrial platforms. Another paper focuses on how the signal from lichens that often cover rocks in the Arctic can be distinguished from the mineralogical signal, with examples of ultramafic rocks such as kimberlite.

One paper presents results from subsurface mapping offshore southern West Greenland using seismic interpretation also including various geological and geochemical analysis. This paper includes new and critical information from oil exploration wells drilled in 2010 and 2011 that penetrated the deeper part of the sedimentary succession and reached underlying basement and volcanic rocks. Another paper uses 3D photogrammetry for lithological mapping and structural analysis, in this case from Karrat Fjord in West Greenland. Such understanding is also important for further evaluation of risk of landslides.

Climate-related research and monitoring at GEUS provide important data for global climate models and are often based on ground-truth data from the ice and fjords or offshore. One paper compares historical records of European trading and whaling in the Disko Bugt region with climate data from marine sediments and show interesting examples of the physical remains from the whaling period. Another paper introduces an important climate indicator – the snowline elevation that is the maximum elevation during the melt season where snow remains from the previous accumulation season. Based on satellite data and direct comparison with

data from PROMICE stations, a series of snowline maps covering all of Greenland from 2011 to 2017 have been constructed.

With new and updated climate models, there are concerns that remains from the former US Camp Century base buried under the ice in the Thule area might get closer to the surface within the next century and that meltwater may interact with its waste long before. GEUS has started a new climate-monitoring programme and has mapped the extent and depth of the debris from the base with an ice-penetrating radar survey; results from the first field season are summarised in one contribution. A second paper describes results from airborne surveys in 2007, 2011 and 2015 where the elevation of the ice surface, top of bedrock, and the variation in thickness of the Greenland ice sheet through time have been measured. Another paper is on the sea-ice distribution along eastern Greenland and Iceland. Original maps by Lauge Koch covering the 19th and 20th century have been digitised and analysed statistically. This can be very useful for future models of sea-ice variation in a changing climate.

Other themes

As the national geological survey, GEUS has a strong obligation to participate in international assessments of resources, use state-of-the-art laboratory equipment, constantly develop new analytical techniques and make the ever-increasing volume of data available with systematic quality control and updated, user-friendly databases and distribution systems.

One paper presents an examination of the supply-demand balance of REE, which is important for future global wind power scenarios; especially lack of neodymium and other elements for permanent magnets may be critical. Another paper describes how analysis of the microchemistry of cod otoliths (ear stones) with the LA-ICP-MS technique can be applied to understand the age, growth history and migration of fish stock. A third paper gives an overview of the development and organisation of a common geological data infrastructure (EGDI) for Europe. EGDI is important for the research collaboration and geological data sharing between the member states of the EuroGeoSurveys. Finally, the last paper presents the procedures for 3D mapping at the photogeological laboratory at GEUS. This is a very strong tool for geological mapping, structural analysis and evaluation of the risk of natural geohazards such as landslides.

Diagenetic impact on reservoir sandstones of the Heno Formation in the Ravn-3 well, Danish Central Graben

Simone Pedersen, Rikke Weibel, Peter N. Johannessen and Niels H. Schovsbo

Oil and gas production from siliciclastic reservoirs has hitherto been in the Danish Central Graben mostly from Palaeogene and Middle Jurassic sandstone. The Ravn field was the first Upper Jurassic field to start operation. The reservoir is composed of sandstone of the Heno Formation. Production takes place at a depth of 4000 m, which makes Ravn the deepest producing field in the Danish North Sea. The Heno Formation mainly consists of marine shoreface deposits, where foreshore, middle and lower shoreface sandstones constitute the primary reservoir. The results of this study of the diagenetic impact on the mineralogical composition, porosity and permeability are presented here. Microcrystalline quartz has preserved porosity in the sandstone, whereas illite, quartz overgrowth and carbonate cement have reduced both porosity and permeability.

Geological background

The Ravn Member of the Heno Formation is located on the Heno Plateau in the Danish Central Graben (Fig. 1; Johannessen 2010). The Ravn field was discovered in the Ravn-1 well in 1986 and subsequently evaluated in the Ravn-2 well in 1987. In 2010, the Ravn-3 well was drilled to test the location of the oil–water contact and to evaluate the reservoir quality of the south-western flank of the field. Oil was found at several intervals and the oil–water contact was located at a depth of 4572 m.

The Ravn Member was deposited during an overall transgression of the Heno Plateau during the Kimmeridgian. The member consists of up to 100 m thick marine shoreface deposits (Johannessen 2010) where foreshore, middle and lower shoreface sandstones constitute the primary reservoirs (Fig. 2). The sediments are strongly bioturbated and are dominated by very fine- to fine-grained or muddy sandstones with occasional white, grey and light brown siltstones.

Methods

Sedimentological description of the Ravn-3 core was made and 18 thin sections were prepared from samples from middle, lower and foreshore sandstones (Fig. 2). Petrographical investigations of the thin sections were undertaken with

transmitted light microscopy. Mineral abundances were quantified by point counting of minimum 500 grains. Additional information was obtained from scanning electron microscopy (SEM) of gold-coated rock chips and carbon-coated thin sections using a Phillips XL 40 SEM with a tungsten filament operating at 17 kV and 50–60 μ A. Porosity and permeability were measured on core plugs according to the API RP-40 standard (American Petroleum Institute 1998) at the Geological Survey of Denmark and Greenland.

Results

The porosity and permeability of sandstone reservoirs reflect, among other things, depositional environmental, mineralogical composition and post-depositional diagenetic changes. In order to understand what affected porosity and permeability, these factors were investigated.

Detrital components – Quartz is the dominant component in all sandstones. The feldspar group consists of K-feldspar and minor albite. K-feldspar is typically partially dissolved and

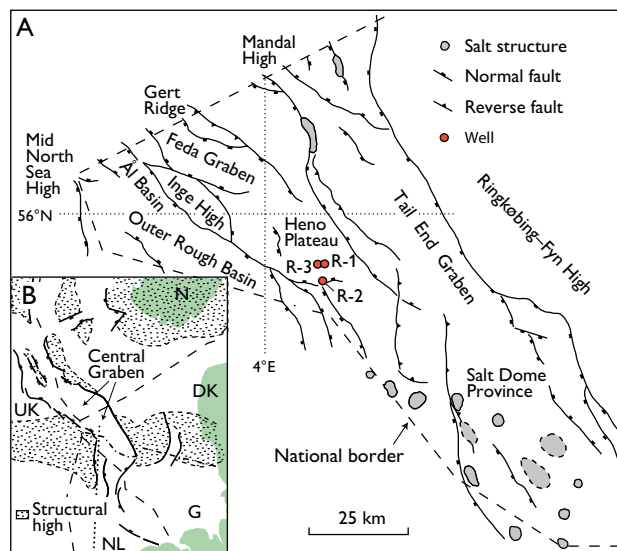


Fig. 1. A: Present structural framework of the Danish sector of the Central Graben. R-1, R-2, R-3: Ravn-1, -2 and -3 wells. B: Overview of the North Sea area. Green: Land. Modified from Johannessen (2010).

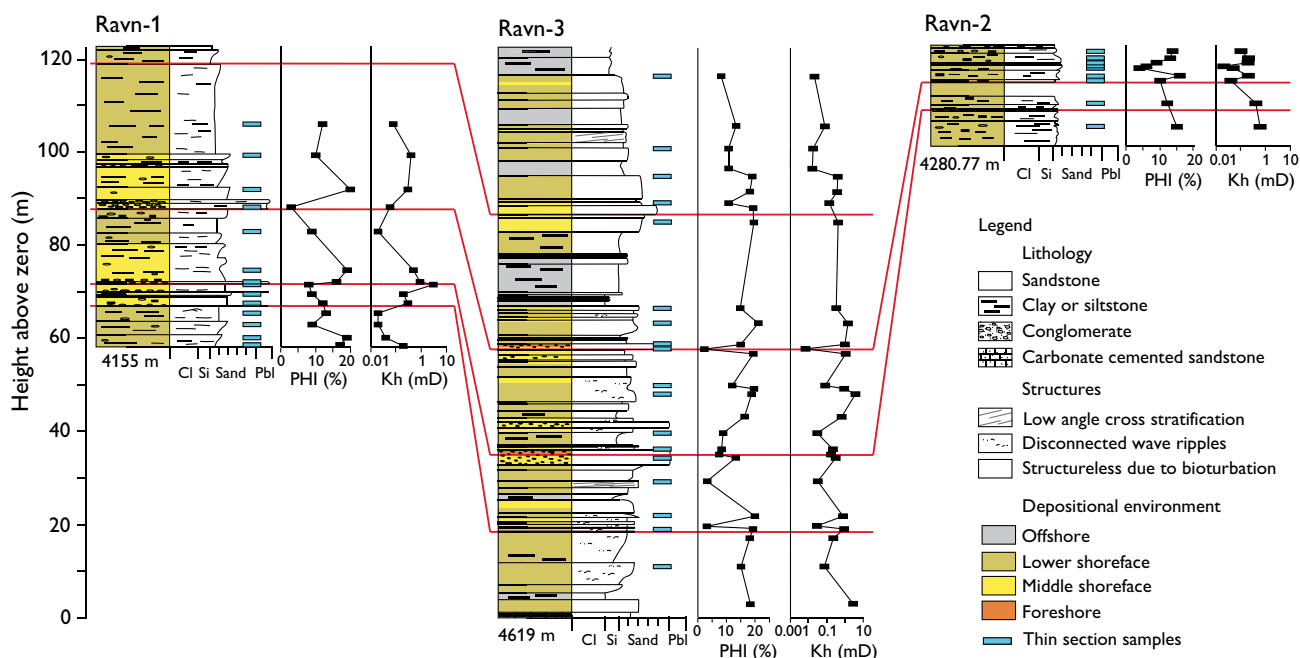


Fig. 2. Correlation panel of the cored parts of the Ravn-1, -2, and -3 wells. The Ravn-1 and Ravn-2 logs are modified from Johannessen (2010), whereas the Ravn-3 core was logged for this study. The depositional environment described in the Ravn-3 well (Panterra 2011) is based on ichnofacies. **PHI**: Porosity. **Kh**: horizontal permeability. **Cl**: clay. **Si**: silt. **Pbl**: pebble.

minor mica, rock fragments and chlorite grains are present. Accessory minerals are tourmaline, zircon and Fe-Ti oxides. Detrital clay occurs as tangential coatings on detrital grains and as deformed clay clasts.

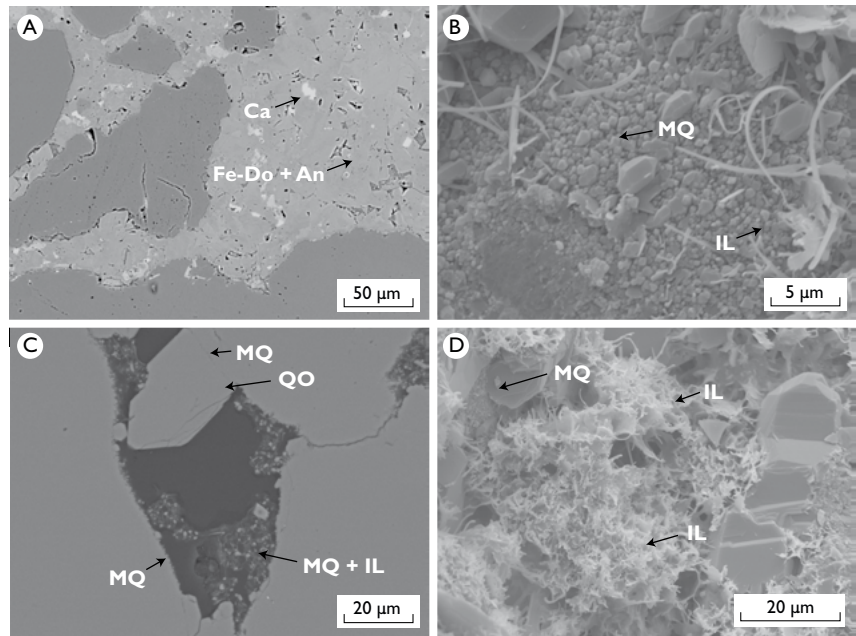
Diagenetic phases – Sandstones are occasionally dominated by abundant sparry Fe-dolomite and ankerite cement (Fig. 3A; Pedersen 2017). Sporadic calcite inclusions occur enclosed in the Fe-dolomite-ankerite cement. Calcite from shell fragments was recognised in one sample. Small amounts of Fe-dolomite-ankerite rhombs are present in samples where cement is not abundant. Microcrystalline quartz coatings are common in several samples independent of depositional environment (Fig. 3B). Occasionally, excessive microcrystalline quartz also occurs in the intergranular pore space (Fig. 3C). In a few sandstones, the detrital grain surfaces of quartz are only partly covered by microcrystalline quartz giving rise to growth of larger quartz overgrowths (Fig. 3C). The amount of quartz overgrowths varies from 0.2 to 10.8 vol%. Illite is present in all samples and depositional environments and occurs as fibrous and honeycomb-structured coatings (Fig. 3D). Authigenic illite occurs as protruding fibres growing from honeycomb-structured illitic-smectitic clay. Illite fibres alternate with quartz overgrowths, and are at times enclosed in quartz overgrowth (Fig. 3D).

Porosity versus permeability – The sandstones with highest porosity and permeability are dominated by microcrystalline

quartz coatings and only little diagenetic illite is present together with a small amount of detrital clay (Fig. 4; Pedersen 2017). These sandstones are from the upper, middle and lower shoreface. Two groups of sandstones are defined based on intermediate porosity and low to intermediate permeability. Of these two groups, sandstones with quartz overgrowths and minor illite have slightly higher permeability than sandstones with microcrystalline quartz coatings and high illite and high detrital clay contents (Fig. 4). These latter samples are from lower and middle shoreface. Also the Fe-carbonate-cemented sandstones, which have the lowest porosity and permeability in the Heno Formation (Fig. 4), represent lower and middle shoreface samples.

Comparison between the Ravn-1, Ravn-2 and Ravn-3 wells – The Ravn-3 well was correlated with the Ravn-1 and Ravn-2 wells based on available core and well log data (Fig. 2). The various diagenetic phases in the Ravn-3 well can be recognised in the other Ravn wells. Variations occur, such as quartz overgrowth and illitisation of detrital clay being more common in the Ravn-1 well, compared to authigenic illite in the Ravn-3 well, but the reservoir units can still be recognised. The variations seen in the Ravn-1 cores are also present in the Ravn-2 cores together with additional fractures filled with barite and ankerite. The porosity and permeability in the Ravn-1 and Ravn-2 wells lie within the same range as the sandstones in the Ravn-3 well (Fig. 4).

Fig. 3. **A:** Abundant Fe-dolomite (Fe-Do) and ankerite (An) occluding porosity and permeability. Remnants of the original early calcite (Ca) cement are present. **B:** Random and abundant microcrystalline quartz (MQ) coating detrital quartz grain, preventing quartz overgrowth (QO). Note the fibrous illite (IL). **C:** Microcrystalline quartz on detrital quartz and in pore space together with authigenic illite. Quartz overgrowth is partly enclosing microcrystalline quartz indicating that the quartz overgrowth precipitated later. **D:** Abundant fibrous illite growing from honeycomb-structured illite succeeding microcrystalline quartz and alternating with quartz overgrowth (QO).



Discussion

Early carbonate cement – Intergrown sparry Fe-dolomite and ankerite cement (Fig. 3A) is interpreted to be sourced from dissolved calcite from shell fragments. Calcite inclusions still occur between Fe-dolomite and ankerite. This is supported by quartz grains appearing to be ‘floating’ in the carbonate cement, which indicates the previous presence of an early carbonate cement or fossils. Fe-carbonates are considered more stable than calcite during late diagenesis and often replace earlier phases of carbonates (Worden & Burley 2003).

Early microcrystalline quartz – When early diagenetic microcrystalline quartz is present in the sandstones only minor quartz overgrowth has precipitated (Fig. 3B). A biogenic opal CT phase, which has been dissolved without trace, may have resulted in supersaturated pore waters that sustained nucleation of microcrystalline quartz. Grain-coating microcrystalline quartz has previously been proposed to preserve reservoir quality by impeding quartz overgrowth, which otherwise may occlude intergranular porosity and reduce permeability (Aase *et al.* 1996; Jahren & Ramm 2000; Weibel *et al.* 2010). The random growth of microcrystalline quartz may retard further development of both new microcrystalline quartz and quartz overgrowth (Jahren & Ramm 2000; Weibel *et al.* 2010). When microcrystalline quartz does not fully cover detrital quartz, it cannot inhibit precipitation of quartz overgrowth (Aase *et al.* 1996; Weibel *et al.* 2010).

Quartz overgrowths – Late diagenetic quartz overgrowths formed where the quartz grains were only partly covered

by microcrystalline quartz. The quartz overgrowths probably formed under low silica oversaturation, which favoured less nucleation and promoted the growth of larger crystals (Fig. 3C; Jahren & Ramm 2000). More intensive quartz ce-

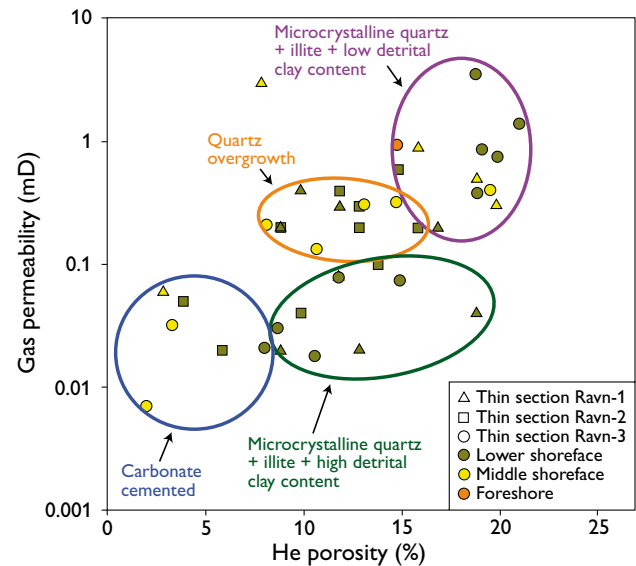


Fig. 4. He porosity versus air permeability for all thin section samples from the Ravn-3 well, together with data from the Ravn-1 and Ravn-2 wells. The thin section samples follow the trends from the Ravn-3 well marked by the four ellipses, which depict the four characteristics of the diagenesis. The purple ellipse comprises samples dominated by microcrystalline quartz, illite and low detrital clay content. The green ellipse includes samples dominated by microcrystalline quartz, illite and high detrital clay content. The orange ellipse comprises samples dominated by quartz overgrowth and the blue ellipse by extensive sparry carbonate cement.

mentation would have been expected in these quartz-rich sandstones (Bjørlykke *et al.* 1989) as they have been buried to a depth of > 4 km and hence exposed to temperatures of 112–117°C as documented by vitrinite reflectance.

As no stylolites were observed and as quartz overgrowth precipitated before and alternating with illite growth, another source for silica must have been present prior to transformation of smectite to illite. The continued precipitation of quartz overgrowth was probably from a silica source from the transformation of smectite to illite and dissolution of K-feldspar (Hower *et al.* 1976; Boles & Franks 1979). This is supported by the honeycomb-structured smectite-illite coatings and partially dissolved detrital K-feldspar.

Illite – Illite occurring as honeycomb structured coatings (Fig. 3D) is a strong indicator of a smectite precursor (e.g. Pollastro 1985). During burial, the percentage of illite in mixed-layer illite/smectite compared to smectite increases since smectite becomes more unstable with increasing temperature and pressure (Pollastro 1985), which may be the reason why only illite is present in the Ravn-3 well.

The honeycomb-structured illite commonly forms nucleation or growth points for fibrous illite. K-feldspar is typically dissolved concomitantly with smectite dissolution, and K-feldspar can be an additional source for K⁺ and Al³⁺ for further illite precipitation (Hower *et al.* 1976; Boles & Franks 1979). The additional K⁺ and Al³⁺ from the dissolution of K-feldspar might have led to further precipitation of the fibrous illite on illite honeycomb structures and singular precipitation in pore space. Fe-dolomite-ankerite rhombs are considered a by-product of the transition from smectite to illite, which may liberate Ca²⁺ and Fe²⁺.

Conclusions

The porosity and permeability of the reservoir sandstones in the Ravn-3 well are controlled by the diagenetic phases formed during early and late diagenesis.

The reservoir sandstones with the highest porosity and permeability are dominated by low to moderate amounts of microcrystalline quartz, illite and detrital clay. However, the more distal lower shoreface sandstones with the same dominating diagenetic phases, but with higher detrital clay content, are considered a poor reservoir due to low porosity and permeability. Sandstones with dominance of quartz

overgrowth and low detrital clay content have moderate to high porosity and low permeability. Carbonate-cemented sandstones are considered non-reservoir due to insignificant porosity and low permeability.

References

- Aase, N.E., Bjørkum, P.A. & Nadeau, P.H. 1996: The effect of grain-coating microquartz on preservation of reservoir porosity. *AAPG Bulletin* **80**, 1654–1673.
- American Petroleum Institute 1998: API Recommended Practice 40. Recommended practices for core analysis, 240 pp. Second edition. Washington DC: API Publishing Services.
- Bjørlykke, K., Ramm, M. & Saigal, G.C. 1989: Sandstone diagenesis and porosity modification during basin evolution. *Geologische Rundschau* **78**, 243–268.
- Boles, J.R. & Franks, S.G. 1979: Clay diagenesis in Wilcox sandstones of southwest Texas: implications of smectite diagenesis on sandstone cementation. *Journal of Sedimentary Research* **49**, 55–70.
- Hower, J., Eslinger, E.V., Hower, M.E. & Perry, E.A. 1976: Mechanism of burial metamorphism of argillaceous sediment: 1. Mineralogical and chemical evidence. *Geological Society of America Bulletin* **87**, 725–737.
- Jahren, J. & Ramm, M. 2000: The porosity-preserving effects of microcrystalline quartz coatings in arenitic sandstones: examples from the Norwegian continental shelf. In: Worden, R.H. & Morad, S. (eds): *Quartz cementation in sandstones*. International Association of Sedimentologists Special Publication **29**, 271–280.
- Johannessen, P.N., Dybkjær, K., Andersen, C., Kristensen, L., Hovikoski, J. & Vosgerau, H. 2010: Upper Jurassic reservoir sandstones in the Danish Central Graben: new insights on distribution and depositional environments, 12–34. In: Vining, B.A. (ed.): *Petroleum Geology: From Mature Basins to New Frontiers*. Proceedings of the 7th Petroleum Geology Conference. Geological Society, London.
- Panterra Geoconsultants 2011: Sedimentology, petrography and reservoir quality of cores from the Ravn-3 well, North Sea, Denmark. GEUS Archive Report File No **28698**.
- Pedersen, S.S. 2017: The diagenetic impact on reservoir sandstones of the Heno Formation in the Ravn-3 well, Danish Central Graben, Denmark. Unpublished Master thesis, University of Copenhagen.
- Pollastro, R.M. 1985: Mineralogical and morphological evidence for the formation of illite at the expense of illite/smectite. *Clays and Clay Minerals* **33**, 265–274.
- Taylor, T.R., Giles, M.R., Hathon, L.A., Diggs, T.N., Braunsdorf, N.R., Birbiglia, G.V., Kittridge, M.G., Macaulay, C.I. & Espejo, I.S. 2010: Sandstone diagenesis and reservoir quality prediction: Models, myths, and reality. *AAPG Bulletin* **94**, 1093–1132.
- Weibel, R., Friis, H., Kazerouni, A.M., Svendsen, J.B., Stokkendal, J. & Poulsen, M.L.K. 2010: Development of early diagenetic silica and quartz morphologies – examples from the Siri Canyon, Danish North Sea. *Sedimentary Geology* **228**, 151–170.
- Worden, R. & Burley, S. 2003: Sandstone diagenesis: the evolution of sand to stone. In: Burley, S.D. & Worden, R.H. (eds): *Sandstone diagenesis: recent and ancient*. International Association of Sedimentologists Special Publication **4**, 3–44.

Authors' addresses

S.P., *University of Copenhagen, Department of Geosciences and Natural Resource Management, Øster Voldgade 10, DK-1350 Copenhagen K, Denmark.*

E-mail: *simonepeder89@gmail.com.*

R.W., N.H.S. & P.J., *Geological Survey of Denmark and Greenland, Øster Voldgade 10, DK-1350 Copenhagen K, Denmark.*

Potential for brine storage near the gas storage facility at Lille Torup, northern Jylland, Denmark

Morten Leth Hjuler, Morten Sparre Andersen, Carsten Møller Nielsen, Anders Mathiesen, Lars Kristensen, Nina Skaarup and Lars Henrik Nielsen

This study is based on a feasibility study for the Danish Energinet.dk to identify potential formations for brine storage near the gas storage facility at Lille Torup, northern Jylland, Denmark (Fig. 1; Hjuler *et al.* 2017).

Located on top of a salt structure, the gas storage facility comprises seven caverns, which have been washed out by circulating water in the salt dome. One cavern contains *c.* 520.000 m³ of intrusive brine that must be disposed of in order to increase the storage volume for gas. One option is to inject the brine into the subsurface if a target with appropriate storage properties can be identified, but it is a prerequisite that the stored brine does not compromise freshwater reservoirs. Due to cost considerations, the brine storage should be situated within a radius of 50 km of the gas storage facility and at a depth not exceeding 2000 m.

Based on the national geothermal research conducted during the last decade, a number of sandy formations are considered potential storage reservoirs (Fig. 2; e.g. Mathiesen *et al.* 2009; Vosgerau *et al.* 2016). Around Lille Torup, these include the Bunter Sandstone/Skagerrak, Gassum, Haldager Sand and Frederikshavn formations where the two former formations are discarded due to present-day burial depths exceeding 2000 m. In addition, the Chalk Group is considered a potential storage formation due to its importance as a hydrocarbon reservoir in the North Sea, however, due to risk of leakage to the younger sediments and risk of environmental issues, the chalk was discarded as potential storage zone.

Geological background

The Lille Torup area is located centrally in the Danish Basin, where the Upper Permian–Mesozoic succession is 5–5.5 km thick. The basin was formed in the Late Carboniferous–Early Permian with basal Rotliegendes coarse-grained clastic sediments and thick Zechstein salts overlain by Triassic sandstone, mudstone, carbonate rocks and salt (Nielsen 2003). These are followed by Lower Jurassic mudstone, Middle Jurassic sandstone, Upper Jurassic–Lower Cretaceous mudstone and siltstone with few sandstone layers. The Mesozoic succession terminates with *c.* 1200 m thick carbonate deposits.

The salt structure at Lille Torup consists of mobilised Zechstein salt penetrating the Mesozoic succession. Its top point is *c.* 250 m below the present-day surface.

The Haldager Sand Formation in the northern part of the basin is 2–150 m thick, but may exceed 200 m in rim synclines of salt structures, where sandstone commonly dominates the lithology. The Frederikshavn Formation is primarily present in the northern part of the basin and frequently includes sandstone layers. Its thickness decreases southwards from 150–300 m to a few metres. The more than 1000 m thick chalk- and limestone-dominated Chalk Group constitutes the topmost pre-Quaternary formation in large parts of the Danish Basin.

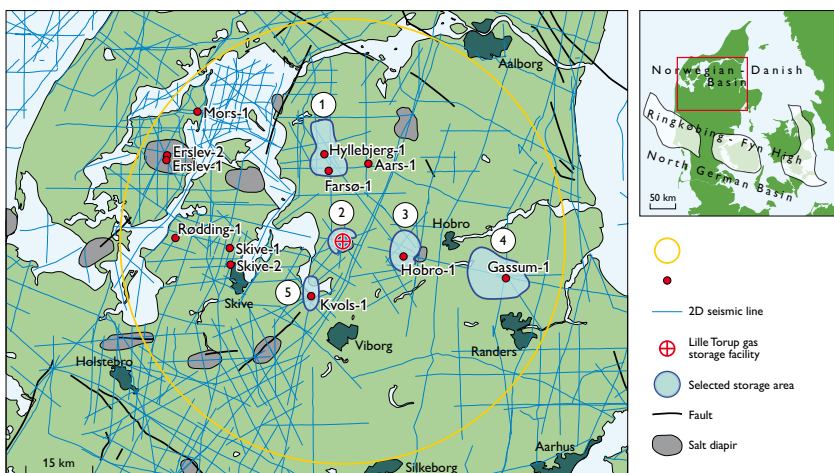


Fig. 1. The study area and selected storage areas within a radius of 50 km of the Lille Torup gas storage facility.

System	Lithostratigraphic unit	
Quaternary	Post Chalk Group	
Cretaceous	Chalk Group	Assumed seal
	Lower Cretaceous unit	Assumed seal
Jurassic	Frederikshavn Fm	Reservoir
	Børglum Fm	
	Flyvbjerg Fm	
	Haldager Sand Fm	Reservoir
	Fjerritslev Fm	Assumed seal
Triassic	Gassum Fm	Reservoir
	Vinding Fm	
	Oddesund Fm	
	Tønder Fm	
	Falster Fm	
	Ørslev Fm	
	Bunter Sandstone Fm	Reservoir
Permian	Zechstein Group	

Fig. 2. Lithostratigraphic chart showing potential reservoirs (yellow) and assumed seals (brown).

Methods

The subsurface within a radius of 50 km of the Lille Torup storage facility was screened for potential sandstone reservoirs suitable for storage. The local database comprises 11 vertical deep wells and an open grid of regional 2D seismic profiles of variable quality and resolution (Fig. 1). Some wells were excluded from the database due to location on top of salt structures (Erslev-1–2 and Skive-1–2), uncertain data quality (Aars-1) or separation from the Lille Torup storage facility by fjord water (Mors-1).

The Danish geothermal WebGIS application (Vosgerau *et al.* 2016) provided maps of formation depth, formation thickness and potential reservoir sandstone thickness as well as reservoir parameters of relevant wells. The potential reservoir sandstone thickness map was developed for assessment of the geothermal potential and is used in this study as an indicator for injection capacity.

Reservoir properties derived from well logs include the depths of formation top and base, formation thickness, gross sand thickness (i.e. cumulated thickness of all sandstone layers), potential reservoir sandstone thickness (i.e. cumulated thickness of sandstone layers with a shale content <30% and a porosity >15%), as well as averaged values of porosity, permeability and transmissivity of the potential reservoir sandstone. For uncertainty considerations, see <http://dybgeotermi.geus.dk/>.

Potential formations for brine storage

Five potential storage areas were defined based on reservoir quality assessments obtained by integration of well-log data and WebGIS data improved with locally refined seismic interpretations. Injectivity assessments were performed using ECLIPSE 100 reservoir simulation software and Petrel software. See Hjuler *et al.* (2017) for details.

The Haldager Sand Formation (Figs 3A–C) is presently buried more than 2000 m in large parts of the study area, but more shallow occurrences exist. The generally 50–150 m thick formation is dominated by sandstone known to be quartz-rich, which points to good reservoir properties. In areas of relatively shallow burial (<2000 m), the Haldager Sand Formation may constitute a storage formation.

The Frederikshavn Formation (Figs 3D–F) is buried less than 2000 m and generally more than 100 m thick; it is thickest east of Lille Torup. Several potential storage reservoirs with sufficient lateral extent can be identified. The Frederikshavn Formation constitutes a storage option.

The Chalk Group (Figs 3G, H) is buried at 100–700 m depth and is more than 1 km thick. On top of the Lille Torup salt structure, the salt movements may have fractured the c. 250 m of chalk, and increased permeability and thus reservoir quality. However, the overlying Quaternary deposits are not expected to possess sealing qualities and brine storage in the chalk could lead to environmental issues. The Chalk Group is therefore discarded as a potential storage formation.

Potential seals

The Chalk Group outside the top of the Lille Torup salt structure is expected to effectively seal off pore water from the sandy formations beneath it due to its low permeability and great thickness. In addition, the clayey Lower Cretaceous unit is assumed to be of sufficiently low permeability to prevent pressure and pore-water propagation from below.

Reservoir parameters of the formations

The Haldager Sand Formation mainly comprises sandstone layers with porosities in the 18–22% range and permeabilities in the 140–360 mD range (Table 1). Disregarding burial depth, the Haldager Sand Formation is assumed to provide suitable storage properties.

The sandstone layers of the Frederikshavn Formation have porosities in the 17–30% range, permeabilities in the 110–1500 mD range and the thickness of potential reservoir sandstone in the 6–66 m range (Table 1). In the Kvol-1 well, however, the formation seems to have little or no storage potential, assumedly because clay minerals reduce both pore

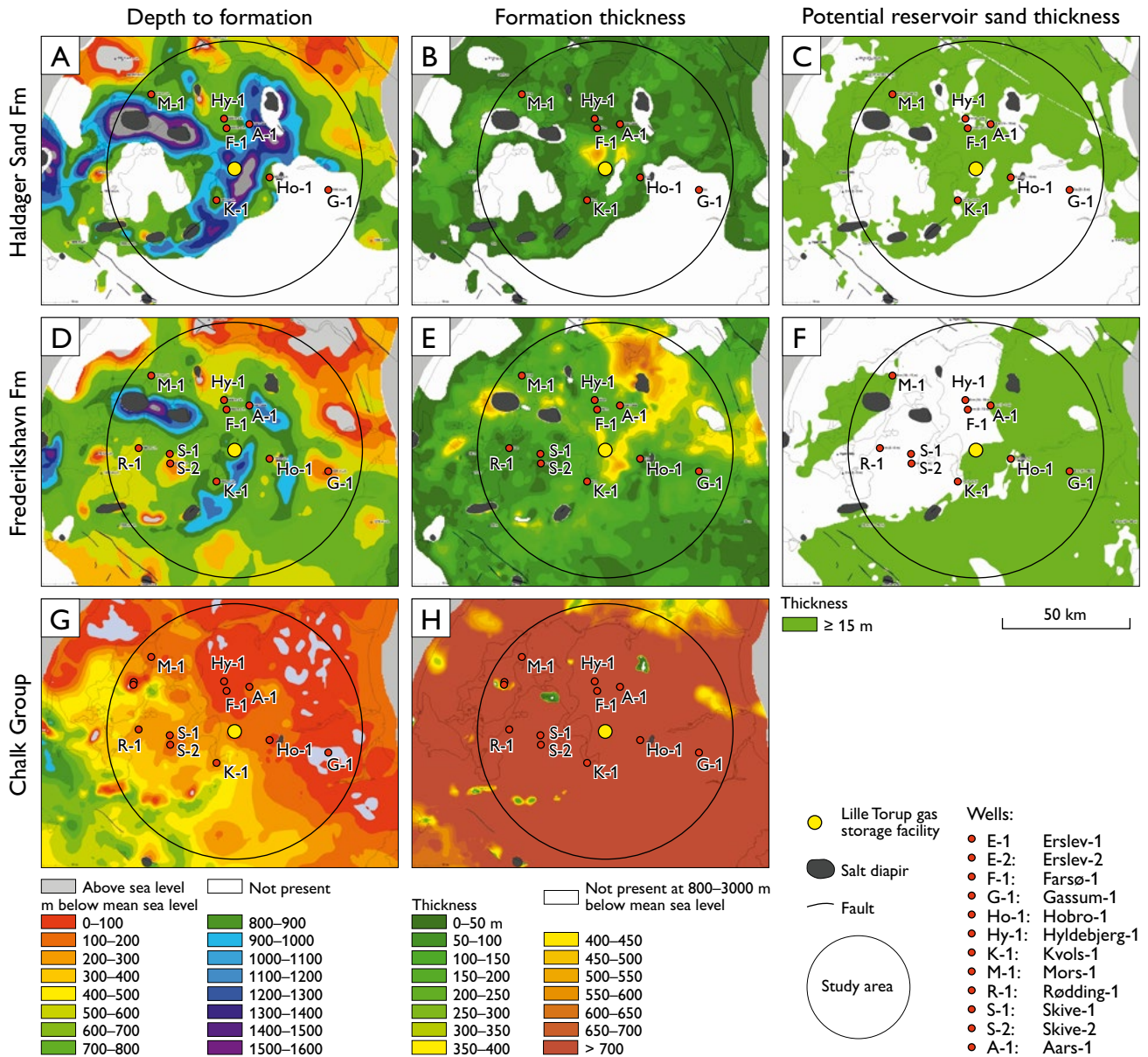


Fig. 3. WebGIS-generated maps of potential brine storage formations in the study area. Reservoir quality is assessed based on depth to formation top, formation thickness and potential reservoir sand thickness.

space and permeability. The thickness of potential reservoir sandstone decreases from east to west (Fig. 3F).

Suggested areas for brine storage

The WebGIS-based maps (Fig. 3) are suitable for assessing reservoir quality trends on a regional scale of tens of kilometres, but not on a local scale of up to a few kilometres as uncertainties will be significant. Thus, the areas suggested for brine storage cover several square kilometres (Fig. 1).

Area 1 includes the Hyldebjerg-1 and Farsø-1 wells (Figs 1, 3), in which the Haldager Sand Formation is evaluated to

provide the better storage reservoir, with higher porosities and permeabilities than the Frederikshavn Formation (Table 1). The two formations offer two storage options within a narrow depth interval.

Area 2 is situated above the rim syncline next to the salt structure beneath Lille Torup (Figs 1, 3), where the Frederikshavn and Haldager Sand formations may be up to 300–400 m thick (Figs 3A, D) and include potential reservoir sandstone units more than 15 m thick at depths shallower than 1400 m. However, existing seismic data are insufficient to confirm these thickness estimates and the formation depths may be closer to 2000 m due to deposition in the rim syn-

Table 1. Reservoir parameters of the Haldager Sand and Frederikshavn formations in five areas suggested for brine storage

Well	Formation	Thickness		Property						
		Top below mean sea level (m)	Base below mean sea level (m)	Formation thickness (m)	Gross sand (m)	Potential reservoir sandstone (m)	Average porosity (mD)	Average reservoir permeability (mD)	Reservoir transmissivity (mD)	Well injection index (m ³ /bar/day)
<i>Area 1</i>										
Farsø-1	Haldager Sand	1934	1952	18	16	11	18	138	2	
Hyllebjerg-1	Haldager Sand	1885	1894	9	9	9	22	344	3	
Average	Haldager Sand	1909	1923	14	12	10	20	241	3	
Farsø-1	Frederikshavn	1689	1839	150	25	9	17	106	1	
Hyllebjerg-1	Frederikshavn	1664	1810	146	37	15	19	188	3	
Average	Frederikshavn	1676	1824	148	31	12	18	147	2	
<i>Area 2</i>										
Average	Haldager Sand	1900	1920	20	16	12	20	255	3	
Average	Frederikshavn	1700	1756	56	33	8	15	133	1	
<i>Area 3</i>										
Hobro-1	Haldager Sand	1852	1891	39	24	18	19	175	3	
Hobro-1	Frederikshavn	1741	1806	65	12	6	19	238	1	
<i>Area 4</i>										
Gassum-1	Haldager Sand	1176	1178	2	2	2	19	188	0.5	
Gassum-1	Frederikshavn	1053	1154	101	66	65	30	1500	97	
<i>Area 5</i>										
Kvols-1	Haldager Sand	1940	1955	15	15	9	21	363	3	
Kvols-1	Frederikshavn	1856	1912	56	56	0	5	0	0	
Well average	Haldager Sand	1757	1774	17	13	10	20	242	2	9
Well average	Frederikshavn	1601	1704	104	39	19	28	406	8	27

Reservoir parameters based on the vertical wells in the suggested areas (Fig. 1). Reservoir parameters of area 2 based on average values of the Hyllebjerg-1, Farsø-1, Hobro-1 and Kvols-1 wells. For detailed descriptions of parameters and uncertainties, see <http://dybgeotermi.geus.dk/>.

cline. Thus, the estimated reservoir parameters are based on average values of the nearby wells, Hyllebjerg-1, Farsø-1, Hobro-1 and Kvols-1.

Area 3 includes the Hobro-1 well (Figs 1, 3), in which the Haldager Sand and Frederikshavn formations are estimated to offer two storage options within a narrow depth interval, the Haldager Sand Formation providing the better reservoir (Table 1).

Area 4 includes the Gassum-1 well (Figs 1, 3). The Frederikshavn Formation is more shallowly buried in this area (<1000 m; Fig. 3D) and offers the most excellent storage properties in the study area (Table 1). The Haldager Sand Formation is not present in Area 4 (Fig. 3A).

Area 5 includes the Kvols-1 well (Figs 1, 3). This well indicates good reservoir properties of the Haldager Sand Formation at a burial depth of 1940–1955 m, but also that the Frederikshavn Formation is a poor reservoir (Table 1).

Assessment of injection rate and pore pressure

Indicative injection rates (shown as a well injection index) and pore pressures for the Frederikshavn and Haldager Sand formations in the entire study area are presented in Table 1. Reservoir parameters are calculated as averages of all wells. The well injection index is assumed to correspond to the well production index; the pressure of the subsurface pore fluid in the formations is assumed to be hydrostatic.

Conclusions

The Frederikshavn and Haldager Sand formations constitute potential brine storage formations in the larger Lille Torup area and are sealed off by the Chalk Group and Lower Cretaceous unit. The Haldager Sand Formation offers the best reservoir properties but at greater depth than the Frederikshavn Formation. The well injectivity index and pore pressure indicate favourable conditions for brine storage. Five potential storage areas are suggested, compromising between burial depth and distance from the gas storage facility.

References

- Hjuler, M.L., Andersen, M.S., Nielsen, C.M., Mathiesen, A., Kristensen, L., Skaarup, N. & Nielsen, L.H. 2017: Potential for establishing an injection well for brine storage near the gas storage facility at Lille Torup. Danmarks og Grønlands Geologiske Undersøgelse Rapport **2017/20**, 34 pp.
- Mathiesen, A., Kristensen, L., Bidstrup, T. & Nielsen, L.H. 2009: Vurdering af det geotermiske potentiale i Danmark. Danmarks og Grønlands Geologiske Undersøgelse Rapport **2009/59**, 85 pp.
- Nielsen, L.H. 2003: Late Triassic – Jurassic development of the Danish Basin and the Fennoscandian Border Zone, southern Scandinavia. In: Ineson, J.R. & Surlyk, F. (eds): The Jurassic of Denmark and Greenland. Geological Survey of Denmark and Greenland Bulletin **1**, 459–526.
- Vosgerau H., Mathiesen A., Andersen M.S., Boldreel L.O., Hjuler M.L., Kamla E., Kristensen L., Pedersen C.B., Pjetursson B. & Nielsen L.H. 2016: A WebGIS portal for exploration of deep geothermal energy based on geological and geophysical data. Geological Survey of Denmark and Greenland Bulletin **35**, 23–26.

Authors' address

Geological Survey of Denmark and Greenland, Øster Voldgade 10, DK-1350 Copenhagen, Denmark. E-mail: MLH@geus.dk.

Shale fabric and organic nanoporosity in lower Palaeozoic shales, Bornholm, Denmark

Lucy Malou Henningsen, Christian Høimann Jensen, Niels Hemmingsen Schovsbo, Arne Thorshøj Nielsen and Gunver Krarup Pedersen

In organic-rich shales, pores form during oil and gas genesis within organic matter (OM) domains. The porosity thus differs markedly from that of conventional reservoir lithologies. Here we present the first description of shale fabric and pore types in the lower Palaeozoic shales on Bornholm, Denmark. The pores have been studied using the focused ion beam scanning electron microscope (FIB-SEM) technique, which allows for high resolution SEM images of ion polished surfaces. Shale porosity is influenced by many factors including depositional fabric, mineralogical composition, diagenesis and oil and gas generation (Schieber 2013). Here we discuss some of these factors based on a study of lower Palaeozoic shale samples from the Billegrav-2 borehole on Bornholm (Fig. 1) undertaken by Henningsen & Jensen (2017). The shales are dry gas-mature (2.3% graptolite reflectance; Petersen *et al.* 2013) and have been extensively used as analogies for the deeply buried Palaeozoic shales elsewhere in Denmark (Schovsbo *et al.* 2011; Gautier *et al.* 2014).

The Danish lower Palaeozoic shale gas play was tested by the Vendsyssel-1 well drilled in northern Jylland in 2015. Gas was discovered within a *c.* 70 m thick gas-mature, organic-rich succession (Ferrand *et al.* 2016). However, the licence was subsequently relinquished, due to a too low gas content. The present study confirms a close similarity of pore development between the shales on Bornholm and in the Vendsys-

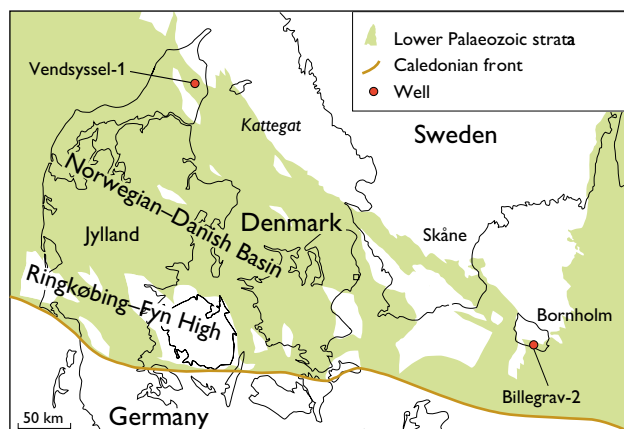


Fig. 1. Distribution of lower Palaeozoic strata and wells mentioned in the text. Modified from Schovsbo *et al.* (2011).

sel-1 indicating a high porosity within this stratigraphic level throughout the subsurface of Denmark. However, the rather different development of porosity in the different shale units presents a hitherto neglected aspect of the Palaeozoic gas play in Denmark.

Methods

Ten samples were selected for thin section and nanoscopic pore analyses based on a screening of 30 samples from the Billegrav-2 borehole (Fig. 2). Total organic carbon (TOC) was determined by measuring CO₂ evolved from the

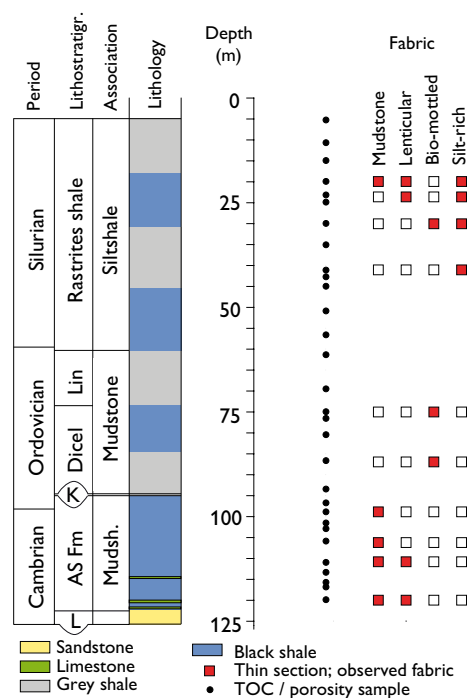


Fig. 2. Stratigraphy of the Billegrav-2 core and overview of samples and fabric types. Modified from Schovsbo *et al.* (2011). Facies associations in the interval 35–125 m are adopted from the Billegrav-1 well described by Pedersen (1989); above this level the association is based on the present text. **AS Fm**: Alum Shale Formation. **Dicel**: Dicellograptus shale. **K**: Komstad Limestone. **Lenticular**: Lenticular clast-rich mudstone. **Lin**: Lindegård Mudstone. **Lithostratigr**: Lithostratigraphy. **L**: Læså Formation. **Mudsh**: Mudshale. Fabric types: see text.

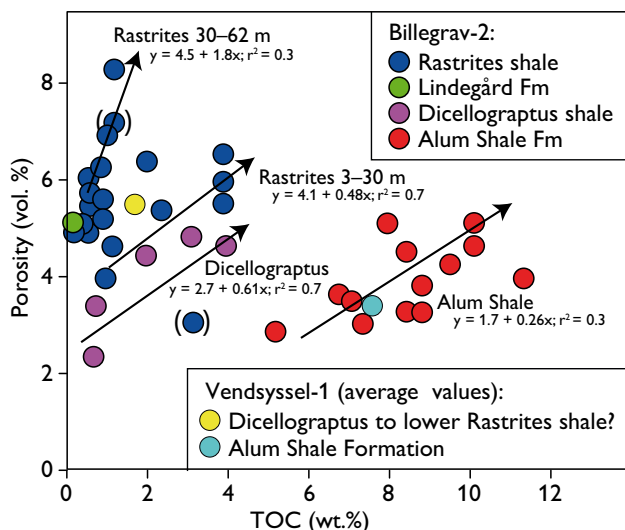


Fig. 3. Total organic carbon (TOC) content versus porosity. Arrows represent positive correlation trends (significant at a calculated probability of 0.1) within the stratigraphical units. Points in brackets represent data omitted in the correlations. Data from Vendsyssel-1 are wire-line, log-derived average values (Ferrand *et al.* 2016).

combustion of acid pre-treated samples at 1300°C. Porosity was measured in a double-chambered helium porosimeter at the Geological Survey of Denmark and Greenland. Thin sections with a thickness of about 20 μm were prepared by Pelcon Material & Testing Aps. The SEM imaging of nano- to microscale porosity was performed on cross-sections that were milled and surface polished using a focused ion beam (FIB) at the Technical University of Denmark. In order to minimise erosion of the ion-cut surface, the selected cross-section site was protected with a 3 μm thick layer of platinum. No coating of the imaged surfaces was applied.

Results

Each of the stratigraphical units shows a statistically significant correlation between TOC and porosity (Fig. 3). The Rastrites shale at 30–62 m in the borehole is the most porous shale and is characterised by the highest ratio between TOC and porosity, whereas the Alum Shale is the least porous shale, characterised by the lowest ratio between TOC and porosity (Fig. 3). The Dicellograptus shale plots between these trends together with samples from the upper 30 m of the Rastrites shale (Fig. 3).

Four shale fabrics are distinguished: (1) a dark-coloured mudstone fabric with high concentrations of OM and pyrite, (2) a lenticular clast-rich mudstone fabric, (3) a silt-rich mudstone fabric and (4) a bio-mottled mudstone fabric.

The dark-coloured mudstone fabric was observed in five samples and it is the dominant fabric in the Alum Shale. The fabric comprises a clay-dominated mudstone with variable silt-content that sometimes contains sand-sized authigenic barite (Fig. 4A). The dark colour is due to high contents of dispersed OM and pyrite. This fabric is attributed to a generally slow settling of particles in a low-energy depositional environment.

The lenticular, clast-rich mudstone fabric is seen in four samples from the Alum and Rastrites shales (Fig. 2). The content of OM and pyrite is highest in the dark grey samples and lowest in the pale grey samples (Fig. 4A). The typical lenticular clasts range in size from 500 μm to more than 2 mm and are composed of clay and silt-sized material. On a macroscopic scale, the lenticular clasts create a laminated appearance to the shale. The clasts are interpreted as deposited during episodic increases in energy in an otherwise low-energy environment.

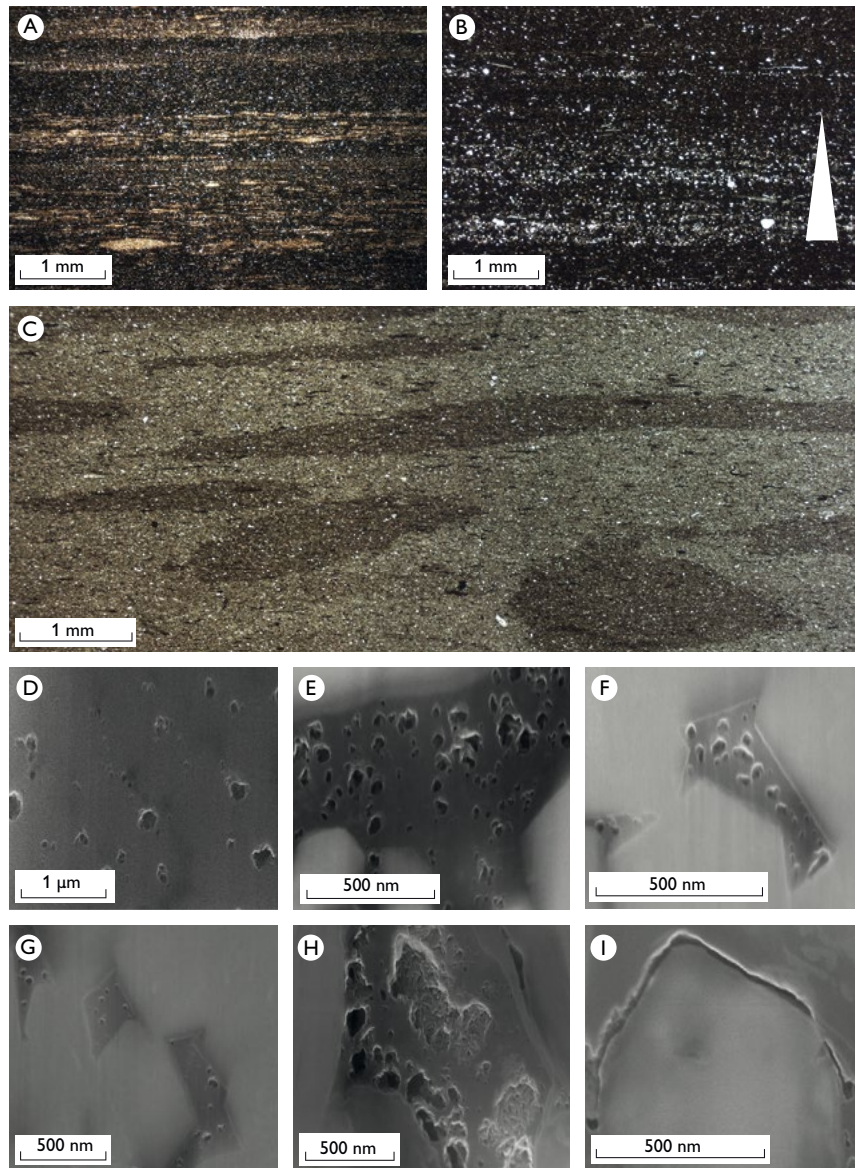
The silt-rich mudstone fabric (Fig. 4B) shows varying concentrations of disseminated silt grains and is observed in four samples from the Rastrites shale (Fig. 2). More dense accumulations of silt grains in laminae and streaks are typically carbonate cemented. The fabric is assumed to be connected to episodic higher-energy currents in the otherwise low-energy depositional environment.

The bio-mottled mudstone fabric (Fig. 4C) occurs in three samples from the Dicellograptus and Rastrites shales. The fabric contains low amounts of OM that also tends to be irregularly distributed, both across and along the bedding planes. The distribution reflects the activities of deposit-feeding organisms. The fabric is interpreted as deposited in a more oxic marine environment characterised by low OM levels and presence of infaunal organisms.

Pores related to the OM vary from simple isolated pores to large pore populations with internally complex structures. Isolated pores are usually discrete and equant in shape and can occur both widely disseminated and in more dense populations (Figs 4D, E). They also occur in OM occupying the space between individual pyrite crystals in framboids (Figs 4F, G). The pore-size is usually <100 nm. More dense populations of <50 nm-sized, foam-like pores are also observed. This pore type seems to populate entire OM domains, but may also be surrounded by non-porous zones in presumably coherent OM domains. A third pore type consists of highly irregular pores with complex internal sub-parts (Fig. 4H). This type has a stalactite-like texture with irregular and serrated internal pore surfaces and may have internal fibrous textures resembling wood wool.

Pores related to the inorganic particles are mainly associated with irregularly shaped grains of quartz and pyrite (Fig. 4I). These pores usually appear as discontinuous slits along parts of the grain surface or as curved embayments into the

Fig. 4. Micrographs of different mudstone fabrics and pores recognised in the Palaeozoic shales. **A:** Dark coloured mudstone fabric intercalated with laminae of lenticular clast-rich mudstone fabric, 119.78–119.80 m (Alum Shale Formation). **B:** Silt-rich mudstone fabric with normal grading, 41.15–41.17 m (Rastrites shale). **C:** Bio-mottled mudstone fabric, presumably *Dicellograptus*, 86.68–86.70 m (Dicellograptus shale). Organic pores: **D:** Rounded pores, 74.77–75.01 m (Dicellograptus shale). **E:** Sub-rounded pores, 24.78–24.80 m (Rastrites shale). **F:** Subrounded to rounded pores in pyrite, 115.63–115.65 m (Alum Shale Formation). **G:** Subrounded to rounded pores in pyrite, 115.63–115.65 m (Alum Shale Formation). **H:** Irregularly shaped and complex pores, 24.78–24.80 m (Rastrites shale). Inorganic pores: **I:** Irregularly shaped pores surrounding silt- to clay-sized grains, 115.63–115.65 m (Alum Shale Formation).



grain, and they are up to several 100 nm long. Other pore types primarily related to inorganic particles are dissolution pores that occur where matrix minerals have become partly dissolved (Fig. 4I). This pore type occurs only along the edges of carbonate minerals, and the pores tend to be elongated and irregularly shaped.

Discussion

The variable correlation between the TOC content and porosity for the Alum, Dicellograptus and Rastrites shales indicates that pores in both organic and inorganic matter contribute to the total porosity. Within each shale unit the TOC content correlates with porosity suggesting that pores hosted in organic matter are dominant in all units but with additional contributions from inorganic porosity. A higher contribution

of inorganic interparticle pores is seen in the Dicellograptus and Rastrites shales that add to the overall more porous nature of these shales (Fig. 3). The Dicellograptus and Rastrites shales belong to the mudstone and siltstone associations of Pedersen (1989) whereas the Alum Shale belongs to the mudshale association (Fig. 2) and apparently the lithofacies was the main controlling factor of the porosity development.

SEM images show that the porosity predominantly occurs within amorphous OM domains intermingled with the inorganic matrix minerals, rather than as inter-particle pores between the matrix minerals. However, not all OM domains contain pores and those that do exhibit considerable variation in quantity, distribution and size of pores.

The presence of OM in the interparticle spaces cannot be explained entirely by the processes of admixing and subsequent compactional deformation of organic and inorganic

particles (cf. Kennedy *et al.* 2002). Instead, it appears that secondary OM migrated into interparticle spaces during maturation. This interpretation is supported by observations of well-connected viscous-like OM domains, which fill the spaces between matrix minerals. The dominant clay mineral in all the samples is illite (cf. Pedersen 1989), which was either a detrital mineral or formed after diagenetic transformation of smectite during burial maturation. It may be assumed that an early migration of secondary OM occurred during the temperature interval, which matches the diagenetic transformation of the clay minerals. This relationship between secondary OM and diagenetically formed illite was also observed by Schieber (2013) in gas-mature samples from the Devonian Marcellus Shale in North America. Loucks *et al.* (2012) suggested that most smectite is transformed to illite during early catagenesis, which supports the observation of presumed migrated OM as interparticle fill.

Comparison with Vendsyssel-1

One of the discouraging results of the Vendsyssel-1 well was the low porosity and the unfavourable pore distribution in the shales (Ferrand *et al.* 2016). The average TOC content and porosity in the Vendsyssel-1 well are within the same range as those measured in the Billegrav-2 core (Fig. 3). SEM images of the Alum Shale from the Vendsyssel-1 well show both non-porous OM in the mudstone fabric and porous OM of presumed secondary origin intermingled with clay minerals (Ferrand *et al.* 2016) similar to the observations from the Billegrav-2 core.

The similarity suggests that the lower Palaeozoic shales known from Bornholm are valid analogues for the deeply buried Palaeozoic shales in Denmark. However, the rather different porosity development in the individual shale units presents a hitherto neglected aspect of the Palaeozoic gas play in Denmark.

Conclusions

The study shows that the porosities of the lower Palaeozoic shales are related to both organic and inorganic matter. The dominating porosity types in all stratigraphical units are those observed within organic matter. A clear relationship between shale fabric and organic nanoporosity has been ob-

served in the lower Palaeozoic shales and this indicates that shale composition, depositional environment, and diagenesis have all influenced the porosity development. The TOC : porosity relationships in the Vendsyssel-1 well are nearly identical to those observed in shales from Bornholm indicating a high porosity. The Alum Shale is a low porous but TOC-rich shale whereas the two other shale units studied are low in TOC but relatively porous. This observation adds another variable factor to the Danish shale gas play (cf. Gautier *et al.* 2014).

Acknowledgements

Louise Belmonte, formerly at the Technical University of Denmark, is thanked for providing access to the FIB-SEM. This paper is a contribution to the GeoCenter Denmark projects 5–2015 and 3–2017.

References

- Ferrand, J., Demars, C. & Allache, F. 2016: Denmark – L1/10 Licence relinquishment recommendations report. Total E&P, Memo 1–9 Available from: <http://www.ft.dk/samling/20151/almdel/efk/bilag/353/1651289.pdf>. Verified 17.01.2018.
- Gautier, D.L., Schovsbo, N.H. & Nielsen, A.T. 2014: Resource potential of the Alum Shale in Denmark. Unconventional Resources Technology Conference (URTeC), 25–27 August 2014, Denver Colorado. SPE-2014-1931754-MS. 10 pp.
- Henningsen, L.M. & Jensen, C.H. 2017: A petrographic analysis of pores and their distribution in Palaeozoic organic-rich shale (the Alum Shale Formation, the Dicollograptus shale, and the Rastrites shale) from the Billegrav-2 core, Bornholm, Denmark, 110 pp. Unpublished Master thesis, University of Copenhagen. GEUS Report Files 34178 and 34179).
- Kennedy, M.J., Pevear, D.R. & Hill, R.J. 2002: Mineral surface control of organic carbon in black shale. *Science* **295**, 657–660.
- Loucks, R.G., Reed, R.M., Ruppel, S.C. & Hammes, U. 2012: Spectrum of pore types and networks in mudrocks and a descriptive classification for matrix-related mudrock pores. *AAPG Bulletin* **96**, 1071–1098.
- Pedersen, G.K. 1989: The sedimentology of Lower Palaeozoic black shales from the shallow wells Skelbro-1 and Billegrav-1, Bornholm, Denmark. *Bulletin of the Geological Society of Denmark* **37**, 151–173.
- Petersen, H.I., Schovsbo, N.H. & Nielsen, A.T. 2013: Reflectance measurements of zooclasts and solid bitumen in Lower Palaeozoic shales, southern Scandinavia: correlation to vitrinite reflectance. *International Journal of Coal Petrology* **114**, 1–18.
- Schieber, J. 2013: SEM observations on ion-milled samples of Devonian black shales from Indiana and New York: the petrographic context of multiple pore types. *AAPG Memoir* **102**, 153–171.
- Schovsbo, N.H., Nielsen, A.T., Klitten, K., Mathiesen, A. & Rasmussen, P. 2011: Shale gas investigations in Denmark: Lower Palaeozoic shales on Bornholm. *Geological Survey of Denmark and Greenland Bulletin* **23**, 9–12.

Authors' addresses

L.M.H., *Energinet, Tonne Kjærvej 65, DK-7000 Fredericia, Denmark; Email: lucymalou@gmail.com.*

C.H.J., *Region Sjælland, Alleen 15, DK-4180 Sorø, Denmark.*

N.H.S. & G.K.P., *Geological Survey of Denmark and Greenland, Øster Voldgade 10, DK-1350 Copenhagen K, Denmark.*

A.T.N., *Department of Geosciences and Natural Resource Management, University of Copenhagen. Øster Voldgade 10, DK-1350 Copenhagen K, Denmark.*

Chalk-glacitectonite, an important lithology in former glaciated terrains covering chalk and limestone bedrock

Stig A. Schack Pedersen, Peter Gravesen and Klaus Hinsby

A glacitectonite is defined as a brecciated sediment or a cataclastic sedimentary rock formed by glaciotectonic deformation (Pedersen 1988). The term tectonite was initially introduced by Sander (1912), mainly for tectonically brecciated metamorphic rocks in the Alps. In the classic work on cataclastic rocks, Higgins (1971) stated that the term covered all rocks with fabric displaying coordinated geometric features related to continuous flow during deformation. Therefore

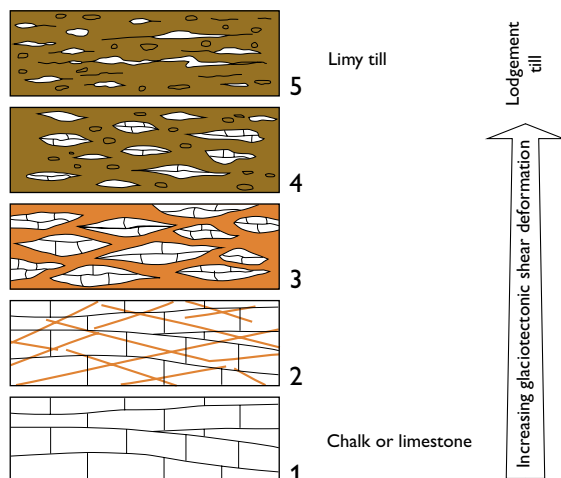


Fig. 1. Five steps in the progressive formation of chalk glacitectonite and limy till developed from bedrock of Danian limestone. The example illustrates the variation of deposits differentiated in the geological mapping of north-eastern Djursland, central Denmark (from Pedersen & Petersen 1997). 1: Undisturbed Danian limestone occurring in the lower part of the coastal cliff at Sangstrup Klint. 2: Anastomosing jointing is found in the limestone in the upper part of the cliff exposure. Note that the smallest angle between joints is located with a half-angle divide in the horizontal plan. This corresponds to a lateral stress in the foreland to an advancing ice margin. 3: Clasts of chalk have been broken off and displaced in a fine-grained matrix; a chalk-glacitectonite is formed. 4: During increased shearing the chalk clasts become more and more crushed with chalk pieces floating in a chalk-clay matrix. In-basinal erratics comprise clasts of Danian limestone and flint, ex-basinal erratics include basement stones (gneiss and granite), which start to appear in the glacitectonite derived from the overlying lodgement till. 5: During the continuous translocation away from the source area the chalk-glacitectonite is transformed into limy till (chalk moraine), which may also be classified as a local till dominated by in-basinal clasts of chalk and flint.

brecciated lithologies formed by glaciotectonic deformations can be termed tectonites. Banham (1977) suggested the prefix glaci- to clarify the relation to glacial dynamics. Furthermore, Pedersen (1988) suggested the application of the bedrock prefix. Thus, a chalk-glacitectonite is a brecciated chalk formed by shear deformation during a glacial advance over an exposed bedrock surface of chalk (Fig. 1). Hence the term describes a sedimentary rock in which the primary structures are so disturbed that they cannot be continuously traced, and a glaciotectonic fabric developed as joint fractures or shear surfaces superimposed on the lithology.

The significance of recognising chalk-glacitectonite from chalk and limestone bedrock is the difference in textural properties, which is fundamental in geological modelling. In areas dominated by glaciotectonic complexes, which include thrust sheets of pre-glacial sedimentary rocks, the sheets are subject to shearing and dragged along the sole of the ice during its movement over the glaciotectonic complex. Due to truncation and shear-drag, the glacitectonite forms at the base of the deformational layer in a lodgement till. From the source area, which typically is a detachment anticline, the



Fig. 2. A one-metre thick chalk-glacitectonite exposed in a cliff section in the northern part of Stevns Klint displays shear banding of clayey till material with cataclasts of chalk and flint. The source area for the chalk is Danian limestone which occurs more than 500 m from the exposure.



Fig. 3. The initial glaciotectionic deformation is a low-angle, anastomosing jointing, which is illustrated by an example of fractured Cretaceous chalk exposed in the northern part of the Stevns Klint cliff section.



Fig. 4. A chalk-glacitectorite developed with a limy matrix and rotated chalk clasts. Thin dark clayey shear bands illustrate the substantial amount of displacement within the rock type. Detail from the cliff section at Hvide Klint, south coast of Møn.

glacitectorite thins out in the direction of transport from 1–2 m (Fig. 2) to a thin shear zone only a few centimetres thick over a distance of one to a few kilometres (Pedersen 1996). Moreover, brecciation of thrust sheets displaced by glacial thrusting occurs within glaciotectionic complexes. The deformation ranges from initially anastomosing jointing (Figs 1, 3) to brecciation with bedrock clasts in crushed bedrock matrix (Fig. 4). The tectonic breccia distributed from the décollement zone at the base to the truncating glacial unconformity at the top may additionally be termed glacitectorites. Here we describe the occurrence and identification of chalk-tectorites.

Occurrences of chalk-glacitectorites

The occurrences of chalk-glacitectorites are naturally related to the areas dominated by bedrock of chalk and limestone which in Denmark includes the eastern, north-eastern and northern regions (Fig. 5). Bedrock exposures are found at Møns Klint and Stevns Klint in eastern Denmark, Sang-

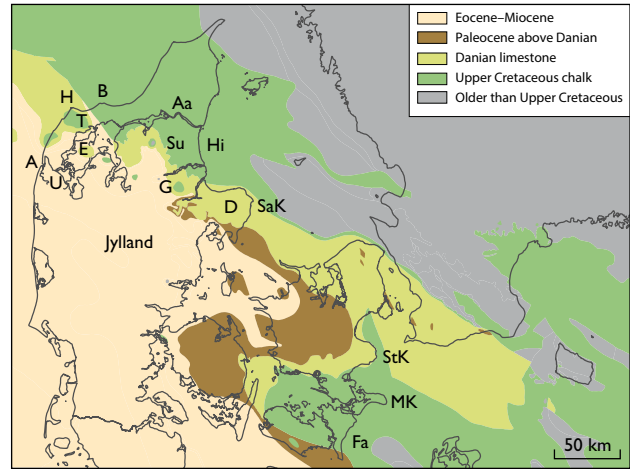


Fig. 5. Geological map showing the distribution of chalk and limestone in the bedrock of Denmark. Modified from Håkansson & Pedersen (1992).

H: Hanstholm. **B:** Bulbjerg. **T:** Thisted. **A:** Agger. **E:** Erslev. **U:** Uglev. **Aa:** Aalborg. **Su:** Suldrup. **Hi:** Himmerland. **G:** Gassum. **D:** Djursland. **SaK:** Sangstrup Klint. **StK:** Stevns Klint. **MK:** Møns Klint. **Fa:** Falster.

strup Klint (NE Djursland) in central Denmark, in the chalk pits in Aalborg and in limestone pits in adjacent areas in NE Himmerland. Chalk-glacitectorites occur at these outcrops. Furthermore, the cliffs at Agger, Bulbjerg and Hanstholm in NW Jylland show outcrops of chalk and limestone. In addition, chalk that appears in the aureole of salt structures at, for example, Gassum, Suldrup, Batum, Erslev, Uglev and Thisted represent potential areas of glacitectorite occurrences.

The relation between the overburden of Quaternary deposits and the formation of glacitectorites is independent of the depth of the deposits. Thus a glacitectorite should always be expected between the top of the chalk and an overlying till. However, the till and glacitectorite may have been removed by erosion.

Identification of chalk-glacitectorites

There is a general understanding of the complexity of hydraulic properties related to areas with limestone and chalk located at shallow depths below Quaternary overburden (Downing *et al.* 1993). This is e.g. recognised in the greater Copenhagen area where groundwater flow paths are difficult to predict and the permeability in the glacially disturbed chalk layers of the København Kalk Formation and the underlying Danian bryozoan limestone are notably higher than in the underlying undisturbed limestones (Klitten *et al.* 2006; Bonnesen *et al.* 2009; Galsgaard *et al.* 2014). Research into the difficulty in predicting groundwater flow paths in shallow chalk aquifers is conducted in an on-going EU project investigating

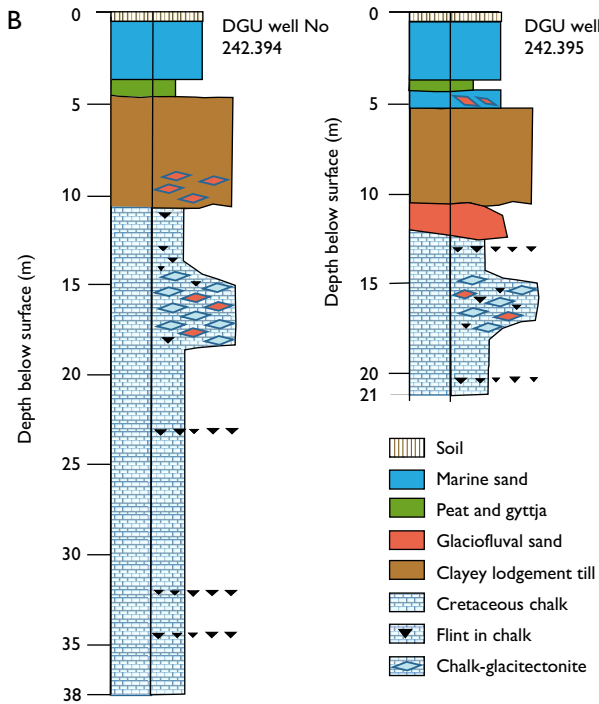
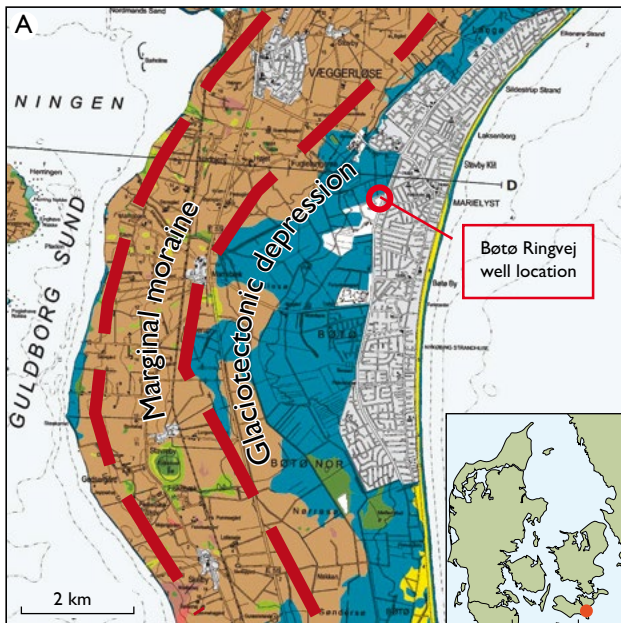
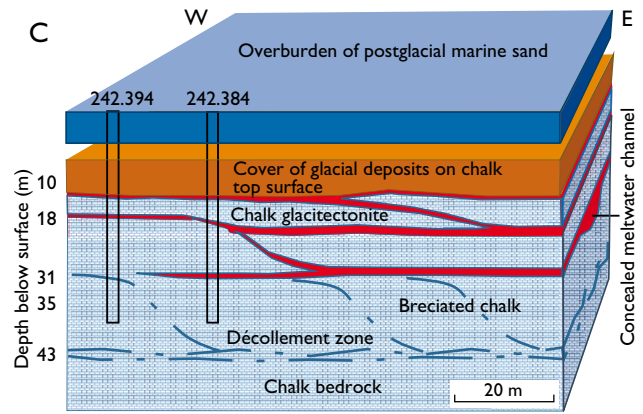


Fig. 6. The hydrogeological investigation site on Falster (the Bøtø case): **A**: geological map of the area demonstrating the glacial geological setting. **B**: two borehole logs demonstrating the lithological settings. **C**: block diagram illustrating the features and glacitectonites in the Upper Cretaceous beds.

subsurface water technologies to control saltwater intrusion (Zuurbier *et al.* 2016) on southern Falster, SE Denmark. The project focuses on the impact of climate change on the salinity of the groundwater resources (Rasmussen *et al.* 2013). At



the study site the top surface of the Upper Cretaceous chalk is situated at about 10 m below the surface; it is overlain by a 5 m thick unit of glacial sediments and 5 m marine sand (Fig. 6). However, at a depth of 15 to 18 m there is a layer of chalk with gravel and pebbles of basement rocks. Based on an evaluation of data from other wells in the area, it became evident that another zone with basement gravel and pebbles existed even deeper at a level from 30 to 40 m below the surface. These findings have implications for the understanding of groundwater flow around the wells as the complexity of the hydraulic characteristics markedly changes the aquifer's behaviour. A model of the glacitectonite occurrence was established based on a glaciodynamic concept of the area (Fig. 6). A resistivity log from a nearby well supported the model predictions with a glacitectonite on top of the undisturbed chalk (Pedersen & Hinsby 2017). On-going studies indicate that in some parts of the chalk reservoir the transmissivity behaves as single porosity aquifers, while other parts behave like fractured dual porosity aquifers.



Fig. 7. An about one-metre thick bed of chalk-glacitectonite separates two till beds exposed at the north coast of Stevns, SE Denmark.

The position of glacitectorites in the glaciodynamic development of the Quaternary successions

The chalk-glacitectorites occur basically at two different positions in the glaciodynamic sequence: either as tectonic breccias on top of chalk bedrock, or as shear translocated chalk debris at the sole of a basal till. In the first position the chalk-glacitectorite may be difficult to distinguish from undeformed bedrock. This is especially the case with identification of lithologies from drill-hole samples. Identification requires that small impurities, basement pebbles etc., displaced into the fractures, are recognised and documented.

The second position of chalk-glacitectorites is easy to recognise due to the unmistakable variation in lithology (Pedersen & Gravesen 2016; Fig. 7). The bedrock material appears in a succession of glacial deposits. The typical glaciodynamic sequence contains a meltwater unit of clay/silt grading up into sand coarsening up into glaciofluvial gravel, eventually with a stone-bed of ice-contact deposits mirroring the proglacial environment. On top of the glaciofluvial sediments the basal till demonstrates the ice advance over the foreland. The till is divided into a basal deformational layer and an upper lodgement layer. Thus the chalk-glacitectorite, representing the deformational layer, documents the transition from the foreland setting to the subglacial setting.

Final remarks

Chalk-glacitectorites are an important lithology to be identified in glacial terrains with bedrock comprising chalk and limestone, i.e. where the pre-Quaternary surface consists of limestones and related carbonate rocks. Chalk-glacitectorites are divided into two main types based on the structural setting in a glaciotectionic complex: (1) brecciated sedimentary rocks deformed within the stratigraphic succession of the deformed bedrock, and (2) brecciated rock deformed below a basal till and shear-mixed into the lodgement till. The recognition of chalk-glacitectorites is important for geological and groundwater-flow modelling addressing hydrogeological and geotechnical problems. Due to the glacial deformation these sedimentary rocks are expected to show higher permeability than undeformed bedrock.

Acknowledgement

This study was part-funded by the EU Horizon2020-project 'SUBSOL' (grant agreement no. 642228, www.subsol.org).

References

- Banham, P.H. 1977: Glacitectorites in till stratigraphy. *Boreas* **6**, 101–105.
- Bonnesen, E., Larsen, F., Sonnenborg, T.O., Klitten, K. & Stemmerik, L. 2009: Deep saltwater in chalk of North-West Europe: origin, interface characteristics and development over geological time. *Hydrogeology Journal* **17**, 1643–1663.
- Downing, R.A., Price, M. & Jones, G.P. (eds) 1993: *The hydrogeology of the chalk of North-West Europe*, 310 pp. Oxford: Oxford University Press.
- Galsgaard, J., Rhode, R., Jakobsen, R. & Jakobsen P.R. 2014: Strømning og stoftransport i kalklagene på den københavnske vestegn. *Geologisk og hydrogeologisk vidensopsamling og typemodell*. GEO projekt 37208, rapport **1**, 87 pp.
- Higgins, M.W. 1971: Cataclastic rocks. U.S. Geological Survey Professional Paper **687**, 97 pp.
- Håkansson, E. & Pedersen, S.A.S. 1992: *Geologisk kort over den danske undergrund, 1:500 000, map sheet*. Copenhagen: Varv.
- Klitten, K., Larsen, F. & Sonnenborg, T.O. 2006: *Saltvandsgrænsen i kalkmagasinerne i Nordøstsjælland, hovedrapport*, 45 pp. Copenhagen: Geological Survey of Denmark and Greenland & Institut for Miljø og Ressourcer.
- Pedersen, S.A.S. 1988: Glacitectorite: Brecciated sediments and cataclastic sedimentary rocks formed subglacially. In: Goldthwait, R.P. & Matsch, C.L. (eds): *Genetic classification of glacial deposits*, 89–91. Rotterdam: A.A. Balkema.
- Pedersen, S.A.S. 1996: Progressive glaciotectionic deformation in Weichselian and Palaeogene deposits at Feggekklit, northern Denmark. *Bulletin of the Geological Society of Denmark* **42**, 153–174.
- Pedersen, S.A.S. & Gravesen, P. 2016: Risikovurdering af skredforhold langs Stevns Klint. Danmarks og Grønlands Geologiske Undersøgelse Rapport **2016/33**, 87 pp.
- Pedersen, S.A.S. & Hinsby, K. 2017: Foreløbige resultater af boreriger ned i skrivetridt ved Bøtø Ringvej, Væggerløse, Falster. Danmarks og Grønlands Geologiske Undersøgelse Rapport **2017/28**, 14 pp.
- Pedersen, S.A.S. & Petersen, K.S. 1997: *Djurslands geologi*, 96 pp. Copenhagen: Danmarks og Grønlands Geologiske Undersøgelse.
- Rasmussen, P., Sonnenborg, T.O., Goncear, G. & Hinsby, K. 2013: Assessing impacts of climate change, sea level rise, and drainage canals on saltwater intrusion to coastal aquifer. *Hydrology and Earth System Sciences* **17**, 421–443.
- Sander, B. 1912: Über einige Gesteinsgruppen des Tauernwestendes. *Jahrbuch der Geologischen Reichsanstalt* **62**, 219–288.
- Zuurbier, K. *et al.* 2016: How subsurface water technologies (SWT) can provide robust, effective, and cost-efficient solutions for freshwater management in coastal zones. *Water Resources Management* **31**, 671–687.

Authors' address

Geological Survey of Denmark and Greenland, Øster Voldgade 10, DK-1350 Copenhagen, Denmark. E-mail: sasp@geus.dk.

Sedimentological and glaciotectonic interpretation of georadar data from the margin of the Vig ice-push ridge, NW Sjælland, Denmark

Cecilie Skovsø Andersen and Peter Roll Jakobsen

Glaciotectonic deformations often result in a high degree of variability, including glaciotectonic and sedimentary variability. Redeposition of sediments during deformation increases the variability. Ground-penetrating radar (GPR) has proven to be a good method to determine sedimentary structures in glaciofluvial deposits (Olsen & Andreasen 1994; Van Overmeeren 1998) as well as glaciotectonic structures (Busby & Merrit 1999; Overgaard & Jakobsen 2001). Reflection facies analysis (radar facies) is a useful tool in the characterisation and interpretation of deformed sediments (Van Overmeeren 1998; Jakobsen & Overgaard 2002; Lerche *et al.* 2014).

A GPR survey was carried out at Jyderup Skov in Odsherred in north-west Sjælland (Fig. 1). The presence of parallel ridges in the area indicates glaciotectonic deformation. The aim of the GPR study was to map the interior of the ridge complex and to interpret the genesis of the ridges.

Geological setting

The morphology of Odsherred in the north-western part of Sjælland in the north-western part of Denmark is dominated by three large arc-shaped ice-push ridges (Fig. 1A). The ice-push ridges (arcs) were formed in the Late Weichselian during the Bælthav readvance and gla-

ciofluvial deposits related to the ridge formation have been dated to be *c.* 17 000 years (Houmark-Nielsen 2008). The arcs cut each other and they were formed by three ice readvances of ice-lobes situated east of them. Each arc is a polymorphological landscape built-up of several landscape types. Data from boreholes show that the arcs contain dislocated Paleocene clay and Weichselian marine deposits indicating that the interior of the arcs is affected by glaciotectonic deformation. The investigated area is located in the western part of the Vig arc (Fig. 1B), which is situated in the centre of three arcs in Odsherred with the reclaimed Sidinge Fjord to the east forming a central depression. On the stoss side towards Sidinge Fjord is a terrain of smooth ground moraine. The upper part of the Vig arc is characterised by hummocky moraine and the western part consists of elongated ice-marginal moraines. Larger flat-topped kames occur within the hummocky moraine landscape and west of the ice-marginal moraine glaciofluvial deposits form an outwash plain. A number of elongated parallel ridges occur in the eastern part of the outwash plain (Fig. 1C). A raw-material investigation shows that at least the upper 10 m consist of sand and gravel (Region Sjælland 2011), and borehole information shows the presence of sandy till.

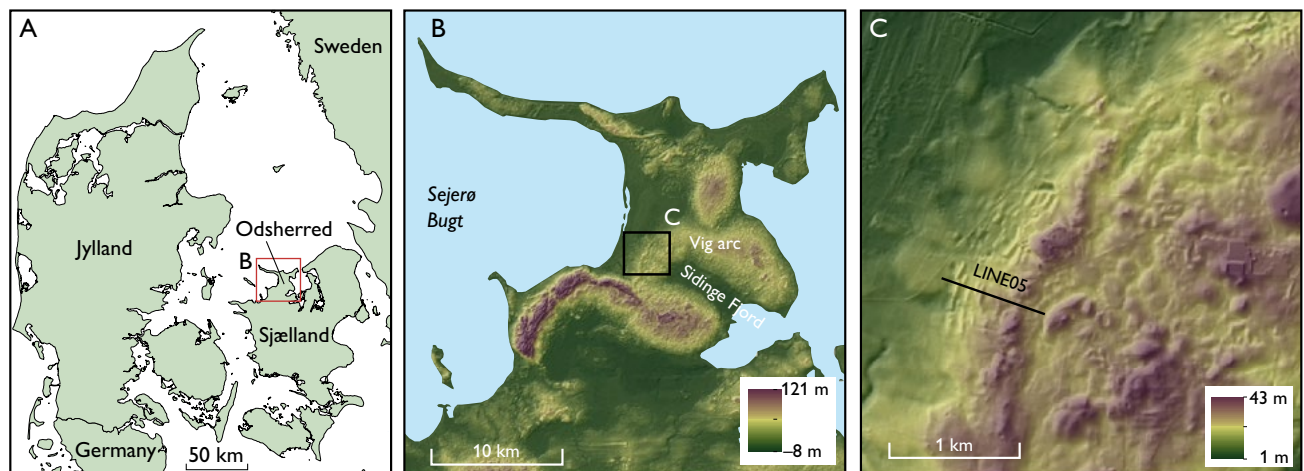


Fig. 1. A: Map of Denmark showing the location of Odsherred. B: Terrain model of Odsherred, NW Sjælland, with index map. C: Terrain model of the investigated area showing the location of the georadar line LINE05 over the ice-margin ridges.

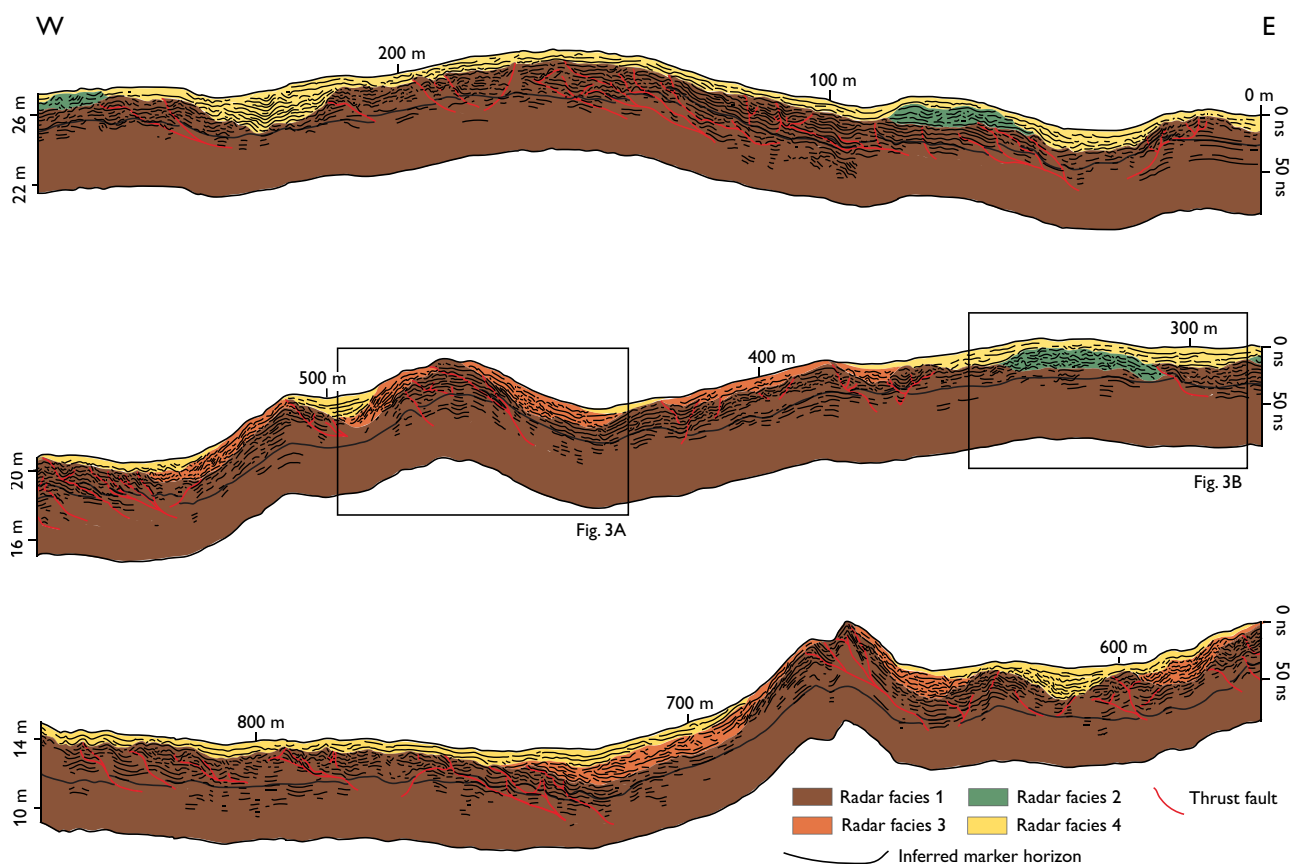


Fig. 2. Interpretation of the ground-penetrating radar profile LINE05. The scale to the left shows metres above sealevel. The scale to the right shows two-way travel time in nanoseconds. The black line is an inferred marker horizon used for structural analysis. The vertical exaggeration is 1:4. The black boxes indicate details shown in Fig. 3.

Georadar survey and processing parameters

Five GPR lines were made perpendicular to the ridges and one was recorded parallel to the overall strike of the ridges. The occurrence of forest roads and paths in Jyderup Skov determined the location of the lines. The data were acquired in October 2015 using a 250 MHz Sensors & Software Inc. georadar. Due to the forest setting shielded antennae on a skid plate were used with a *c.* 40 cm offset. The traces were sampled with a step size of *c.* 5 cm and then stacked by a factor of 8.

The line LINE05 provides the best image of the internal structure of the ridges (Figs 1B, 2). Processing of the raw LINE05 was carried out using PulseEKKO software by Sensors & Software Inc. in the following steps: first, a Dewow filter with an operational length of 1 pulse width was applied, followed by a Stolt migration with an estimated velocity of 0.133 mns^{-1} , which is typical value for dry sand. An automatic gain control with a pulse width of 1 and a maxi-

mum scaling factor of 700 was then applied, before the final topographic corrections were added. The vertical resolution is *c.* 20 cm.

Georadar facies description and interpretation

The LINE05 profile is 850 m long and cross-cuts 10 ridges excluding the moraine and the two ridges behind the ice-marginal moraine of the Vig arc (Fig. 2). Four radar facies are distinguished in the profile.

Radar facies 1 (Fig. 2) is interpreted as glaciofluvial sand and gravel based on the relatively strong parallel to subparallel reflections with high contrast, which are moderately continuous to discontinuous. Borehole data indicate that glaciofluvial sand and gravel are found to a depth of *c.* 20 m below the terrain surface. The reflections are primarily planar to wavy shaped, but antiforms and synforms are also found (8.5 m wide on average; Figs 2, 3A). The antiforms have a slightly asymmetric appearance with the western flank being steeper

(typically $c. 12^\circ$) than the eastern flank (typically $c. 6^\circ$). The antiform has an interlimb angle of typically $c. 160^\circ$. The reflectors show frequent displacements, which we interpret as thrust faults (Figs 2, 3A). The offset is between 0.20 m and 4.80 m with an average of 1.36 m. The reflections dip 4.0° to 13.6° dominantly to the east and are generally steepening upwards in a gentle concave to steep convex dipping pattern. The facies is truncated by facies 2, 3 and 4 in a concordant and erosional way (Fig. 2). We describe the detailed characteristics of the thrusts in the next section.

In radar facies 2 (Figs 2, 3B) the reflections are discontinuous and show a relatively low amplitude contrast. The reflection pattern is chaotic at $c. 280$ m to subparallel at $c. 325$ m (Fig. 3B) and $c. 75$ m, where the reflections dip downwards at the ends of the facies. Based on the facies characteristics, this facies is interpreted as a gravely ablation till. Facies 2 is found in patches and it drapes facies 1.

Radar facies 3 (Figs 2, 3A) consists of steepening upward (on average 10°) moderately continuous to discontinuous and subparallel reflections, this facies is mainly found on the western slope of the ridges. The reflection pattern is similar to facies 1. Based on the position of the facies and the reflection pattern, facies 1 is likely to be the source of the sediments of facies 3 that were redeposited as solifluction sediments. This interpretation is in good agreement with the primary location of the facies on the western flank of the ridges, where it is more inclined to slope failure.

In radar facies 4 (Fig. 2) the reflection pattern can be described as continuous, parallel and diverging with a high density of downlaps and onlaps in the crests between ridges. The facies drapes the other three facies, and in some areas, it truncates facies 1 in an erosional way. Facies 4 has a strong relative amplitude contrast. Based on the reflection pattern, facies 4 is interpreted as sand and gravel. The facies is typically thin and lacking on top of some of the ridges (Figs 2, 3A). However, it is locally thick on the crests. The facies is interpreted as post-deformation deposits.

Structural geology

The thrust-fault planes are commonly concave and convex rotating listric faults steepening upwards following and cross-cutting the bedding, with a dip of 2.5° to 21.9° (13.4° on average) mainly to the east. The westward dipping thrust faults are usually small and often back-thrusts from the more extensive eastward dipping thrusts. Some of the thrusts are clustered in a complex splay pattern, where the main thrust jacks up with each splaying thrust. These thrust faults are interpreted as linked contractional, leading imbricate stacks, originating from the same root at a detachment. The dis-

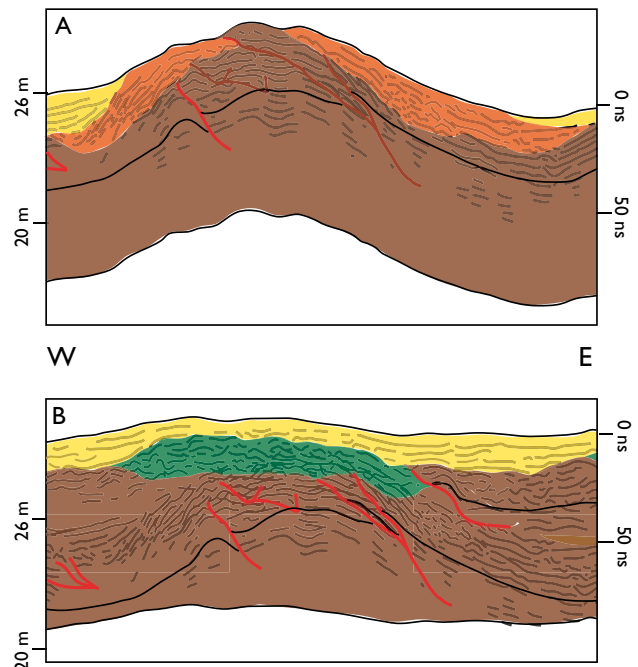


Fig. 3. Details from Fig. 2 (same legend as Fig. 2). A: Ridge formed by thrusting, and subsequently smoothed by radar facies 3 and 4. B: Relationship between radar facies 1, 2 and 4.

placement is greatest at the frontal thrust sheet. The leading imbricate stacks are primarily located beneath the ridges on the eastern flank, but they also occur on the western flanks in association with antiforms and synforms. Fault-bend-folding style of thrusting with hanging-wall ramp-flat-ramps and footwall flat-ramp-flats is evident from the concave-convex shape of the bedding along the fault plane. Fault propagation folding is seen in the imbricate stacks where the tip line terminates in the bedding. By drawing an inferred marker horizon (Fig. 2) on LINE05, the shortening of the line, caused by thrusting and folding, is calculated to be 12% of its initial length before deformation.

Formation of the ridges

The formation of the ridges can be described tectono-stratigraphically in three steps:

Pre-tectonic deposits: Radar facies 1 was deposited as glacio-fluvial sand and gravel on a pro-glacial outwash plain. During a syn- and post-depositional event, radar facies 1 was folded and thrust into gentle anti- and synforms. The thrusts are dense on the eastern flank of the antiforms, and occur as thick, wide, complex imbricate fans. The slight asymmetry of the anti- and synforms and the dip direction of the thrusts

and bedding indicate a direction of primary deformational stress from the east.

Tectonically penecontemporaneous deposits: Radar facies 2 was deposited penecontemporaneously as an ablation till. It occurs in patches and is only seen in one borehole (DGU no 190.196) *c.* 250 m south-west of LINE05, where the upper 2 m consist of sandy and gravelly till. Radar facies 2 is recognised in three places along LINE05, at *c.* 75 m, *c.* 280 m and *c.* 325 m. At *c.* 325 m, the radar section cuts an elevated area, which does not have the distinct ridge morphology seen elsewhere. The flattened morphology is in good agreement with deposition of ablation till, in contrast to the deformed elongated ridges elsewhere in the area. At *c.* 75 m the radar section is within an area of former stagnant ice, where ablation till should be expected.

Post-tectonic deposition: After the deformation came to an end, erosion of radar facies 1 occurred, and some thrust sheets are clearly truncated by solifluction sediments (radar facies 3) and post-deformation deposits (radar facies 4).

The small parallel ridges west of the large Vig arc may have been formed in a single deformational event creating a thin-skinned thrust-fault complex in a gravity-spreading environment (Jakobsen & Overgaard 2002; Pedersen 2005) or as annual moraines formed at an oscillating ice-margin (Krüger 1995; Benediktsson *et al.* 2009). The presence of till deposits within the area with the small ridges indicates that the ice margin was situated in the area. The topographic relief of the ridges is pronounced and there is no indication of erosion of the top of the ridges. Thus, the glacier has not moved past the individual ridges. We therefore suggest that the ridges were formed as ice-marginal push moraines created by seasonal advances and retreats of the ice margin.

Conclusions

Ground-penetrating radar was used to map the sedimentological and glaciotectionic structures of a series of parallel morine ridges of an area west of the Vig arc in Odsherred. The GPR profiles have a high resolution that allows detailed sedimentological and structural analyses. Four radar facies are distinguished which represent different sedimentary environments and degrees of deformation and three tectono-

stratigraphic sequences are recognised: pre-tectonic, tectonically penecontemporaneous and post-tectonic deposits.

The interior of the ridges is characterised by thrust faults and folds created by deformation from the east and the ridge morphology is clearly associated with the deformation structures. Subsequently the ridge morphology has been smoothed by post-tectonic sedimentation. We suggest that ridges seen on the proximal part of the outwash plain, west of the Vig arc, were formed as ice-push moraines by seasonal advances and retreats of the ice margin.

References

- Benediktsson, Í.Ö., Ingólfsson, Ó., Schomacker, A. & Kjær, K.H. 2009: Formation of submarginal and proglacial end moraines: implications of ice-flow mechanism during the 1963-64 surge of Brúarjökull, Iceland. *Boreas* **38**, 440–457.
- Busby, J.P. & Merritt, J.W. 1999: Quaternary deformation mapping with ground penetrating radar. *Journal of Applied Geophysics* **41**, 75–91.
- Houmark-Nielsen, M. 2008: Testing OSL failures against a regional Weichselian glaciation chronology from southern Scandinavia. *Boreas* **37**, 660–677.
- Jakobsen, P.R. & Overgaard, T. 2002: Georadar facies and glaciotectionic structures in ice marginal deposits northwest Zealand, Denmark. *Quaternary Science Reviews* **21**, 917–927.
- Krüger, J. 1995: Origin, chronology and climatological significance of annual-moraine ridges at Myrdaljöklull, Iceland. *The Holocene* **5**, 420–427.
- Lerche, H., Jakobsen, P.R. & Pedersen, S.A.S. 2014: Ribbed moraines formed during the retreat of the Scandinavian ice sheet from eastern Himmerland, NE Jylland, Denmark. *Geological Survey of Denmark and Greenland Bulletin* **31**, 39–42.
- Pedersen, S.A.S. 2005: Structural analysis of the Rubjerg Knude Glaciotectionic Complex, Vendsyssel, northern Denmark. *Geological Survey of Denmark and Greenland Bulletin* **8**, 192 pp.
- Olsen, H. & Andreasen, F. 1994: Sedimentology and ground-penetrating radar characteristics of a Pleistocene sandur deposit. *Sedimentary Geology* **99**, 1–15.
- Overgaard, T. & Jakobsen, P.R. 2001: Mapping of glaciotectionic deformation in an ice marginal environment with ground penetrating radar. *Journal of Applied Geophysics* **47**, 191–197.
- Region Sjælland 2011: Råstofkortlægning. Rapport **8**, sand, grus, sten, Jyderup, Odsherred Kommune, 38 pp. <http://jupiter.geus.dk/Rapportdb/Grundvandsrapport.seam?grundvandsrapportRapportid=90959>
- Van Overmeeren, R.A. 1998: Radar facies of unconsolidated sediments in the Netherlands: A radar stratigraphic interpretation method for hydrogeology. *Journal of Applied Geophysics* **40**, 1–18.

Authors' addresses

C.S.A., *Orbicon, Linnés Alle 2, 2630 Taastrup*, E-mail: cesa@orbicon.dk.

P.R.J., *Geological Survey of Denmark and Greenland, Øster Voldgade 10, DK-1350 Copenhagen K, Denmark*.

Miocene oil-bearing diatom ooze from the North Sea

Emma Sheldon, Erik S. Rasmussen, Karen Dybkjær, Tor Eidvin, Fridtjof Riis and Rikke Weibel

In recent years there has been an increased interest in Neogene hydrocarbon accumulations in the North Sea. The production of gas from Pliocene–Quaternary deposits in the Dutch sector, the discovery of oil-bearing Miocene sands in the Lille John area and oil accumulation in middle Miocene deposits in the T-1 well in the northern part of the Danish Central Graben area, have documented Neogene hydrocarbon accumulations. Some of these deposits are of economic interest. This study presents an oil-bearing, middle Miocene diatom ooze in the Valhall Field (well 2/8-G-2), within the Norwegian sector (Fig. 1). The Valhall Field is located just north of the Danish–Norwegian sector boundary.

Geological setting

During the Miocene, the North Sea formed a silled-bound basin with connection to the Atlantic Ocean via a strait between Norway and Shetland (Rasmussen *et al.* 2008; Fig.

1). The main sediment source areas were the Shetland Platform, which supplied sediments to the northern North Sea and the southern Scandes from which sediments were routed southwards into the south-eastern North Sea (Fig. 1). During the early Miocene relatively large delta complexes formed from these areas and resulted in eastward progradation off the Shetland Platform (Skade Formation; Eidvin *et al.* 2014) and south-westward progradation south of the southern Scandes (Ribe Group; Rasmussen *et al.* 2010). During the

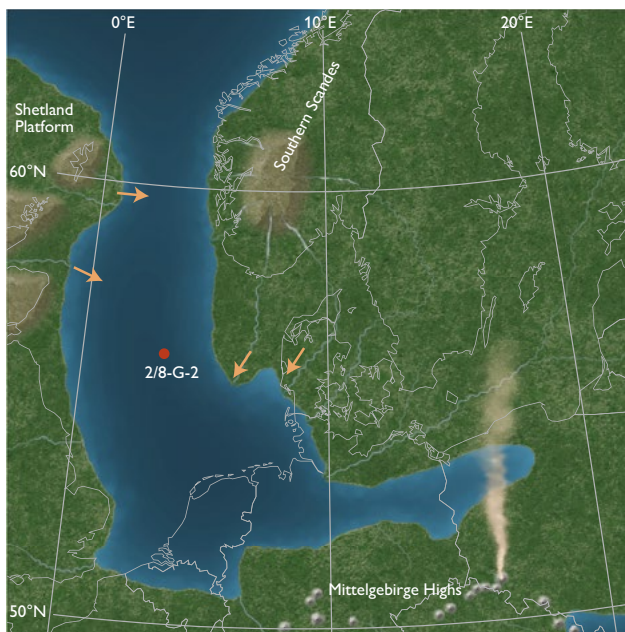


Fig. 1. Palaeogeographical reconstruction of the early Miocene North Sea. Note that the main sediment influx from the Shetland Platform (yellow arrows) filled the northern North Sea and that sediment supply to the eastern North Sea had its source in southern Scandes. Based on Rasmussen *et al.* (2008).

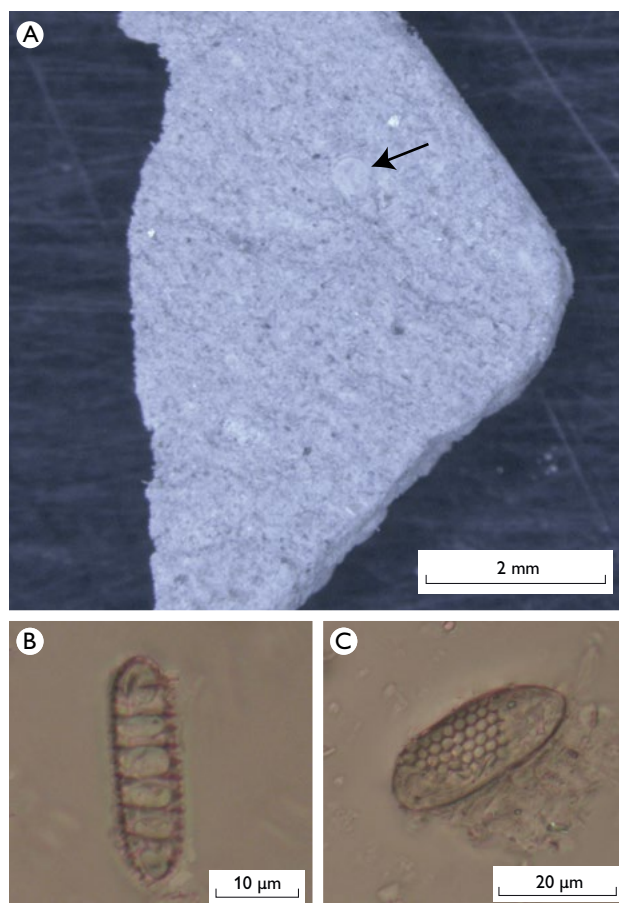


Fig. 2. Cored diatom ooze from the Valhall Field, Norwegian sector of the North Sea. **A:** Optical microscope image of chip of diatom ooze, note the diatom in the upper part (black arrow). **B:** ?*Denticulopsis kanayae*. **C:** ?*Denticulopsis nicobarica*.

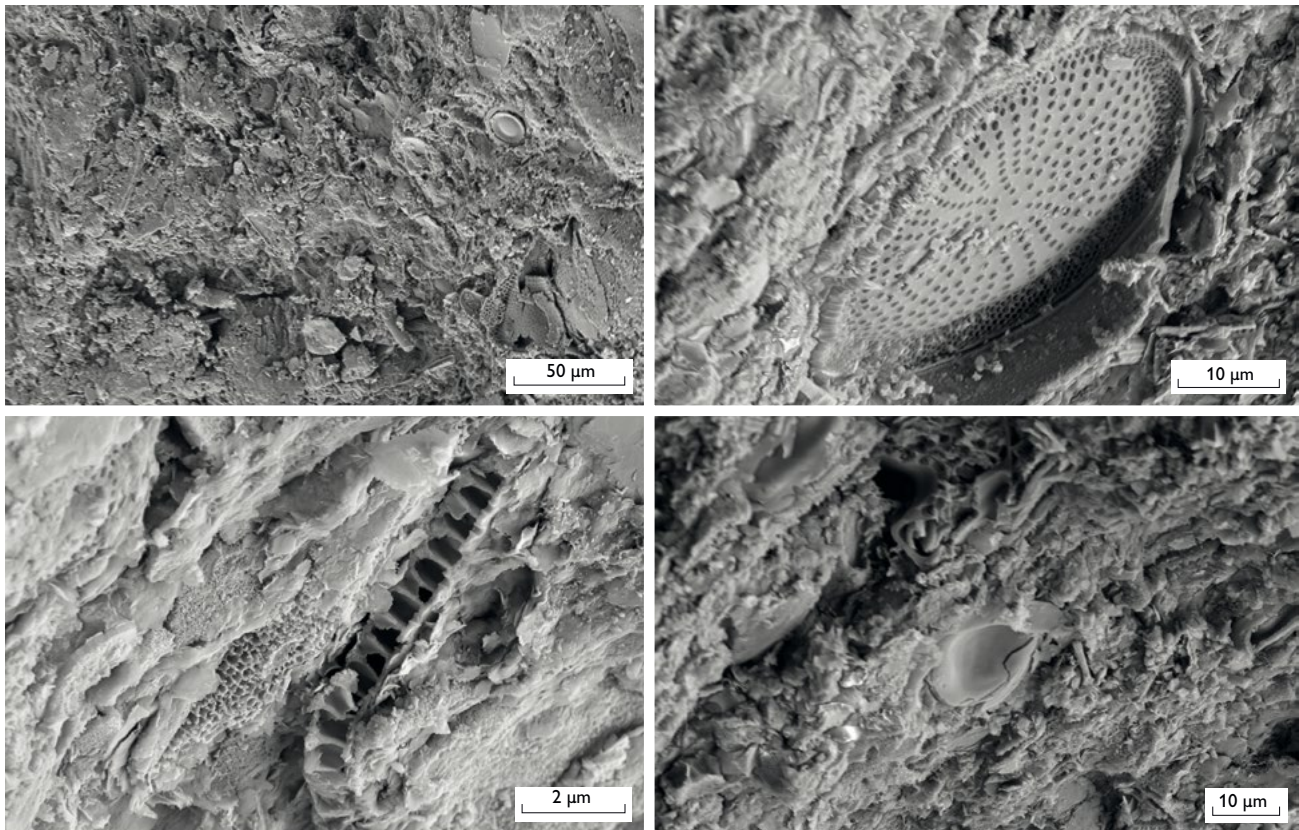


Fig. 3. Four scanning electron microscope images of the diatom ooze. Note the valve of the centric diatom *Thalassiosira* spp. in the upper right image.

middle Miocene these delta complexes were flooded due to reorganisation of the tectonic regime in North-West Europe which resulted in accelerated subsidence of the basin margins. Consequently, much of the North Sea was starved of sediment during the middle and early late Miocene.

The North Sea area was located in the western wind belt with seasonal storms. Therefore, the coast was strongly influenced by wave action. In the deeper basin, which was up to *c.* 1000 m deep, hemipelagic deposition predominated. A counter-clockwise current system redistributed and reshaped muddy sediments along the delta and shelf slopes within the basin (e.g. Hansen *et al.* 2004). During the early Miocene a humid, warm temperate climate predominated, similar to present day western Florida (USA). A change to a cooler climate commenced in the middle Miocene which probably also resulted in the enhanced influence of cold-water current systems from the Atlantic Ocean. Under these cooler climatic conditions diatoms bloomed and resulted in deposition of diatom ooze.

Diatom ooze

The diatom ooze is fine-grained and grey to brown, since it contains oil (Fig. 2). Diatom valves and radiolarians could be

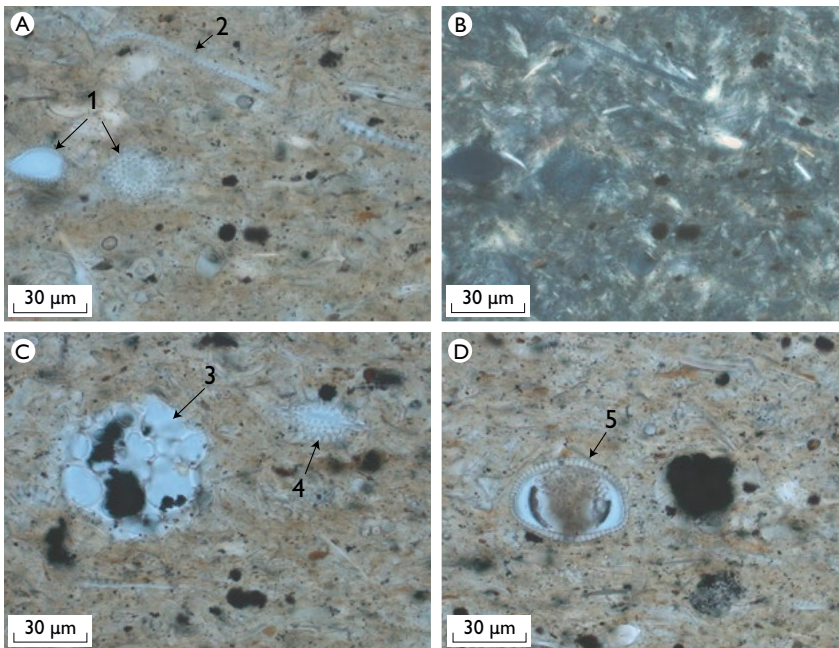
seen in optical and scanning electron microscopes (Figs 3, 4). The diatom ooze consists of a mixture of abundant diatom valves, radiolarians and clay (Fig. 4). The porosity is 50–60%.

Porosity is mainly associated with diatom valves and either occurs inside the valves or in pockets next to the valves or other fossils. Reduced porosity is observed in some samples, attributed to clay intruding into the diatom valves. The permeability is assumed to be low, due to the small size of the pores and tortuous connectivity between the largest pores. The measured porosity of the diatom ooze would correspond to a permeability of 0.006–0.02 mD in diatom ooze from various localities in the Pacific Ocean (Gamage *et al.* 2011).

Nannofossils and microfossils

Core sample (1802.7 m from the well 2/8-G-2) was analysed for nannofossil, microfossil and the presence of diatoms. Diatom valves and debris were found to be common. Diatoms include ?*Thalassiosira* spp., ?*Denticulopsis kanayae* and ?*Denticulopsis niobarica*. *D. kanayae* and *D. niobarica* range from the early to middle Miocene (Barron 1985; Fig. 2). The sample was barren with respect to nannofossils and the mi-

Fig. 4. Optical microscope images of the diatom ooze. The ooze comprises siliceous microfossils (e.g. diatoms and radiolarians) and clay. Porosity inside microfossils is recognised by the blue staining of the epoxy impregnating the ooze. A and B are identical; B with crossed nicols. 1: *Stephanopyxis turris* (diatom). 2: cross section of a diatom valve. 3: ?*Peridinium longispinum* (radiolarian), 4: ?*Stephanopyxis turris*. 5: diatom frustule. Alexander Mitlehner, UK, kindly helped with the identification of the diatoms.



crofossil fraction yielded one radiolarian (*Cenodiscus* spp.) and no foraminifera.

Palynology

Six core samples were analysed for palynology (1797.0 m, 1802.7 m, 1803.4 m, 1813.0 m, 1819.0 m and 1827.0 m). In all samples, the assemblages of organic particles are characterised by a dominance of marine dinoflagellate cysts (dinocysts). Bisaccate and non-saccate pollen and wood particles occur very sporadically while no freshwater algae were recorded. The dinocyst assemblage is rich and diverse and

the consistent presence of *Nematosphaeropsis* spp. and *Impagidinium* spp. indicates an outer neritic to oceanic setting (Brinkhuis 1994). An increase in cold-water tolerant dinocyst taxa (mainly *Habibacysta tectata*) was found (Fig. 5), ranging from no recordings in the lowermost sample, to sporadic occurrences in the next samples and common occurrences in the two uppermost samples. The occurrences of the dinocyst species *Unipontodinium aquaductum* in all six samples (Fig. 5) strongly indicate that the cored interval should be referred to the *Unipontodinium aquaductum* Zone of Dybkjær and Piasecki (2010). The age of this zone is mid-Langhian to early Serravallian (middle Miocene). The

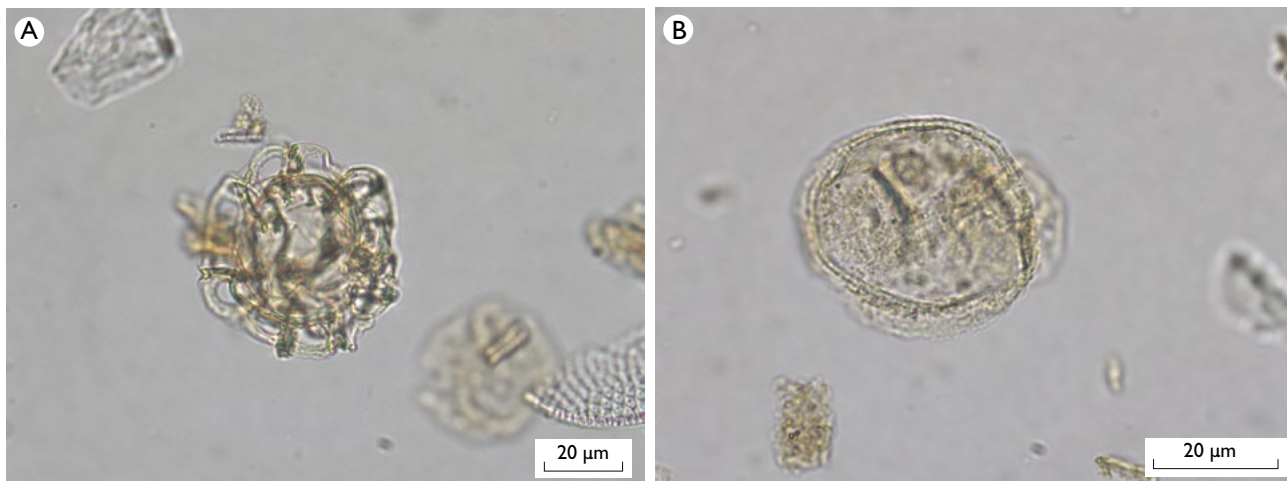


Fig. 5. Dinoflagellate cysts from the oil-bearing cores. A: *Unipontodinium aquaductum*. B: *Habibacysta tectata*. Increased abundance of *Habibacysta tectata*, a cold-water tolerant species, is probably associated with the climatic deterioration in the middle Miocene (Serravallian).

Unipontodinium aqueductum Zone occurs in the upper part of the Hodde Formation defined onshore Denmark which correlates with the lowermost part of the Nordland Group.

Depositional environment

Based on palynology and seismic stratigraphic studies (e.g. Rasmussen *et al.* 2005), the depositional setting was outer neritic to oceanic, with a water depth just below 1000 m. Late early Miocene biosiliceous, organic-rich sediments of the upper Lark Formation in the Central Graben area have been described by Sulsbrück & Toft (2018). This part of the upper Lark Formation was deposited at the termination of shoreline progradation from the southern Scandes (Ribe Group). The studied section represents slightly younger deposits than those laid down during the transgression of the lower Miocene Ribe Group. Consequently, the depositional environment was sediment starved and fully marine. The occurrence of cold water dinocysts in the studied cores, probably reflects the beginning of the middle Miocene (Serravalian) global climatic deterioration (Zachos *et al.* 2001).

Petroleum system

The oil-bearing Miocene diatom ooze from the Norwegian sector of the North Sea described here documents oil migration into younger deposits, which are normally considered to be non-prospective. In the Danish North Sea area, a number of wells have penetrated hydrocarbon-bearing strata of Miocene and Pliocene ages as described above. The oil-bearing deposits are found in the western and central parts of the Danish and Norwegian Central Graben. The oil probably has a source in the Jurassic shale deep in the Central Graben. Migration into Cenozoic deposits probably occurred along salt structures. Due to early Quaternary tilting of the North Sea Basin (Rasmussen *et al.* 2005), up-dip migration into stratigraphic and structural traps located in the eastern part of the Central Graben area and the Ringkøbing–Fyn High may have occurred. This calls for a total re-evaluation of the petroleum system of the Cenozoic succession in the North Sea area.

References

- Barron, J.A. 1985: Miocene to Holocene planktic diatoms. In: Bolli, H.M., Saunders J.B. & Perch-Nielsen, K. (eds): Plankton stratigraphy, 763–809. Cambridge: Cambridge University Press.
- Brinkhuis, H. 1994: Late Eocene to Early Oligocene dinoflagellate cysts from the Priabonian type-area (Northeast Italy): biostratigraphy and palaeoenvironmental interpretation. *Palaeogeography, Palaeoclimatology, Palaeoecology* **107**, 121–163.
- Dybkjær, K. & Piasecki, S. 2010: Neogene dinocyst zonation in the eastern North Sea Basin, Denmark. *Review of Palaeobotany and Palynology* **161**, 1–29.
- Eidvin, T., Riis, F. & Rasmussen E.S. 2014: Oligocene to Lower Pliocene deposits of the Norwegian continental shelf, with correlation to the Norwegian Sea, Greenland, Svalbard, Denmark and their relation to the uplift of Fennoscandia. *Marine and Petroleum Geology* **56**, 184–221.
- Gamage, K., Screaton, E., Bekins, B. & Aiella, I. 2011: Permeability-porosity relationships of subduction zone sediments. *Marine Geology* **279**, 19–36.
- Hansen, J.P.V., Clausen, O.R. & Huuse, M. 2004: 3D seismic analysis reveals the origin of ambiguous erosional features at a major sequence boundary in the eastern North Sea: near top Oligocene. *Geological Society Memoirs (London)* **29**, 83–90.
- Rasmussen, E.S., Vejbæk, O.V., Bidstrup, T., Piasecki, S & Dybkjær, K. 2005: Late Cenozoic depositional history of the Danish North Sea Basin: implications for the petroleum systems in the Kraka, Halfdan, Siri and Nini fields. In: Dore, A.G. & Vinding, B.A. (eds): *Petroleum geology: North-West Europe and global perspectives*. Proceedings of the 6th petroleum geology conference, 1347–1358. London: Geological Society.
- Rasmussen, E.S., Heilmann-Clausen, C., Waagstein, R. & Eidvin, T. 2008: Tertiary of Norden. *Episodes* **31**, 66–72.
- Rasmussen, E.S., Dybkjær, K. & Piasecki, S. 2010: Lithostratigraphy of the Upper Oligocene – Miocene succession of Denmark. *Bulletin of the Geological Survey of Denmark and Greenland* **22**, 92 pp.
- Sulsbrück, H. & Toft, J. 2018: A new observation of a biosiliceous opal bearing sequence in the Miocene Lark Formation in the Danish North Sea. 33rd Nordic Geological Winter meeting, Lyngby. Abstract <http://2dgf.dk/foreningen/33rd-nordic-geological-winter-meeting/ngwm-2018-abstracts/3-sedimentary-rocks-and-processes/>
- Zachos, J.C., Pagani, M., Sloan, L., Thomas, E. & Billups, K. 2001: Trends, rhythms, and aberrations in global climate 65 Ma to Present. *Science* **292**, 686–693.

Authors' addresses

E.S., E.S.R., K.D. & R.W., *Geological Survey of Denmark and Greenland, Øster Voldgade 10, DK-1350 Copenhagen K, Denmark*. E-mail: es@geus.dk.
T.E. & F.R. *Norwegian Petroleum Directorate (NPD), P. O. Box 600, N-4003 Stavanger, Norway*.

Initial observations of the shallow geology in Tannis Bugt, Skagerrak, Denmark

Matthew J. Owen, Nicky H. Witt, Ziad Al-Hamdani, Niels Nørgaard-Pedersen, Katrine J. Andresen and Jørgen O. Leth

During August 2017, as part of the habitat mapping of Natura2000 areas, a geophysical survey of a large area within the Skagerrak was undertaken by the Geological Survey of Denmark and Greenland. In this article, we use the acquired data to discuss the geology of Tannis Bugt (Fig. 1), a large shallow bay at the north-west coast of Vendsyssel. The bay extends 40 km between Hirtshals in the west and Skagen in the east forming the northern-most Danish Skagerrak coast.

Geological setting and glacial history

In northern Vendsyssel, the Late Quaternary succession is 250 m thick and underlain by Cretaceous or Triassic strata (Håkansson & Pedersen 1992). Tertiary sediments are assumed to be absent (Sandersen *et al.* 2009). Vendsyssel was subjected to several ice advances during the Saalian and Weichselian, which resulted in a succession that is generally dominated by marine to glaciolacustrine clay (Knudsen *et al.* 2009; Larsen *et al.* 2009a). The oldest Quaternary deposits in Vendsyssel are represented by the clay-rich Skærumhede Till Formation, which is followed by the marine Lower Skærumhede Clay Formation. The till units of the Brønderslev and Åsted formations of the Early to Middle Weichselian reflect a change to a colder environment. Boulders are found throughout the till units (Pedersen 2005; Knudsen *et al.* 2009; Larsen *et al.* 2009a; Larsen *et al.* 2009b). The changing climate resulted in ice retreat and the deposition of the marine sediments of the Upper Skærumhede Clay Formation, which gradually

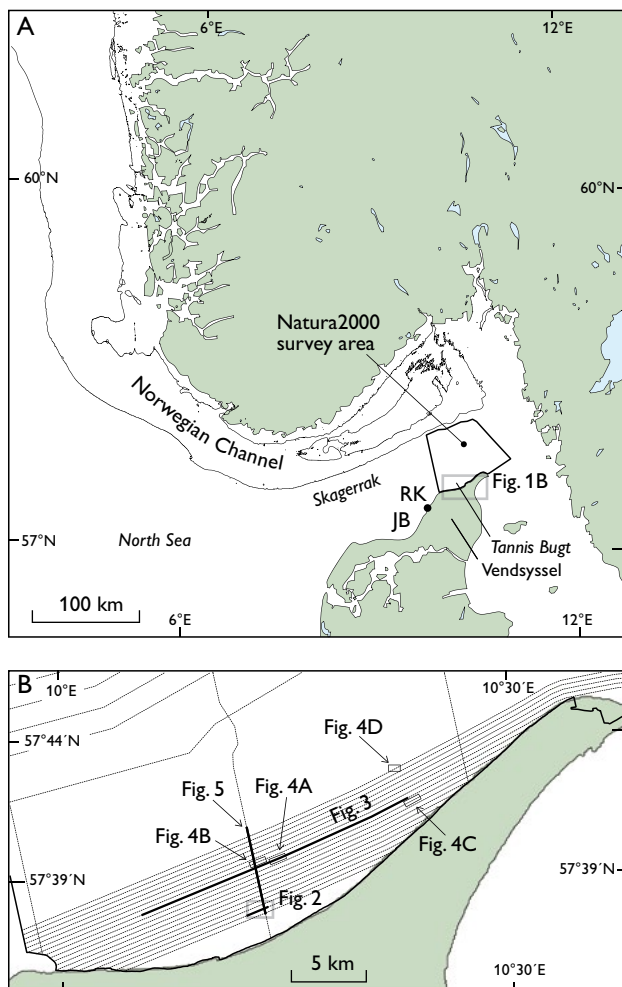


Fig. 1. Locality map. **A**: Regional setting of the study area. **JB**: Jammerbugt. **RK**: Rubjerg Knude. **B**: Tannis Bugt with location of data shown.

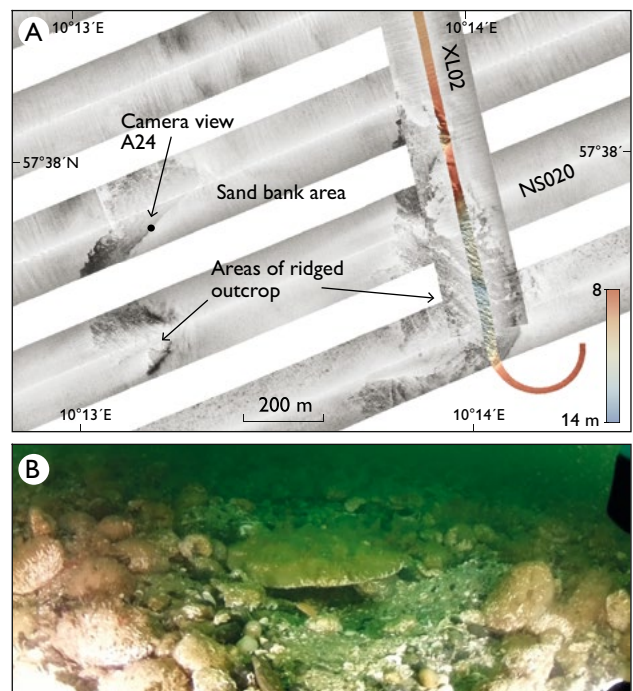


Fig. 2. **A**: Seabed morphology with location of Innomar lines XL02 and NS020 (shown in Fig. 4). **B**: Video view of the sea floor (A24).

developed into the glaciolacustrine Lønstrup Klint Formation, and the transition continues into terrestrial and glacial sediments of the Kattegat Till Formation. The Late Weichselian sediments consist of several phases of till and glaciolacustrine units. By *c.* 18 ka BP, as the ice retreated, large parts of Vendsyssel were inundated by the sea leading to the deposition of the marine Vendsyssel Formation.

Associated with the advance and retreat of ice sheets, the area was strongly influenced by isostatic rebound with a regression occurring from the Late Glacial to the present day.

Raised late-glacial shorelines are found up to *c.* 60 m above sea level (Richardt 1996). A number of glaciotectonic complexes have been mapped in northern Jylland (Fig. 1A) and tend to exhibit thrusting from the east or north-east (Pedersen & Boldreel 2015). The oceanographic setting has varied in response to the interplay between isostasy and eustasy. As such, the setting is inferred to have varied between an isolated embayment, extending from the Atlantic via the Norwegian Channel, to the present-day setting as a deep-water component of the North Sea.

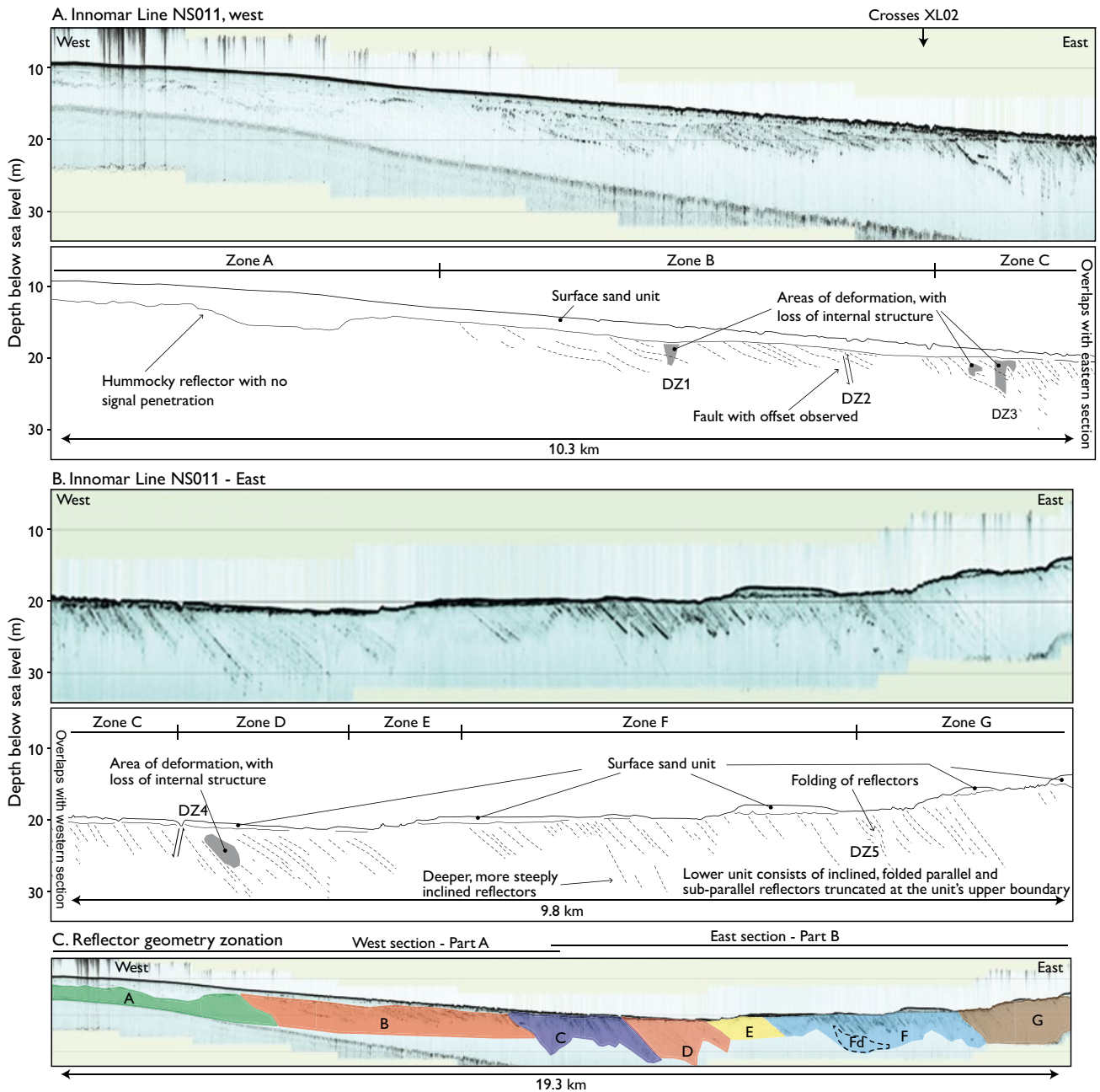


Fig. 3. WSW–ENE-orientated Innomar profile NS011. A: Western part. B: Eastern part. C: Full profile with zones described in Table 1. DZ: deformation zone. Vertical exaggeration 70 times.

Table 1. Summary of Innomar data shown on line NS011 (Fig. 3).

Zone	Length (m)	Facies characteristics	Representative reflector inclination
A	3270	Upper unit with a smooth and convex up upper boundary. The lower boundary shows undulation and a hummocky character. No Innomar penetration below.	NA
B	4650	Upper unit thins and pinches out eastward. The seabed becomes increasingly incised with small notches moving east. This unit rests unconformably on a lower unit characterised by northeastwardly dipping reflectors. Folded and offset reflectors are apparent (DZ1 and DZ2).	0.3°
C	2640	An upper unit is generally present, though it pinches out occasionally and is <1 m thick. Below, reflectors of the lower unit are inclined and appear to be more densely spaced, with deformation visible (DZ3). The upper surface of the lower unit becomes more irregular to the east.	0.9°
D	1800	Upper unit is present, though <1 m thick, in the west and pinches out and is absent in the east. Curvilinear, inclined reflectors characterise the lower unit, an apparent loss of internal structure is also visible (DZ4).	0.6°
E	930	Lack of penetration, cuesta-like scarps of ~1 m height visible on the seabed.	NA
F	4750	A semi-transparent upper unit with a lens-like morphology is intermittently present and <2 m thick. Below, densely spaced reflectors are inclined giving the seabed a cuesta morphology where they outcrop. Innomar penetration is variable. Area of folding in the east (DZ5).	0.9°
Fd		Deeper, more steeply inclined reflectors separate from the shallower units.	1.5°
G	2070	Intermittent upper unit, with a semi-transparent facies and lens-like morphology, resting unconformably atop of the irregular upper surface of the lower unit with inclined linear reflectors. The seabed shoals and Innomar penetration reduces in the east.	1.0°

Marine survey

The dataset obtained in the survey consists of multibeam bathymetry, side-scan sonar and Innomar sub-bottom profiler data. Some 2150 km of data were acquired using the vessel R/V *Aurora* (Fig. 1b), covering the northern coast of Vendsyssel between Skagen and Hirtshals. WSW–ENE-orientated nearshore lines were spaced at 300 m intervals and N–S-orientated crossing lines at 15 km intervals. In addition, 24 video views were made of the sea floor in the shallow-water area.

Camera view at site A24 – The site is located at a water depth of 12 m in an area characterised by a high-amplitude, irregular, acoustic seabed facies, in a depression adjacent to a low-amplitude shallow-banked area (Fig. 2A). To the east an adjacent depression is characterised by a similarly high-amplitude acoustic facies, but traversed by NW–SE-orientated linear ridges. When visible, the apparent strike of the bedding is generally SE, though in some instances a NE strike is also visible. The camera view (Fig. 2B) shows a mixture of coarse gravel, cobbles and boulders. The larger clasts appear to be sub-rounded to well rounded.

Innomar data – Figures 3 to 5 show a selection of the Innomar data from Tannis Bugt. The facies visible in these figures are representative of those observed across the site. The W–E-orientated Innomar profile NS011 (Fig. 3) shows a semi-transparent upper unit, which is intermittently present. It overlies a deeper unit with reflectors that dip to the north-east. An additional deeper unit, with more steeply

inclined reflectors, is occasionally visible. To aid description the data shown in Fig. 3 are divided into zones A to G from west to east (Table 1).

At least five zones of deformation (DZ1–DZ5; Fig. 3) are apparent in the Innomar data. Indications of deformation include folding, offset reflectors and loss of structure. Some of these complex features are shown in more detail in Fig. 4. Innomar examples (4A–C) show deformed reflectors, areas of lost structures and apparent faults. The side-scan example (Fig. 4D) shows an area of wave-like bedding outcropping at the seabed.

Figure 5 shows the N–S-orientated Innomar line XL02, which crosses the profile NS011 shown in Fig. 3 as well as the area shown in Fig. 2. As with the data shown in Fig. 3, an upper semi-transparent unit rests unconformably on a unit with truncated dipping reflectors. In the southern half of the profile, the upper unit thickens, where it is associated with large sand banks. The reflectors of the lower unit show steeper inclination in the northern third of Fig. 5, where inclination of 1.8° is found. Near the crossing of NS011, shown in Fig. 3, DZ3 (Fig. 3, Table 1) is visible and marks a divide between the more steeply inclined reflectors farther north and the more gently inclined reflectors to the south, where inclinations of 0.7° are measured.

At the far south, reflectors outcrop at the seabed with an inclination of 0.5°. Blanking of the Innomar data is particularly apparent in Fig. 5 north of DZ3; here reflectors are clearly cut by blanking zones rising from depth. South of DZ3 penetration ends abruptly and is variable. Some deformation is visible in Fig. 5 (folded reflectors below the thickening surface unit and some loss of structure at DZ3), though it is less apparent than in the data shown in Figs 3, 4.

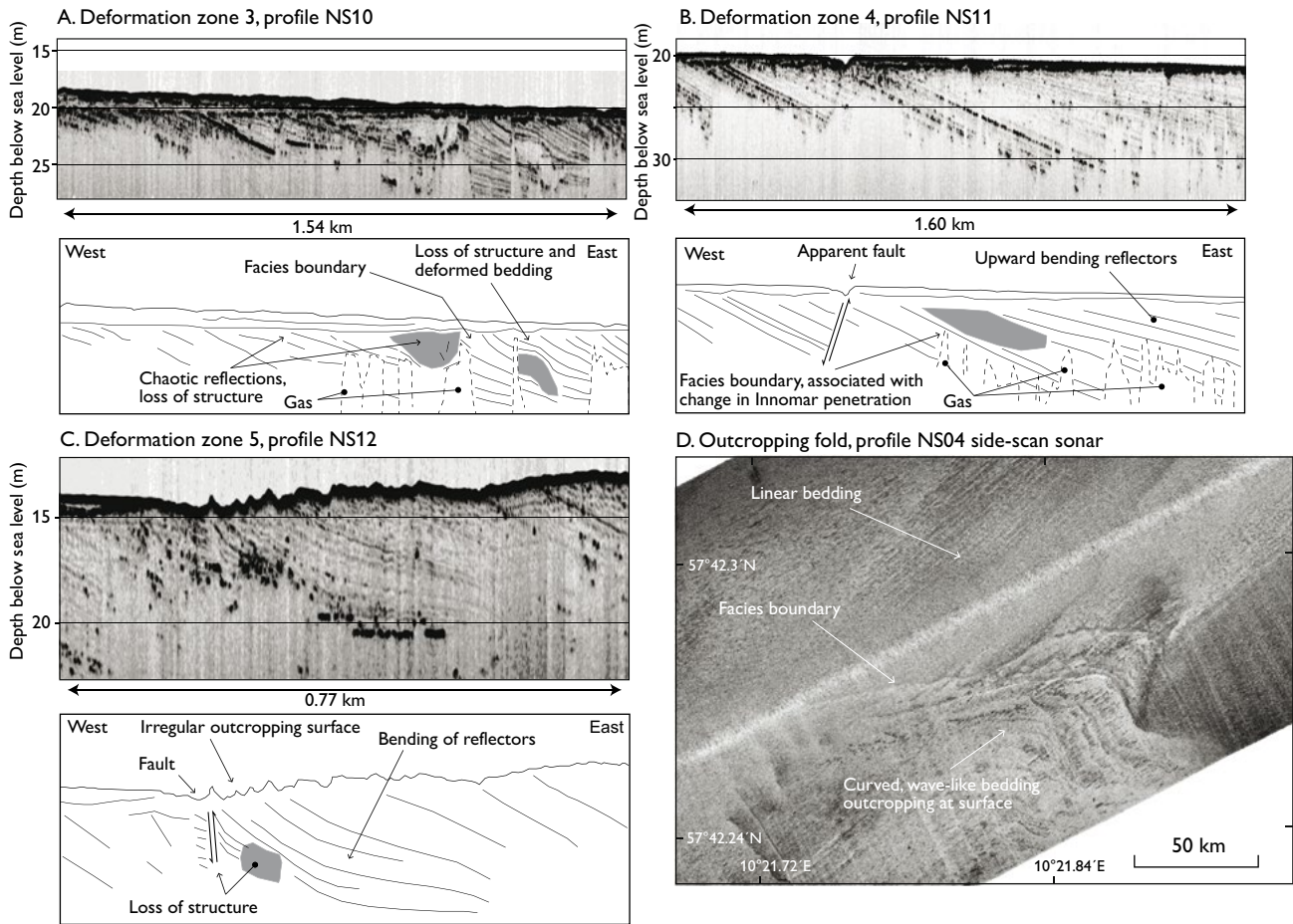


Fig. 4. Examples of deformations within Tannis Bugt. A–C: Innomar data shown with a vertical exaggeration of 28 times. D: Side-scan sonar data.

Discussion

Interpretation of Innomar and video data – The upper units visible in the Innomar data are interpreted as Holocene marine sand and gravel. Interpretation of the deeper unit is complicated by limited penetration from the Innomar system and no ground control. However, as indicated by the zoning in Figs 3 and 5, and the facies characteristics outlined in Table 1, there is a clear variation in reflector geometry, and we make some provisional observations.

One of the most striking aspects of the Innomar data is the inclined nature of the reflectors, representing bedding planes, and the truncated, often irregular upper surface. As shown in Table 1, inclination (as distinct from angle of dip due to the oblique orientation of the survey lines with respect to direction of dip) is low and measures between 0.3° and 1.5° within the W–E-orientated NS011 profile; it is generally greater in the east. Measured inclinations from the N–S-orientated XL02 profile (Fig. 5) are greater, with 1.8° . There is also clear variation in angle between zones B–D, F and G (zones A and E do not show inclined reflectors).

The parallel bedding appears to have undergone deformation (folds and faults are visible in Figs 3, 4) in the centre and east of the site. Some deformation is apparent in Fig. 5, though it is less clear. Areas of deformation separate zones B and C, C and D, and F and G. The reflective facies within the zones are distinct and display features indicative of further deformation. Shown in Fig. 5, there is a clear reduction in bedding inclination between zones C and B. Innomar penetration is reduced by a factor of three in zone B compared to zone C and blanking cuts the bedding within zone C (indicating gas migration), whereas it does not in the more depth-limited imaging of zone B. This indicates a change in lithology between zones, with zone B potentially consisting of a less permeable and more dense material. Referring to Fig. 3, the reflectors in zone D display a lower angle of inclination and appear folded. Zone E is characterised by no sub-surface penetration and the presence of cuesta-like scarps on the seabed. Gas does not appear to be present in this location and the surface unit is thin or absent, therefore the lack of signal could be due to the presence of a massive or more dense unit.

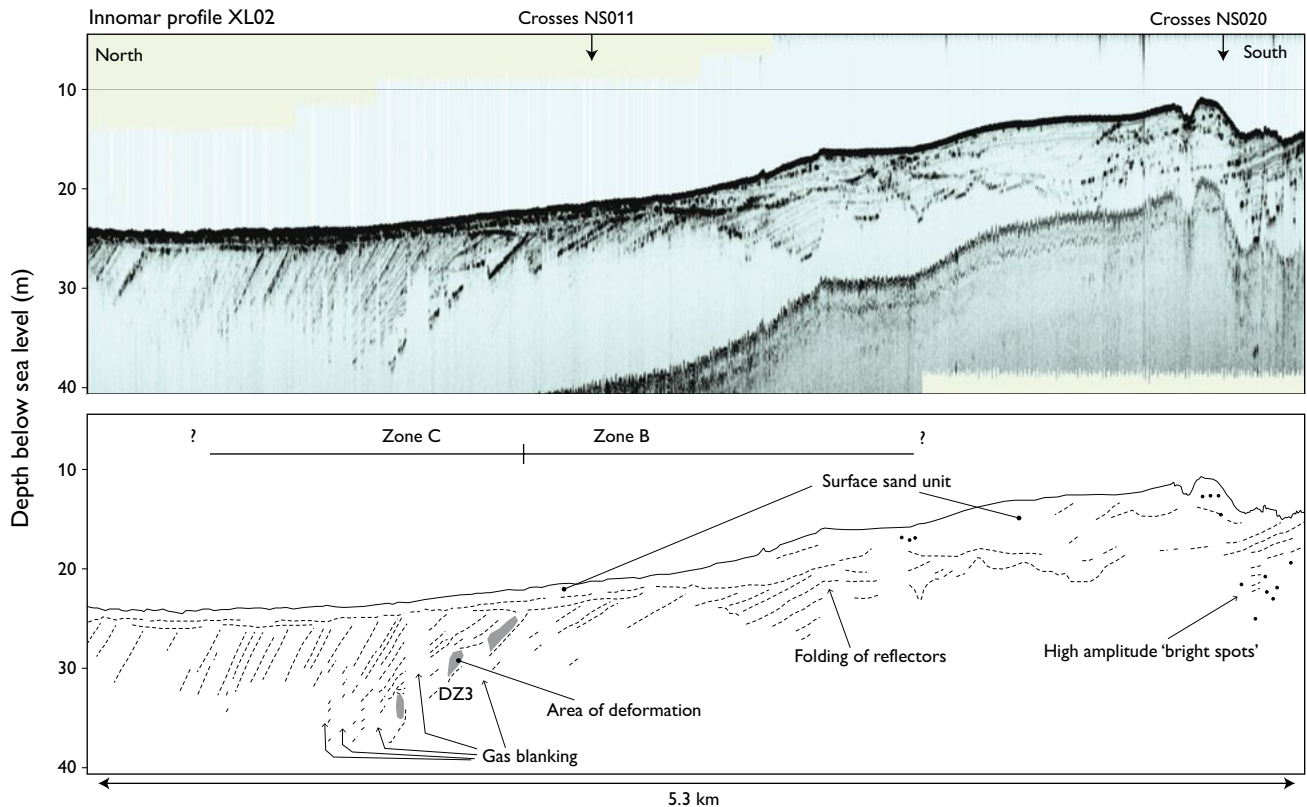


Fig. 5. N–S-orientated Innomar profile XL02. See Fig. 2 for location. Vertical exaggeration 40 times.

Inclined reflectors are again apparent in zone F, sub-surface penetration varies and is generally limited. Outcropping bedding is apparent in zone G, matching the acoustic facies visible on the side scan record: where outcropping strata are visible as ridges (Fig. 2A).

Cobbles and boulders visible in camera view A24 (Fig. 2B), where Innomar data show high amplitude seabed in an area with outcropping strata, appear to have two possible origins: either a winnowed deposit from a Quaternary till or drop-stone unit, or eroded pre-Quaternary bedrock. The density of the clasts visible would require a large, though not impossible, initial thickness of till to yield such a high number of clasts. The presence of pre-Quaternary geology would be unexpected; however, shown by the bedding visible in Figs 3 and 5, outcrop in the location of camera site A24 is stratigraphically older than the lithological units located north and eastward, which extend for up to 20 km.

Origin and contributing geological processes – One of the more puzzling aspects of the geology of Tannis Bugt is the difference to the onshore data which show a succession of till, glaciomarine and lacustrine units that are incised by tunnel valleys covered by a thick succession of Late Glacial and Holocene marine deposits (Larsen *et al.* 2009a; Sandersen

et al. 2009). Whilst the change in facies observed in the Innomar data could occur due to transitions between till and glaciomarine or lacustrine units, the bedding inclination is not so simple to explain.

It is possible that the deeper facies could represent cross-bedding associated with the development of the Skagen spit, or palaeo-Skagen spit(s), with marine transgressive erosion surfaces noted on the north-western coastline of the present spit, which is migrating eastward (Nielsen & Johannessen 2009). However, the observed facies are too deep and, due to the regressive nature of the shoreline, would have been significantly deeper prior to the early Holocene (Richardt 1996).

The inclination and north-eastward dipping of the beds in Tannis Bugt could indicate deposition within a prograding system during the development of the shallow-water area off Vendsyssel, which extends some 20 km from the coastline. The truncated, inclined facies shown in Figs 3, 5 are similar to a delta facies which may undergo deformation via gravity-driven processes (Postma 1995; Patruno *et al.* 2015). However, if a delta complex is present in Tannis Bugt, the age and sediment source are unknown. Early Quaternary deltaic units are present in the central and southern North Sea (Lamb *et al.* 2018), but these dip in a westerly direction. If deltaic, the NE–SE-direction of dip observed in Tannis Bugt

would indicate progradation into the Skagerrak and Norwegian Channel. This suggests that the inclined bedding could represent subaqueous shelf-prism clinoforms (Patruno *et al.* 2015), deposited within the Skagerrak embayment during low stands (producing the observed SW–NE-orientated strike) and as a consequence of the stronger south-west flow from the North Sea during high stands (producing the SW–NE-orientated strike).

Glaciotectonic activity is documented near Tannis Bugt, with complexes at Rubjerg Knude (Pedersen 2005) and in Jammerbugt (Pedersen & Boldreel 2017; Fig. 1), and could also cause the observed facies. Tannis Bugt has a dip geometry (to the north-east) that is similar to Jammerbugt, though the measured reflector inclination of *c.* 1–2° is less than the *c.* 6° thrust plane dip seen in the proximal part of the Jammerbugt complex (Pedersen & Boldreel 2017). The lower angle of inclination could be due to limited penetration of the Innomar data not revealing the unit's true geometry, or it could represent a low-angled thrust component, such as a flat (Pedersen & Boldreel 2015). However, it is perhaps more likely that the facies are a result of the combined processes of clinoform deposition, causing the observed inclination, and glaciotectonic activity causing the deformation.

If the deformation in Tannis Bugt is glaciotectonic, it is unclear whether it is part of a larger Tannis–Jammerbugt complex, or whether there are two separate complexes. In any case, their geographical proximity and similar direction of dip indicate that they could be formed by a similar process such as an advance from the Norwegian Channel ice stream.

Conclusion

Inclined and deformed bedding planes dipping predominantly to the north-east have been identified in Tannis Bugt, off the north coast of Vendsyssel. A bouldery area, representing either winnowed glacial unit or eroded pre-Quaternary bedrock, has been identified near the coastline in the centre of the bay. If the inclined bedding represents a prograding sequence with an eroded upper surface then the outcrop long section could represent a unit of significant age, with the possibility of pre-Quaternary geology exposed at the seabed. If the inclination and deformation are the result of glaciotectonic deformation then the site represents a newly discovered glaciotectonic complex. Deeper penetrating multichannel

seismic data and geological samples will be required to fully understand the geology of Tannis Bugt and how it relates to the development of northern Denmark.

Acknowledgements

We thank the Danish Environmental Protection Agency for permission to publish data acquired during the survey of Natura2000 areas, the captain and crew of the R/V *Aurora* for their assistance during the survey and Orbicon A/S for the acquisition of video data.

References

- Håkansson, E. & Pedersen, S.A.S. 1992: Geologisk kort over den danske underground, map sheet. Copenhagen: Varv.
- Knudsen, K.L., Kristensen, P. & Larsen, N.K. 2009: Marine glacial and interglacial stratigraphy in Vendsyssel, northern Denmark: foraminifera and stable isotopes. *Boreas* **38**, 787–810.
- Lamb, R.M., Harding, R., Huuse, M., Stewart, M. & Brocklehurst, S.H. 2018: The early Quaternary North Sea Basin. *Journal of the Geological Society* **175**, 275–290.
- Larsen, N.K., Knudsen, K.L., Krohn, C.F., Kronborg, C., Murray, A.S. & Nielsen, O.L.E.B. 2009a: Late Quaternary ice sheet, lake and sea history of southwest Scandinavia – a synthesis. *Boreas* **38**, 732–761.
- Larsen, N.K., Krohn, C.F., Kronborg, C., Nielsen, O.B. & Knudsen, K.L. 2009b: Lithostratigraphy of the Late Saalian to Middle Weichselian Skaerumhedehede Group in Vendsyssel, northern Denmark. *Boreas* **38**, 762–786.
- Nielsen, L.H. & Johannessen, P.N. 2009: Facies architecture and depositional processes of the Holocene–Recent accretionary forced regressive Skagen spit system, Denmark. *Sedimentology* **56**, 935–968.
- Patruno, S., Hampson, G.J. & Jackson, C.A.-L. 2015: Quantitative characterisation of deltaic and subaqueous clinoforms. *Earth Science Reviews* **142**, 79–119.
- Pedersen, S.A.S. 2005: Structural analysis of the Rubjerg Knude Glaciotectonic Complex, Vendsyssel, northern Denmark. *Geological Survey of Denmark and Greenland Bulletin* **8**, 192 pp.
- Pedersen, S.A.S. & Boldreel, L.O. 2015: Thrust-fault architecture of glaciotectonic complexes in Denmark. *Geological Survey of Denmark and Greenland Bulletin* **33**, 17–20.
- Pedersen, S.A.S. & Boldreel, L.O. 2017: Glaciotectonic deformations in the Jammerbugt and glaciodynamic development in the eastern North Sea. *Journal of Quaternary Science* **32**, 183–195.
- Postma, G. 1995: Sea-level-related architectural trends in coarse-grained delta complexes. *Sedimentary Geology* **98**, 3–12.
- Richardt, N. 1996: Sedimentological examination of the Late Weichselian sea-level history following deglaciation of northern Denmark. In: Andrews, J.T. *et al.* (eds): Late Quaternary Palaeoceanography of the North Atlantic Margins. Geological Society (London), Special Publication **111**, 261–273.
- Sandersen, P.B.E., Jørgensen, F., Larsen, N.K., Westergaard, J.H. & Auken, E. 2009: Rapid tunnel-valley formation beneath the receding Late Weichselian ice sheet in Vendsyssel, Denmark. *Boreas* **38**, 834–851.

Authors' addresses

M.J.O., N.H.W., Z.A.-H., N.N.-P., J.O.L., *Geological Survey of Denmark and Greenland, C.F. Møllers Allé 8, DK-8000 Aarhus C, Denmark.*

E-mail: *mow@geus.dk.*

K.J.A., *Department of Geoscience, Aarhus University, Høegh-Guldbergs Gade 2, DK-8000 Aarhus C, Denmark.*

Update of the seamless 1:500 000 scale geological map of Greenland based on recent field work in the Wandel Sea Basin, eastern North Greenland

Kristian Svennevig

Geological maps are core products of national geological surveys and represent the sum of geological knowledge of any given area. However, dedicated and extensive mapping projects in the Arctic are mostly a thing of the past due to difficulty in financing such costly basic research efforts. Today, an overview of the geology of Greenland is portrayed by a seamless digital 1:500 000 scale geological map (Kokfelt *et al.* 2013; Pedersen *et al.* 2013), based on printed maps on this scale produced since 1982 by the Geological Survey of Denmark and Greenland (GEUS; see Holst *et al.* 2013). The digital map now makes it possible to update smaller areas with new, published or otherwise quality-controlled geological data (e.g. Kolb *et al.* 2016). This ensures that the map reflects the current state of geological knowledge without undertaking extensive new mapping to update individual map sheets, as has previously been the modus operandi. An online

version of the map is available from www.greenmin.dk/map. However, procedures are required to ensure that updates are carried out routinely and that the quality and coherence of the updated map is of the Survey's standards.

Results of recent field work in the Wandel Sea Basin (Fig. 1) and in particular the publication of a new geological map sheet Kilen on a scale of 1:100 000 (Svennevig in press) have implications for the geology shown on the above mentioned 1:500 000 scale seamless geological map of Greenland. The post-Devonian part of this map in eastern North Greenland has been updated according to the results of studies published since the publication of the original printed maps (Bengaard & Henriksen 1986; Jepsen 2000). The changes do not call for an update of the 1:2 500 000 scale geological map of Greenland (Henriksen *et al.* 2009).

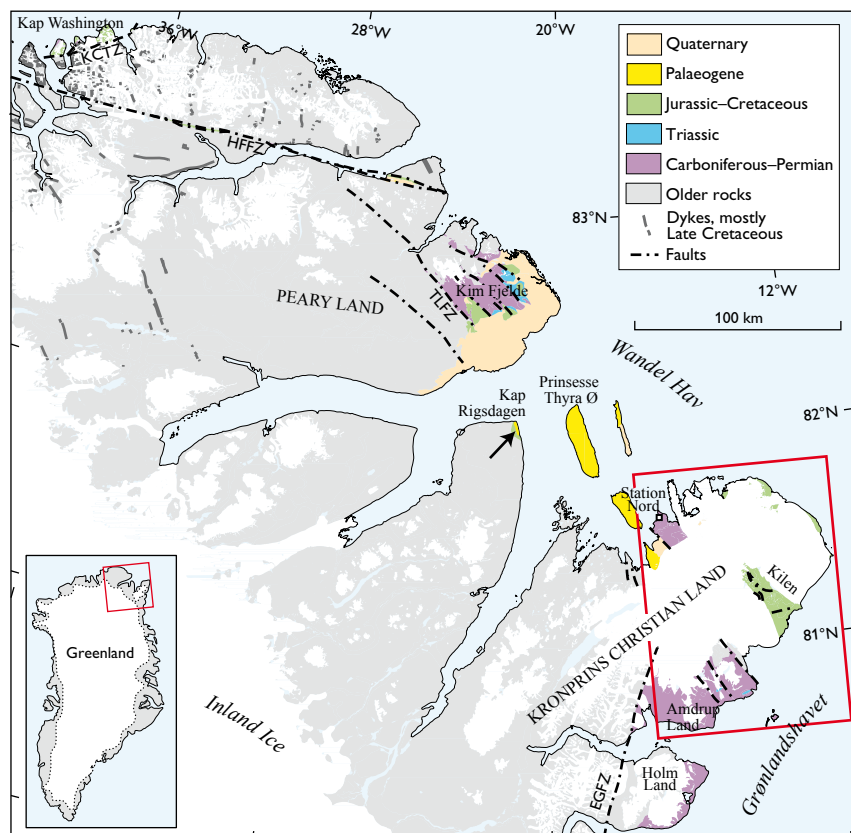


Fig. 1. Simplified geological map of the Wandel Sea Basin showing the major structural elements and Upper Palaeozoic to Palaeogene sediments. Modified from Bengaard & Henriksen (1986) and Henriksen (2003) with updates from Kilen modified from Svennevig (in press). **EGFZ**: East Greenland Fault Zone. **HFFZ**: Harder Fjord Fault Zone. **KCTZ**: Kap Cannon Thrust Zone. **TLFZ**: Trolle Land Fault Zone. Red frame shows the position of Fig. 2 and black arrow shows the new occurrence of Thyra Ø Formation.

Updates to the geological map based on recent field work in the Wandel Sea Basin

Parts of the seamless 1:500 000 geological map of Greenland (Kokfelt *et al.* 2013; Pedersen *et al.* 2013) have been updated. These updates are based on data from extensive field work in 2012, 2013 and 2016 in the Carboniferous–Palaeogene Wandel Sea Basin in eastern North Greenland (Bojesen-Koefoed *et al.* 2014; Hovikoski *et al.* in press; Piasecki *et al.* in press), the results of a recent PhD-thesis (Svennevig in press; Svennevig *et al.* 2016, 2017) and previously published work (Pedersen & Håkansson 1999; Henriksen 2003). In the course of this work, two old map units have been emended and four new ones established. Furthermore, four map units

have been expanded to encompass new areas. The legend of the seamless map has been updated accordingly.

Twenty-one lithological units from the new 1:100 000 scale map sheet (Svennevig in press) are reduced to five units in the 1:500 000 scale map, and the revised stratigraphic resolution is seen in Fig. 2B. The letter codes mentioned below (IF, C2, MM, LP, MI, Tr, J, JC, LC and UC) refer to the code used in the GEUS map database.

1. *Expansion of unit C2: Upper Carboniferous sediments.* A small occurrence of tentatively dated Upper Palaeozoic melange unit at Kilen is included in the unit 'Upper Carboniferous sediments' (C2) found on Amdrup and Holm Land.

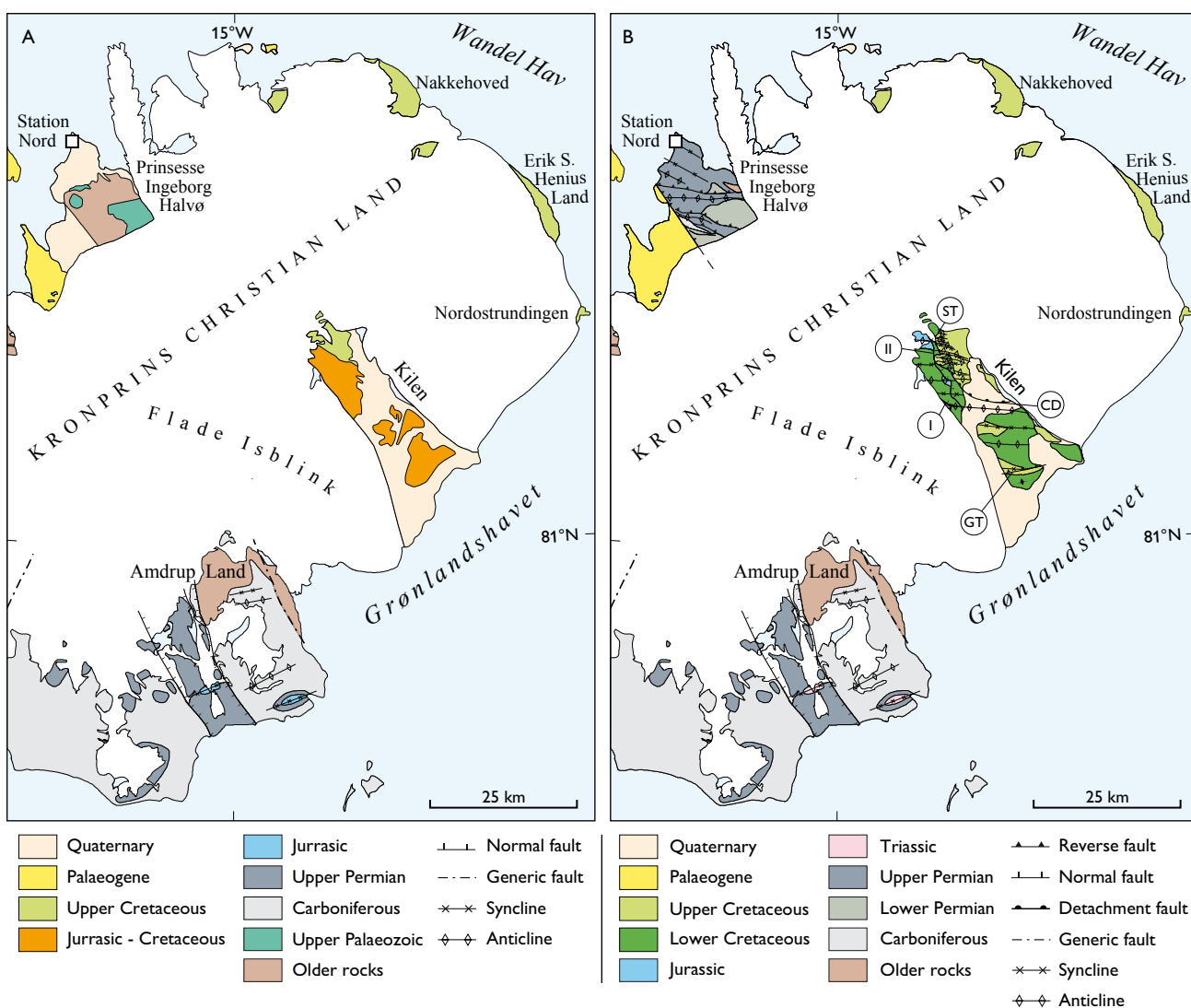


Fig. 2. Geological maps of Kronprins Christian Land showing the geology before (A) and after (B) the update of the digital map. One of the items on the new map (Fig. 2B) is a N–S-verging fold and thrust belt covering Prinsesse Ingeborg Halvø and Kilen as described by Svennevig (in press) and Svennevig *et al.* (2016, 2017). Faults on Fig. 2B adopted from Svennevig (in press): I and II: Normal Fault I and II. CD: Central Detachment, ST: Sadelfjeld Thrust. GT: Gåseslette Thrust.

Furthermore, the ‘Mallemuk Mountain Group’ (MM) in Kim Fjelde on Peary Land, a relic from the old printed map (Benggaard & Henriksen 1986), is included in the C2 unit following (Stemmerik *et al.* 1996, 2000) and the map unit ‘Mallemuk Mountain Group’ (MM) has thus been emended. The unit is also found on Prinsesse Ingeborg Halvø (see below, Fig. 2).

2. Erection of a new unit Tr: Triassic siliciclastic sediments, undivided. The newly discovered Triassic Isrand Formation at Kilen and the Triassic on Amdrup Land (Alsen *et al.* 2017), is combined in a new map unit called ‘Triassic siliciclastic sediments, undivided’ (Tr). The strata on Amdrup Land were previously mapped as Jurassic (Fig. 2A; Stemmerik *et al.* 2000).

3. Erection of a new unit J: Jurassic siliciclastic sediments, undivided. Jurassic formations at Kilen: the Gletscherport, Mågensfjeld, Birkelund Fjeld and Kuglelejet Formations (Hovikoski *et al.* in press; Svennevig *et al.* in press) are combined into the new map unit ‘Jurassic siliciclastic sediments, undivided’ (J) which is only found at Kilen.

4. Erection of a new unit LC: Lower Cretaceous siliciclastic sediments, undivided. The lowermost Lower Cretaceous formations at Kilen, the Dromledome and Lichenryg Formations, are combined with the Upper Aptian – early to middle Cenomanian Galadriel Fjeld Formation (Hovikoski *et al.* in press; Svennevig *et al.* in press) in the new map unit ‘Lower Cretaceous siliciclastic sediments, undivided’ (LC).

5. Expansion of the unit UC: Upper Cretaceous siliciclastic sediments, undivided. The Sølverbæk Formation at Kilen (Hovikoski *et al.* in press; Svennevig *et al.* in press) is included in the unit UC, ‘Upper Cretaceous siliciclastic sediments, undivided’, together with small occurrences of Upper Cretaceous sediments at Kap Washington in northernmost Greenland.

A number of regionally significant faults and fold axes from the 1:100 000 scale Kilen map sheet have also been adapted for the 1:500 000 scale map. These are the normal Fault I and II and the reverse faults of the Central Detachment, the Gåseslette Thrust, and the Saddelfjeld Thrust (Fig 2B; Svennevig in press; Svennevig *et al.* in press).

Updates based on published work on Prinsesse Ingeborg Halvø

The geology on Prinsesse Ingeborg Halvø has also been updated (Fig. 2). In the original version of the 1:500 000 scale

map this area was mapped as mainly “Undivided Upper Proterozoic to Lower Palaeozoic sediments” (Benggaard & Henriksen 1986; Kokfelt *et al.* 2013). Since the publication of the printed map in 1986, a map was published as fig. 7 in Pedersen & Håkansson (1999). This figure was also adapted for a 1:1 000 000 scale map of the Caledonian orogeny (Henriksen 2003). The 1:500 000 scale seamless map has been updated according to this and now contains three Carboniferous–Permian map units of the Wandel Sea Basin: ‘Upper Carboniferous sediments’ (C2), the new unit ‘Lower Permian sediments, undivided’ (LP) which is only found at Prinsesse Ingeborg Halvø, and the Upper Permian ‘Midnatsfjeld and Kim Fjelde Formations’ (MI). Furthermore, a fault sliver of Proterozoic basement of the ‘Independence Fjord Group’ (IF) has also been mapped (Fig. 2B).

Updates based on recently published work on the Kap Rigsdagen beds

Following a recent publication identifying these beds as belonging to the Upper unit of the Early Cretaceous Ladegårdsåen Formation (Piasecki *et al.* in press), the outcrops found at Kap Rigsdagen (Fig. 1) are also assigned to the new map unit LC. Likewise, a small locality in southern Kim Fjelde in Peary Land is interpreted as Lower Cretaceous (Håkansson *et al.* 1981). In previous versions of the 1:500 000 scale map (Benggaard & Henriksen 1986) these two areas were assigned to the very broad map unit JC (Upper Jurassic – Lower Cretaceous sediments) along with strata at Kilen. This map unit is thus no longer necessary for the 1:500 000 scale map and has been emended. Piasecki *et al.* (in press) further ascribed a new occurrence of the Paleocene to possibly Eocene Thyra Ø Formation on top of the Ladegårdsåen Formation at Kap Rigsdagen. This occurrence has been shown as a small polygon with dashed outline on the updated map, since the lateral distribution of the formation at this locality is unknown (Fig. 1, arrow).

Suggested procedure for updating geological maps at GEUS

In order to make sure that the maps published by GEUS reflect the current state of geological knowledge, the digital geological maps should be routinely updated by including results from of multi-year regional field work such as the 2012, 2013 and 2016 expeditions to the Wandel Sea Basin, and which was also done after field work in South-East Greenland (Kolb *et al.* 2016).

In order to ensure the quality of the maps, it is important that only quality-tested and preferably peer-reviewed data

are used for the updates and that there is a fixed procedure for how they are carried out and reported. A map editor or potentially an external reviewer, checks the map and legend for consistency and quality. Before the update is carried out, the previous versions of the map are saved in the database and the changes to the map are recorded and documented in the metadata of the mapped elements. Finally, the details of the changes are reported as a GEUS map sheet description or in a brief paper such as the present one. When an area corresponding to a map sheet (see Holst *et al.* 2013, p. 59) has been sufficiently updated to justify printing of a new version, the updated map sheet can be printed along with a description.

There is a significant backlog in updating GEUS' series of map sheets with already published data. As exemplified above, systematic updating has not previously been the custom. Conducting this is important to make sure that the official maps published by GEUS reflect the current state of geological knowledge.

Acknowledgements

Thanks are due to S. Bernstein and G.K. Pedersen for helpful suggestions to earlier versions of this manuscript. W. Weng implemented the changes to the digital map.

References

- Alsen, P., McRoberts, C., Svennevig, K., Bojesen-Koefoed, J.A., Hovikoski, J. & Piasecki, S. 2017: The Isrand Formation: a Middle Triassic *Daonella*-bearing, black shale unit in Kilen, North Greenland (with a note on the Triassic in Amdrup Land). *Newsletters on Stratigraphy* **50**, 31–46.
- Bengaard, H.-J. & Henriksen, N. 1986: Geological map of Greenland, 1:500 000, Peary Land, sheet 8. Copenhagen: Geological Survey of Greenland.
- Bojesen-Koefoed, J.A., Alsen, P. & Christiansen, F.G. 2014: Six years of petroleum geological activities in North-East Greenland (2008–2013): projects and a view of the future. *Geological Survey of Denmark and Greenland Bulletin* **31**, 59–62.
- Henriksen, N. 2003: Caledonian Orogen, East Greenland 70°–82°N. *Geological Map 1:1 000 000. A compilation of lithostructural data*. Copenhagen: Geological Survey of Denmark and Greenland
- Henriksen, N., Higgins, A.K., Kalsbeek, F. & Pulvertaft, T.C.R. 2009: Greenland from Archaean to Quaternary. Descriptive text to the 1995 Geological map of Greenland, 1:2 500 000. 2nd edition. *Geological Survey of Denmark and Greenland Bulletin* **18**, 126 pp.
- Holst, J., Glendal, E.W. & Dawes, P.R. 2013: Catalogue of Survey publications on Greenland. Copenhagen: Geological Survey of Denmark and Greenland, 108 pp.
- Hovikoski, J., Pedersen, G.K., Alsen, P., Lauridsen, B.W., Svennevig, K., Nøhr-Hansen, H., Sheldon, E., Dybkjær, K., Bojesen-Koefoed, J.A. & Piasecki, S. 2018. in press: The Jurassic–Cretaceous lithostratigraphy of Kilen, Kronprins Christian Land, eastern North Greenland. *Bulletin of the Geological Society of Denmark* **66**, 61–114.
- Håkansson, E., Birkelund, T. & Piasecki, S. 1981: Jurassic-Cretaceous boundary strata of the extreme Arctic (Peary Land, North Greenland). *Bulletin of the Geological Society of Denmark* **30**, 11–42.
- Jepsen, H.F. 2000: Geological map of Greenland 1:500 000, Lambert Land, sheet 9. Copenhagen: Geological Survey of Denmark and Greenland.
- Kokfelt, T.F., Keulen, N., Weng, W.L. & Pedersen, M. 2013: Geological map of Greenland, 1 : 500 000. Copenhagen: Geological Survey of Denmark and Greenland.
- Kolb, J., Steensgaard, B.M. & Kokfelt, T.F. 2016: Geology and mineral potential of South-East Greenland. *Danmarks og Grønlands Geologiske Undersøgelse Rapport* **2016/38**, 1–157.
- Pedersen, M., Weng, W.L., Keulen, N. & Kokfelt, T.F. 2013: A new seamless digital 1:500 000 scale geological map of Greenland. *Geological Survey of Denmark and Greenland Bulletin* **28**, 65–68.
- Pedersen, S.A.S. & Håkansson, E. 1999: Kronprins Christian Land Orogeny deformational styles of the end Cretaceous transpressional mobile belt in eastern North Greenland. *Polarforschung* **69**, 117–130.
- Piasecki, S., Nøhr-Hansen, H. & Dalhoff, F. 2018. in press: Revised stratigraphy of Kap Rigsdagen beds, Wandel Sea Basin, North Greenland. *Newsletters on Stratigraphy*, 15 pp. <http://dx.doi.org/10.1127/nos/2018/0444>
- Stemmerik, L., Håkansson, E., Madsen, L., Nilsson, I., Piasecki, S., Pinnard, S. & Rasmussen, J.A. 1996: Stratigraphy and depositional evolution of the Upper Palaeozoic sedimentary succession in eastern Peary Land, North Greenland. *Grønlands Geologiske Undersøgelse Bulletin* **171**, 45–71.
- Stemmerik, L., Larsen, B.D. & Dalhoff, F. 2000: Tectono-stratigraphic history of northern Amdrup Land, eastern North Greenland: implications for the northernmost East Greenland shelf. *Geology of Greenland Survey Bulletin* **187**, 7–19.
- Svennevig, K. 2018. in press: Geological map of Greenland, 1:100 000, Kilen 81 Ø.1 Syd. Copenhagen: Geological Survey of Denmark and Greenland.
- Svennevig, K., Guarnieri, P. & Stemmerik, L. 2016: Tectonic inversion in the Wandel Sea Basin: a new structural model of Kilen (eastern North Greenland). *Tectonics* **35**, 2896–2917.
- Svennevig, K., Guarnieri, P. & Stemmerik, L. 2017: 3D restoration of a Cretaceous rift basin in Kilen, eastern North Greenland. *Norwegian Journal of Geology* **97**, 21–32.
- Svennevig, K., Alsen, P., Guarnieri, P., Hovikoski, J., Lauridsen, B.W., Pedersen, G.K., Nøhr-Hansen, H. & Sheldon, E. 2018. in press: Descriptive text to the geological map of Greenland, 1:100 000, Kilen 81 Ø.1 Syd. *Geological Survey of Denmark and Greenland Map Series* **8**.

Author's address

Geological Survey of Denmark and Greenland (GEUS), Østeer Voldgade 10, DK-1350 Copenhagen K, Denmark. E-mail: ksv@geus.dk.

Base-metal and REE anomalies in lower Palaeozoic sedimentary rocks of Amundsen Land, central North Greenland: implications for Zn-Pb potential

Diogo Rosa, John F. Slack and Hendrik Falck

During the 2013 field season, siliciclastic and carbonate rocks of the lower Palaeozoic sedimentary succession of the Franklinian Basin in Amundsen Land, central North Greenland, were collected for whole-rock geochemical analysis. These data are evaluated here in an attempt to identify possible hydrothermal signatures related to sediment-hosted Zn-Pb mineralisation, similar to that found in correlative strata at the large Citronen Fjord deposit located *c.* 100 km to the east-north-east. In this paper, we use the term Sedex in a broad sense to describe stratiform, sediment-hosted deposits that formed either by syngenetic (exhalative) processes or by sub-sea-floor replacement coeval with sedimentation (e.g. Emsbo *et al.* 2016); the term Mississippi Valley-type (MVT) is used for non-stratiform Zn-Pb deposits that formed epigenetically during late diagenesis or tectonism (e.g. Leach *et al.* 2010).

Regional setting

The Late Precambrian to Devonian Franklinian Basin extends *c.* 2000 km from the Canadian Arctic Islands to eastern North Greenland (Higgins *et al.* 1991). In eastern North Greenland, this basin fill overlies the Proterozoic Independence Fjord Group and the Hagen Fjord Group, corresponding to the passive continental margin of Laurentia. The Franklinian Basin is characterised by a transition from

a deep-water trough, with mainly fine-grained siliciclastic strata, separated from shelf carbonates to the south (Fig. 1; Higgins *et al.* 1991). As summarised in Kolb *et al.* (2016), Zn-Pb mineralisation in the Franklinian Basin resulted from two different events: early exhalative and/or sub-sea-floor replacement in deep-water siliciclastic rocks, and late epigenetic MVT mineralisation in shelf carbonates. The present study concerns the potential for Zn-Pb mineralisation in the Lower Ordovician to Lower Silurian Amundsen Land Group, in Amundsen Land. In the study area, the Amundsen Land Group comprises black bedded chert and laminated mudstone, commonly siliceous, with subordinate thin-bedded siliceous turbidites and greenish siltstone; locally, thick redeposited chert and limestone conglomerate interbedded with thick calcareous turbidites are present (Friderichsen *et al.* 1982). The chert contains radiolarians (Higgins *et al.* 1991), implying that biogenic silica is responsible for the quartz-rich nature of these rocks, and the siliceous mudstone.

Approximately 100 km east-north-east of the study area, in northern Peary Land, correlative siliciclastic rocks host the large undeveloped, sediment-hosted Citronen Fjord deposit (Fig. 1; van der Stijl *et al.* 1998), with reported total resources (measured + indicated + inferred), at a 2.0% Zn cut off, of 132 Mt with 4.0% Zn and 0.4% Pb (Ironbark Zinc

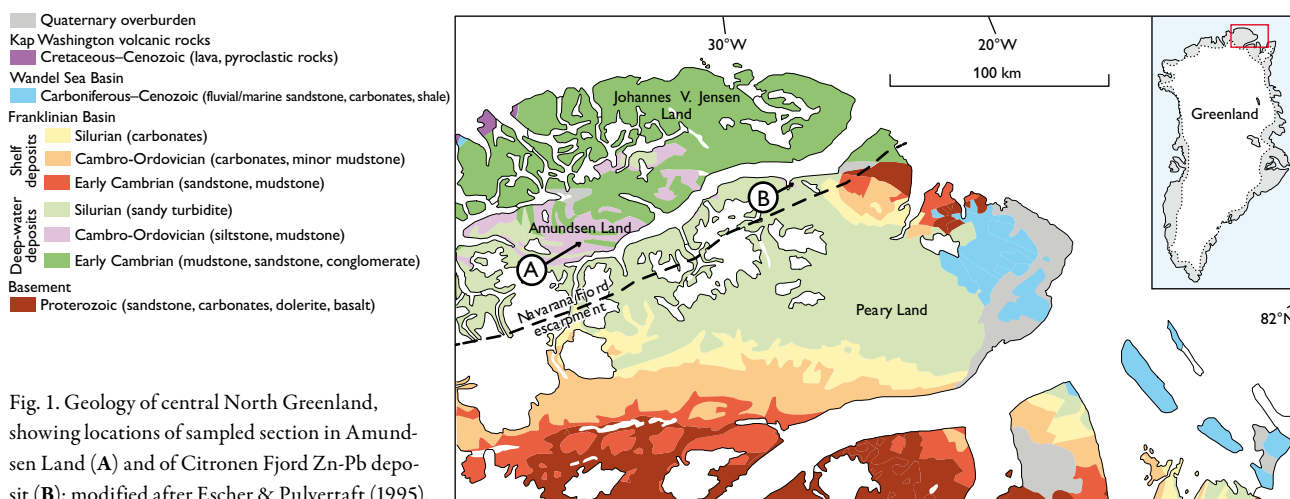


Fig. 1. Geology of central North Greenland, showing locations of sampled section in Amundsen Land (A) and of Citronen Fjord Zn-Pb deposit (B); modified after Escher & Pulvertaft (1995).

2012). In the model of Slack *et al.* (2015), this deposit formed predominantly by exhalative processes.

Younger epigenetic, carbonate-hosted, MVT Zn-Pb occurrences, found in the carbonate shelf in southern Peary Land, are related to the migration of basinal brines expelled by tectonism and/or hydraulic head caused by Ellesmerian orogenic uplift during the Middle to Late Devonian (Rosa *et al.* 2016). In Amundsen Land, no carbonate shelf exists, so this mineralisation style is not expected to be present, although effects of the Ellesmerian orogeny are well expressed by open to recumbent folds and local thrust faults.

Methods

All samples were collected along one section across strata of the Amundsen Land Group at WGS84 longitude 35°3647 W and latitude 82°9655 E (Fig. 1). Twenty-two samples of silty limestone, dolomitic mudstone and mudstone were analysed using a variety of methods. All data are from Acme Analytical Laboratories Ltd. in Vancouver, British Columbia (Canada), except Y and rare-earth elements (REE) that were determined at Activation Laboratories Ltd. in Ancaster, Ontario (Canada). Detailed information on methods, standards, and uncertainties are given on the respective web sites (www.acmelab.com; www.actlabs.com). Complete analyses of all 22 samples are available in *Appendix A* (online Excel file).

Results

Several samples have distinctive bulk compositions. For major-element oxides, one of three grey mudstones contains slightly high Fe_2O_3^T (7.83 wt%) relative to average shale (6.75 wt%; Appendix IV in Krauskopf & Bird 1995); this sample also has elevated MnO (0.14 wt%) in contrast to the other samples that contain <0.05 wt% MnO. The three mudstones have uniformly low total S and organic C (<0.8 wt% and <0.7 wt%, respectively). For metals of economic and exploration interest, one mudstone sample is noteworthy for having slightly anomalous Zn (174 ppm), Pb (29.6 ppm), Ni (75.0 ppm) and As (24.7 ppm) relative to average concentrations in shale (Zn = 95 ppm; Pb = 20 ppm; Ni = 68 ppm; As = 13 ppm; Krauskopf & Bird 1995, Appendix IV). One sample of silty limestone has the highest total S (1.27 wt%) and Pb (63.0 ppm) among all 22 analysed samples, the latter concentration being highly anomalous relative to the average of 3.1 ppm Pb for unaltered limestone (Hartree & Veizer 1982).

Abundances of REE vary greatly from 0.6–2.0 × average Post-Archaean Australian Shale (PAAS; Fig. 2). Most of the mudstone and all of the carbonate-rich samples (silty limestone, dolomitic limestone, calcareous shale) display

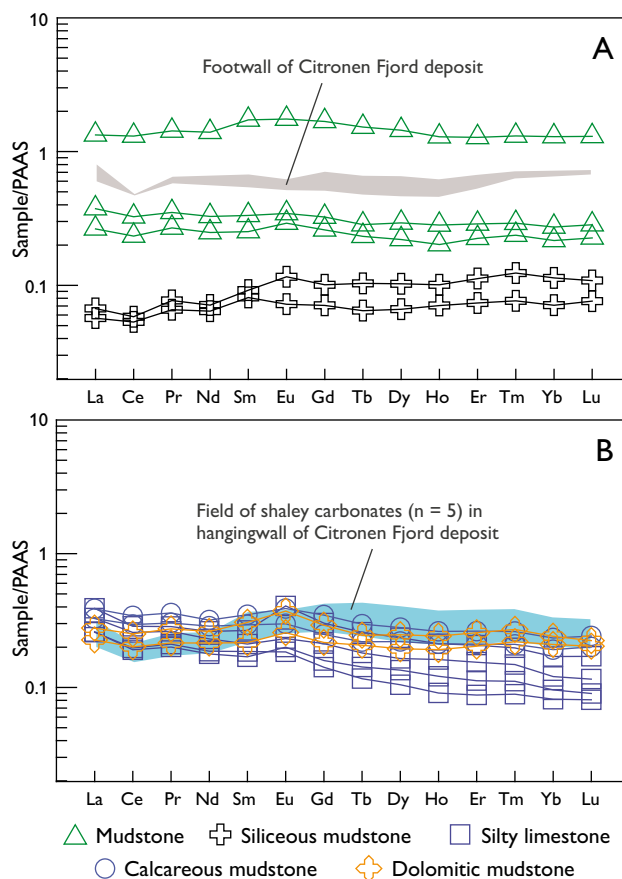


Fig. 2. Plots of rare-earth element concentrations of representative samples of early Palaeozoic sedimentary rocks from Amundsen Land Group in Amundsen Land. **A:** mudstone and siliceous mudstone. **B:** Calcareous mudstone, dolomitic mudstone, and silty limestone. Field of samples hosting the Citronen Fjord deposit are included (Slack *et al.* 2015), for comparison; note that small positive Eu anomalies for these samples (1.16–1.29) are not evident due to overlapping patterns. Normalisations are to average Post-Archaean Australian Shale (PAAS); data from Taylor & McLennan (1985).

relatively flat PAAS-normalised patterns, which are typical of sedimentary rocks from throughout the geological record (e.g. McLennan 1989). However, one mudstone and both siliceous mudstone samples show slight depletion of light rare-earth elements (LREE). Most of the silty limestone samples display slight enrichment of LREE. Calculated Eu anomalies (Eu/Eu^*), relative to PAAS, range from 0.90 to 1.51; 20 of 22 samples have positive anomalies, the three highest values (1.41–1.51) occurring in silty limestone. These Eu anomalies are not an analytical artifact of Ba interference on Eu (e.g. Slack *et al.* 2004), because no correlation exists between Eu/Eu^* and Ba. Also important is the fact that all samples display small negative Ce anomalies (Ce/Ce^*), which relative to PAAS vary from 0.81 to 0.95; most are true anomalies (i.e., unrelated to anomalous La enrichment), based on a discriminant plot of Pr/Pr^* vs Ce/Ce^* (Fig. 3).

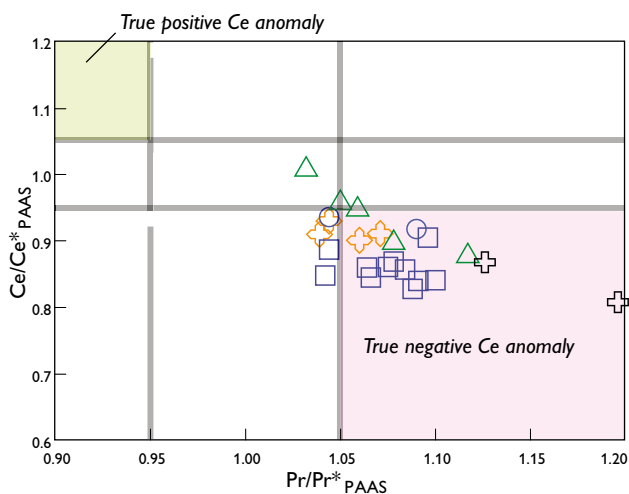


Fig. 3. Plot of Ce anomaly (Ce/Ce^*) vs Pr anomaly (Pr/Pr^*) for analysed samples of early Palaeozoic sedimentary rocks from the Amundsen Land Group in Amundsen Land. Data are normalised to PAAS. Fields after Bau & Dulski (1996). Symbols as in Fig. 2.

Discussion

The presence in one mudstone sample of slightly high $Fe_2O_3^T$, Zn, Pb, Ni and As is permissive evidence of a hydrothermal component being present in the basin. The small LREE depletion in this sample and in the two siliceous mudstone samples (Fig. 2A), likely reflects the dissolution of detrital apatite, which in low-temperature sedimentary environments occurs by interaction with acidic fluids and not typical seawater-derived pore fluids (see Slack *et al.* 2017).

The geochemical data for this mudstone sample, namely elevated MnO together with very low Mo, record sedimentation and early diagenesis in oxic bottom waters (e.g. Slack *et al.* 2017). Oxic bottom waters are consistent with the presence of small negative Ce anomalies in this sample, in both siliceous mudstone samples, and in most of the carbonate-rich rocks. These conditions, as well as the apparently low availability of H_2S in pore fluids beneath the palaeo-sea floor (total S < 0.8 wt%), were also proposed by Slack *et al.* (2015) for the host sedimentary rocks during initial formation of the Citronen Fjord deposit. However, according to their model for that deposit, only after emplacement of debris flows that physically restricted the local basin and sealed off communication with the larger oxic ocean, did the venting of hydrothermal fluids turn the bottom waters anoxic and possibly locally very reducing (euxinic) and allow for sulphide preservation. If this model for the redox evolution of the Citronen Fjord deposit is correct, an analogous scenario for Amundsen Land (this study) hinges on verifying the local presence of anoxic to euxinic bottom waters, a requirement as yet unachieved, without supporting evidence from additional sampling and analyses.

The presence of small positive Eu anomalies in most samples is consistent with a hydrothermal component (e.g. Lottermoser 1992). However, other non-hydrothermal processes can also create small positive Eu anomalies in sedimentary rocks, both siliciclastic and carbonate. For example, in organic-rich black shales, small positive Eu anomalies may form diagenetically in euxinic pore fluids (Slack *et al.* 2017, and references therein), but no evidence of such fluids exists in the geochemically anomalous mudstone, based on its elevated MnO (0.14 wt%) coupled with low organic C (0.37 wt%) and very low Mo (1.75 ppm) contents, which together indicate oxic (not anoxic or euxinic) bottom waters and pore fluids (see Slack *et al.* 2017). Furthermore, TOC values lack any correlation with metal concentrations. The relatively high $Fe_2O_3^T$ content of this mudstone sample could be a hydrothermal signature, but might also reflect a detrital component derived from a Fe-rich source area. Regarding the positive Eu anomalies present in all of the carbonate samples, a possible non-hydrothermal origin for this anomaly may be related to a large clay component (Tostevin *et al.* 2016), but this explanation is ruled out by the fact that the samples with the highest Eu/Eu* values (1.41–1.51) have uniformly low Al_2O_3 (0.49–0.62 wt%). Given these observations, we conclude that the small positive Eu anomalies reflect a hydrothermal signature, involving the passage of reduced fluids that preferentially carried Eu^{2+} (Bau 1991). Importantly, a hydrothermal origin has also been proposed by several workers for positive Eu anomalies in the carbonate gangue and carbonate-rich wall rocks and country rocks of several stratiform Sedex deposits (e.g. Slack *et al.* 2004; Frimmel 2009).

The inferred hydrothermal component in the early Palaeozoic siliciclastic and carbonate rocks of the studied section can be ascribed to either a distal or a proximal source, or both. In the case of a distal source, the likely prolonged (*c.* 10^5 – 10^6 y) venting of hydrothermal fluids into seawater to form the Citronen Fjord deposit could account for the Eu incorporated into the distal mudstones and carbonates of Amundsen Land during sedimentation, by mixing of hydrothermally derived Eu with seawater. In the latter case, involving a proximal source, the observed base-metal and REE anomalies – both Eu and LREE – in the samples analysed here could record a hydrothermal signature from a local system of either syngenetic or epigenetic origin. Given the apparent lack of organic-rich black shales in the study area with anoxic or euxinic redox signatures, a syngenetic origin for this postulated Zn–Pb mineralisation is considered unlikely, either by purely exhalative or downward-penetrating brine processes (Emsbo *et al.* 2016; Sangster 2018). The occurrence of undiscovered MVT Zn–Pb deposits is also possible (Rosa *et al.* 2016), but this type of mineralisation is characterised by negative, not

positive, Eu anomalies in carbonate host rocks and gangue minerals (e.g. Graf 1984; Souissi *et al.* 2013).

In summary, considering all available field and geochemical data, including the lack of evidence for anoxic or euxinic bottom waters during sedimentation, we suggest that the base-metal and REE anomalies highlighted in this study from the Amundsen Land Group, in Amundsen Land, favour a potential for local Sedex Zn-Pb mineralisation that formed mainly by the sub-sea-floor replacement of carbonate-rich sediments. Additional sampling and geochemical analysis are recommended for the study area, in order to better evaluate this mineral potential.

Acknowledgements

This work was financially supported by GEUS and the Ministry of Mineral Resources of Greenland, through the Nordzinc project. Additional support was provided by the Northwest Territories Geological Survey, Canada. Per Kalvig and Erik Vest Sørensen of GEUS are acknowledged for collaboration during field work. We thank Hartwig Frimmel (University of Würzburg) and Steve Piercey (Memorial University of Newfoundland) for helpful reviews.

Online Appendix A: Whole-rock analyses of early Palaeozoic sedimentary rocks from the Amundsen Land Group in Amundsen Land.

References

- Bau, M. 1991: Rare-earth element mobility during hydrothermal and metamorphic fluid-rock interaction and the significance of the oxidation state of europium. *Chemical Geology* **93**, 219–230.
- Bau, M. & Dulski, P. 1996: Distribution of yttrium and rare-earth elements in the Penge and Kuruman iron-formations, Transvaal Supergroup, South Africa. *Precambrian Research* **79**, 37–55.
- Emsbo, P., Seal, R.R., Breit, G.N., Diehl, S.F. & Shah, A.K. 2016: Sedimentary exhalative (Sedex) zinc-lead-silver deposit model. U.S. Geological Survey Scientific Investigations Report **2010–5070–N**, 57 pp.
- Escher, J.C. & Pulvertaft, T.C.R. 1995: Geological map of Greenland, 1:2 500 000. Copenhagen: Geological Survey of Greenland.
- Friderichsen, J.D., Higgins, A.K., Hurst, J.M., Pedersen, S.A.S., Soper, N.J. & Surlyk, F. 1982: Lithostratigraphic frameworks of the Upper Proterozoic and lower Palaeozoic deep water clastic deposits of North Greenland. *Rapport Grønlands Geologiske Undersøgelse* **107**, 19 pp.
- Frimmel, H.E. 2009: Trace element distribution in Neoproterozoic carbonates as palaeoenvironmental indicator. *Chemical Geology* **258**, 338–353.
- Graf, J.L., Jr. 1984: Effects of Mississippi Valley-type mineralization on REE patterns of carbonate rocks and minerals, Viburnum Trend, southeast Missouri. *Journal of Geology* **92**, 307–324.
- Hartree, R. & Veizer, J. 1982: Lead and zinc distribution in carbonate rocks. *Chemical Geology* **37**, 351–365.
- Higgins, A.K., Ineson, J.R., Peel, J.S., Surlyk, F. & Sønderholm, M. 1991: Lower Palaeozoic Franklinian Basin of North Greenland. *Bulletin Grønlands Geologiske Undersøgelse* **160**, 71–139.
- Ironbark Zinc Ltd. 2012: Citronen January 2012 Resource. <http://ironbark.gl/projects/greenland/citronen/>
- Kolb J., Keiding J.K., Steenfelt A., Secher K., Keulen N., Rosa, D. & Stensgaard, B.M. 2016: Metallogeny of Greenland. *Ore Geology Reviews* **78**, 493–555.
- Krauskopf, K.B. & Bird, D.K. 1995: *Introduction to Geochemistry*, 647 pp., third edition. New York: McGraw-Hill, Inc.
- Leach, D.L., Taylor, R.D., Fey, D.L., Diehl, S.F., Saltus, R.W. 2010: A deposit model for Mississippi Valley-type lead-zinc ores. U.S. Geological Survey Scientific Investigations Report **2010–5070–A**, 52 pp.
- Lottermoser, B.G. 1992: Rare earth elements and hydrothermal ore formation processes. *Ore Geology Reviews* **7**, 25–41.
- McLennan, S.M. 1989: Rare earth elements in sedimentary rocks: influence of provenance and sedimentary processes. *Reviews in Mineralogy* **21**, 169–200.
- Rosa, R., Schneider, J. & Chiaradia, M. 2016: Timing and metal sources for carbonate-hosted Zn-Pb mineralization in the Franklinian Basin (North Greenland): constraints from Rb-Sr and Pb isotopes. *Ore Geology Reviews* **79**, 392–407.
- Sangster, D.F. 2018: Toward an integrated genetic model for vent-distal SEDEX deposits. *Mineralium Deposita*, **53**, 509–527.
- Slack, J.F., Kelley, K.D., Anderson, V.M., Clark, J.L. & Ayuso, R.A. 2004: Multistage hydrothermal silicification and Fe-Tl-As-Sb-Ge-REE enrichment in the Red Dog Zn-Pb-Ag district, northern Alaska: geochemistry, origin, and exploration applications. *Economic Geology* **99**, 1481–1508.
- Slack, J.F., Rosa, D. & Falck, H. 2015: Oxidic to anoxic transition in bottom waters during formation of the Citronen Fjord sediment-hosted Zn-Pb deposit, North Greenland. In: André-Mayer, A.-S. *et al.* (eds): *Mineral Resources in a Sustainable World: Proceedings of 13th Biennial SGA Meeting (Nancy, France)*, **5**, 2013–2016.
- Slack, J.F., Falck, H., Kelley, K.D. & Xue, G.G. 2017: Geochemistry of host rocks in the Howards Pass district, Yukon-Northwest Territories, Canada: sedimentary environments of Zn-Pb and phosphate mineralization. *Mineralium Deposita* **52**, 565–593.
- Souissi, F., Jemmali, N., Souissi, R. & Dandurand, J.L. 2013: REE and isotope (Sr, S, and Pb) geochemistry to constrain the genesis and timing of the F-(Ba-Pb-Zn) ores of the Zaghoun district (NE Tunisia). *Ore Geology Reviews* **55**, 1–12.
- Taylor, S.R. & McLennan, S.M. 1985: *The Continental Crust: Its Composition and Evolution*, 312 pp. Oxford, UK: Blackwell Scientific Publications.
- Tostevin, R., Shields, G.A., Tarbuck, G.M., He, T., Clarkson, M.O. & Wood, R.A. 2016: Effective use of cerium anomalies as a redox proxy in carbonate-dominated marine settings. *Chemical Geology* **438**, 146–162.
- van der Stijl, F.W. & Mosher, G.Z. 1998: The Citronen Fjord massive sulphide deposit, Peary Land, North Greenland: discovery, stratigraphy, mineralization and structural setting. *Geology of Greenland Survey Bulletin* **179**, 40 pp.

Authors' addresses

D.R., *Geological Survey of Denmark and Greenland, Øster Voldgade 10, DK-1350 Copenhagen K Denmark*. E-mail: dro@geus.dk.

J.F.S., *U.S. Geological Survey (Emeritus), National Center, MS 954, Reston, VA 20192 USA*.

H.F., *Northwest Territories Geoscience Survey, P.O. Box 1320, Yellowknife, NWT X1A 2L9 Canada*.

Mineral mapping by hyperspectral remote sensing in West Greenland using airborne, ship-based and terrestrial platforms

Sara Salehi and Simon Mose Thaarup

While multispectral images have been in regular use since the 1970s, the widespread use of hyperspectral images is a relatively recent trend. This technology comprises remote measurement of specific chemical and physical properties of surface materials through imaging spectroscopy. Regional geological mapping and mineral exploration are among the main applications that may benefit from hyperspectral technology. Minerals and rocks exhibit diagnostic spectral features throughout the electromagnetic spectrum that allow their chemical composition and relative abundance to be mapped.

Most studies using hyperspectral data for geological applications have concerned areas with arid to semi-arid climates, and using airborne data collection. Other studies have investigated terrestrial outcrop sensing and integration with laser scanning 3D models in ranges of up to a few hundred metres, whereas less attention has been paid to ground-based imaging of more distant targets such as mountain ridges, cliffs or the walls of large pits. Here we investigate the potential of using such data in well-exposed Arctic regions with steep topography as part of regional geological mapping field campaigns, and to test how airborne hyperspectral data can be combined with similar data collected on the ground or from moving platforms such as a small ship. The region between the fjords Ikertoq and Kangerlussuaq (Søndre Strømfjord) in West Greenland was selected for a field study in the summer of 2016. This region is located in the southern part of the Palaeoproterozoic Nagssugtoqidian orogen and consists of high-grade metamorphic ortho- and paragneisses and metabasic rocks (see below). A regional airborne hyperspectral data set (i.e. HyMAP) was acquired here in 2002 (Tukiainen & Thorning 2005), comprising 54 flight lines covering an area of *c.* 7500 km²; 19 of these flight lines were selected for the present study (Fig. 1). The target areas visited in the field were selected on the basis of preliminary interpretations of HyMap scenes and geology (Korstgård 1979).

Two different sensors were utilised to acquire the new hyperspectral data, predominantly a Specim AisaFenix hyperspectral scanner due to its wide spectral range covering the visible to near infrared and shortwave infrared parts of the electromagnetic spectrum. A Rikola Hyperspectral Imager constituted a secondary imaging system. It is much smaller

and lighter than the Fenix scanner, but is spectrally limited to the visible near infrared range. The results obtained from combining the airborne hyperspectral data and the Rikola

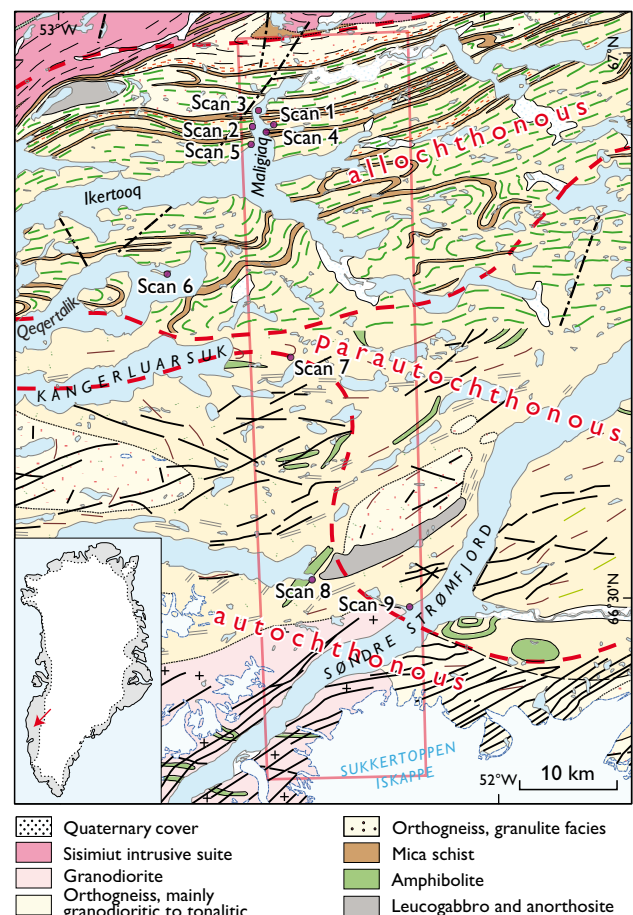


Fig. 1. Geological map across the southern Nagssugtoqidian Orogen simplified from Garde & Marker (2010) and locations of scanned areas mentioned in the text. Red frame: coverage of airborne hyperspectral data selected for this study. From south to north this region comprises (K. Sørensen, personal communication 2018): an autochthonous zone in which deformation regularly increases towards the parautochthonous zone expressed in clockwise rotation of Kangâmiut basic dykes, a parautochthonous zone in which Nagssugtoqidian deformation and metamorphism are highly heterogeneous, and an allochthonous zone where juvenile metasedimentary rocks are interfolded and thrust-stacked with Archaean gneisses containing amphibolitic metadykes.

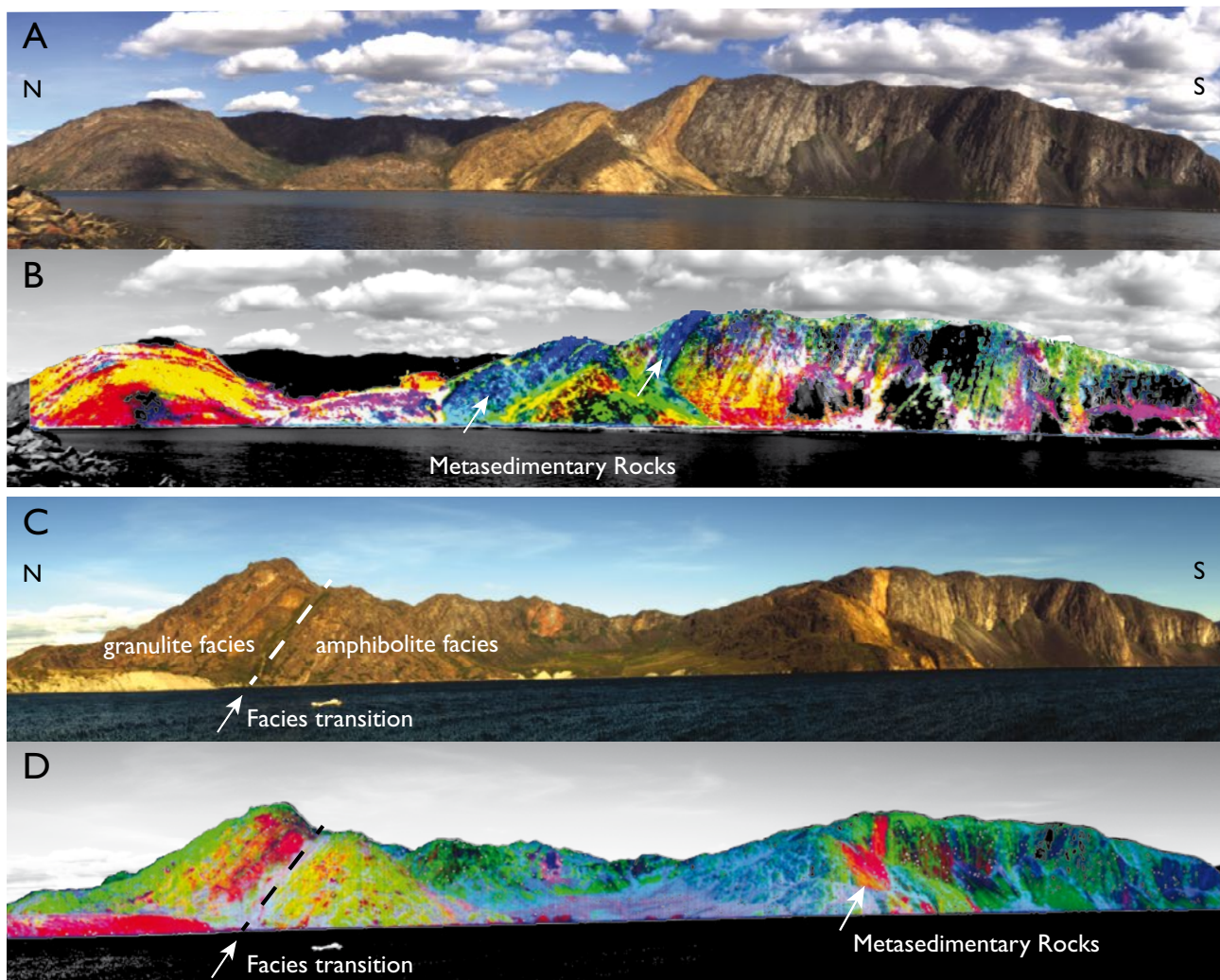


Fig. 2. A, C: True colour Fenix hyperspectral scenes from the Maligiaq area. See Fig. 1 for scene locations. B, D: Minimum Noise Fraction false colour image: Red: band 2. Green: band 7. Blue: band 8, overlain on grayscale hyperspectral images.

instrument are presented in Salehi (2018), this volume. In addition, representative samples of the main rock types were collected for subsequent laboratory analysis. A parallel study was integrated with geological and 3D photogrammetric mapping in Karrat region farther north in West Greenland (Rosa *et al.* 2017; Fig. 1).

Analysis of surface mineralogy using sub-horizontal hyperspectral data collection

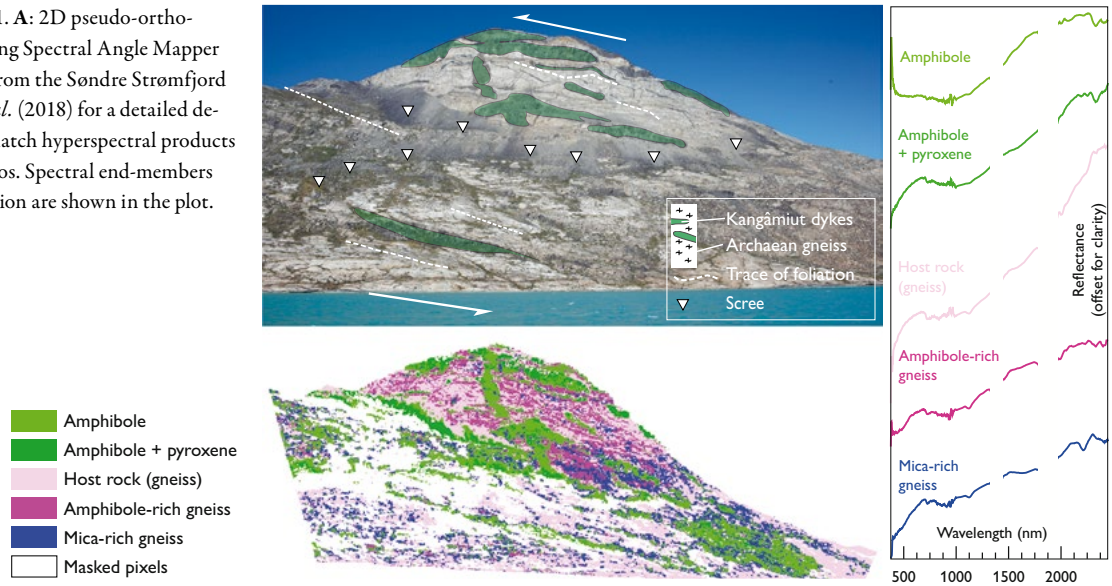
The extreme influence of atmospheric effects and topography-induced illumination differences in long-range ground-based spectra data cannot be corrected by means of correction tools commonly used for nadir satellite or airborne data. An adapted workflow is presented in Lorenz *et al.* (2018) to overcome the challenges of long-range outcrop sensing, including atmospheric and topographic corrections. Minimum Noise

Fraction transformation (Boardman 1993) and Spectral Angle Mapper classification (Kruse *et al.* 1993) were applied to test the applicability of the data for mapping the main rock-forming minerals. The former is important for dimensionality reduction and filtering of noise from hyperspectral data. This method can extract spatially coherent information and show the variations between bands in the hyperspectral data. The Spectral Angle Mapper classification permits rapid mapping of the similarity between image and reference spectra.

Long-range terrestrial hyperspectral scanning in the southern Nagssugtoqidian orogen

In the summer of 2016, new hyperspectral datasets from relatively distant targets were acquired in the allochthonous (Fig. 1, scans 1–6) and autochthonous (Fig. 1, scan 8) zones of the

Fig. 3. Scan 9 in Fig. 1. **A:** 2D pseudo-ortho-photo. **B:** The resulting Spectral Angle Mapper classification image from the Søndre Strømfjord region. See Salehi *et al.* (2018) for a detailed description of how to match hyperspectral products to pseudo-orthophotos. Spectral end-members used in the classification are shown in the plot.



Nagssugtoqidian orogen. Metasedimentary rocks in the allochthonous zone are tectonically interleaved with quartzofeldspathic gneisses between the southern shore of Qeqertalik fjord and the northern border of the Ikertoq shear zone (Figs 1, 2). Parts of this zone are well exposed along the eastern shore of Maligiaq and were scanned with the Fenix instrument from a distance of *c.* 2–3 km (see Fig. 1 and below). The metasedimentary rocks are predominantly biotite-garnet paragneisses but also comprise aluminous schists and graphitic-sulfidic varieties with up to a few percent graphite and iron sulfides, and they may include both Archaean and Palaeoproterozoic components (see legend to the regional map of Garde & Marker 2010). The scanned area also transects an amphibolite–granulite facies boundary, which follows one of the shear zone branches (Fig. 2). Such facies transitions may be difficult to precisely identify in the field, because the occurrence of the granulite facies index mineral hypersthene depends on bulk rock composition in addition to *P*, *T* and xH_2O conditions; hypersthene first occurs in mafic rocks and will be absent from leucocratic metasedimentary and magmatic rocks at similar metamorphic grade. Besides, granulite facies rocks can be retrogressed along younger shear zones.

The result generated from the Fenix spectral data (Fig. 2) highlights the metasedimentary screens. The graphite- and sulphide-bearing schists mapped using such data are shown with purple colour in Fig. 2B and pink in Fig. 2D. The general colour differences are caused by changes in illumination conditions between the acquisition of the two datasets. While graphitic and sulfidic lithologies are readily detected with the Minimum Noise Fraction method used here, the metamorphic transition from amphibolite facies to granulite facies (Korstgård 1979) is not distinguishable; this might be due to absence of diagnos-

tic, hypersthene-bearing lithologies. The boundary might be detected e.g. Matched Filtering (Harsanyi & Chang 1994) and Mixture-tuned Matched Filtering (Boardman 1998), where changes in mineral chemical composition and information on relative abundances of the lithologies are enhanced.

Integration of ship-based hyperspectral scanning and 3D photogrammetry

Mobile mapping of steep coastal cliffs using ship-based hyperspectral scanning was tested – for the first time – in the outer part of the Kangerlussuaq area (Figs 3, 4) and in the related study in the Karrat region mentioned in the introduction. The data processing related to such data acquisition has been fully discussed in Salehi *et al.* (2018).

Our analysis in the former area reveals Kangâmiut dykes intruding intensely deformed Archaean gneisses, besides other metabasic bodies (Fig. 3). The gneissic foliation is clearly identifiable, and several ductile and brittle structures can be observed in the dykes and other metabasic rocks, where amphiboles are the dominant minerals and mica and pyroxene are present with secondary abundances.

The spectral mapping products were integrated with 3D photogrammetric data to create accurate, large-scale outcrop models, which are well suited for quantitative purposes in geological analysis or in preparation for field operations (Fig. 4). For this, a dense and accurate dataset of topographic points (also referred to as a point cloud) can be generated from stereo images describing the terrain surface in three dimensions. The implemented algorithms work reliably even for complex geometries, and with high accuracy. Slightly distorted data, such as images over a low-relief landscape, can be

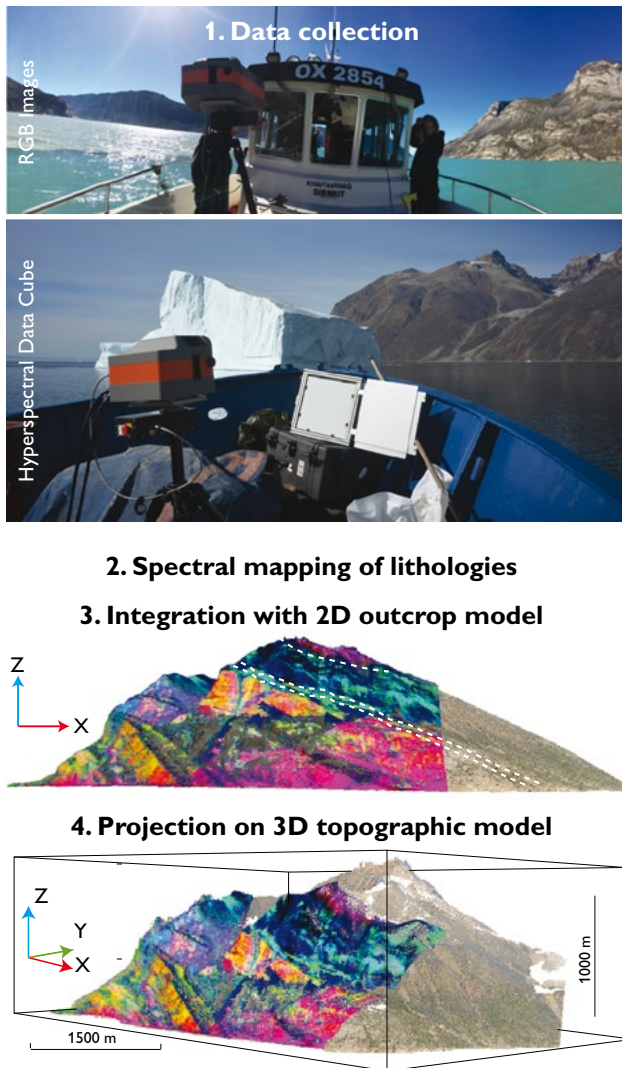


Fig. 4. General workflow for 3D-integration of hyperspectral data cubes and point clouds.

treated quickly using homographic or polynomial transformations, and even data with high local distortions caused by the underlying topography can be processed.

Concluding remarks

The workflow presented here for the acquisition of spectral data from moving platforms and long-range, ground-based hyperspectral scanning opens up a range of new possibilities in the application of hyperspectral imagery by significantly enlarging the scale of measurements. The proposed auto-

matic approach to combine spectral and point cloud data is a fast alternative to manual approaches and has high potential for field geologists who wish to establish accurate outcrop models in areas of difficult access that can be brought to life and visualised in 3D surface models.

Acknowledgments

Kai Sørensen is thanked for constructive discussions on geology. The Helmholtz Institute Freiberg is thanked for the use of the SPECIM AisaFenix hyperspectral scanner and the Rikola Hyperspectral Imager.

References

- Boardman, J. 1993: Automated spectral unmixing of AVIRIS data using convex geometry concepts: In: Summaries of the Fourth Annual JPL Airborne Geoscience Workshop October 25–29, 1993. Pasadena, CA: Summaries, JPL Publication 93-26. Vol. 2.
- Boardman, J.W. 1998: Leveraging the high dimensionality of AVIRIS data for improved sub-pixel target unmixing and rejection of false positives: mixture tuned matched filtering. In: Summaries of the Seventh Annual JPL Airborne Geoscience Workshop, **97**(1), 55–56.
- Garde, A.A. & Marker, M. 2010: Geological Map of Greenland, 1:500 000, Sondre Strømfjord–Nuussuaq, Sheet 1. Second edition. Copenhagen: Geological Survey of Denmark and Greenland.
- Harsanyi, J.C. & Chang, C.I. 1994: Hyperspectral image classification and dimensionality reduction: an orthogonal subspace projection approach. *IEEE Transactions on geoscience and remote sensing* **32**, 779–785.
- Korstgård, J.A. 1979: Nagsugtoqidian Geology. Rapport Grønlands geologiske undersøgelser **89**, 63–75.
- Kruse, F.A., Lefkoff, A., Boardman, J., Heidebrecht, K., Shapiro, A., Barloon, P. & Goetz, A. 1993: The spectral image processing system (SIPS) – interactive visualization and analysis of imaging spectrometer data. *Remote Sensing of Environment* **44**, 145–163.
- Lorenz, S., Salehi, S., Kirsch, M., Zimmermann, R., Unger, G., Sørensen, E.V. & Gloaguen, R. 2018: Radiometric correction and 3D integration of long-range ground-based hyperspectral imagery for mineral exploration of vertical outcrops. *Remote Sensing* **10**, 23 pp., <http://dx.doi.org/10.3390/rs10020176>
- Rosa, D. *et al.* 2017: Architecture and mineral potential of the Palaeoproterozoic Karrat Group, West Greenland. Results of the 2016 Season. Danmarks og Grønlands Geologiske Undersøgelse Rapport **2017/114**.
- Salehi, S. 2018: Hyperspectral analysis of lithologies in the Arctic in the presence of abundant lichens. *Geological Survey of Denmark and Greenland Bulletin* **41**, 51–55 (this volume).
- Salehi, S., Lorenz, S., Sørensen, E.V., Zimmermann, R., Fensholt, R., Heincke, B.H., Kirsch, M. & Gloaguen, R. 2018: Integration of vessel-based hyperspectral scanning and 3D-photogrammetry for mobile mapping of steep coastal cliffs in the Arctic. *Remote Sensing* **10**, 26 pp., <http://dx.doi.org/10.3390/rs10020175>
- Tukiainen, T. & Thorning, L. 2005: Detection of kimberlitic rocks in West Greenland using airborne hyperspectral data: the HyperGreen 2002 project. *Geological Survey of Denmark and Greenland Bulletin* **7**, 69–72.

Authors' address

S.S. & S.M.T., *Geological Survey of Denmark and Greenland, Øster Voldgade 10, DK-1350 Copenhagen K, Denmark.* E-mail: ssal@geus.dk.

Hyperspectral analysis of lithologies in the Arctic in areas with abundant lichen cover

Sara Salehi

Lithological mapping using remote sensing depends, in part, on the identification of rock types by their spectral characteristics. Chemical and physical properties of minerals and rocks determine their diagnostic spectral features throughout the electromagnetic spectrum. Shifts in the position and changes in the shape and depth of these features can be explained by variations in chemical composition of minerals. Detection of such variations is vital for discriminating minerals with similar chemical composition. Compared with multispectral image data, airborne or spaceborne hyperspectral imagery offers higher spectral resolution, which makes it possible to estimate the mineral composition of the rocks under study without direct contact.

Arctic environments provide challenging ground for geological mapping and mineral exploration. Inaccessibility commonly complicates ground surveys, and the presence of ice, vegetation and rock-encrusting lichens hinders remote sensing surveys. This study addresses the following objectives:

1. Modelling the impact of lichen on the spectra of the rock substrate;
2. Identification of a robust lichen index for the deconvolution of lichen and rock mixtures and
3. Multiscale hyperspectral analysis of lithologies in areas with abundant lichens.

Modelling the impact of lichen cover

Spectral mixing of lichens and bare rock can shift the wavelength positions of characteristic absorption features and complicate the spectral mapping of minerals and lithologies. Salehi *et al.* (2017) investigated how surficial lichen cover affects the characteristics of shortwave infrared mineral absorption features and the efficiency of automated extraction of absorption features. For this purpose, mixed spectra were synthetically generated from laboratory spectra of common rock-forming minerals and lichens. Wavelength displacements of characteristic absorption features for each mixed spectrum were then analysed as a function of lichen cover percentage (see an example in Fig. 1). By quantifying lichen

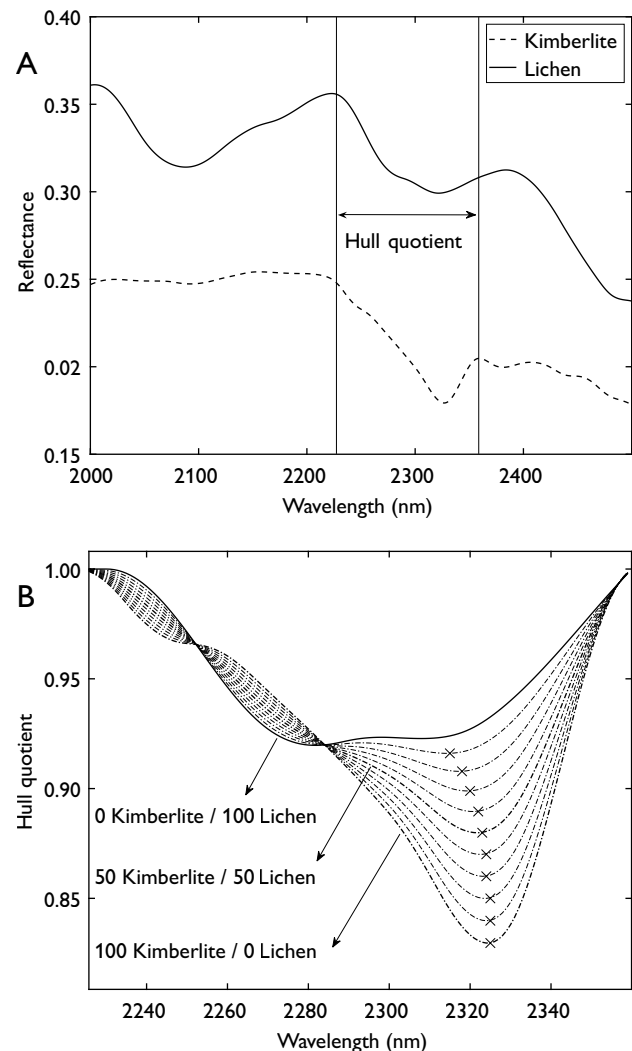


Fig. 1. **A:** Averaged spectra of pure rock and lichen for a kimberlite substrate in shortwave infrared range. **B:** The corresponding hull quotient (Clark & Roush 1984) and band centres of mixed spectra associated with the antigorite absorption feature. The 10% spectral intervals used to investigate the main absorption features are highlighted. x: wavelength positions of local minima (Salehi *et al.* 2017).

cover effects on mineral absorption features, this study highlights the importance cautious interpretation in areas characterised by abundant, lichen-covered outcrops. This can be of significant importance for mineral and deposit identification, because slightly shifted features for a given spectrum caused by lichen cover can be erroneously identified as a path to a deposit. Salehi *et al.* (2017) showed that spectral shifts caused by lichens are not constant, i.e. each mineral spectral feature may be affected differently depending on the shape of the lichen spectrum. For example, the absorption feature related to the chlorite mineral group around 2254 nm is shifted towards longer wavelength, while the one around 2320 nm is shifted towards shorter wavelength and the 2380 nm band maintains its spectral characteristics. Spectral shifts are not only related to rock/lichen proportions but also to the modal abundance of minerals in certain rock types. Background minerals and associated overlapping features will have an effect on the related absorption depth and play a critical role in the scale of wavelength displacement.

Identification of a robust lichen index

The ability to distinguish a lichen cover from its rock/mineral substrate is important, and decomposition of a mixed pixel into a collection of pure reflectance spectra can improve the use of hyperspectral methods for mineral exploration. In order to identify spectral indices that can directly reflect the ratio of the rock and lichen in hyperspectral data, a number of index structures were assigned to an optimisation algorithm, which was tasked to find the best values for the location of the bands along the reflectance spectra measured in the laboratory (Salehi *et al.* 2016). In order to further investigate the functionality of the indices for the airborne platform, the spectra were resampled to HyMAP resolution.

The indices proposed by Salehi *et al.* (2016) proved robust to the type of the substrate rock and permitted an estimate of the lichen cover with acceptable, albeit varying, levels of error. The results revealed that the ratio between $R_{894-1246}$ and R_{1110} explains most of the variability in the hyperspectral data at the original laboratory resolution ($R^2=0.769$). However, the normalised index incorporating $R_{1106-1121}$ and $R_{904-1251}$ yields the best results for the HyMAP resolution ($R^2=0.765$).

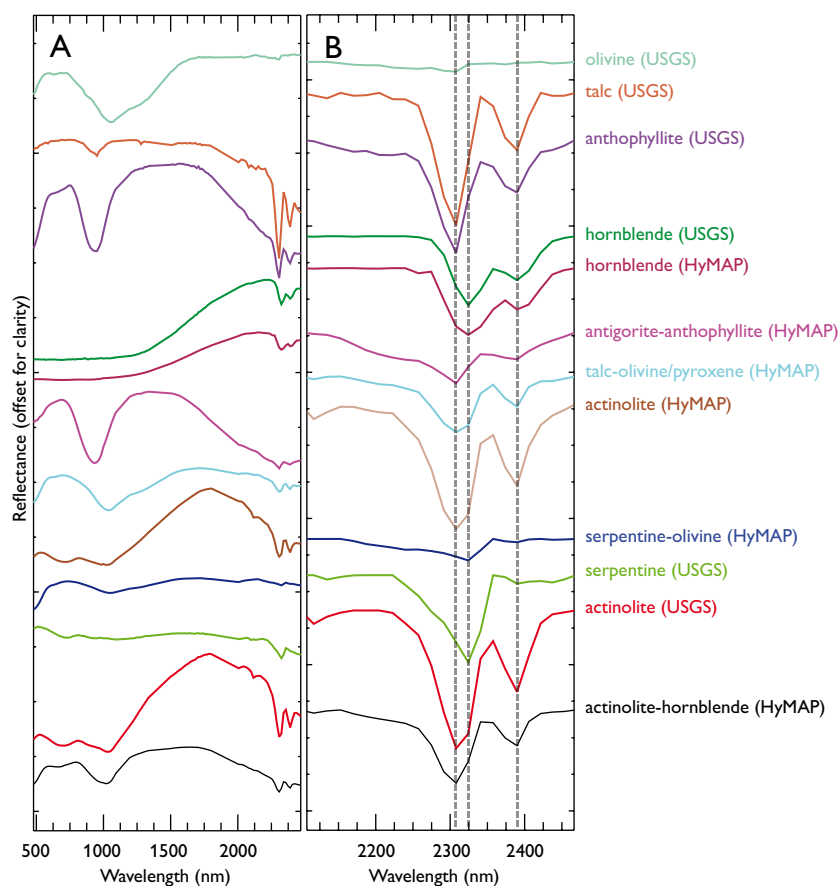
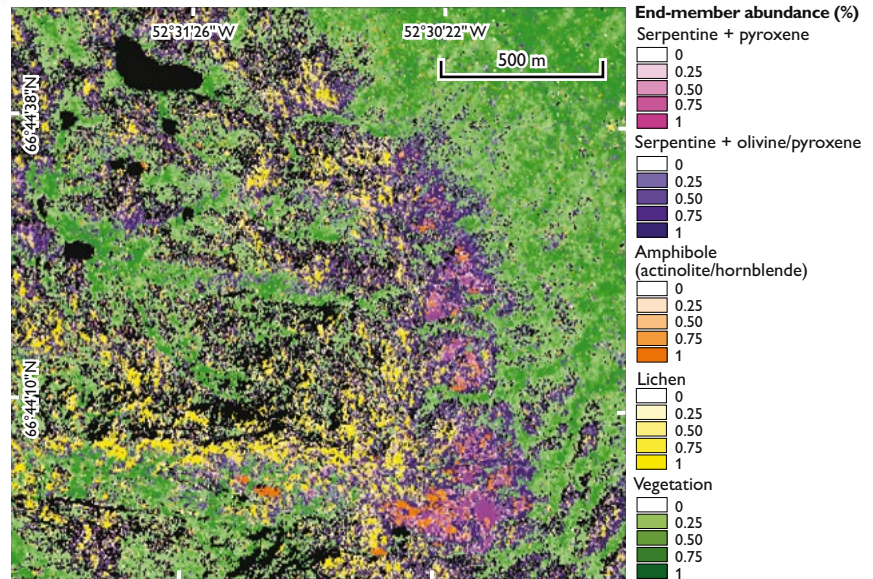


Fig. 2. Spectra of extracted end members compared with selected minerals from the USGS spectral library in ENVI software. **A:** full spectral range. **B:** shortwave infrared range.

Fig. 3. The result of unmixing analysis and the abundance of mafic-ultramafic minerals using HyMAP data. Masked pixels are indicated by black colour.



The proposed methodology has the advantage of not requiring *a priori* knowledge about the exact effects of lichens – or any other substance – on the reflectance of the mixtures. Instead, this information is obtained by an automated trial and error process. Therefore, this technique can also be beneficial for identification of sensitive bands and indices for deconvolution of any other mixed spectra, whether synthetic as in this case, or obtained directly from the samples.

Multiscale hyperspectral analysis of lithologies with abundant lichen cover

Two sets of hyperspectral data acquired by airborne HyMAP (350–2500 nm) and light-weight Rikola (500–900 nm) sensors were chosen to investigate the potential of visible near infrared and shortwave infrared spectral range for detailed lithological mapping in the Nagssugtoqidian orogen of West Greenland, where an ultramafic rock unit with abundant lichen cover is exposed. The extent to which geological information derived from airborne data is retained in the Rikola

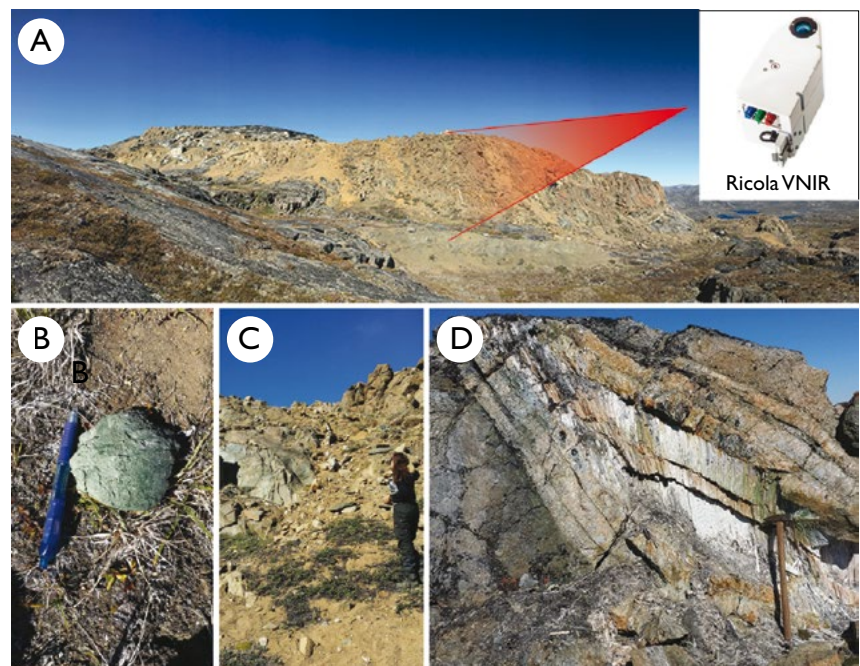


Fig. 4. A: Supracrustal rocks in the Innarsuaq region comprising a kilometre-sized body of mafic-ultramafic, looking north. B: bright green and black amphibole and biotite at the corner (alteration zone). C: Host ultramafic rock; green amphibole to the left and white talc vein in the middle. D: 50 cm long asbestos fibres.

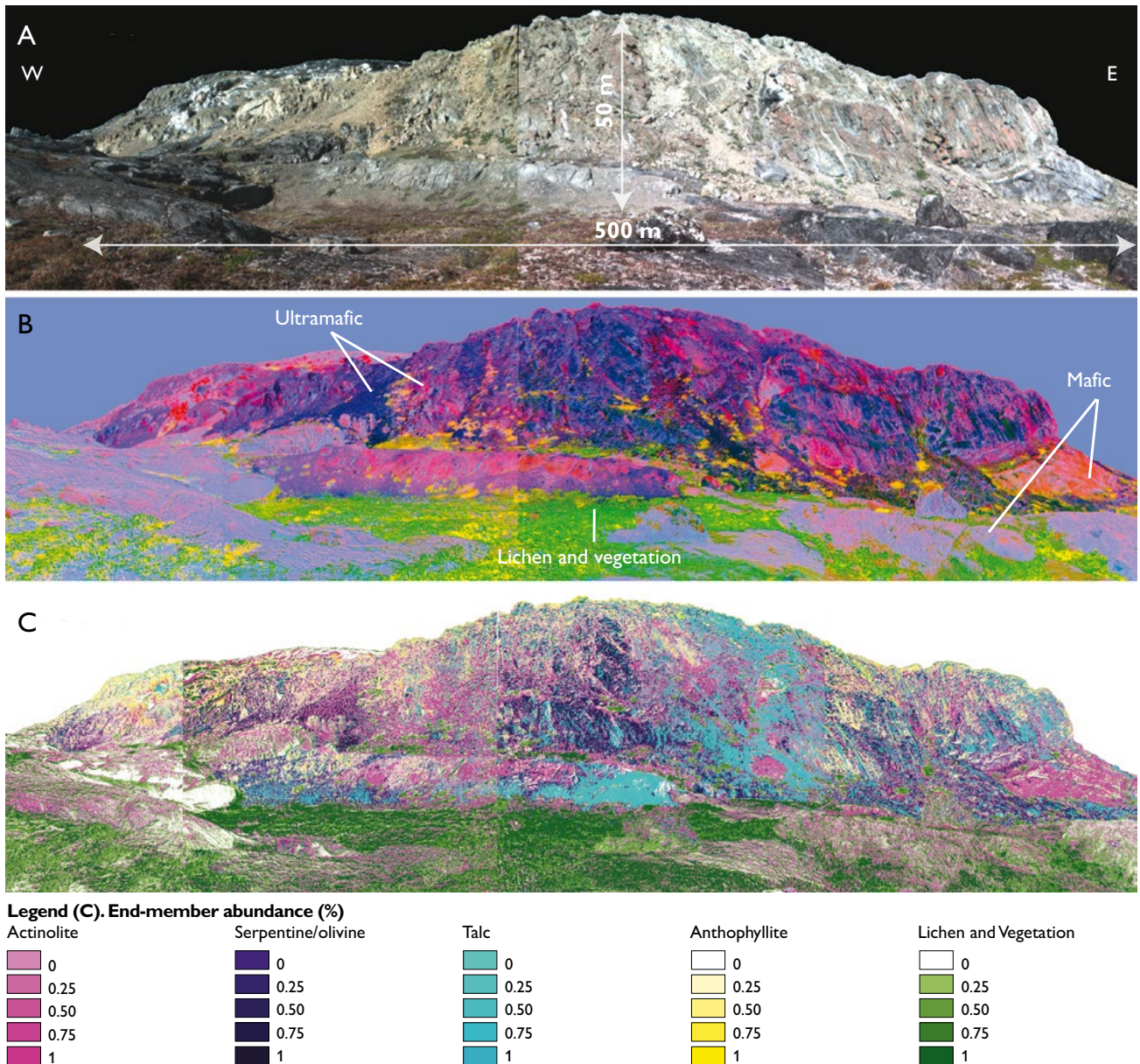


Fig. 5. **A:** True-colour hyperspectral image mosaic generated using the Rikola camera. **B:** Minimum Noise Fraction false-colour image: **Red:** Band 6. **Green:** Band 2. **Blue:** Band 1. **C:** result of spectral unmixing analysis and the abundance of mafic-ultramafic minerals.

hyperspectral data, is examined as an insight to future drone-based hyperspectral mapping capabilities and the possibility of extracting valuable mineralogical and lithological information using such platforms.

The airborne hyperspectral dataset is corrected for abnormal pixels and removal of bad bands (such as water vapour absorption features and noisy bands) prior to atmospheric correction. Dark pixels, snow, clouds and water were filtered out. Next, the spatial-spectral end-member extraction method (Rogge *et al.* 2007) is used to derive an image end-member set. This makes an assessment of subtle litho-

logical variability across a given study area possible. These end members are then sorted based on expert knowledge of known spectral features (water, snow, vegetation, lichen and geological materials) followed by a more detailed sorting into individual classes within each category. Subtle shortwave infrared features related to key minerals in the geological materials are particularly important. The resulting sorted end-member classes are subsequently averaged to produce a final end-member set. A final set of six geological end members (Fig. 2), and two end members related to vegetation and lichens are deducted from expert-based analysis. Figure 2

shows a plot of the extracted end members using the spatial–spectral end-member extraction method and the corresponding signatures from the United States Geological Survey (USGS) spectral library (Kokaly *et al.* 2017). The shortwave infrared spectral characteristics of the ultramafic rocks studied here were controlled by amphibole minerals as exemplified by hornblende, actinolite and anthophyllite (Fig. 3). The absorption features in the shortwave infrared region are located at 2320 and 2380 nm and are of the same order of magnitude. The shortwave infrared spectrum of olivine-rich rocks clearly reflects a mixture of antigorite serpentine with a characteristic stronger absorption feature at 2320 nm. A less distinct absorption feature at 2310 nm is present for rocks enriched in talc. Fractional abundances of the end members within the scene are determined using an iterative implementation of spectral mixture analysis method (Rogge *et al.* 2007).

The interpretation of HyMap data revealed a number of mafic and ultramafic complexes in the border area between the parautochthonous and allochthonous zones of the Nagssugtoqidian orogen. One such complex occurs to the east of the head of the fjord Kangerluarsuk, here referred to as Innarsuaq (see fig. 1 of Salehi & Thaarup 2018, this volume). As can be seen from Fig. 3, the predictive map from the Innarsuaq area displays a complex distribution of exposed bedrock, a feature confirmed during a brief field visit. The results were validated using expert knowledge of spectral characteristics of lichens and mineralogy, as well as spectral measurements of field samples and associated XRD results.

The Rikola camera was operated in ground-based mode and panned stepwise to acquire a set of five overlapping images. The images were corrected for geometric, radiometric and topographic effects and stitched to a continuous mosaic (Figs 4, 5). The distribution of lithological units were then mapped using the Minimum Noise Fraction method (Kruse *et al.* 1993). The information regarding mineral abundances were retrieved using the Spectra Unmixing procedure (Fig. 5).

Conclusions

1. Lichen effects on the spectra of their rock substrate have important implications for the geological analysis of airborne/spaceborne hyperspectral data where rock-encrusting lichens partially obscure exposed bedrock.
2. Analysis of airborne hyperspectral data can result in high-quality regional mapping products capable of discriminat-

ing geological materials of interest based on subtle spectral differences. The map product generated from the Rikola scenes in this study captures the broad geological patterns and many of the lithologies generated from the airborne data, although some spectral and lithological discrimination is lost due to its more limited wavelength range.

3. The performance of hyperspectral data acquired from different platforms and at various scales is investigated for qualitative mapping of arctic mineral resources in the presence of abundant lichens. The application of such technologies to extract detailed geological information from complex inaccessible regions of Greenland certainly has a very low cost/benefit ratio in comparison to traditional geological fieldwork. Future space-borne hyperspectral sensors will offer new possibilities to expand the scale of mapping in Greenland. Integration with other remote sensing datasets such as magnetic data will simplify mineral exploration and geological mapping in the Arctic.

Acknowledgments

The Helmholtz Institute Freiberg is thanked for the use of Rikola Hyperspectral Imager.

References

- Clark, R.N. & Roush, T.L. 1984: Reflectance spectroscopy: Quantitative analysis techniques for remote sensing applications. *Journal of Geophysical Research: Solid Earth* **89**(B7), 6329–6340.
- Kokaly, R.F., Clark, R.N., Swayze, G.A., Livo, K.E., Hoefen, T.M., Pearson, N.C., Wise, R.A., Benzel, W.M., Lowers, H.A., Driscoll, R.L. & Klein, A.J. 2017: USGS Spectral Library Version 7. U.S. Geological Survey Data Series **1035**, 61 pp., <http://dx.doi.org/10.3133/ds1035>
- Kruse, F.A., Lefkoff, A., Boardman, J., Heidebrecht, K., Shapiro, A., Barloon, P. & Goetz, A. 1993: The spectral image processing system (SIPS) – interactive visualization and analysis of imaging spectrometer data. *Remote Sensing of Environment* **44**, 145–163
- Rogge, D.M., Rivard, B., Zhang, J., Sanchez, A., Harris, J., & Feng, J. 2007: Integration of spatial–spectral information for the improved extraction of endmembers. *Remote Sensing of Environment* **110**, 287–303.
- Salehi, S. & Thaarup, S. 2018: Mineral mapping by hyperspectral remote sensing in West Greenland using airborne, ship-based and terrestrial platforms. *Geological Survey of Denmark and Greenland Bulletin* **41**, 47–50 (this volume).
- Salehi, S., Karami, M. & Fensholt, R. 2016: Identification of a robust lichen index for the deconvolution of lichen and rock mixtures using pattern search algorithm (case study: Greenland). *International Archives of the Photogrammetry, Remote Sensing & Spatial Information Sciences* **XLI-B7**, 973–979.
- Salehi, S., Rogge, D., Rivard, B., Heincke, B.H. & Fensholt, R. 2017: Modeling and assessment of wavelength displacements of characteristic absorption features of common rock forming minerals encrusted by lichens. *Remote Sensing of Environment* **199**, 78–92.

Author's address

S.S., *Geological Survey of Denmark and Greenland, Øster Voldgade 10, DK-1350 Copenhagen K, Denmark.* E-mail: ssal@geus.dk.

New subsurface mapping offshore southern West Greenland using geophysical and geological data

Ulrik Gregersen, Morten S. Andersen, Henrik Nøhr-Hansen, Emma Sheldon, Thomas F. Kokfelt, Mette Olivarius, Christian Knudsen, Kristian G. Jakobsen and Jan S. Adolphsen

The West Greenland continental margin has been the subject of petroleum exploration by companies and research projects since the 1970s and many data have been acquired since. Licensing rounds issued by the Greenland authorities in 2002 and 2004 offshore southern West Greenland resulted in company licenses which led to data acquisition and three exploration wells. The extensive new data form a basis for updated mapping by means of data, new analyses of the subsurface geology and improved understanding of the stratigraphy and the geological development. The Geological Survey of Denmark and Greenland (GEUS) has recently completed a comprehensive mapping project of the subsurface in an area covering 116 000 km² offshore southern West Greenland (Fig. 1). The results include maps displaying large structural highs and faults, Cretaceous sedimentary basins and volcanic areas, illustrated by cross-sections through the area. A new seismic stratigraphy with eight mega-units from the seabed to the basement was also defined. In addition, studies from wells of biostratigraphy and petrology were carried out that provide important new information. The new data include extensive 2D seismic data and eight wells including the three exploration wells AT2-1, AT7-1 and LF7-1 drilled in 2011 by Cairn Energy (Fig. 1). Key results of the work are summarised below.

Geological setting and scope of project

The southern West Greenland continental margin is located between West Greenland to the east and the oceanic crust and parts of the Davis Strait High to the west (Fig. 2). A number of rifted basins with large structural highs are interpreted to have developed offshore southern West Greenland during the Cretaceous (Chalmers *et al.* 1993; Sørensen 2006; Gregersen 2014). Cretaceous and Cenozoic sedimentary successions were previously defined from wells and outcrops on the central and southern West Greenland continental margin (Rolle 1985; Dam *et al.* 2009; Nøhr-Hansen *et al.* 2016). During the Paleocene and Eocene, oceanic crust developed between Canada and Greenland, and the Cretaceous rifted continental margin of West Greenland was separated from eastern Canada (Oakey & Chalmers 2012). The large-scale

movements between Greenland and Canada generated new structures during the Palaeogene and reactivated faults within Cretaceous basins.

The purpose of the research-based project described here was to update previous subsurface mapping with the most recent data to provide an improved knowledge of the structures and the geological development, which can lead to an evaluation of the resource potential. The project was carried out in 2015–2017 for the Ministry of Mineral Resources in Nuuk and incorporated a number of sub-tasks including: (1) seismic interpretation and mapping; (2) well correlation; (3) biostratigraphy; (4) analyses of potential reservoir rocks in wells from 2011 and (5) analyses of igneous rocks, basement and provenance. This paper describes some of the key results from the seismic interpretation, mapping and well data-re-

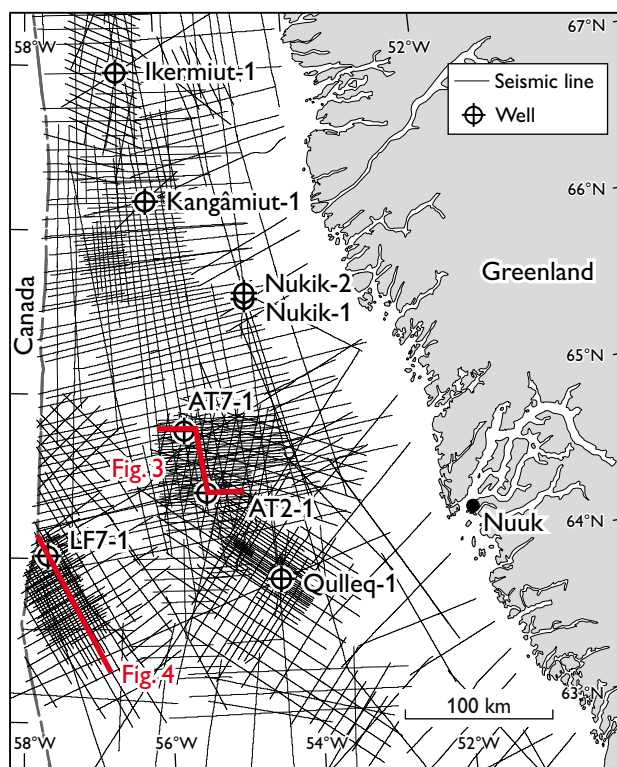


Fig. 1. Map of the study area offshore southern West Greenland with positions of 2D seismic lines and exploration wells. The positions of Figs 3 and 4 are also shown.

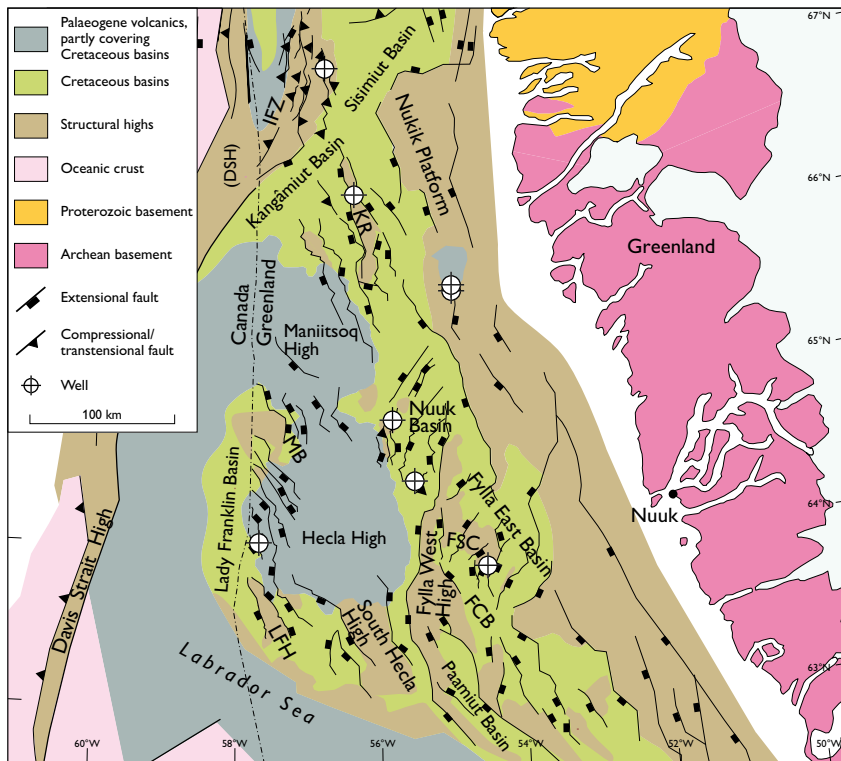


Fig. 2. Structural elements map of the southern West Greenland continental margin. The map shows areas with structural highs, faults, Cretaceous basins and Palaeogene volcanic cover. The majority of the large structures and faults trends towards the NW with a few towards the NE. In addition, the positions of the wells and the boundary to Canada are shown. **FSC**: Fylla Structural Complex with its composite structures, incl. **FCB**: Fylla Central Basin. **LFH**: Lady Franklin High. **MB**: Maniitsoq Basin. **KR**: Kangamiut Ridge. **IFZ**: Ikermiut Fault Zone. Structural element names are mainly from Chalmers *et al.* (1993), Sørensen (2006) and Døssing (2011). The geological map of West Greenland onshore is from Henriksen *et al.* (2009). The position of the oceanic crust and the Davis Strait High in the Canadian sector are from Oakey & Chalmers (2012). The names of the wells are shown in Fig. 1.

lated tasks. The lateral extent of the main tectonic elements, including structural highs, faults and basins, is outlined in a structural elements map (Fig. 2).

Methods

Interpretation of seismic stratigraphic horizons and units was carried out using Schlumberger Petrel © software and included data from wells and seismic surveys (Fig. 1). In addition, other data including gravity and magnetic surveys and seabed sampling were used for the interpretation and mapping. Most structural highs and basins are defined and outlined by seismic interpretation in combination with gravity- and magnetic anomaly maps, and are supported by other data such as published refraction models. A number of methods were used at GEUS for the other studies, including scanning electron microscopy, porosity & permeability measurements, and rock/mineral analyses and radiometric dating using a laser ablation inductively coupled plasma mass spectrometer. Biostratigraphic dating based on palynology and micropalaeontology was carried out on a total of more than 200 samples from the AT2-1, AT7-1 and LF7-1 wells.

Seismic stratigraphy and structures

A robust stratigraphic framework was established with eight seismic stratigraphic mega-units (A–H) divided by horizons

from the seabed (A1) to the top of Pre-Cretaceous sedimentary rocks or the acoustic basement (H1) shown in Fig. 3. The mega-units include internal tops of sub-units (E2, Ev, F2, Fv and Hx) described below, and new biostratigraphy was used to constrain ages of the units. The units and most horizons are shown in seismic cross-sections across deep rifted basins separated by large structural highs (Figs 3, 4). Most of the structural highs, faults and basins trend SE–NW but a few strike in a more northerly direction or towards NE (Fig. 2). The total succession between the seabed and the basement has been mapped and shows thick basins between the main structures (Fig. 5), and also more local structures where the wells were drilled. Some basins and parts of basins are untested by wells.

Mega-unit H; Pre-Cretaceous basement

Mega-unit H includes the lower parts of basins and the basement of pre-Cretaceous ages (Fig. 3). It mostly includes the acoustic basement in large structures below the Cretaceous and Cenozoic basins, and was drilled in the AT7-1 and LF7-1 wells (Figs 3, 4). GEUS' analyses of igneous rock samples from lower parts of the AT7-1 well mainly reveal granites, granodiorites and tonalities. U–Pb dating of zircons from some of the samples gives ages of *c.* 2730–3190 Ma. The samples are from the lower part of mega-unit G and the uppermost part of mega-unit H in the drilled structure (Fig. 3) in a succession

with interbedded sedimentary layers. Similar igneous rocks, some of which have been weathered, were also reported from the succession by Cairn Energy (2011). The rocks are mostly similar in age and composition to parts of the basement terrane in southern West Greenland. Metamorphic rocks reported by Cairn Energy (2011) from the lowermost part of the LF7-1 well occur just below the H1 horizon. However, pre-Cretaceous sedimentary rocks are also expected to be locally preserved in basins such as in the Sisimiut Basin (Fig. 2), where a sub-unit is present in the upper part of mega-unit H. Ordovician marine carbonates were sampled from the seabed over the Davis Strait High, where some possibly are *in situ* (Stouge *et al.* 2007). Such rocks may also occur in the adjacent basins. In addition, an organic-rich Ordovician sample from the Davis Strait was considered to have source rock potential (Bojesen-Koefoed 2011). Cretaceous and Paleocene oil seeps have been described from the Nuussuaq Basin farther north with a possible wider occurrence in West Greenland (Bojesen-Koefoed 2011).

Mega-unit G; Early to mid-Cretaceous

Large rift structures, local wedge-shaped units within mega-unit G and extensional faults developed during the Early to mid-Cretaceous (Figs 3, 4). Bowl or V-shaped, strong reflections near the G1 horizon (Fig. 3) are interpreted as sills of a larger sill complex in the Nuuk Basin and Lady Franklin Basin. Mega-unit G is most likely late Albian to Cenomanian in age. A seismic correlation (Fig. 3) with the AT7-1 well shows that the G1 surface divides a Cenomanian–Turonian sedimentary succession. The overlying lower part of mega-unit F is dominated by sandstones with conglomerates and thin claystones. The underlying mega-unit G includes a thick succession dominated by conglomerates and a lowermost late Albian – early Cenomanian succession including rocks from an igneous basement, interbedded thin sandstones, conglomerates and claystones. Lithologies in the AT2-1, AT7-1 and LF7-1 wells were determined by Cairn Energy (2011) and in this study.

Mega-unit F; Late Cretaceous – Paleocene

The present study shows that the lower succession of mega-unit F is mainly of Cenomanian–Turonian age. Variable reservoir properties were found from the study of well samples. In the lower part of mega-unit F of the AT7-1 well, the analysed conglomerate samples show intermediate to good reservoir quality, e.g. a sidewall core sample with 24.77% porosity and 78.73 mD permeability. The sandstones and overlying diatomite have high porosities, and medium to low and low

permeability, respectively. The other Cretaceous rocks, analysed in the other two wells (AT2-1 and LF7-1), mostly show poorer reservoir quality. However, sandstones with reservoir potential are expected to be present in some of the structures. A 323 m thick succession dominated by sandstones of late Santonian age with reservoir potential is described from the lower part of the Qulleq-1 well in the Fylla Structural Complex (Christiansen *et al.* 2001; Fig. 2) and its top is also mapped in this study.

During parts of the Late Cretaceous, relative tectonic quiescence prevailed in most areas and thick claystone-dominated units were deposited in the basins. This study shows that parts of mega-unit F (Figs 3, 4) are dominated by thick Upper Cretaceous to Paleocene successions, which consist mostly of claystones. Such successions are drilled in the LF7-1, AT2-1, Qulleq-1 and Ikermiut-1 wells, which include the Ikermiut Fm (Rolle 1985). However, tectonic movements and erosion probably related to rifting and/or uplift may have occurred in the study area during Late Cretaceous to Paleocene, in some places indicated by truncation and faulting of structures (see also Chalmers *et al.* 1993). Erosion or non-deposition may also be indicated by missing sections in wells. Hiati of different timespans seem to occur during the Late Cretaceous to Early Paleocene (mostly from within the late Campanian to Danian) in the AT2-1 and AT7-1 wells (in AT7-1 even to the Coniacian), and were also previously noted in the Qulleq-1 and Ikermiut-1 wells (Nøhr-Hansen *et al.* 2016).

Volcanism

The lower parts of the AT2-1 well succession contain volcanic rocks and thin claystones, which are biostratigraphically dated in the present study as late Cenomanian to early Turonian. The horizon Fv correlates with the top of the volcanic succession which may partly cross or overlie mega-unit G (Fig. 3).

During the Paleocene–Eocene, flood basalts and other volcanic rocks were deposited in large parts of the West Greenland continental margin (Skaarup 2001; Sørensen 2006; Larsen *et al.* 2016). The tops of extensive volcanic areas and highs are mapped offshore southern West Greenland (Fig. 2) primarily from seismic reflection data at horizon Ev (Fig. 4) and from magnetic anomaly data. These volcanic areas include the Hecla High, the Maniitsoq High, the Davis Strait High and parts of the Nukik High (Fig. 2). The Nukik-2 well on the Nukik High includes a lower succession with hyaloclastite beds and thicker intrusives (dolerites), where the upper part has been biostratigraphically dated as Late Paleocene (Hald & Larsen 1987). An almost 700 m thick succession with Paleocene subaerial basaltic lava flows was drilled in the lower

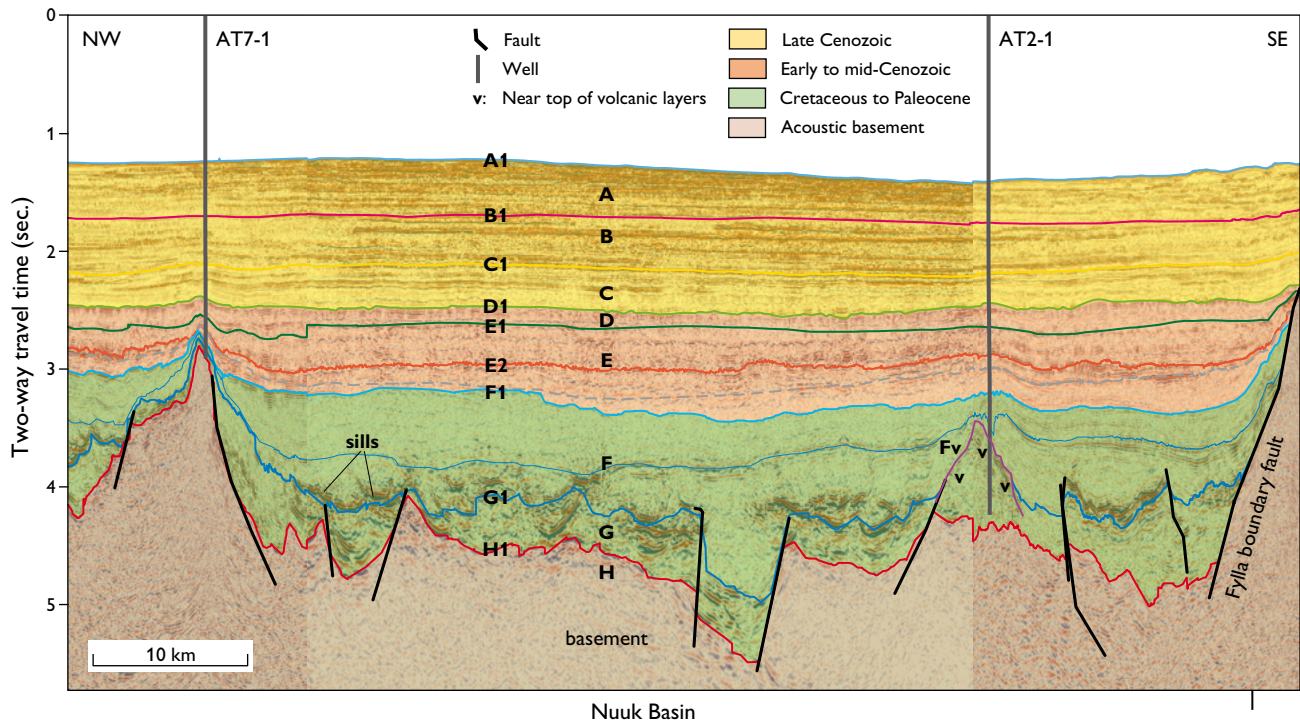


Fig. 3. Composite NW–SE seismic section across the Nuuk Basin with large structures and the AT2-1 and AT7-1 wells. The succession from the seabed to the basement is divided by seismic stratigraphic horizons A1–H1 into seismic mega-units A–H and tentative ages (maximum timespans) of major successions are shown in colour. The deeper parts of the section are dominated by a Cretaceous sedimentary succession with rifted basins, and with a local volcanic succession and sills. The seismic lines shown (TGS-GREEN2003-29, TGS-GR2000-215 and ENC2005-1) are courtesy of TGS-NOPEC Geophysical Company ASA. The location of the section is shown in Fig. 1.

part of the Hellefisk-1 well (Hald & Larsen 1987) north of the study area. Paleocene basalts were sampled from the seabed over the Davis Strait High and south of the Hecla High, where additional Early Eocene basalts were recovered (Larsen & Dalhoff 2006). A refraction seismic study by Funck *et al.* (2007) also shows basalts in the western parts of the study area and farther west with a tie to the Canadian Gjoa G-37 well. This well includes basalts with thinner mudstones in a >1 km thick Danian to Thanetian interval (Nøhr-Hansen *et al.* 2016). The Palaeogene volcanic rocks mostly cover parts of structures and Cretaceous sedimentary basins in the study area (Figs 2, 4), in parts of the Davis Strait – southern Baffin Bay areas (Gregersen & Bidstrup 2008) and in the Nuussuaq Basin (Dam *et al.* 2009; Larsen *et al.* 2016). The top of the volcanic successions (Ev) is overlain by the seismic horizon E2 of Late Paleocene age (late Thanetian from Nøhr-Hansen *et al.* 2016) towards the south (Fig. 4).

Geological development of younger units

The West Greenland continental margin moved towards NE and N in connection with the Palaeogene sea-floor spreading between Canada and Greenland (Oakey & Chalmers 2012).

These movements caused compression–transension tectonism with thrust faults and associated basins along the Davis Strait High and the Ikermit Fault Zone during the Late Paleocene to Eocene (Fig. 2; Gregersen & Bidstrup 2008). Seismic geometries in mega-units E and D with irregular sub-units near faults and basin mounds suggest mass-flows including slumps and basin fans (Fig. 3). They were formed during mainly the Eocene and Miocene and may include potential leads for hydrocarbon. Parts of the mass-flows may be related to movements during the formation of Palaeogene oceanic crust. Parts of upper Eocene, Oligocene and lower Miocene successions are mostly absent in wells from the area (Nøhr-Hansen *et al.* 2016). The upper parts of mega-unit D and mega-unit C are Miocene in age, mega-unit B is possibly Late Miocene to Pliocene and mega-unit A is probably Late Pliocene to Pleistocene in age (Fig. 3). The ages of the mega-units are indicated from biostratigraphy (Piasecki 2003; Nøhr-Hansen *et al.* 2016). In Miocene to Pleistocene successions, fewer large faults and other indications of tectonism are found. Large contourite drifts, slides and other forms of mass-mobilisation developed during the Miocene to Pleistocene (Nielsen *et al.* 2011) within mega-units A–C (Fig. 4). In addition, S- and SW-directed shelf progradation occurred,

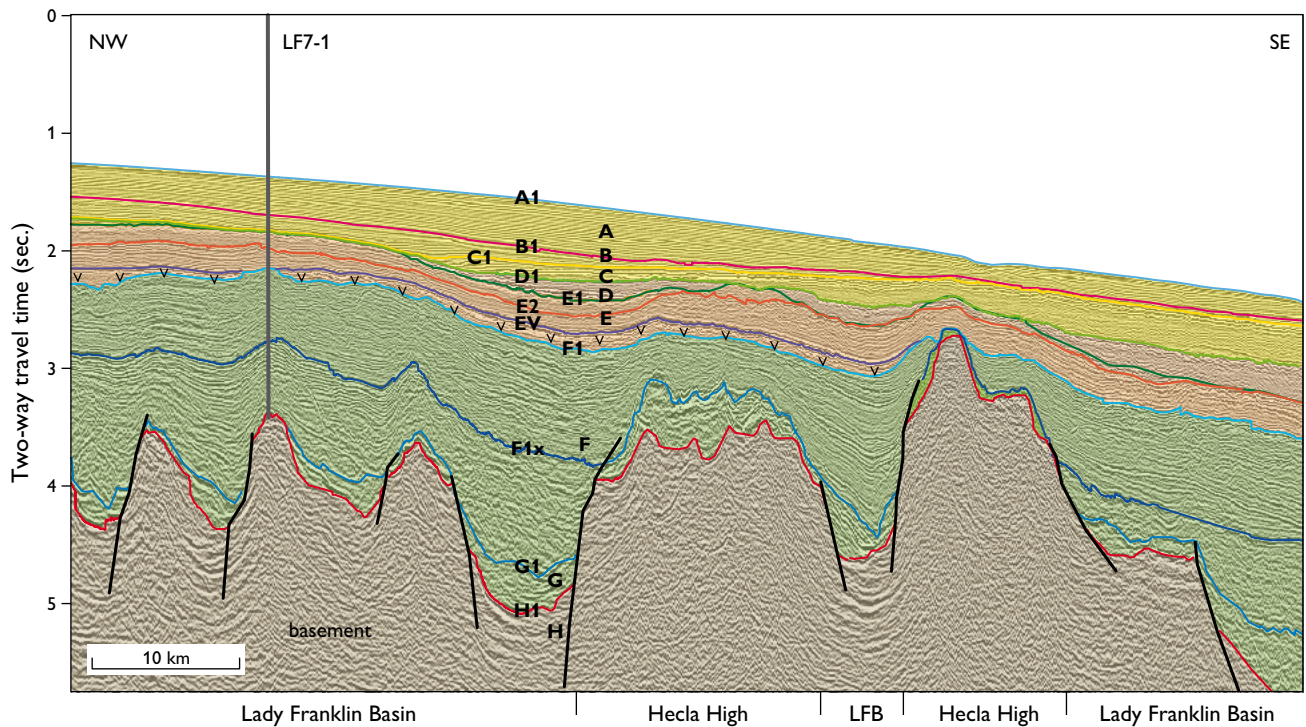
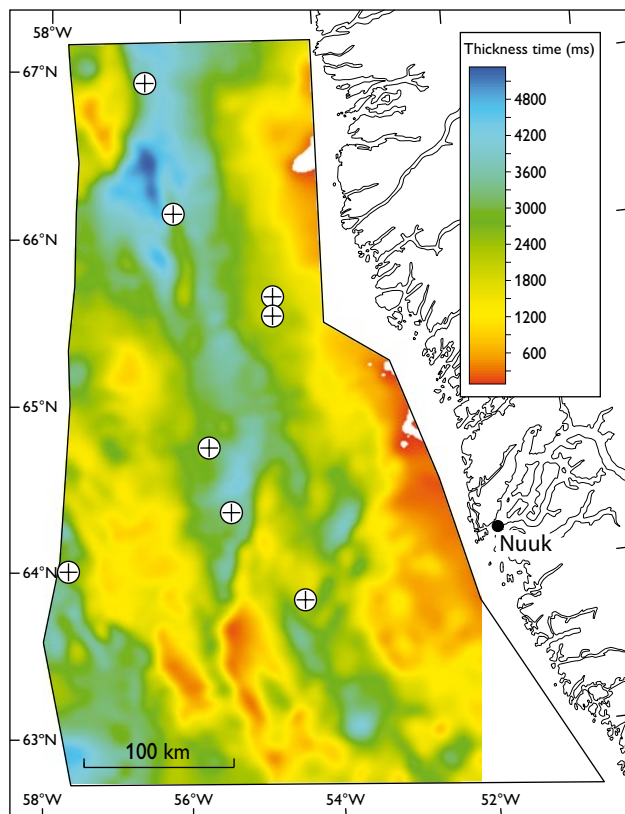


Fig. 4. The LF7-1 well and a composite NW–SE seismic section across the Lady Franklin Basin. The succession from the seabed to the basement is divided by seismic stratigraphic horizons A1–H1 into seismic mega-units A–H and tentative ages of major successions are shown in colour (Fig. 3). It is dominated by Cretaceous successions of mega-units F and G and includes rifted structures. Mega-unit F is overlain by a probably thin Palaeogene volcanic succession. A Miocene–Pliocene contourite succession of mega-units B and C occurs south-east of the LF7-1 well. The seismic line shown (TGS-BLF2005-43) is courtesy of TGS-NOPEC Geophysical Company ASA. The location of the section is shown in Fig. 1.



probably as a result of glaciations, and a near-horizontal succession also formed in mega-unit A.

Conclusions

A study was carried out with subsurface mapping using geophysical and well data offshore southern West Greenland. A seismic stratigraphy with eight mega-units (A–H) from the seabed to the pre-Cretaceous basement has been defined in the area and shown on cross-sections. A new structural elements map displaying the main structures, basins and faults, as well as a sedimentary thickness map are presented.

Fig. 5. Thickness isochore map in two-way travel time (ms) between the seabed (A1 horizon) and the Pre-Cretaceous basement (H1 horizon). The map includes mostly sedimentary successions but locally also includes volcanic successions as illustrated in Figs 2–4. Thick dominantly sedimentary successions occur in mainly the Lady Franklin Basin, the Fylla East Basin, the Nuuk Basin, the Kangâmiut Basin and the Sisimiut Basin, whereas successions thin over structural highs (Figs 2–4). The names of the wells are shown in Fig. 1.

Biostratigraphic ages, radiometric dating and lithologies from well data are correlated to parts of the mega-units. The studied wells comprise Cretaceous to Cenozoic sedimentary successions, a volcanic succession and granitic rocks from the basement. The results presented here are based on analyses from this study and recently released data from the wells drilled in 2011 by Cairn Energy (AT2-1, AT7-1 and LF7-1). The results have improved the understanding and outline of the large-scale structures, basins and provide input for further work in the region including new resource-potential evaluations, but also point out uncertainties and risks that require clarification.

Acknowledgements

The study was co-financed by the Ministry of Mineral Resources (Government of Greenland) and GEUS. The constructive comments from the referees Kate Dickie and Christopher Harrison are much appreciated. The displayed seismic lines are courtesy of TGS-NOPEC Geophysical Company ASA.

References

- Bojesen-Koefoed, J.A. 2011: West Greenland petroleum systems. An overview of source rocks and oil seepages and their implications for offshore petroleum exploration. *Danmarks og Grønlands Geologiske Undersøgelse Rapport* **2011/42**, 49 pp.
- Cairn Energy 2011: Licensing reporting of Cairn Energy including the geological end of well reports and the composite well-logs from the AT2-1, AT7-1 and LF7-1 exploration wells.
- Chalmers, J.A., Pulvertaft, T.C.R., Christiansen, F.G., Larsen, H.C., Laursen, K.H. & Ottesen, T.G. 1993: The southern West Greenland continental margin: rifting history, basin development, and petroleum potential. In: Parker, J.R. (ed.): *Petroleum Geology of NW Europe: Proceedings of the 4th Conference*. Geological Society, London, 915–931.
- Christiansen, F.G., Bojesen-Koefoed, J.A., Chalmers, J.A., Dalhoff, F., Mathiesen, A., Sønderholm, M., Dam, G., Gregersen, U., Marcussen, C., Nøhr-Hansen, H., Piasecki, S., Preuss, T., Pulvertaft, C.R., Rasmussen, J.A. & Sheldon, E. 2001: Petroleum geological activities in West Greenland in 2000. *Geology of Greenland Survey Bulletin* **189**, 24–33.
- Dam, G., Pedersen, G.K., Sønderholm, M., Midtgaard, H., Larsen, L.M., Nøhr-Hansen, H. & Pedersen, A.K. 2009: Lithostratigraphy of the Cretaceous-Paleocene Nuussuaq Group, Nuussuaq Basin, West Greenland. *Geological Survey of Denmark and Greenland Bulletin* **19**, 171 pp.
- Døssing, A. 2011: Fylla Bank: structure and evolution of a normal-to-shear rifted margin in the northern Labrador Sea. *Geophysical Journal International* **187**, 655–676.
- Funck, T., Jackson, H.R., Loudon, K.E. & Klingelhöfer, F. 2007: Seismic study of the transform-rifted margin in Davis Strait between Baffin Island (Canada) and Greenland: What happens when a plume meets a transform. *Journal of Geophysical Research* **112**, 1–22.
- Gregersen, U. 2014: The West Greenland Continental Margin. In: Hopper, J.R. *et al.* (eds): *Tectonostratigraphic Atlas of the North-East Atlantic region*. Copenhagen: Geological Survey of Denmark and Greenland, 321–325.
- Gregersen, U. & Bidstrup, T. 2008: Structures and hydrocarbon prospectivity in the northern Davis Strait area, offshore West Greenland. *Petroleum Geoscience* **14**, 151–166.
- Hald, N. & Larsen, J.G. 1987: Early Tertiary, low-potassium tholeiites from exploration wells on the West Greenland shelf. *Grønlands Geologiske Undersøgelse Rapport* **136**, 25 pp.
- Henriksen, N., Higgins, A.K., Kalsbeek, F. & Pulvertaft, T.C. 2009: Greenland from Archaean to Quaternary – Descriptive text to the 1995 Geological map of Greenland 1:2 500 000. 2nd edition. Geological Survey of Denmark and Greenland Bulletin **18**, 126 pp.
- Larsen, L.M. & Dalhoff, F. 2006: Composition, age, and geological and geotectonic significance of igneous rocks dredged from the northern Labrador Sea and the Davis Strait. *Danmarks og Grønlands Geologiske Undersøgelse Rapport* **2006/43**, 67 pp.
- Larsen, L.M., Pedersen, A.K., Tegner, C., Duncan, R.A., Hald, N. & Larsen, J.G. 2016: Age of Tertiary volcanic rocks on the West Greenland continental margin: volcanic evolution and event correlation to other parts of the North Atlantic Igneous Province. *Geological Magazine* **153**, 487–511.
- Nielsen, T., Andersen, C., Knutz, P.C. & Kuijpers, A. 2011: The Middle Miocene to Recent Davis Strait Drift Complex: implications for Arctic–Atlantic water exchange. *Geo-Marine Letters* **31**, 419–426.
- Nøhr-Hansen, H., Williams, G.L. & Fensome, R.A. 2016: Biostratigraphic correlation of the western and eastern margins of the Labrador-Baffin Seaway and implications for the regional geology. *Geological Survey of Denmark and Greenland Bulletin* **37**, 74 pp.
- Oakey, G.N. & Chalmers, J.A. 2012: A new model for the Palaeogene motion of Greenland relative to North America: Plate reconstructions of the Davis Strait and Nares Strait regions between Canada and Greenland. *Journal of Geophysical Research* **117**, 1–28.
- Piasecki, S. 2003: Neogene dinoflagellate cysts from Davis Strait, offshore West Greenland. *Marine and Petroleum Geology* **20**, 1075–1088.
- Rolle, F. 1985: Late Cretaceous–Tertiary sediments offshore central West Greenland: lithostratigraphy, sedimentary evolution, and petroleum potential. *Canadian Journal of Earth Science* **22**, 1001–1019.
- Skaarup, N. 2001: Offshore volcanic rocks in Baffin Bay. A seismic interpretation of the structures and development of the Palaeogene offshore volcanic rocks in central West Greenland and on the Baffin Island margin eastern Canada. PhD thesis from University of Copenhagen. *Danmarks og Grønlands Geologiske Undersøgelse Rapport* **2001/117**, 154 pp.
- Sørensen, A.B. 2006: Stratigraphy, structure and petroleum potential of the Lady Franklin and Maniitsoq Basins, offshore southern West Greenland. *Petroleum Geoscience* **12**, 221–234.
- Stouge, S., Ineson, J.R., Rasmussen, J.A. & Dalhoff, F. 2007: Sedimentary dredge samples from the Davis Strait High: stratigraphic and palaeoenvironmental implications. *Danmarks og Grønlands Geologiske Undersøgelse Rapport* **2007/19**, 49 pp.

Authors' addresses

U.G., M.S.A., H.N.-H., E.S., T.F.K., M.O. & C.K., *Geological Survey of Denmark and Greenland, Øster Voldgade 10, DK-1350 Copenhagen K, Denmark.*

E-mail: ug@geus.dk.

K.G.J. & J.S.A., *Ministry of Mineral Resources, Government of Greenland (Nuuk), P.O. Box 930, DK-3900 Nuuk, Greenland.*

Remote geological mapping using 3D photogrammetry: an example from Karrat, West Greenland

Erik Vest Sørensen and Pierpaolo Guarnieri

The geology of the Palaeoproterozoic Karrat Group in West Greenland (71°–74°50'N) was investigated during the field seasons 2015–2017, using a combination of digital photogrammetry and traditional field work in a collaboration between the Geological Survey of Denmark and Greenland and the Ministry of Minerals Resources of Greenland. The area is characterised by steep alpine terrain with more than 2000 m of relief that in many places is completely inaccessible, which makes field work extremely difficult. Therefore 3D mapping using digital photogrammetry is an invaluable tool in the investigation of the region. Early geological investigations of the area involved the first use of photogrammetry in Greenland (Henderson & Pulvertaft 1987). This contribution serves as an example of the present-day use of photogrammetry in geological interpretation, following the workflow outlined in Sørensen & Dueholm (2018). During the last three years, more than 50 000 stereo images have been collected using handheld, calibrated digital cameras while conducting field work in the area (Rosa *et al.* 2016, 2017, 2018). The images, which cover large parts of the steep cliff sections in which the geology is superbly exposed, are essential to the ongoing revision of the geological map sheets covering the area. Here we present a small subset of the data from the island of Karrat (Fig. 1), showcasing the potential

of 3D geological mapping in Greenland as well as presenting new insights into the geology of the Karrat Group.

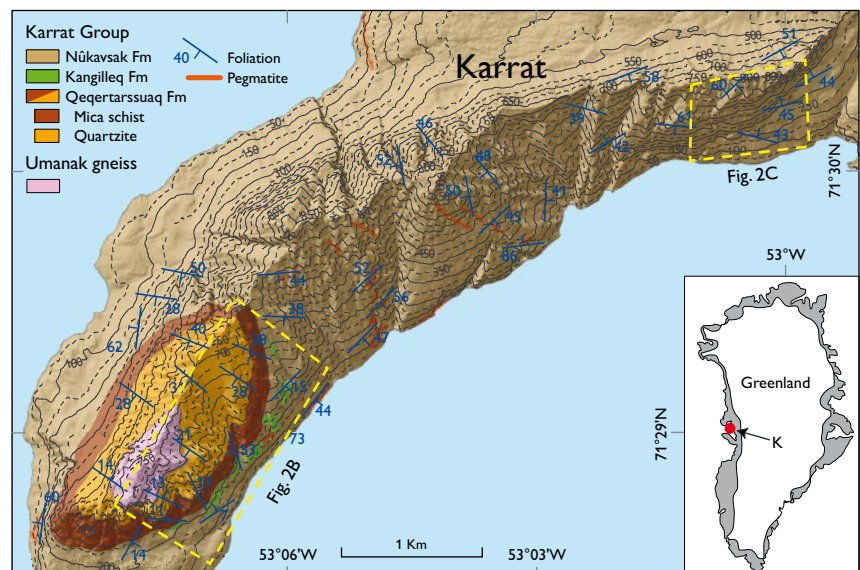
Regional Geology

The Karrat region is part of the Rinkian fold belt of West Greenland (Henderson & Pulvertaft 1967). The area mainly consists of reworked Archaean gneisses overlain by supracrustal successions of the Palaeoproterozoic Karrat Group. The group initially comprised two formations: the Qeqertarsuaq and Nûkavsak Formations, but was later extended to also include the Marmorilik Formation (Henderson & Pulvertaft 1987), originally considered to be of Archaean age but later shown to be Palaeoproterozoic and resting with a depositional unconformity on Archaean gneiss (Garde 1978). The Karrat Group and its Archaean basement were metamorphosed and folded during the Rinkian orogeny *c.* 1.9–1.8 Ga (Henderson & Pulvertaft 1987; Grocott & Pulvertaft 1990).

Data acquisition and preparation

Stereo images were collected with calibrated, hand-held digital SLR cameras from a boat (which served as base-camp) and from a helicopter used for day excursions and to sup-

Fig. 1. Part of the new geological map of Karrat island (location in Greenland marked on inset map), prepared as part of an ongoing revision of the 1:100 000 scale regional geological map sheets. The digital elevation model was generated from the oblique stereo-images collected during field work. Inset boxes show the approximate positions of Figs 2B, C.



port field camps. The images were typically collected while moving along the cliff faces in straight or gently curving trajectories tens to hundreds of kilometres long at varying distances to the cliffs. We here present results from a subset of the images collected from boat and helicopter flights around Karrat. We used a hand-held Nikon D800E (36 megapixel) digital, single lens reflex camera equipped with a Carl Zeiss Distagon 35 mm lens that was pointed perpendicularly to the slope of interest through an open helicopter window or from boat. With the images we have almost complete coverage of the island with a resolution of c. 0.1–0.5 m (pixel size on the ground).

The images were prepared for 3D mapping following the exact workflow of Sørensen & Dueholm (2018). GPS positional data collected together with the images during field work were used as a first approximation for absolute positioning. The absolute orientation was subsequently refined through a proper bundle adjustment also including pass points measured stereoscopically in monochrome aerial photographs on a scale of 1:150 000 (i.e. points also identified in the oblique stereo-images), as well as planar levelling points (sea-level points) measured in the oblique images. The absolute accuracy of the stereoscopic models is around 3 m (xyz) while the photogrammetric or relative accuracy is in the millimetre to centimetre range.

The images were subsequently used to extract elevation data for Karrat, using SURE software from Nframes. A digital elevation model of Karrat island with a 2×2 m grid (Fig. 1) was produced to assist in the geological interpretation, as well as a so-called point cloud (a set of data points in 3D space representing the terrain surface) of the island to be used for visualisation purposes (Fig. 2A).

Data interpretation – 3D mapping

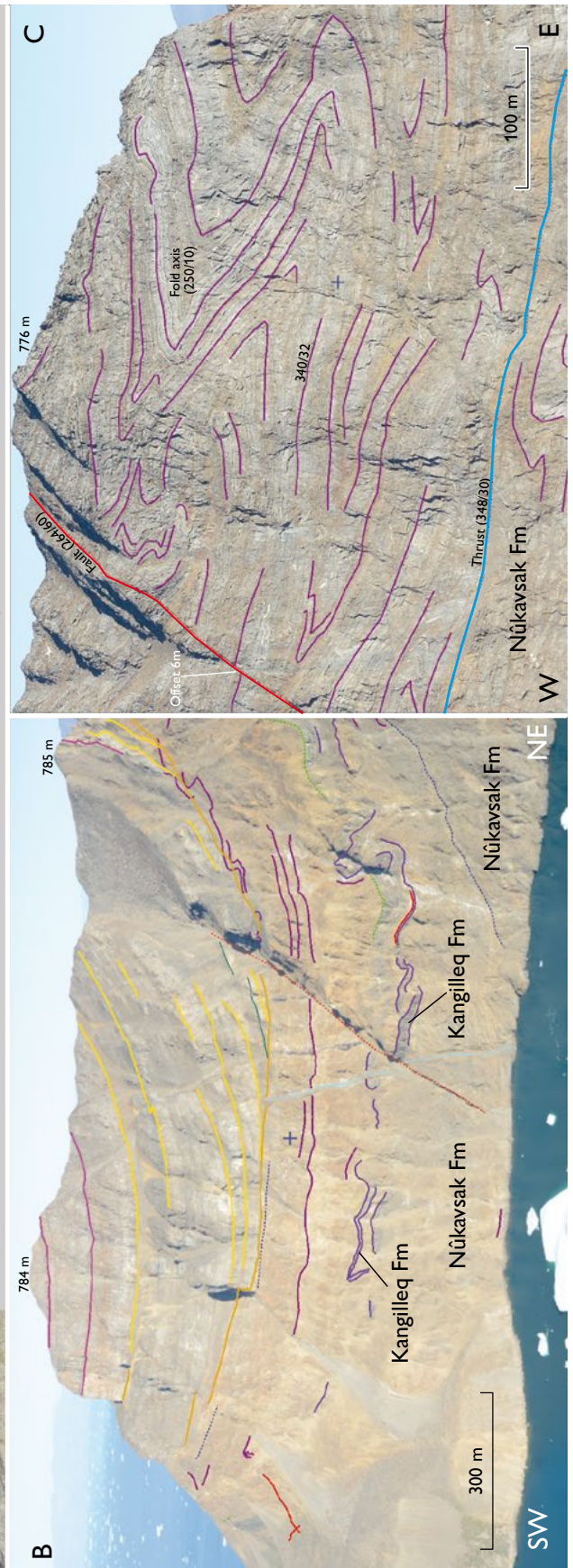
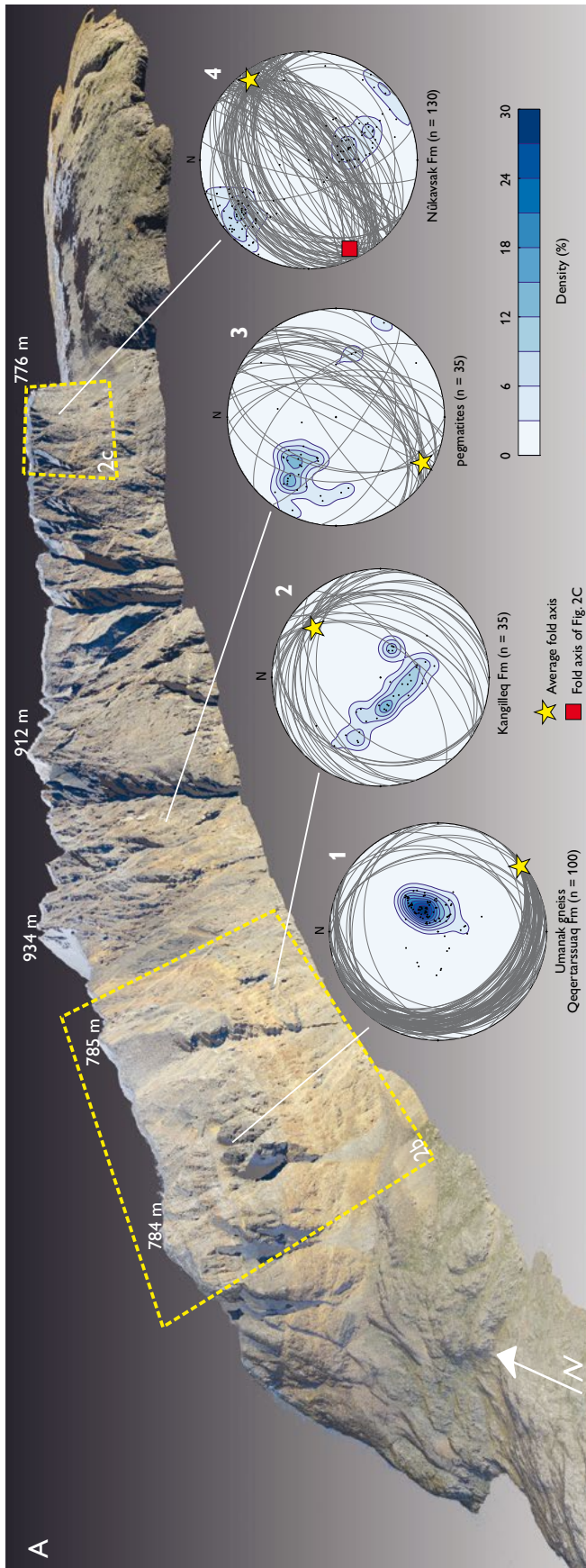
With the images properly oriented in 3D, essentially all corners of the island can be visited stereoscopically with the ease of a mouse-click and a geological interpretation can be performed. In this way it is possible, so to speak, to bring the rock exposures into the laboratory where the geology can be analysed. Whereas previous geological investigations have taken place in the more accessible lower parts of Karrat, here we focus on the inaccessible, higher parts of the island. Karrat represents the north-westernmost exposure of the Kigarsima Nappe (Henderson and Pulvertaft 1987). The south-western top of the island displays the overturned basement core of this tectonic nappe that forms an inverted sequence of Archaean banded gneiss (Umanak gneiss) with amphibolite layers sitting structurally on top of garnet-mica schist and quartzite of the Qeqertarsuaq Formation, metavolcanic

rocks of the Kangilleq Formation and biotite schist of the Nûkavsak Formation (Fig. 2).

In addition to the actual 3D mapping with tracing of geological units, bedding and foliation (Figs 2B, C), a powerful feature of the 3D mapping tool is the possibility to gather structural data remotely. This makes it possible to extend structural information from the shoreline, from where most structural data are usually collected during field work, up to outcrops at the top of the mountain (Fig. 2A). This is important as it gives a more complete data coverage, and because the Karrat region is structurally complex with multiple deformation stages (Henderson & Pulvertaft 1987; Grocott & McCaffrey 2017).

The structural data obtained with 3D photogrammetry consist of strike and dip of bedding/foliation, faults and thrusts together with traces of the geological boundaries between lithological or lithostratigraphic units. The data are stored as points (vertexes) along vectorised lines, so-called polylines. The strike and dip measurements presented here were calculated for each vertex of the polylines obtained through the 3D mapping as a moving average of best fitted planes by least square adjustment. More specifically, for each individual vertex a search window including seven adjacent vertexes was used in the calculation. In this way strike and dip measurements were generated for all vertexes of the mapped polylines. The measurements were subsequently filtered based on the standard deviation of each measurement. The result of this is a dataset of georeferenced points with calculated strikes and dips of their associated planar surfaces, which can be plotted on a geological map and analysed using stereoplots (Fig. 2). The Karrat island dataset consists of foliation in the Umanak gneiss and amphibolites, bedding/foliation in quartzites of the Qeqertarsuaq Formation, bedding of folded metavolcanic rocks of the Kangilleq Formation and the intensely folded metagreywacke strata of the Nûkavsak Formation, as well as folded pegmatites.

Fig. 2. Point cloud model of Karrat, looking north. **A:** Lower hemisphere stereographic plots 1–4 of foliation and bedding measurements obtained from 3D polylines and shown as pole-to-bedding great circles and density averages. Average fold axis orientations are defined by the intersection of great circles, shown with stars on the individual stereoplots. **B:** Structural data from the southern part of the Karrat showing the overturned limb of the Kigarsima Nappe (Umanak gneiss and Qeqertarsuaq Formation), folded metavolcanic rocks of the Kangilleq Formation and Nûkavsak Formation metagreywackes. **C:** Detailed close-up of the intense kink folds (purple lines) in the Nûkavsak Formation (numbers indicate dip direction/dip angle. Blue line at the base: thrust fault dipping 30° NW compatible with the average fold trends. Red line: normal fault dipping 60° W with a measured offset of 6 m.



Previously, Grocott and McCaffrey (2017) described the emplacement of the Kigarsima Nappe towards ENE as established by structural analysis of stretching lineations along a basal thrust contact. The authors also described an intersection lineation between cleavage and bedding, gently plunging towards SW, which appears to be compatible with a stretching lineation defined by hornblende and biotite minerals oriented WNW–ESE that they related with a later top-to-NW tectonic transport overprinting the Kigarsima structures.

Our new data presented in Fig. 2 are in good agreement with the observations of Grocott and McCaffrey (2017). At Karrat island only the lower limb of the Kigarsima Nappe is preserved, represented by the Umanak gneiss and Qeqertarsuaq Formation (Fig. 2B). The *c.* 100 new foliation measurements (Fig. 2 stereoplot 4) calculated from the mapped 3D polylines (Fig. 2B) describe the geometry of a large recumbent fold with a subhorizontal, NNW–SSE- to NW–SE-trending fold axis. This structural trend is compatible with ENE–WSW to NE–SW compression that is consistent with the ENE- to NE-tectonic transport suggested by Grocott and McCaffrey (2017). In contrast, a different structural trend is observed in the younger lithostratigraphic units. From the structural data (Fig. 2A stereoplots 1–3) it appears that the structural trends are rotated almost 90°. In fact, the 40 measurements obtained from the folded metavolcanic rocks of the Kangilleq Formation (Fig. 2A stereoplot 2) located in the overturned limb of the Kigarsima Nappe show an average NE-plunging fold axes that is similar to the fold axes obtained from the 130 measurements (Fig. 2A stereoplot 4) from the large kink folds observed in the Nûkvsak Formation (Fig. 2C). These trends of folds are compatible with NW–SE compression that in turn seems to be consistent with the top-to-NW tectonic transport indicated by Grocott and McCaffrey (2017). Similar fold axis trends are observed in the mapped pegmatites that cut the stratigraphy in the central part of the island (Figs 1 and 2A stereoplot 3). This establishes an important cross-cutting relationship between the folding event and the pegmatites which are probably related to high temperature metamorphism dated at *c.* 1830 Ma (Rosa *et al.* 2017; Kirkland *et al.* 2017).

Summary

This study demonstrates how 3D mapping can be used for geological mapping in remote and inaccessible areas such as Greenland following the procedures of Sørensen & Dueholm (2018). This is done with an example from the island of Karrat, West Greenland. Using just a digital camera, we have

generated a new revised geological map of Karrat including topography, geology and structural data. Our approach and methodology offer great support to standard field work where detailed outcrop information can be extended into regional-scale mapping.

Acknowledgments

This work was carried out within the framework of an ongoing project financed by the Geological Survey of Denmark and Greenland and the Ministry of Mineral Resources of Greenland. We thank Asger Ken Pedersen and Ken McCaffrey for the helpful comments and suggestions.

References

- Garde, A.A. 1978: The Lower Proterozoic Marmorilik Formation, east of Marmorilik, West Greenland. *Meddelelser om Grønland* **200**(3), 71 pp.
- Grocott, J. & Pulvertaft, T.C.R. 1990: The Early Proterozoic Rinkian belt of central West Greenland. In: Lewry, J.F. & Stauffer, M.R. (eds): The Early Proterozoic Trans-Hudson Orogen of North America. Geological Association of Canada, Special Paper **37**, 443–463.
- Grocott, J. & McCaffrey, K.J.W. 2017: Basin evolution and destruction in an Early Proterozoic continental margin: the Rinkian fold–thrust belt of central West Greenland. *Journal of the Geological Society (London)* **174**, 453–467.
- Henderson, G. & Pulvertaft, T.C.R. 1967: The stratigraphy and structures of the Precambrian rocks of the Umanak area, West Greenland. *Meddelelser Dansk Geologisk Forening* **17**, 1–20.
- Henderson, G. & Pulvertaft, T.C.R. 1987: Geological Map of Greenland, 1:100 000, Marmorilik 71 V.2 Syd, Nûgâtsiaq 71 V.2 Nord, Pangnertôq 72 V.2 Syd. Descriptive text. 72 pp., 8 plates. Copenhagen: Geological Survey of Greenland.
- Kirkland, C.L., Hollis, J., Danišik, M., Petersen, J., Evans, N. J., & McDonald, B.J. 2017: Apatite and titanite from the Karrat Group, Greenland; implications for charting the thermal evolution of crust from the U–Pb geochronology of common Pb bearing phases. *Precambrian Research* **300**, 107–120.
- Rosa, D., Guarnieri, P., Hollis, J., Kolb, J., Partin, C., Petersen, J., Sørensen, E.V., Thomassen, B., Thomsen L. & Thrane, K. 2016: Architecture and mineral potential of the Paleoproterozoic Karrat Group, West Greenland. *Danmarks og Grønlands Geologiske Undersøgelse Rapport* **2016/12**, 98 pp.
- Rosa, D., Dewolfe, M., Guarnieri, P., Kolb, J., LaFlamme, C., Partin, C., Salehi, S., Sørensen, E.V., Thaarup, S., Thrane, K. & Zimmermann, R. 2017: Architecture and mineral potential of the Paleoproterozoic Karrat Group, West Greenland – Results of the 2016 Season. *Danmarks og Grønlands Geologiske Undersøgelse Rapport* **2017/5**, 98 pp.
- Rosa, D., Bernstein, S., Dewolfe, M., Dziggel, A., Grocott, J., Guarnieri, P., Kolb, J., Partin, C., Sørensen, E.V. & Zimmermann, R. 2018: Architecture and mineral potential of the Paleoproterozoic Karrat Group, West Greenland – Results of the 2017 Season. *Danmarks og Grønlands Geologiske Undersøgelse Rapport* **2018/23**, 102 pp.
- Sørensen, E.V. & Dueholm, M.: 2018: Analytical procedures for 3D mapping at the Photogeological Laboratory of the Geological Survey of Denmark and Greenland. *Geological Survey of Denmark and Greenland Bulletin* **41**, 99–104 (this volume).

Authors' address

Geological Survey of Denmark and Greenland, Øster Voldgade 10, DK-1350 Copenhagen K, Denmark. E-mail: evs@geus.dk.

European trading, whaling and climate history of West Greenland documented by historical records, drones and marine sediments

Naja Mikkelsen, Antoon Kuijpers, Sofia Ribeiro, Mikkel Myrup, Inge Seiding and Ann E. Lennert

The European trading and whaling activities of the 17th–19th centuries provide records of climate and sea-ice conditions off West Greenland in the form of ships' logs and other official documents in many archives around Europe. These documents, combined with evidence from marine sediments, help describe climate changes in general, and sea-ice volume changes in particular, in connection with human activity in the region. The Greenland National Museum & Archives in Nuuk (NKA) hosts a unique collection of original documents presenting detailed insight into weather and ice conditions as well as the daily life of the colonial centres and outposts recorded by the documents of the Danish administration. These documents also reveal many aspects of the interaction between the Inuit and Europeans from 1779 onwards. Information retrieved from the archives in Nuuk has been combined with results from palaeo-environmental investigations of marine sediment cores to unravel climate variability and changes in sea ice. This information has been supplemented with data from an extensive field programme using drones to document onshore remains from the whaling period in the Disko Bugt region (Fig. 1).

History of European whaling off West Greenland

European Arctic whaling around Svalbard and Jan Mayen declined in the early 18th century, and it has been debated whether over-exploitation (e.g. Nansen 1924) or climate change (e.g. Vibe 1967) was responsible for the decline. European summer temperature records (Luterbacher *et al.* 2016) indicate that the decline coincided with a marked climate cooling in Europe. High hunting pressure on the whales and thick sea-ice cover in Svalbard waters early in the 18th century apparently forced the whale population to seek away from inshore areas into the ice-loaded waters farther offshore. As a consequence, European whaling companies began to look for other areas, which led them to explore the whale resources of the Davis Strait. Taking a general 'seesaw' winter-climate pattern between (West) Greenland and Europe into consideration (Seidenkrantz *et al.* 2008), in contrast to the cold conditions around Svalbard (Luterbacher *et al.* 2016), the sea-ice and whaling conditions in Disko Bugt around 1700

were likely more favourable. A large part of the European whaling fleet therefore moved their activities to the Davis Strait off West Greenland where the Disko Bugt region became the focal point of whaling activities. In the region, the European whalers' contact with the local Inuit population significantly impacted their culture and living conditions through the exchange of goods and social interaction.

In 1719, an increased number of Dutch whaling vessels started to operate in the Davis Strait (Leinenga 1995; Hacquebord 2006) with the Greenland (bowhead – *Balaena mysticetus*) whale as the main target. Whaling activities in the



Fig 1. Disko Bugt was the focus of whaling activities in past centuries. Areas investigated in 2016 and 2017 were Rodebay embayment, Hundejland and Pullat. A sediment core POR16_RB#1 was retrieved just outside the Rodebay embayment.



Fig 2. Whales caught by Danish shore-based whaling stations were numbered and often drawn as cartoons in Danish reports. This document clearly illustrates that whaling had been successful for the period reported (source NKA Archives, Nuuk).

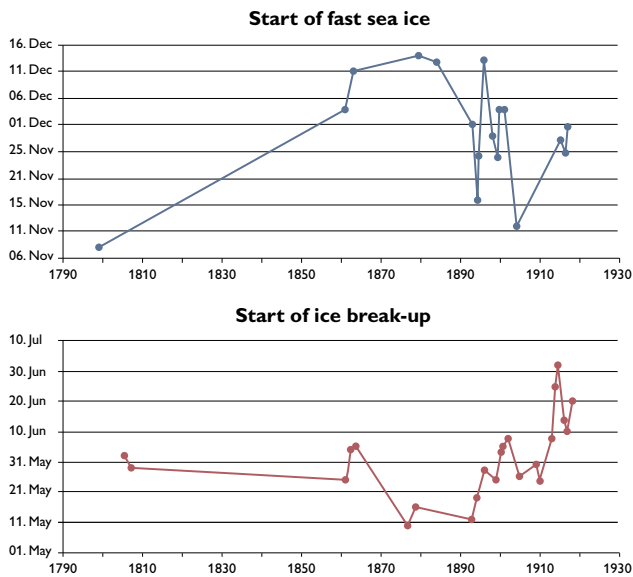


Fig. 3. Dates of freezing and ice breakup in the Upernavik district plotted from archival data. The time of sea-ice breakup shows a clear shift, with the sea-ice duration increasing by *c.* 40 days over a period of *c.* 30 years (*c.* 1890–1920; A. Kuijpers, unpublished data 2014).

Davis Strait were concentrated around Disko Bugt. In 1721, Denmark affirmed sovereignty over Greenland and in 1776 established the state-owned Royal Greenland Trade Department (KGH) with whales and seals as the primary commodities. This Danish initiative had difficulty competing with other highly efficient whaling fleets and after disappointing catches, further attempts with Danish sea-going whaling ceased after 1780. Instead Danish activities primarily used shore-based stations for sealing and whaling and this hunting turned out to be economically successful in the following decades.

After the Napoleonic wars, European demand for whale products increased, and new Danish coastal whaling projects were started in the Davis Strait area (e.g. the island of Pullat off the coast at Aasiaat – Egedesminde). However, due to increasing industrial use of coal and other types of oil in Europe and as a consequence of a series of severe ship losses early in the 19th century, the Davis Strait whaling lost its importance.

Evidence from historical archive data

Data from several whaling settlements are available in the archives in Nuuk and provide a wealth of detailed information after 1779 on weather, sea ice occurrence, number of whales caught (Fig. 2) as well as results from hunting, fishing, travelling, social life, health conditions, religious celebrations and occasional visits by European whalers (NKA archives). Successful coastal whaling was only possible with participation of the local Inuit population, in many cases also involving

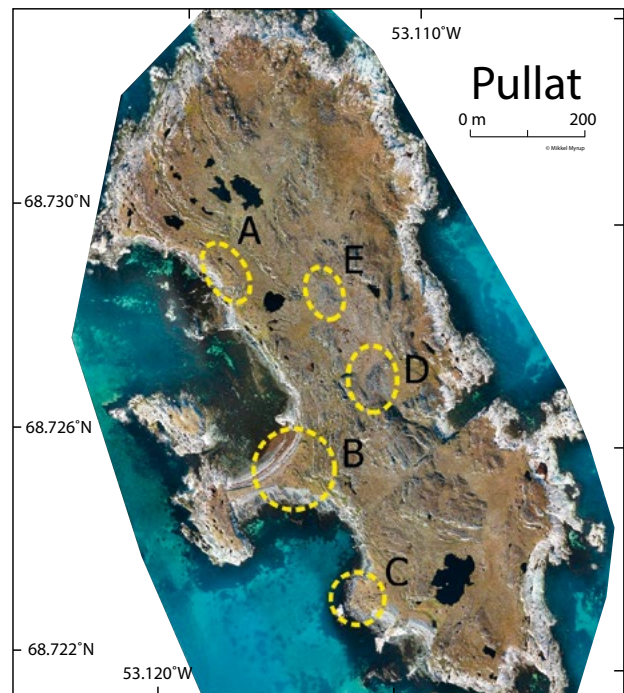


Fig. 4. Remains from the coastal whaling period on the island of Pullat are documented on the orthophotomosaic based on drone flights. **A:** winter house. **B:** the main structures from the whaling station period 1823–1825. **C:** winter houses. **D, E:** grave fields. Photo: M. Myrup 2017.

women. The European whaling activities thus had significant impact on the previously prosperous Inuit hunting and their traditional way of life. The Inuit women's national costume rich in bead decoration, and various forms of folk dance music are examples of social interaction between the two groups. Although Dutch whaling activities along the West Greenland coast had virtually ceased by 1800, a series of geographical Dutch names are a reminder of this period, such as: Vaigat (Dutch for windy passage), Rodebay, Fortunebay, Grønne Ejland, and Hunde Ejlande.

In the early 20th century, Scottish whalers, the only group still active in the area, moved their centre of activity northwards and made port calls at Upernavik instead of Disko Bugt. As can be seen in the historical records from Upernavik (Fig. 3), this period is clearly characterised by longer sea-ice seasons than in the later part of the 19th century suggesting that better whaling conditions in the early 20th century had shifted northwards into more ice-affected areas along the west coast of Greenland.

Tracing past whaling activities onshore

The coastal areas of the Disko Bugt region display a rich variety of physical remains from the whaling period. To locate and investigate former whaling sites, Mikkel Myrup from



Fig. 5. Among the graves in the ‘Old Whalers Graveyard’ on Kitsissuarsuit (Hunde Ejlande), two graves are marked with plain squared timbers. This type of grave marking has only been found in the old whalers’ graveyard on Svalbard established in the 17th century. Modern graves with the traditional white painted wooden crosses are seen in the background.

NKA in 2017 undertook a number of drone operations in three areas in the Disko Bugt region: Oqaatsut (Rodebay), Kitsissuarsuit (Hunde Ejlande) and Pullat (Fig. 1).

The small Greenlandic settlement Oqaatsut (Rodebay) is located in a protected embayment just north of Ilulissat. In the 1600s, this area was called ‘Roo Baj – Red Bay’ by the Dutch. Whales caught locally by traditional whaling techniques were pulled ashore on the flat rocks where blood from the butchered animals coloured the small embayment red. Today remains from the whaling activities are visible in the form of natural butchering places created by rock depressions with winches still present.

Amongst other structures still visible are the remains of a whaling station established by Danish authorities on the island of Pullat in 1823 (Fig. 4). It was a sudden and intense effort by KGH to boost the coastal-based whaling activity in the area and also to counteract the strong presence of European whalers interacting with the Inuit farther north. The whaling station at Pullat, however, was closed after only two years due to unsuccessful whale hunting. Towards the middle of the 19th century, KGH eventually gave up the whaling outposts in the Disko Bugt region and focused its efforts on seal hunting and procuring other Greenlandic products.

The graveyard on Kitsissuarsuit (Hunde Ejlande) hosts modern graves with traditional white-painted wooden crosses and a central section from the European whaling period. This central section known as ‘the Old Whalers Graveyard’ is occupied by *c.* 100 graves covered by elongated stone piles. Unlike the modern white crosses, two of these graves are marked with plain wooden, squared posts (Fig. 5). Similar old graves are reported from the graveyard ‘Liknesset’ on north-western Svalbard, which was established by Dutch whalers in the 17th century.

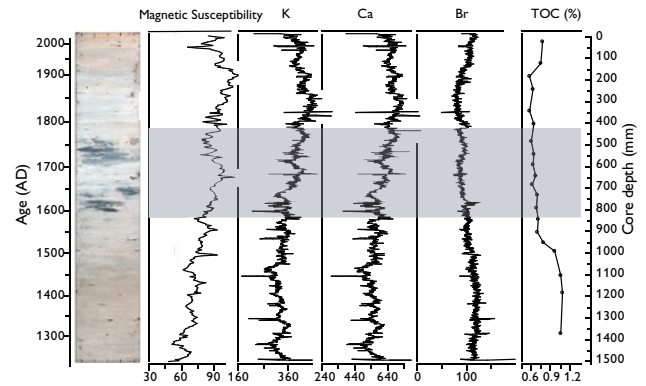


Fig. 6. Sediment core POR16_RB#1 was retrieved just outside the Rodebay embayment. The geochronology of this 158 cm core was based on ^{210}Pb and ^{137}Cs analyses of the upper 15 cm, and 3 AMS ^{14}C dates on marine bivalves. The prominent dark colouring of the interval corresponding to the period *c.* AD 1600–1750 of the Little Ice Age reveals the presence of non-oxic conditions most likely due to persistent sea-ice cover. Sediments deposited after AD 1600 display regular oscillations in K and Ca with a duration of close to 80 years.

Evidence from marine sediment records

In August 2016, A sediment coring campaign was undertaken from the Research Vessel *Porsild*. Twelve sediment cores were retrieved from the Rodebay area to obtain a record of climate and hydrographic changes and possible environmental effects of human activity in this area spanning the whaling period. Cores collected from the enclosed inner part of the Rodebay area consist of unconsolidated mud with high organic contents are underway. DNA analyses will be performed on these cores to identify which mammalian species were slaughtered at the site throughout the whaling period. To capture changes in the marine environment a core (Core POR16_RB#1) was retrieved just outside the Rodebay embayment. The geochronology of this 158 cm core was based on ^{210}Pb and ^{137}Cs analyses of the upper 15 cm, and 3 AMS ^{14}C dates on marine bivalve shells. The age-model was constructed using Bayesian analyses with the BACON package available in the R platform. The radiocarbon offset used was 140 ± 60 years, and radiocarbon dates were calibrated using the Marine13 calibration curve. The core was XRF scanned and analysed in terms of magnetic susceptibility and total organic carbon (TOC) content (Fig. 6). The prominent dark colouring of the interval corresponding to the period *c.* AD 1600–1750 reveals the presence of poorly oxygenated sediments. Locally enhanced organic matter fluxes can be expected at this site to originate from whale butchering colouring the sediments black. However, this dark interval precedes by *c.* 100 years the beginning of intensive whaling activity in the region, and the organic carbon content does

not indicate enhanced fluxes in organic matter. Instead, local hydrographic conditions with reduced bottom-water oxygenation are likely to be responsible for the dark layers. This sediment interval corresponds to one of the more severe Little Ice Age cooling episodes during which the sea-ice cover along the coast of the inner part of Disko Bugt may have persisted throughout most of the year (Ribeiro *et al.* 2011).

During cold intervals of the Little Ice Age, the mean annual temperature in the Disko Bugt region area was 2–4°C lower than present day values (Humlum 1999). Prior to this period of generally colder climate, about 1000 years ago, the regional atmospheric climate was relatively mild in West Greenland, but soon after, i.e. close to AD 1200, average temperatures started abruptly to decline by as much as 4°C over about 80 years (D'Andrea *et al.* 2011). This climate deterioration involved an increase of widespread ice formation in the inshore waters and fjords of West Greenland (Kuijpers *et al.* 2014). Regional climate since then has remained generally colder until about 150 years ago, although with large fluctuations (Ribeiro *et al.* 2011).

The XRF data of core POR16_RB#1 reveal regular oscillations in the upper part of the core that appear to occur on a multi-decadal time scale. During the past 1000 years, 60–80 years periodicity is noted in sea-surface conditions of the Disko Bugt areas (Allan *et al.* 2018) suggesting clear linkages with the 'Atlantic Multidecadal Oscillation' (AMO) in which warmer and more saline North Atlantic surface-water conditions alternate with cooler and less saline conditions around AD 1910 (Reverdin 2010).

Based on historical information from the KGH records from Upernavik (A. Kuijpers, unpublished data 2014), the temperature and salinity may also be reflected by the duration of the sea-ice season off West Greenland, which in the beginning of the 20th century extended into June (Fig. 3). Such a relationship between winter sea-ice conditions in the north-western North Atlantic and 'Atlantic Multidecadal Oscillation' has also been reported by Chan *et al.* (2017), who found that during the past four centuries an extended sea-ice cover and associated reduced ice productivity can be linked to the cool phase of the 'Atlantic Multidecadal Oscillation'.

Acknowledgements

This study was part of the EU funded project ICE-ARC (*Ice, Climate and Economics in the Arctic*) and supported by funding from the European Union 7th Framework Programme, grant number 603887 and by funding

from the National Museum and Archives (NKA), Nuuk, project *Encounters*. Niels Frandsen, former head of the archive, is gratefully acknowledged for research support (AK) in Nuuk in 2014.

References

- Allan, E., de Vernal, A.E., Knudsen, M.F., Hillaire-Marcel, C., Moros, M., Ribeiro, S., Oulet-Bernier, M.-M. & Seidenkrantz, M.-S. 2018: Late Holocene sea surface instabilities in the Disko Bugt area, West Greenland, in phase with $\delta^{18}\text{O}$ oscillations at Camp Century. *Paleoceanography and Paleoclimatology* **33**, 227–243, <http://dx.doi.org/10.1002/2017PA003289>
- Chan, P., Halfar, J., Adey, W., Hetzinger, S., Zack, T., Moore, G.W.K., Wortmann, U.G., Williams, B. & Hou, A. 2017: Multicentennial record of Labrador Sea primary productivity and sea-ice variability archived in coralline algal barium. *Nature Communications* **8**, 15543, 10 pp., <http://dx.doi.org/10.1038/ncomms15543>
- D'Andrea, W.J., Huang, Y., Fritz, S.C. & Anderson, N.J. 2011: Abrupt Holocene climate change as an important factor for human migration in West Greenland. *Proceedings of the National Academy of Sciences of the United States of America* **108**(24), 9765–9769.
- Hacquebord, L. 2006. Two Centuries of Bowhead whaling around Spitsbergen; its impact on the Arctic avifauna. In: Ringstad, J.E. (ed.): *Whaling and History II, New Perspectives*, 87–94. Sandefjord: Kommandør Chr. Christensens Hvalfangst Museum.
- Humlum, O. 1999: Late-Holocene climate in central West Greenland: meteorological data and rock-glacier isotope evidence. *The Holocene* **9**(4), 581–594.
- Kuijpers, A., Mikkelsen, N., Ribeiro, S. & Seidenkrantz, M.-S. 2014: Impact of Medieval fjord hydrography and climate on the Western and Eastern Settlements in Norse Greenland. *Journal of the North Atlantic, Special Volume* **6**, 1–13.
- Leinenga, J.R. 1995: *Arctische walvisvangst in de achttiende eeuw, de betekenis van Straat Davis als vangstgebied*, 237 pp. PhD thesis, University of Groningen. Amsterdam: De Bataafsche Leeuw.
- Luterbacher, J., Werner, J.P. & Smerdon, J.E. 2016: European summer temperatures since Roman times. *Environmental Research Letters* **11**(2), 024001. <http://dx.doi.org/10.1088/1748-9326/11/2/024001>
- NKA Archives. Inspektoratet for Nordgrønland. Modtagne embedsdaagbøger & journaler: Arkiv Nr. 01.02 O7.20 10; Nr. 01.02. 07.20. 14; Nr. 01. O2. 07.20. 15; Nr. 01.02. 19.20. 3; Nr. 01. O2 73.45. 3. NKA 01.01/13.22/: 01.02/73.42/7; 01.02/13.22/9.
- Nansen, F. 1924: *Blant sel og bjørn. Min første Ishavs-ferd*, 285 pp. Kristiania: Jacob Dybwads Forlag.
- Reverdin, G. 2010: North Atlantic Subpolar Gyre Variability (1895–2009). *Journal of Climate* **23**, 4571–4584.
- Ribeiro, S., Moros, M., Ellegaard, M. & Kuijpers, A. 2012: Climate variability in West Greenland during the last 1500 years – evidence from a high-resolution marine palynological record from Disko Bay. *Boreas* **41**, 68–83.
- Seidenkrantz, M.-S., Roncaglia, L., Fischel, A., Heilmann-Clausen, C., Kuijpers, A. & Moros, M. 2008: Variable North Atlantic seesaw patterns documented by a late Holocene marine record from Disko Bay, West Greenland. *Marine Micropaleontology* **68**, 66–83.
- Vibe, C. 1967: Arctic animals in relation to climatic fluctuations. *Meddelelser om Grønland* **170**(5), 227 pp.

Authors' addresses

N.M., A.K. & S.F., *Geological Survey of Denmark and Greenland, Øster Voldgade 10, DK-1350 Copenhagen K, Denmark*. E-mail: NM@geus.dk.
 M.M. & I.S. *Greenland National Museum & Archives, Hans Egedesvej 8, 3900 Nuuk, Greenland*.
 A.E.L., *The Polar Museum, Søndre Tollbodgate 11B, 9008 Tromsø, Norway*.

The Greenland ice sheet – snowline elevations at the end of the melt seasons from 2000 to 2017

Robert S. Fausto and the PROMICE team*

The Arctic region is warming more rapidly than the global average (AMAP 2017) and it is well established that this warming is at least partially responsible for the Greenland ice sheet losing mass at an accelerating rate, raising concern worldwide (e.g. Kahn *et al.* 2015; Rahmstorf *et al.* 2015). It is essential to monitor the changes of the Greenland ice sheet to be able to assess the potential environmental, social and economic implications around the globe, and to provide decision-makers with reliable data. The annual mass-budget deficit of the Greenland ice sheet has grown over the past two decades due to increases in surface melting (Van den Broeke *et al.* 2017) and ice-flow acceleration (Kahn *et al.* 2015). Currently, and for the last two decades, the Greenland ice sheet is the single largest Arctic cryospheric contributor to global sea-level rise and the Greenland ice-surface melt rates are projected to increase as the Arctic continues to warm (AMAP 2017).

The snowline is here defined as the maximum elevation during the melt season at which snow remains from the previous accumulation season (Cogley *et al.* 2011). The snowline is a valuable climate indicator as its position integrates the competing effects of melt (increasing snowline elevation) and snow accumulation (decreasing snowline elevation). Thus the snowline provides a key holistic variable indicating climate change.

We have developed a methodology that determines snowline elevation utilising the moderate resolution imaging spectroradiometer (MODIS) sensor on the Terra satellite. The MODIS sensor produces a global dataset on a daily basis, with a resolution varying between 250 m and 1 km, in 36 bands covering the visible to thermal wavelengths. Using MODIS, we derived the maximum snowline altitude for the Greenland ice sheet for the years 2000–2017. We are producing a freely available, consistent dataset that provides an important tool for the monitoring of the long-term impact of climate change on the Greenland ice sheet. Direct comparison with field observations from automatic weather stations (AWSs) from the Programme for Monitoring of the Green-

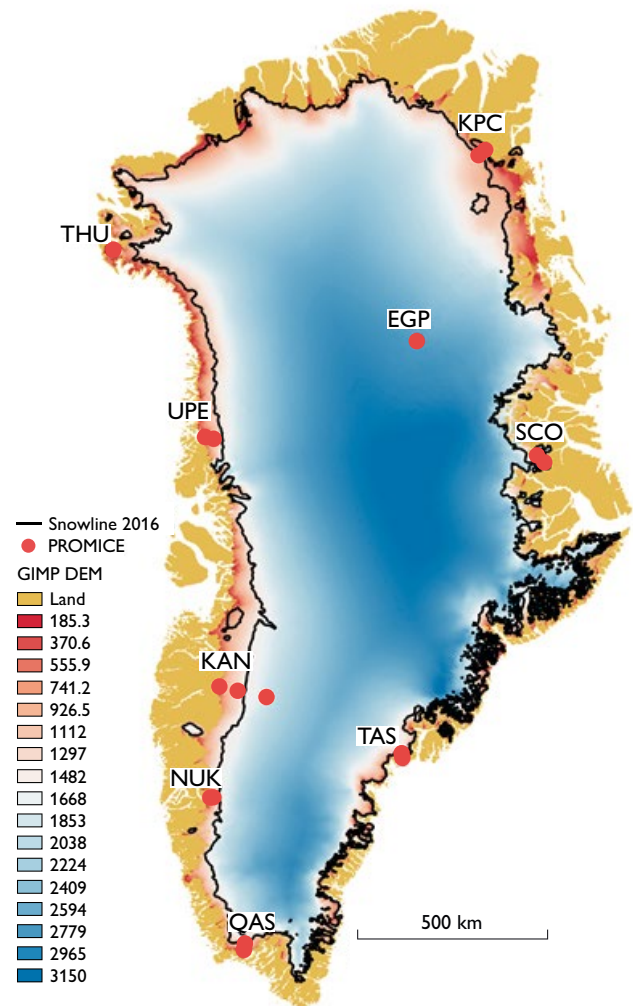


Fig. 1. Greenland map showing the location of PROMICE automatic weather stations and the 2016 snowline as derived from Terra satellite data using the moderate resolution imaging spectro-radiometer (MODIS) sensor. The locations of the ground-control automatic weather stations (PROMICE) are indicated. EGP: East GRIP. KAN: Kangerlussuaq. KPC: Kronprins Christian Land. NUK: Nuuk. QAS: Qassimiut. SCO: Scoresby Sund. TAS: Tasiilaq. THU: Thule. UPE: Upernavik. DEM: Digital elevation model. GIMP: Greenland ice mapping project.

* Signe B. Andersen, Andreas P. Ahlstrøm, Dirk van As, Jason E. Box, Daniel Binder, Michele Citterio, William Colgan, Konstanze Haubner, Karina Hansen, Nanna B. Karlsson, Kenneth D. Mankoff, Allan Ø. Pedersen, Anne Solgaard and Baptiste Vandecrux

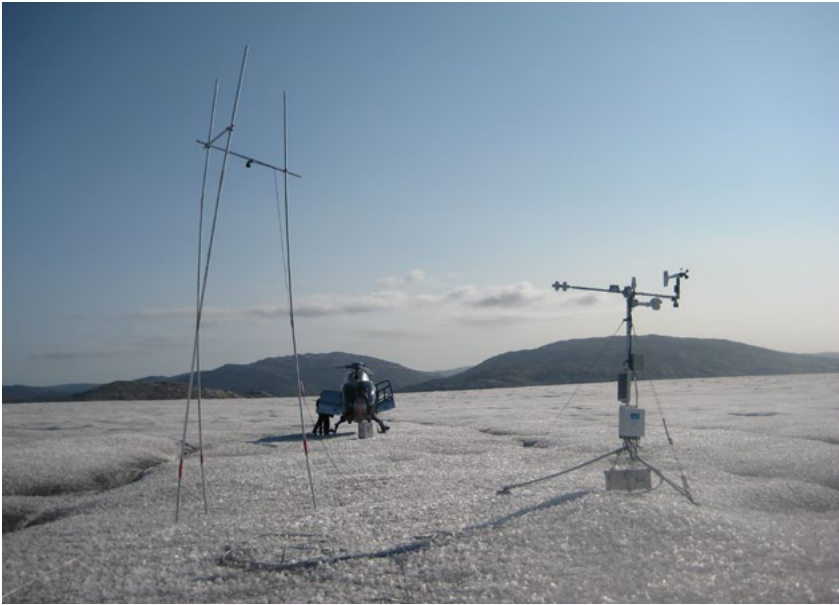


Fig. 2. South Greenland PROMICE automatic weather station at the end of the 2013 melt season. From the stakes to the left of the weather station, the amount of melt (*c.* 4 m) is directly visible. The melt is also measured with a pressure transducer system drilled into the ice.

land Ice Sheet (PROMICE) network validates the snowline dataset derived from MODIS. We use the services of the CryoClim internet portal, providing an operational and permanent service for long-term systematic climate monitoring of the cryosphere, to distribute our snowline product. More specifically, end-of-melt season, 1 km² resolution raster grids illustrating snow and bare-ice surfaces, and snowline shape files can be downloaded via CryoClim. Here, we describe the snowline classification algorithm, its validation and its inter-annual variations for 18 years spanning 2000–2017.

Snowline classification algorithm

We processed all MODIS MOD12KM and MOD03 scenes covering Greenland from late July to the beginning of September 2000–2017. We used the surface-type detection algorithm of Fausto *et al.* (2015) that distinguishes between bare-ice and snow surfaces. Fausto *et al.* (2015) uses normalized thresholds (Th) from calibrated radiances (MOD021KM) between the near-infrared band 5 (1230–1250 nm) and the visible band 10 (483–493 nm) with surface-type thresholds $Th_{dry\ snow} \leq 0.86$, $0.86 < Th_{melting\ snow} < 0.94$ and $Th_{glacier\ ice} \geq 0.94$. The classification algorithm is updated by implementing a new surface-type threshold to address a ‘noisy’ snow classification over the northern part of the ice sheet identified by Fausto *et al.* (2015). The algorithm is thus supplemented by $Th_{bare\ ice} > 265 - 2.1 \times LAT$, where LAT is latitude. $Th_{bare\ ice}$ is defined as:

$Th_{bare\ ice} = c_0 + c_1 \times b_1 + c_2 \times b_2 + c_3 \times b_3 + c_5 \times b_5 + c_7 \times b_7$
 where $c_0 = -0.0015$, $c_1 = 0.160$, $c_2 = 0.291$, $c_3 = 0.243$, $c_5 = 0.112$, $c_7 = 0.081$ and b_1 to b_7 designate band 1 to band 7.

Cloud-covered regions are removed using the MOD35_L2 dataset. Subsequently pixels are classified for every MODIS scene as either snow or bare ice for the whole Greenland ice sheet.

Daily classification scenes are aggregated to yield a maximum extent of bare ice to define an end-of-melt-season snowline. Snowlines from peripheral glaciers are generally excluded, and the snowline products are based on an algorithm success rate of over 95% classified pixels.

Validation

To help validate the MODIS data we make use of the PROMICE automatic weather station network that currently consists of two or three stations primarily in the ablation area in eight ice sheet regions. Each automatic weather station records a suite of meteorological and glaciological measurements, supplemented by e.g. surface-height changes due to accumulation or ablation (Fig. 1; Van As *et al.* 2016).

To validate the classified snowline elevation at the end of the melt season, we use the mass-budget values from the PROMICE weather stations (Fig. 2; e.g. Fausto *et al.* 2012) at different elevations to calculate the vertical surface mass-balance gradient for all eight PROMICE transects to determine the equilibrium line altitude (ELA, zero mass budget), for direct comparison with MODIS estimated snowline elevation (Fig. 1). AWS balance profiles from the Upernavik region, and those indicating an ELA above 2000 m are excluded as we find them unrealistic. The location of the upper AWS should be close to the actual ELA to get the best balance profiles. In total, we exclude 25% or 17 out of 67 balance profiles.

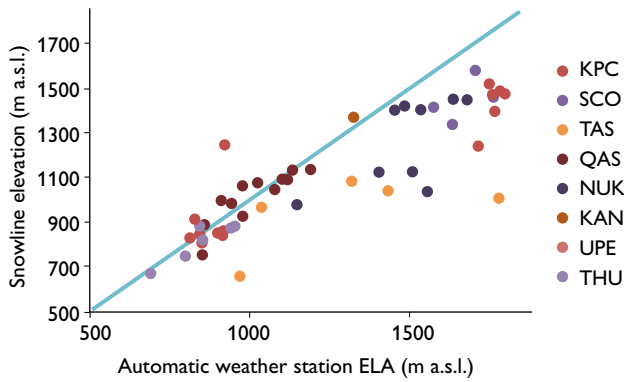


Fig. 3. The end-of-melt-season snowline elevation for 2000 to 2017 from MODIS vs. the PROMICE AWS-derived equilibrium line altitude (ELA). The blue line gives the 1:1 relation. The locations of the PROMICE automatic weather stations are shown in Fig. 1.

Figure 3 illustrates the performance of the MODIS end-of-melt-season snowline algorithm for all PROMICE regions in Greenland. The correlation ($r=90\%$, $p=0.0001$, $n=50$) and the root-mean-square error (RMSE=200 m) are reasonable as the ELA and snowline elevation can be different due to superimposed ice formation (Cogley 2011). The mean difference between snowline altitude and ELA is -104 m.

Results and discussion

Figure 1 illustrates the location of remotely sensed snowline plotted on top of the digital elevation model (DEM) from the Greenland Ice Mapping Project (GIMP, Howat *et al.* 2014). The snowline is easily visible in the southern, western, and northern parts of Greenland due to the relatively even terrain, while the snowline shows a more complicated pattern in the mountainous terrain in East Greenland (Fig. 1).

The snowline separates bare ice from snow areas and can therefore be used to document the change in bare-ice areas. We find the extent of bare-ice exposure to be increasing in the period 2000–2017 at an average rate of *c.* 500 km^2 per year (Fig. 4), which roughly corresponds to the size of the Danish island of Bornholm. This increase in the bare-ice area is insignificant, but it demonstrates a small average gain of melt over accumulation since 2000. The increasing trend in the bare-ice area is consistent with increasing Greenland mass loss due to surface processes (Van den Broeke *et al.* 2017). Both independent, *in situ* observations (Machguth *et al.* 2016) and remotely sensed observations (Hall *et al.* 2012; Tedesco *et al.* 2017) show that the Greenland melt area is expanding to higher elevations. Further, the increase in bare ice enhances the positive feedback mechanism of a darkening ice

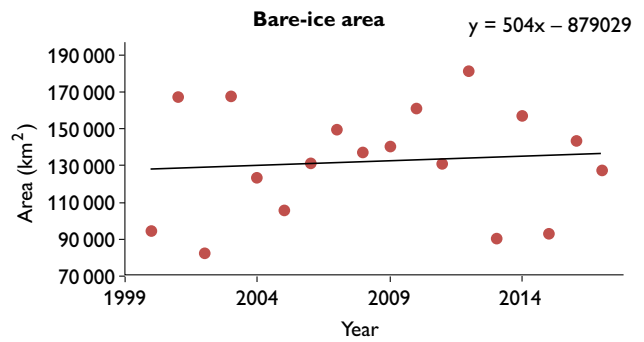


Fig. 4. End-of-melt-season bare-ice area for the Greenland ice sheet for the years 2000–2017.

sheet surface (ice is darker than snow), which affects the surface mass and energy balance of the Greenland ice sheet (Box *et al.* 2012). Figure 4 also illustrates the inter-annual variability of the 2000–2017 snowlines, which is highly dependent on the complicated seasonal weather systems around Greenland. For instance, the below average snowline of the snowy year of 2016/2017 is consistent with positive albedo anomalies that reduced melting in 2017 (Tedesco *et al.* 2017).

Uncertainties associated with the different surface-type detection are assessed with the ELAs derived from the AWS surface mass-budget observations. Figure 3 shows a significant correlation between the MODIS snowline and ELAs derived independently from PROMICE AWSs. A reason for the difference between the two can be that the MODIS data have a spatial resolution of 1 km^2 , pan-ice sheet coverage and quasi-daily temporal coverage, while the footprints of the *in situ* measurements are small ($5\text{--}50 \text{ m}^2$), and surface patchiness is clear in aerial photography (Stroeve *et al.* 2006).

Fausto *et al.* (2015) discuss an August anomaly in their monthly surface-type data set during the 2010–2014 period, illustrated by a noisy melting-snow classification in the northern ice sheet, which was most likely due to false classification. However, with the updated bare-ice threshold, we improve the detection of snow and ice surfaces (Fig. 1), visualised by a less noisy snow classification of snow in the northern part of the ice sheet, resulting in a more reliable climate indicator for Greenland.

Conclusions

Remotely sensed MODIS data can yield daily, automated classification of the Greenland ice sheet surface type (snow and ice). Validation indicates a high correlation (0.9) between MODIS-derived snowline altitudes and ELAs estimated from *in situ* measurements. The end-of-melt-season

snowline is useful as an ice-sheet climate indicator for the competing processes of surface accumulation and ablation, quantified by an average annual increase of *c.* 500 km² of the bare-ice area for the 2000–2017 period.

Acknowledgements

The Programme for Monitoring of the Greenland Ice Sheet (PROMICE) is funded by the Geological Survey of Denmark and Greenland (GEUS) and the Danish Ministry of Energy, Utilities and Climate under the Danish Cooperation for Environment in the Arctic (DANCEA), and is conducted in collaboration with DTU Space, Denmark's National Space Institute, and Asiaq (Greenland Survey). The NUK and KAN stations were/are (co-)funded by the Greenland Climate Research Centre (GCRC) and the Greenland Analogue Project (GAP), respectively. This study was funded by DK ESA-PRODEX under the CryoClim project.

References

- AMAP 2017: Snow, water, ice and permafrost in the Arctic (SWIPA) 2017, 269 pp. Oslo: Arctic Monitoring and Assessment Programme (AMAP).
- Box, J.E., Fettweis, X., Stroeve, J.C., Tedesco, M., Hall, D.K. & Steffen, K. 2012: Greenland ice sheet albedo feedback: thermodynamics and atmospheric drivers. *The Cryosphere* **6**, 821–839.
- Cogley, J.G., Hock, R., Rasmussen, L.A., Arendt, A.A., Bauder, A., Braithwaite, R.J., Jansson, P., Kaser, G., Moller, M., Nicholson, L. & Zemp, M. 2011: Glossary of glacier mass balance and related terms. IHP-VII Technical Documents in Hydrology **86**, IACS Contribution 2. Paris: UNESCO-IHP.
- Fausto, R.S., Van As, D. & PROMICE project team 2012: Ablation observations for 2008–2011 from the Programme for Monitoring of the Greenland Ice Sheet (PROMICE). *Geological Survey of Denmark and Greenland Bulletin* **26**, 25–28.
- Fausto, R.S. *et al.* 2015: Greenland ice sheet melt area from MODIS (2000–2014). *Geological Survey of Denmark and Greenland Bulletin* **33**, 97–100.
- Hall, D.K., Comiso, J.C., DiGirolamo, N.E., Shuman, C.A., Key, J.R. & Koenig, L.S. 2012: A satellite-derived climate-quality data record of the clear-sky surface temperature of the Greenland ice sheet. *Journal of Climate* **25**, 4785–4798.
- Howat, I.M., Negrete, A. & Smith, B.E. 2014: The Greenland Ice Mapping Project (GIMP) land classification and surface elevation datasets. *The Cryosphere* **8**, 1509–1518. <http://dx.doi.org/10.5194/tc-8-1509-2014>
- Khan, S.A., Aschwanden, A., Bjørk, A.A., Wahr, J., Kjeldsen, K.K. & Kjær, K.H. 2015: Greenland ice sheet mass balance: a review. *Reports on Progress in Physics* **78**, 046801, 26 pp. <http://dx.doi.org/10.1088/0034-4885/78/4/046801>
- Machguth, H., MacFerrin, M., van As, D., Box, J.E., Charalampidis, C., Colgan, W., Fausto, R.S., Meijer, H.A.J., Mosley-Thompson, E. & van de Wal, R.S.W. 2016: Greenland meltwater storage in firn limited by near-surface ice formation. *Nature Climate Change* **6**, 390–393. <http://dx.doi.org/10.1038/nclimate2899>
- Rahmstorf, S., Box, J., Feulner, G., Mann, M., Robinson, A., Rutherford, S. & Schaffernicht, E. 2015: Exceptional twentieth-Century slowdown in Atlantic Ocean overturning circulation. *Nature Climate Change* **5**, 475–480. <http://dx.doi.org/10.1038/nclimate2554>
- Stroeve, J.C., Box, J.E. & Haran, T. 2006: Evaluation of the MODIS (MOD10A1) daily snow albedo product over the Greenland ice sheet. *Remote Sensing of Environment* **105**, 155–171. <http://dx.doi.org/10.1016/j.rse.2006.06.009>
- Tedesco, M., Box, J.E., Cappelen, J., Fausto, R.S., Fettweis, X., Hansen, K., Mote, T., Sasgen, I., Smeets, C.J.P.P., van As, D., Velicogna, I. & van de Wal, R.S.W. 2017: Greenland ice sheet: contribution to the Arctic Report Card 2017.
- Van As, D., Fausto, R.S., Cappelen, J., Van de Wal, R.S.W., Braithwaite, R.J., Machguth, H. & PROMICE project team 2016: Placing Greenland ice sheet ablation measurements in a multi-decadal context. *Geological Survey of Denmark and Greenland Bulletin* **35**, 71–74.
- Van den Broeke, M.R., Box, J.E., Fettweis, X., Hanna, E., Noël, B., Tedesco, M., van As, D., van de Berg, W.J. & van Kampenhout, L. 2017: Greenland ice sheet surface mass loss: recent developments in observation and modelling. *Current Climate Change Reports* **3**, 345–356. <http://dx.doi.org/10.1007/s40641-017-0084-8>

Authors' address

Geological Survey of Denmark and Greenland, Øster Voldgade 10, DK-1350 Copenhagen K, Denmark. E-mail: rsf@geus.dk.

Initial field activities of the Camp Century Climate Monitoring Programme in Greenland

William Colgan, Allan Pedersen, Daniel Binder, Horst Machguth, Jakob Abermann and Mike Jayred

Camp Century was a military base constructed by the US Army Corps of Engineers in 1959 in the near-surface layers of the Greenland ice sheet at 77.13°N, 61.03°W and 1886 m above sea level (Clark 1965; Fig. 1). The base housed up to 200 military personnel and was continuously occupied until 1964. After three years of additional seasonal operation, the base was abandoned with minimal decommissioning in 1967. Recent Danish scholarship has documented the political and military history of Camp Century in detail (Nielsen & Nielsen 2016).

In 2016, the Geological Survey of Denmark and Greenland (GEUS) participated in a multi-nation study that presented regional climate simulations that suggested the ice-sheet surface mass balance at Camp Century may change from net accumulation to net ablation by 2100 under the UN Intergovernmental Panel on Climate Change RCP8.5 ‘business-as-usual’ climate scenario. However, according to Colgan *et al.* (2016), net accumulation would persist beyond 2100 at Camp Century under the climate-change mitigation characterised by RCP4.5, an approximately ‘Paris Agreement’ climate scenario.

In 2017, in response to concerns from the Government of Greenland over the potential to remobilisation of contaminants from Camp Century within the next century, the Government of Denmark established a programme for long-term climate monitoring and detailed one-time surveying of the debris field at Camp Century (Colgan *et al.* 2017). This report describes the initial field activities of the Camp Century Climate Monitoring Programme in the context of the four programme goals:

1. To continuously monitor relevant climate variables, including the depth to which meltwater percolates, at the Camp Century site.
2. To regularly update annual likelihoods of meltwater interacting with abandoned materials at the Camp Century site over the next century.
3. To map the estimated spatial extent and vertical depth of abandoned wastes across the Camp Century site.
4. To publicly report all findings from the Camp Century Climate Monitoring Programme in a timely manner.

Field logistics

Field activities of the Camp Century Climate Monitoring Programme were initiated in summer 2017, when a six-person team spent two weeks at the Camp Century site (19 July to 3 August). There is no abandoned infrastructure visible at the ice-sheet surface at Camp Century (Fig. 2). Debris field location, as well as zones of restricted drilling depth, were estimated prior to field work (Fig. 3). This was done by georeferencing a historical site map using a single tie-point, the location of the original drill tower, corrected for motion since its last precise survey in 1986 (Gundestrup *et al.* 1987). The 2017 summer camp, which consisted of three common

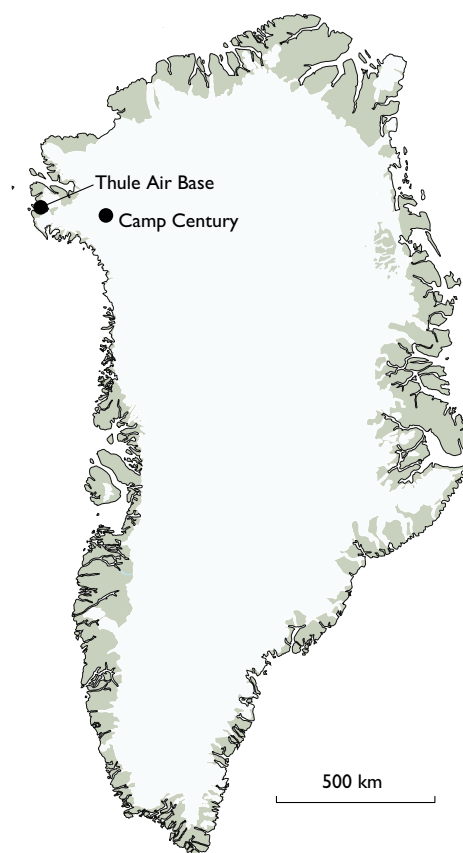


Fig. 1. Location of Camp Century that was constructed by the US Army Corps of Engineers in 1959 in the Greenland ice sheet. Camp Century was abandoned in 1967.



Fig. 2. The temporary ice-sheet camp at 1600 UTC on 20 July 2017. The camp consisted of three common tents and six personal tents. There was persistent cloud cover with frequent storm conditions and a mean wind speed of 8.8 m/s. No abandoned infrastructure is visible at the ice-sheet surface; the entire debris field is now subsurface as a result of net snow accumulation since closure.

tents and six personal tents, was established within the debris field, approximately aligned with the location of post-closure summer camps (Kovacs 1970). Although decamped entirely, the footprint of the 2017 summer camp will likely be visible in subsequent ice-penetrating radar surveys due to the formation of massive wind-sculpted snowdrifts around it.

During field work, there was persistent cloud cover with frequent storm conditions. The mean wind speed was 8.8 m/s, and the maximum 1 hour mean wind speed was 18.3 m/s (Beaufort 8). Thule Air Base, located approximately 200 km west, served as logistical base for the field work. A ski-equipped Twin Otter aircraft was used to transport 3200 kg of equipment and supplies to and from the ice sheet. Field work consisted of installing three automated instrument stations, drilling boreholes for instrument installation and firn sampling, surveying velocity stakes, and collecting ice-penetrating radar

profiles. Of the 175 m firn core drilled, 135 m were analysed in the field and 40 m were transported to Copenhagen for more detailed radionuclide analysis by the Center for Nuclear Technologies at the Technical University of Denmark.

Instruments and data

Climate measurements were initiated using automated weather station technology previously developed by GEUS. The automatic weather station design has a proven record of more than 175 station-years of deployment in Greenland since its introduction in 2007 (Citterio *et al.* 2015). The primary weather station at Camp Century (CEN) measures air temperature and humidity, wind speed and direction, atmospheric pressure, upward and downward shortwave and long-wave radiation, subsurface (snow/ice) temperatures to 10 m

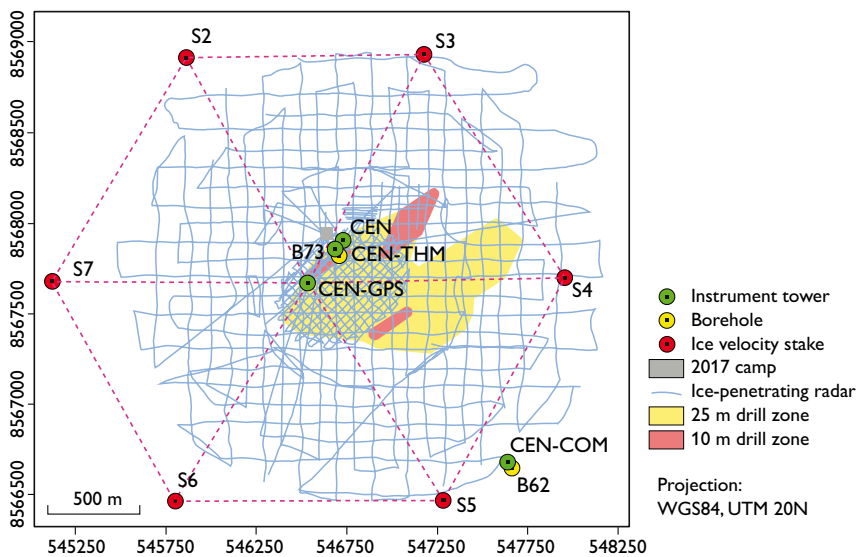


Fig. 3. Overview of initial field activities at Camp Century. Recently constructed instrument towers refer to the primary weather station ('CEN'), the supplementary thermistor station (CEN-THM), the supplementary compaction station (CEN-COM) and the supplementary global positioning system (CEN-GPS; to be installed). Boreholes refer to the 73 (B73) and 62 (B62) m firn cores. Restricted drill zone depths were assessed based on georeferencing of a historical as-built site map (Kovacs 1970).

depth, and snow depth, as well as diagnostic parameters such as battery voltage. The temperature of the relatively porous near-surface ice-sheet layer known as firn is also measured by a supplementary thermistor station (CEN-THM) to a depth of 73 m, which approximates local pore close-off depth (Fig. 3).

Ice-sheet structure was analysed with 73 and 62 m deep firn cores, hereafter referred to as B73 and B62. Firn density and melt percentage were measured to a minimum depth of 62 m at locations inside and outside the debris field (Fig. 4). A third automatic station was deployed to measure the compaction rate of snow into ice, or vertical strain, over the 0 to 5 m, 0 to 20 m and 1 to 62 m depth ranges. This third automatic station, the supplementary compaction station (CEN-COM), is located outside the debris field. All three automatic stations satellite-transmit their measurements in near-real-time to www.campcenturyclimate.dk. A fourth station that records observations from the global positioning system (CEN-GPS) will be installed to continuously monitor ice flow. These climate and ice data will be used to calibrate and validate future simulations of firn evolution.

Preliminary interpretation

The measurements from the automated weather station (CEN) record that midday air temperature exceeded 0°C for three days during the operational period of the 2017 summer camp. The maximum one-hour mean air temperature was

1.8°C. Under these warm conditions, surface melt quickly froze to moving drill parts when the drill was lowered into cold winter firn. This necessitated a two-day suspension of drilling. Preliminary analysis of the B73 deep thermistor measurements, located within the debris field, indicates that the annual temperature cycle in near-surface snow and ice temperatures penetrates to *c.* 12 m depth (Fig. 4). Beyond this depth, year-round firn temperatures appear to remain *c.* -24°C. In summer 2017, there was limited meltwater production and refreezing, with no apparent change in firn temperature beyond this annual diffusion cycle.

Preliminary analysis of near-surface firn structure indicates that refrozen meltwater layers are readily identifiable in the uppermost 15 m of the firn. The largest of these layers is *c.* 8 cm thick, which represents the melt-and-refreeze of *c.* 25% of annual snowfall (Buchardt *et al.* 2012). The firn cores suggest that meltwater movement beyond the annual layer is unlikely. Near-surface firn densities are similar both inside and outside the debris field to 32 m depth (Fig. 4). Between 32 and 35 m depth, firn density is significantly greater within the debris field. This high-density layer is slightly discoloured in appearance and likely reflects enhanced compaction and pollution during the *c.* 1960–1964 active period. Below this active layer, firn densities are similar inside and outside the debris field. After drilling B73 through the high-density active layer, pressurised hydrocarbon vapours vented from the borehole until it was backfilled. Mobile hydrocar-

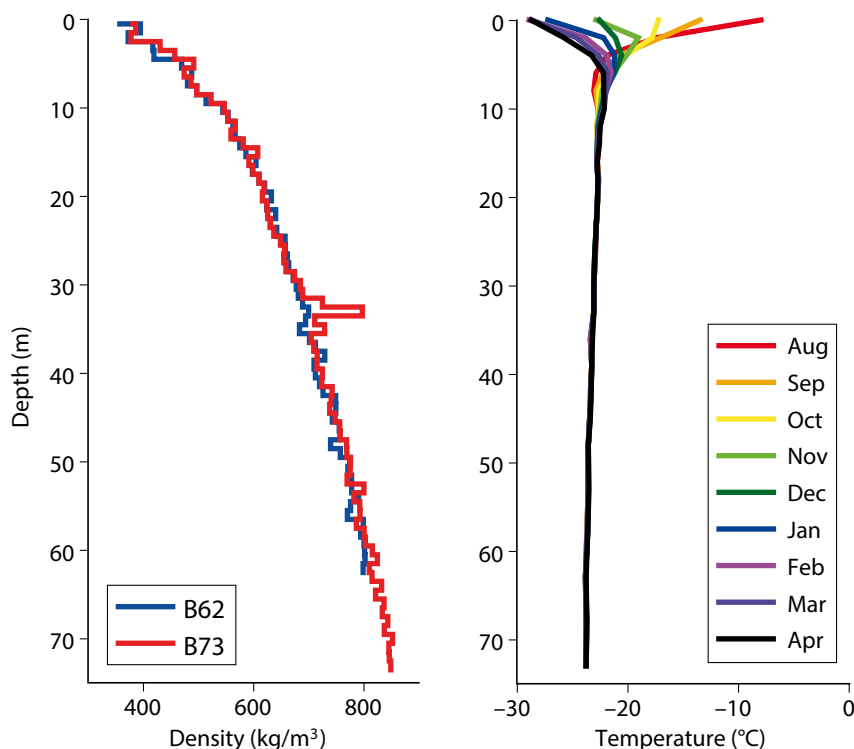


Fig. 4. **Left:** Near-surface firn density profiles measured both inside (B73) and outside (B62) the debris field. The high-density layer between 32 and 35 m depth within the debris field likely reflects enhanced compaction during the *c.* 1960–1964 active period. **Right:** Near-surface snow/ice temperatures at B73 inside the debris field. The annual temperature cycle penetrates to *c.* 12 m depth, with year-round firn temperatures remaining *c.* -24°C below this depth.

bon vapours were not anticipated, and vapour-tight equipment was not available on-site to opportunistically sample these vapours.

Radar survey

Data from the one-time summer 2017 radar survey are being analysed to perform a detailed assessment of the horizontal extent and vertical range of the debris field. 100 and 250 MHz ice-penetrating radar data were collected by cross-country skiing in a dense grid pattern over the Camp Century debris field (Fig. 3). The radar profiles, each tagged with global positioning system coordinates, will be available on the programme website. A preliminary field analysis of the ice-penetrating radar data shows that the sub-surface debris field is *c.* 2 km in diameter, with debris ranging between *c.* 20 and 100 m depth. This ice-penetrating radar data will permit improved geo-referencing of historical as-built site maps, via precisely positioning key subsurface infrastructure features, which will facilitate delineating the debris field beyond the extent recorded by as-built site maps.

Programme outlook

This report describes the initial field activities of the Camp Century Climate Monitoring Programme in the context of programme goals. Near-real-time climate and ice measurements from automated stations, ice-penetrating radar profiles, as well as programme outreach materials and publications, can be accessed at www.campcenturyclimate.dk. Subsequent field work at Camp Century will be undertaken, as needed, to service deployed instrumentation. During these subsequent site revisits, ice-velocity stakes will be resurveyed to precisely measure the relatively slow (<5 m/yr) ice velocity over several years.

Data analysis, in support of observationally-constrained numerical simulations of the evolution of meltwater and firn, is the major programme focus. While climate change now gives Camp Century previously unanticipated social significance, the sustained effort of the Camp Century Climate Monitoring Programme will continue to provide Danish

and Greenlandic stakeholders open access to relevant *in situ* measurements and model projections. Refined knowledge of the spatial extent and vertical range of the debris field, as well as the changes in firn structure and meltwater production anticipated under climate change, will inform science-based discussions of the shifting fate of Camp Century.

Acknowledgements

The Camp Century Climate Monitoring Programme is jointly funded by GEUS and the Danish Cooperation for Environment in the Arctic (DANCEA) within the Danish Ministry for Energy, Utilities and Climate. J.A. was supported by the Greenlandic Ministry of Independence, Foreign Affairs and Agriculture. The 2017 field team (W.C., A.P., D.B., H.M., J.A. and M.J.) warmly thank Danish liaison officers Kim Marchuard Mikelsen and Jens Alsing for logistical assistance at Thule Air Base.

References

- Buchardt, S., Clausen, H., Vinther, B. & Dahl-Jensen, D. 2012: Investigating the past and recent $\delta^{18}\text{O}$ -accumulation relationship seen in Greenland ice cores. *Climate of the Past* **8**, 2053–2059.
- Clark, E.F. 1965: Camp Century evolution of concept and history of design, construction and performance. Cold Regions Research and Engineering Laboratory. Technical Report **174**, 69 pp.
- Citterio, M. *et al.* 2015: Automatic weather stations for basic and applied glaciological research. Geological Survey of Denmark and Greenland Bulletin **33**, 69–72.
- Colgan, W., Machguth, H., MacFerrin, M., Colgan, J.D., van As, D. & MacGregor, J.A. 2016: The abandoned ice sheet base at Camp Century, Greenland, in a warming climate. *Geophysical Research Letters* **43**, 8091–8096.
- Colgan, W., Andersen, S.B., van As, D., Box, J.E. & Gregersen, S. 2017: New programme for climate monitoring at Camp Century, Greenland. Geological Survey of Denmark and Greenland Bulletin **38**, 57–60.
- Gundestrup, N.S., Clausen, H.B., Hansen, B.L. & Rand, J. 1987: Camp century survey 1986. *Cold Regions Science and Technology* **14**, 281–288.
- Kovacs, A. 1970: Camp Century a pictorial overview June 1969. Cold Regions Research and Engineering Laboratory, Special Report **150**, 59 pp.
- Nielsen, H. & Nielsen, K. 2016: Camp Century – cold war city under the ice. In: Doel, R., Harper, K. & Heymann, M. (eds): *Exploring Greenland: cold war science and technology on ice*, 195–216. New York: Palgrave Macmillan US.

Authors' addresses

W.C., A.P., D.B., *Geological Survey of Denmark and Greenland, Øster Voldgade 10, DK-1350 Copenhagen K, Denmark*. E-mail: wic@geus.dk.

H.M., *University of Fribourg, Avenue de l'Europe 20, SX 1700 Fribourg, Switzerland*.

J.A., *Asiaq Greenland Survey, Qatserisut 8, DK 3900 Nuuk, Greenland*.

M.J., *University of Wisconsin, Madison, Wisconsin 53706, USA*.

Circum-Greenland, ice-thickness measurements collected during PROMICE airborne surveys in 2007, 2011 and 2015

Louise Sandberg Sørensen, Sebastian B. Simonsen, René Forsberg, Lars Stenseng, Henriette Skourup, Steen Savstrup Kristensen and William Colgan

The Greenland ice sheet has experienced an average mass loss of 142 ± 49 Gt/yr from 1992 to 2011 (Shepherd *et al.* 2012), making it a significant contributor to sea-level rise. Part of the ice-sheet mass loss is the result of increased dynamic response of outlet glaciers (Rignot *et al.* 2011). The ice discharge from outlet glaciers can be quantified by coincident measurements of ice velocity and ice thickness (Thomas *et al.* 2000; van den Broeke *et al.* 2016).

As part of the Programme for monitoring of the Greenland Ice Sheet (PROMICE; Ahlstrøm *et al.* 2008), three airborne surveys were carried out in 2007, 2011 and 2015, with the aim of measuring the changes in Greenland ice-sheet thicknesses. The purpose of the airborne surveys was to collect data to assess the dynamic mass loss of the Greenland ice sheet (Andersen *et al.* 2015). Here, we present these datasets of observations from ice-penetrating radar and airborne laser scanning, which, in combination, make us able to determine the ice thickness precisely. Surface-elevation changes between surveys are also presented, although we do not provide an in-depth scientific interpretation of these.

Instrumentation

All three surveys were conducted using the same Air Greenland/Norlandair De Havilland DHC-6 Twin Otter aircraft, currently registered as TF-POF. This Twin Otter has been modified in such a way that part of the fuselage can be removed in the rear cargo hole providing an unobstructed view of the surface below the aircraft when airborne. The precise position of the aircraft (and instruments) is tracked by three geodetic dual-frequency GPS receivers each connected to one of two GPS antennas mounted on top of the aircraft. The orientation of the instruments is monitored by an inertial navigation system (INS). The primary INS is of the type Honeywell H-764G. During the last two flights, we also installed a back-up INS of the type OxtS Inertial+2.

For measuring snow- or ice-surface elevations, a near infrared, airborne laser scanner (ALS; Forsberg *et al.* 2001) was mounted in the rear cargo hole, alongside the INSs. The ALS flown on the Twin Otter in 2007 was of the type Riegl LMS-Q140i-60, which was upgraded to a Riegl LMS-Q240i in 2011 and 2015. In 2007 and 2011, a 60 MHz coherent ice-penetrating radar, developed at the Technical University of Denmark (DTU), was also mounted to measure bedrock topography (Christensen *et al.* 2000).

Survey design

The survey flight path was designed as a polygon to encircle the entire Greenland ice sheet where the surface of the ice

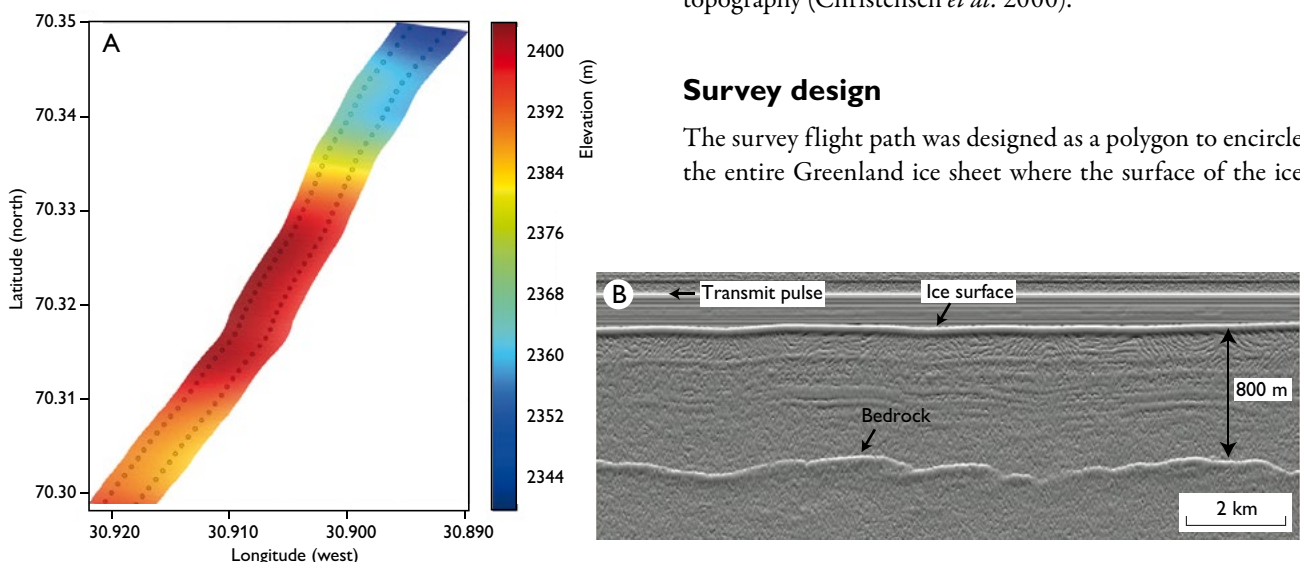


Fig. 1. **A:** Example of full-resolution versus reduced-resolution (circles) airborne laser scanner (ALS) data. **B:** Example of radargramme with a clear bedrock reflector.

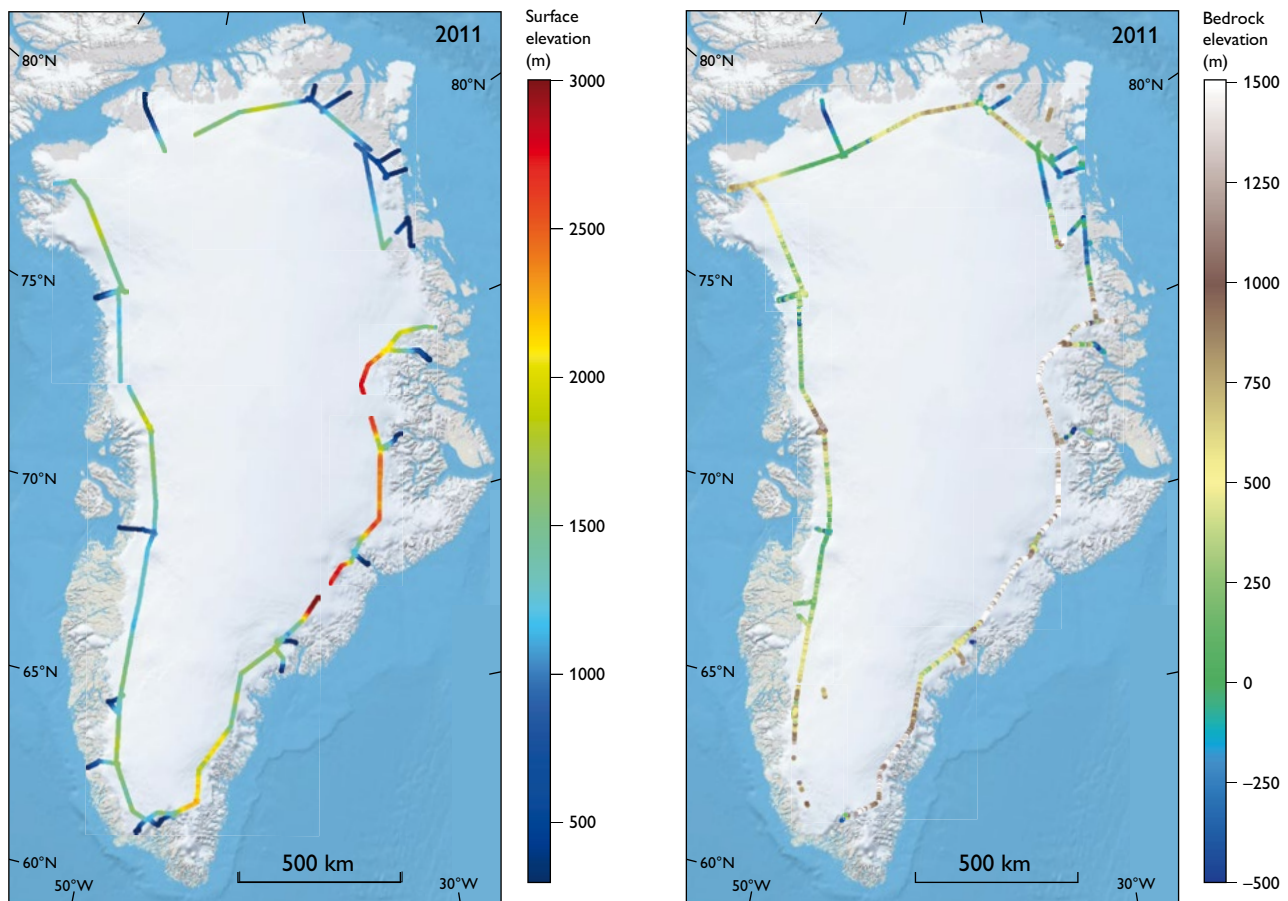


Fig. 2. **A:** Surface elevations along the PROMICE circum-Greenland flights in 2011. **B:** Bedrock elevations along the PROMICE circum-Greenland flights in 2011.

is at an elevation of *c.* 1700 m above sea level, as well as to include survey lines over the centerline of several main outlet glaciers. The surveys have been carried out at four-year intervals (2007, 2011 and 2015). The planned flight path in 2007 left a data gap on the east coast (from *c.* 72N to *c.* 74N) which was bridged during the 2011 and 2015 surveys.

All three surveys were planned to be carried out in August, as this timing represents the end of the melt season and ensures that the changes observed in surface elevations are not affected by individual accumulation events. Due to bad weather conditions in August 2015, half of the survey (the part from Constable Pynt in East Greenland clockwise to Kangerlussuaq in West Greenland) was carried out in October. The late acquisition of these data thus results in a potential bias of individual accumulation events due to snowfall in this dataset compared to the surveys in 2007 and 2011. As the flight path from 2011 was repeated in 2015, and since the bedrock elevation is not expected to change within this time frame, it was decided not to utilise the ice-penetrating radar on the last survey in 2015.

Surface-elevation data

The ALS operates in the near-infrared wavelength band, which is reflected from the snow or ice surface. This means that data can only be acquired during periods without clouds or fog below the aircraft. The sampling frequency of the ALS instrument is 10 kHz, resulting in 40 across-track scan lines per second. Each of these scan lines consists of 250 individual elevation measurements on-ground. The scan angle of 60° and the typical flight height of *c.* 300 m result in a swath width on ground of *c.* 300 m with *c.* 1 m resolution.

The processing of the ALS data combines the raw ALS data with the positioning data from the GPS and altitude data from the INS. Post-processing of the data includes visual inspection to filter out laser reflections from clouds. The positional uncertainty in both latitude and longitude is estimated to be ± 1 m, while the elevation uncertainty is estimated from track cross-over differences to be ± 0.05 to 0.1 m over flat surfaces.

To reduce the file size and to create a dataset which is more comparable to the resolution of the bedrock data, the full-resolution ALS data have been reduced to a spatial resolution of *c.* 100 m. This has been done through simple averaging.

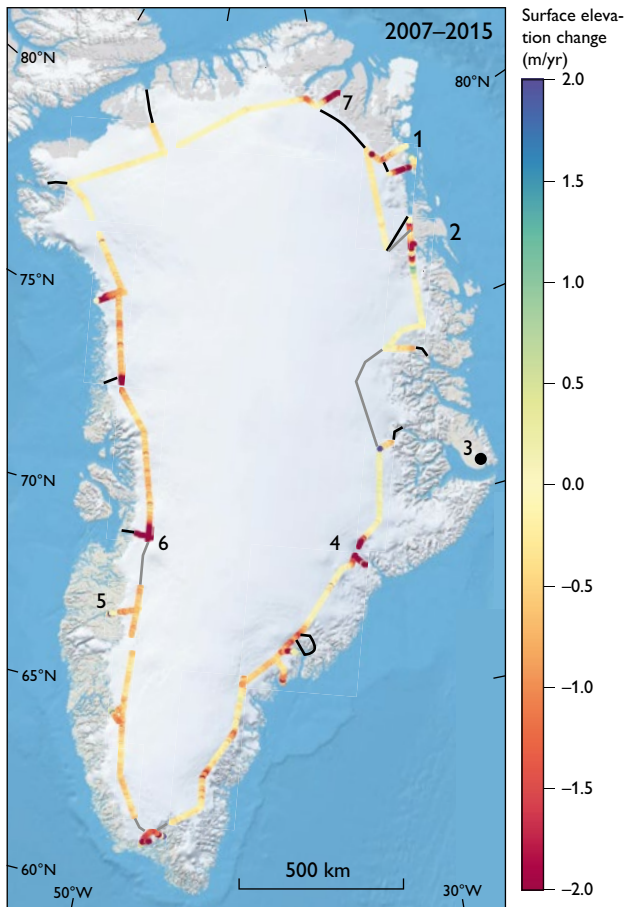


Fig. 3. Mean annual surface-elevation changes between 2007 and 2015 along the PROMICE circum-Greenland flight-paths. The part of the flight track for which only 2007 data are available is indicated in black, while 2015-only is indicated in grey. 1: Nioghalvfjærdsfjorden. 2: Storstrømmen. 3: Constable Pynt. 4: Kangerlussuaq Gletscher. 5: Kangerlussuaq. 6: Jakobshavn Isbræ. 7: Hagen Bræ.

ing of available height measurements along and across track. An example of full-resolution versus reduced-resolution data is shown in Fig. 1A. The data are compiled in one file per year (ALS_YYYY.ave) and can be downloaded from <http://promice.dk/Download.Airborne.html>. As an example, the elevations from 2011 are shown in Fig. 2A.

Bedrock-elevation data

The ice-penetrating data acquisition consists of transmitting pulses at a pulse repetition frequency of 10 kHz (i.e. sampling in the flight direction) and sampling the returned echo at 75 MHz, which results in 4096 samples per transmitted pulse. While internal scattering masks the desired echo, reflection and absorption within the ice sheet reduce the strength of the returned echo. Substantial processing is therefore carried

out to produce a radargramme that enhances the detection of the echo from the bottom of the ice-sheet.

A semi-automatic layer detection program is used to digitalise the surface and bedrock layers individually. In some areas, primarily near the ice margin in South Greenland, the radar was not able to detect the bedrock due to heavily crevassed ice or water present within the ice. Figure 1B shows a good example of a radargramme where a bottom echo was obtained. Based on radar system setup, vertical uncertainty in radar-derived ice-sheet bed elevation is estimated to be ± 35 m, which is confirmed by the cross-over differences between the two surveys.

The data are compiled in one file per year (ARS_YYYY.ave), which is also available for download from <http://promice.dk/Download.Airborne.html>. As an example, the bedrock elevations from 2011 are shown in Fig. 2B.

Surface-elevation changes

Having three surveys of surface elevations spanning eight years enables us to derive and analyse surface elevation changes along the flight lines. In Fig. 3, we show the mean annual surface-elevation changes between August 2007 and August/October 2015. The map was generated by computing height differences between any points in the two (reduced resolution) datasets for the two years. Height differences are computed only if the points are located not more than 200 m apart. By knowing the exact date of the survey, the rate of surface-elevation change can be computed. In the map in Fig. 3, the part that was only flown in 2007 is plotted with black, while the parts only surveyed in 2015 are shown in grey. There are some clearly visible gaps: One leg of the flight line is missing in north-eastern Greenland from Nioghalvfjærdsfjorden to Hagen Bræ and similarly and a part of the line is also absent south of Jakobshavn Isbræ. The gap in the north is caused by gaps in the 2015 dataset due to time and weather constraints. The gap south of Jakobshavn Isbræ is due to cloud cover in 2007.

Figure 3 shows that the mean annual elevation changes in the period 2007–2015 is clearly dominated by thinning with some main outlet glaciers such as Jakobshavn Isbræ and Kangerlussuaq Gletscher thinning rapidly. Only a few places along the flight line are associated with thickening, e.g. at Storstrømmen. The sections of the flight path in the south-eastern parts that actually show modest thickening might be a result of accumulation since these parts of the 2015 survey were mapped in October after some snowfall in the area.

Elevation change data, such as presented here, are scientifically very valuable e.g. to validate satellite data and ice-sheet models. Furthermore, the data presented here represents an important supplement to the heights and height differences

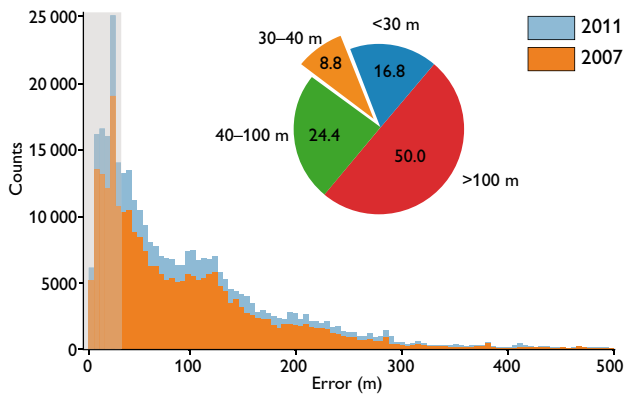


Fig. 4. Histograms showing the errors of the BedMachine bed topography grid in all the points where PROMICE bedrock elevation data are available. The grey area shows the <35 m interval (uncertainty in the bedrock data). The pie chart shows to what extent the BedMachine model error is 0–30 m, 30–40 m, 40–100 m and more than 100 m.

available from the NASA Operation IceBridge field surveys (Krabill *et al.* 2009; Krabill 2014) as the flight lines cover different areas, and also our measurements are made at the end of the melt season while Operation IceBridge data are collected mainly in the spring.

Comparison to BedMachine v3 bedrock elevations

The bedrock elevation dataset described above also represents a valuable legacy dataset that can be used by a wider scientific community. Knowledge of bedrock elevations in Greenland is essential in, e.g. ice-discharge studies and ice-sheet modelling. One widely used bedrock topography model is the one available in BedMachine v3 (Morlighem *et al.* 2017) which is based on the conservation of mass and constrained by available measurements. The BedMachine v3 model is provided together with an error map, which shows how the error increases with increasing distance to measurement points. To evaluate whether the PROMICE dataset can potentially contribute to an improvement of the BedMachine model in the future, we have extracted the BedMachine error values for all the 2007 and 2011 bedrock elevations in the PROMICE datasets. The two corresponding histograms in Fig. 4 show that in *c.* 50% of the data locations the error in the BedMachine v3 model is greater than 100 m, indicating that

the PROMICE dataset with an uncertainty of ± 35 m could indeed contribute positively to a future, improved version of the model. It may also be noted that only 25% of the BedMachine data are related with similar or lower errors than the PROMICE dataset.

Acknowledgements

This is a publication in the framework of The Programme for Monitoring of the Greenland Ice Sheet (PROMICE) – a Danish government initiative funded through the Danish Cooperation for Environment in the Arctic (DANCEA).

References

- Ahlström, A. & the PROMICE team 2008: A new programme for monitoring the mass loss of the Greenland ice sheet. *Geological Survey of Denmark and Greenland Bulletin* **15**, 61–64.
- Andersen, M. *et al.* 2015: Basin-scale partitioning of Greenland ice sheet mass balance components (2007–2011). *Earth and Planetary Science Letters* **409**, 89–95.
- Christensen, E.L., Reeh, N., Forsberg, R., Jørgensen, J.H., Skou, N. & Woelders, K. 2000: A low-cost glacier-mapping system. *Journal of Glaciology* **46**, 531–537.
- Forsberg, R., Keller, K. & Jacobsen, S.M. 2001: Laser monitoring of ice elevations and sea-ice thickness in Greenland. *International Archives of Photogrammetry and Remote Sensing* **34**, 163–168.
- Krabill, W.B. 2014: IceBridge ATM L2 Icesn Elevation, Slope, and Roughness. Boulder, Colorado, USA. <http://nsidc.org/data/ilatm2.html> (NASA Distributed Active Archive Center at the National Snow and Ice Data Center).
- Krabill, W.B. *et al.* 2009: Operation Ice Bridge =verview and results from aircraft laser altimetry. American Geophysical Union, Fall Meeting 14–18 December 2009. San Francisco: Abstract 3 pp.
- Morlighem, M. *et al.* 2017: BedMachine v3: Complete bed topography and ocean bathymetry mapping of Greenland. From multibeam echo sounding combined with mass conservation. *Geophysical Research Letters* **44**, 11051–11061, <http://dx.doi.org/10.1002/2017GL074954>
- Rignot, E., Velicogna, I., van den Broeke, M.R., Monaghan, A. & Lenaerts, J.T. 2011: Acceleration of the contribution of the Greenland and Antarctic ice sheets to sea level rise. *Geophysical Research Letters* **38**, L05503.
- Shepherd, A. *et al.* 2012: A reconciled estimate of ice-sheet mass balance. *Science* **338**, 1183–1189.
- Thomas, R.R., Akins, T., Csatho, B., Fahnestock, M., Gogineni, P., Kim, C. & Sonntag, J. 2000: Mass balance of the Greenland ice sheet at high elevations. *Science* **289**, 426–428.
- van den Broeke, M.R., Enderlin, E.M., Howat, I.M., Kuipers Munneke, P., Noël, B.P.Y., van de Berg, W.J., van Meijgaard, E. & Wouters, B. 2016: On the recent contribution of the Greenland ice sheet to sea level change. *The Cryosphere* **10**, 1933–1946. <http://dx.doi.org/10.5194/tc-10-1933-2016>

Authors's addresses

L.S.S., S.B.S., R.F., L.S. & H.S., *Technical University of Denmark, DTU Space, Geodynamics department, DK-2800 Kongens Lyngby, Denmark.*

E-mail: slss@space.dtu.dk.

S.S.K., *Technical University of Denmark, DTU Space, Microwave & remote sensing department, DK-2800 Kongens Lyngby, Denmark.*

W.C., *Geological Survey of Denmark and Greenland, Øster Voldgade 10, DK-1350 Copenhagen K, Denmark.*

Observationally constrained reconstruction of 19th to mid-20th century sea-ice extent off eastern Greenland

Danielle A.M. Hallé, Nanna B. Karlsson, Anne Munck Solgaard and Camilla S. Andresen

Arctic sea ice has a significant impact on the global radiation budget, oceanic and atmospheric circulation and the stability of the Greenland ice sheet (Vaughan *et al.* 2013). Prior to the era of aircraft and satellite, information on sea-ice extent relied on observations from ships and people living at the coast. This information is a valuable contribution to better understand the history of sea ice. However, the information exists in a range of formats, e.g., sea-ice extent before the late 1800s is typically reported in the literature as an annual index from a single geographical point or as hand-drawn maps. This makes it difficult to assess and compare data across time and space. The combination of digitised historical maps and single-point data makes the information more accessible and provides a record that can help understand the dynamics and processes of the climate and its interactions with the cryosphere (Chapman & Walsh 1993).

In this study, maps of sea-ice extent by Koch (1945) were digitised. We use these maps in combination with sea-ice charts from the Danish Meteorological Institute (DMI) and Koch's sea-ice index from 1820 to 1939, to map estimated sea-ice extent between Iceland and Greenland going back to 1821. This information has not been included in even the most recent databases of Arctic sea ice (Walsh *et al.* 2015, 2017). Furthermore, we extract time series of sea-ice extent at a number of locations and investigate the relationship between them.

Our observation area is along eastern Greenland, between the southern tip of Greenland at 59°46'N northwards to 77°21'N.

Digitising Lauge Koch's maps

Koch's (1945) monograph comprises over 400 small maps that show monthly sea-ice extent from 1877 to 1939. We digitised the maps for the months in those years that contained sea ice. The data used by Koch were compiled by Thoroddsen (1884) from annals that describe the sea-ice extent off Iceland. The final result is 134 digital maps showing sea-ice extent from 1877 to 1939. These maps are available for download at <http://dx.doi.org/pangaea.de/10.1594/PANGAEA.887453>

Reconstructing the extent of sea ice between Greenland and Iceland from Koch's index

Koch's monograph contains a sea-ice index that categorises the width of the ice belt off Iceland, based on observations from 1820 to 1939. The Koch index has three main categories from A to C and subcategories from 1 to 3 for each letter (Table 1). A represents a narrow ice belt year, B is a broad ice belt year and C depicts a very broad ice belt year. The number next to the letter indicates how far the sea ice spread off Iceland. A subcategory value of 1 means the ice did not reach Iceland, 2 means it had spread along the northern coast and 3 indicates it had spread down as far as the southern coast of Iceland. Koch described an A year as the least severe sea-ice

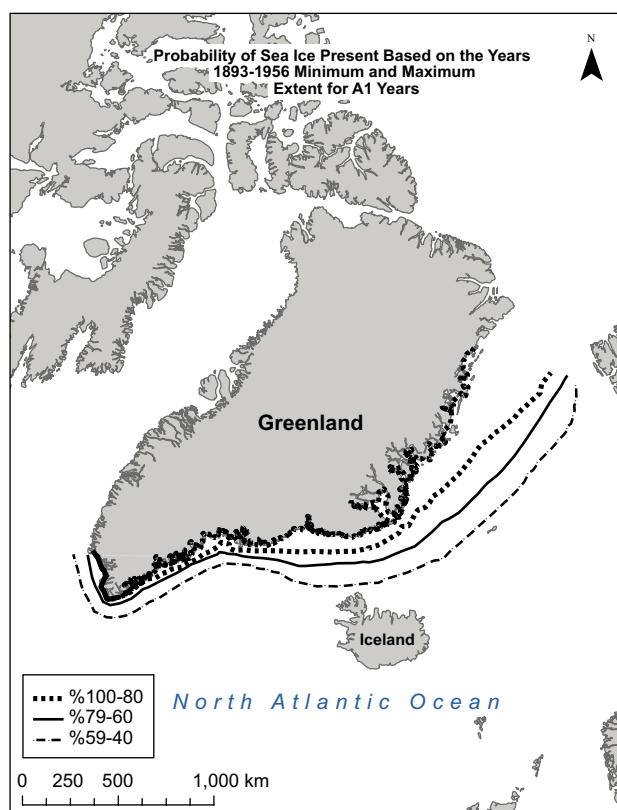


Fig. 1. Example of the final map, available for downloading, showing the probability of sea-ice extent based on historical maps from 1893 to 1956.

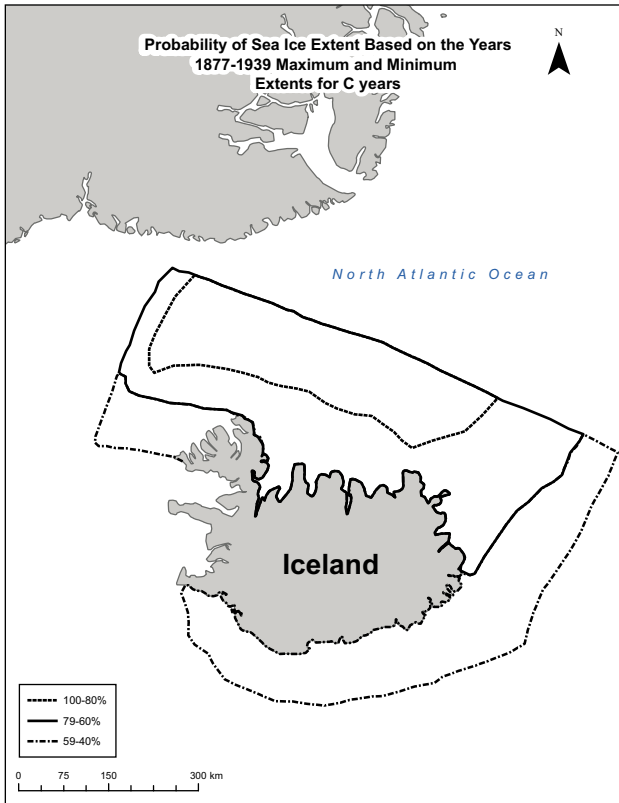


Fig. 2. Example of probability map of sea ice off Iceland 1877 to 1939.

year, whereas C is the most severe sea-ice year, with B being of intermediate severity. For example, the year 1895 is classified as B3 because it had a wider area of sea ice that touched on northern Iceland. Table 1 gives a summary of the index for each year. The duration of sea ice is not taken into consideration in these indexes.

The dataset we produced comes from three different sources of historical maps. The first is the digitised Icelandic maps, the second source is the DMI sea-ice charts that we digitised for 1893 to 1900 for the months between March and September each year. We have only digitised sea-ice ex-

tent along the east coast to the southern tip of Greenland from the DMI charts. These charts were based on ice conditions from variable sources such as land-based observations, scientific explorations and ship logs.

The third source is shapefiles from DMI that are available online. These files contain digitised sea-ice data from 1901 to 1956 (Underhill *et al.* 2014). We subsequently used these data to create the digitised maps. The DMI shapefiles were downloaded from the NSIDC at: <https://nsidc.org/data/G10007/versions/1>. The original maps used to create the shapefiles from 1893 to 1956 can be found on the NSIDC website: <https://nsidc.org/data/G02203/versions/1#>. Due to World War II, there is a gap in the data from 1939 to 1946.

Digitisation of the maps was done using ArcMap and exported as completed map files in jpeg format. Next, and for ease of data manipulation, the images were processed to convert the values into binary arrays, so that sea ice has a value of 1 and no sea ice has a value of 0. This was done in order to better visualise and plot the data. For each category (A1, A2...C) of the index, where there are at least 10 years present (Table 1) we created a map showing the probability that sea ice had a certain extent. The maps contain three lines of sea ice that depict 80–100%, 60–79% and 40–59% probability of sea-ice extent (Fig. 1). The percentages are calculations of the average sea-ice extent. We used the average sea-ice extent for each year belonging to each category to calculate the frequency of the extent. For example, the dataset shows that in 80–100% of those years within a certain category the sea ice extended to the thick dashed line, 60–79% of the time the extent reached the solid black line and only 40–59% of the time did the sea ice extend to the thin dashed line. The result of this procedure is six maps (A1, A2, A3, B1, B2 and C) from 1893 to 1956. In some cases, we can go even further back in time; three maps showing Iceland only (B2, B3 and C) have been constructed for the years 1877 to 1939. Figure 2 shows an example of a C year. There are no probability maps for A years for the Iceland-only maps, because of a lack of data.

Table 1. Summary of how Koch's index was classified for each year from 1821 to 1939

Index	A1	A2	A2	A2	A3	A3	B1	B1	B2	B2	B3	B3	B3	C	C	C
Year	1884	1823	1853	1924	1830	1902	1862	1913	1836	1916	1821	1861	1914	1822	1868	1911
	1922	1832	1867	1928	1831	1903	1876		1838	1917	1824	1870	1915	1828	1869	1918
	1926	1839	1899	1930	1835	1923	1877		1850	1921	1825	1875	1919	1837	1878	
	1927	1841	1904	1933	1854	1925	1879		1880	1932	1827	1883	1938	1840	1881	
	1931	1843	1905	1937	1864	1929	1889		1885		1829	1886		1855	1882	
	1934	1844	1908		1871		1889		1890		1834	1895		1856	1887	
	1935	1845	1909		1872		1893		1897		1857	1896		1858	1888	
	1936	1846	1910		1873		1894		1898		1859	1906		1865	1891	
	1939	1848	1920		1901		1900		1912		1860	1907		1866	1892	
Total	9			23		14		10		13			22			20

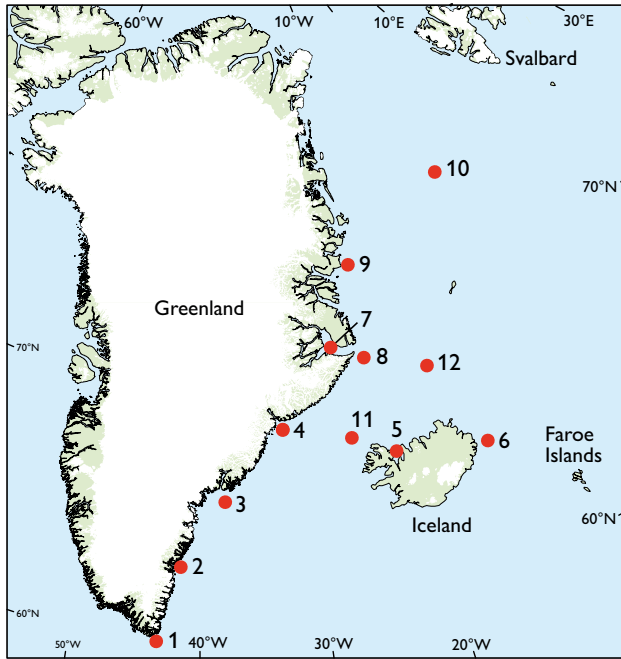


Fig. 3. Map of the location of the twelve points used for the probability matrix.

For further analyses of the sea-ice data, 12 points were selected (Fig. 3) to pinpoint areas of interest in order to investigate if there is a relationship between the points. A conditional probability matrix (Table 2) was created to analyse the relationship between the 12 selected points using the digitised datasets described above. We calculated the probability that if there is sea ice at a given point then there is sea ice at another point. For example, the value 0.177 in the last column indicates that if point 12 has sea ice then there is a 0.177 probability that point 11 also has sea ice. A strong

probability is defined as a value of 0.850 to 1.000, a medium probability is defined as a value of 0.490 to 0.849 and a weak probability is less than 0.490.

Results

In this section, we discuss the observed relationship between the East Greenland sea ice and the sea ice off Iceland using nine probability maps and the conditional probability matrix (Table 2). Koch describes an A1 year as a year when the ice between Greenland and Iceland would have been narrow and Iceland free of ice throughout that year. During A1 years the probability maps show that sea ice would definitely have been present along the coast of Greenland, down to the southern tip with fluctuations out from the coast but the ice would not have reached Iceland. In A2 years, sea ice is approaching the north coast of Iceland, but Iceland itself would have been almost completely free of ice. It is further estimated that 80–100% of the time, sea ice would most likely have been at the northern part of the coast, and for only 60–79% of the time to be present at the southern part of Iceland. In A3 years the sea-ice belt would have been wider at times extending into the northern fjords of Iceland.

In B years, the sea ice would have formed a broad belt north of Iceland. Koch describes in his report that the ice edge reached near 67°N and 15°W, which corroborates the digitised data. In B1 years, the probability maps reflects a wider range of sea-ice extent along the coast of Greenland. For example, at Scoresby Sund (point 7), the maps show that the fjord is not always covered by ice during those years. In B2 years, the probability map shows that the probability of 80 to 100% covers a larger area along Greenland’s east coast, and has an extent of sea ice that reached further along the

Table 2. A conditional probability matrix

	Known point with sea ice											
	1	2	3	4	5	6	7	8	9	10	11	12
1	1.000	0.916	0.896	0.942	0.789	0.625	0.889	0.898	0.880	0.969	0.828	0.169
2	0.924	1.000	0.948	0.942	0.842	0.500	0.937	0.933	0.930	0.984	0.841	0.171
3	0.896	0.940	1.000	0.919	0.789	0.625	0.913	0.918	0.907	0.977	0.832	0.168
4	0.976	0.976	0.960	1.000	0.842	0.500	0.980	0.988	0.981	0.977	0.845	0.165
5	0.060	0.064	0.060	0.062	1.000	0.750	0.063	0.063	0.062	0.094	0.082	0.316
6	0.020	0.016	0.020	0.015	0.316	1.000	0.016	0.016	0.016	0.031	0.026	0.375
7	0.900	0.940	0.924	0.950	0.842	0.500	1.000	0.961	0.946	0.961	0.823	0.163
8	0.920	0.948	0.940	0.969	0.842	0.500	0.972	1.000	0.965	0.984	0.845	0.169
9	0.912	0.956	0.940	0.973	0.842	0.500	0.968	0.976	1.000	0.984	0.828	0.167
10	0.498	0.502	0.502	0.481	0.632	0.500	0.488	0.494	0.488	1.000	0.509	0.305
11	0.771	0.777	0.775	0.754	1.000	0.750	0.758	0.769	0.744	0.922	1.000	0.177
12	0.977	1.000	0.977	1.000	0.140	0.070	0.953	1.000	1.000	0.907	0.953	1.000

The left hand column indicates the point with sea ice (in relation to Fig. 2), while the rows show the probability of sea ice present relative to that point

Icelandic northern coast. Unlike that observed in B1 years, for B2 years Scoresby Sund was often filled with sea ice. Finally, during C years, sea ice was present along the entire East Greenland coast and for 40–59% of the years the ice would extend down the eastern coast of Iceland.

Of the nine maps, the remaining three show sea-ice data off Iceland from 1877 to 1939. These maps provide more details on sea-ice extent during a more severe ice period in the 1880s (Kelly *et al.* 1987, based largely on Koch's index of Icelandic sea-ice occurrence). In B2 years, there was a 40 to 59% probability of sea ice reaching all along the northern coast of Iceland, but persisting mainly between Iceland and Greenland. The B3 years have a wider area between Greenland and Iceland and cover a further range along the northern Icelandic coast. Kelly *et al.* (1987) discuss three of the B3 years (1914, 1915 and 1938) as being years with extensive sea ice around Iceland. During C years, the sea ice extended to the south coast of Iceland. Seven of these years (1881, 1882, 1887, 1888, 1892, 1911 and 1918) were severe sea-ice years for Iceland (Kelly *et al.* 1987).

A statistical analysis was carried out to see if there is any correlation between sea ice being present at one point (Table 2) to other points on the map. The strongest probabilities are the points along eastern Greenland, points 1–4 and 7–9. This implies that if there is sea ice at one point along the coast then it is very likely that the rest of the eastern coast of Greenland would have been filled with ice. Point number 12 is located farther from the coast but has a perfect correlation with points 2, 4, 8 and 9 along the coast. The points farther from the coast 10–12 have a range of weak to strong probability with the other points. Point 12 also shows a relatively higher probability value of 0.316 and 0.375 with points 5 and 6 than the other points closer to Greenland, which all have weak values of less than 0.094.

Lauge Koch's index extends further back in time than the maps of the spatial extent. When using the probability maps, it is now possible to see how extensive the sea ice was likely to have been in the period from 1821 to 1893. The final application of the maps is to use them in combination with Table 1 to be able to estimate sea-ice extent back to 1821.

Conclusion

134 maps showing sea-ice extent from 1877 to 1939 are available as jpeg files and shapefiles. Detailed probability maps have been created from observed and estimated sea-ice condi-

tions from observed data that date back to the early 1800s. These probability maps can be downloaded at <https://dx.doi.org/10.1594/PANGAEA.887452> where the maps are available as jpeg files. The datasets can be used in further studies to help understand the characteristics of sea ice during the 19th and 20th centuries. Previous studies have used Koch's sea-ice index to infer atmospheric circulation patterns (Kelly *et al.* 1987). Our new dataset can provide important input to studies of climatic variability in the (sub)Arctic including the link between ice and atmospheric circulation modes such as the Arctic and North Atlantic Oscillations (AO/NAO) and thus helps predicting how the climate may respond to future sea-ice loss (Screen *et al.* 2017).

References

- Chapman, W.L. & Walsh, J.E. 1993: Recent variations of sea ice and air temperature in high latitudes. *Bulletin of the American Meteorological Society* **74**, 33–47.
- Kelly, P.M., Goodess, C.M. & Cherry, B.S.G. 1987: The interpretation of the Icelandic sea ice record. *Journal of Geophysical Research: Oceans* **92**(C10), 10835–10843.
- Koch, L. 1945: The East Greenland Ice. *Meddelelser om Grønland* **130**(3), 373 pp.
- Screen, J.A. 2017: The missing northern European winter cooling response to Arctic sea ice loss. *Nature communications* **8**, 14603.
- Thoroddsen, T. 1884: Den grønlandske drifisen vid Island. *Ymer* **1884**, 145–160.
- Underhill, V., Fetterer, F. & Petersen, C. 2014: Arctic sea ice concentration and extent from Danish Meteorological Institute sea ice charts, 1901–1956, Version 1. Boulder: NSIDC (National Snow and Ice Data Center), <https://dx.doi.org/10.7265/NSMPS17M>
- Vaughan, D.G. *et al.* 2013: Observations: Cryosphere. In: Stocker, T.F. *et al.* (eds): *Climate Change 2013: The Physical Science Basis. Contribution of working group I to the Fifth Assessment Report of the Intergovernmental Panel on Climate Change*, 317–382. Cambridge: Cambridge University Press.
- Walsh, J.E., Chapman, W.L. & Fetterer, F. 2015, updated 2016: Gridded monthly sea ice extent and concentration, 1850 onwards, Version 1.1, Boulder: National Snow and Ice Data Center. Digital media, <http://dx.doi.org/10.7265/NS833PZ5>
- Walsh, J.E., Fetterer, F., Stewart, J.S. & Chapman, W.L. 2017: A database for depicting Arctic sea ice variations back to 1850. *Geographical Review* **107**, 89–107, <http://dx.doi.org/10.1111/j.1931-0846.2016.12195.x>

Authors' address

Geological Survey of Denmark and Greenland, Øster Voldgade 10, DK-1350 Copenhagen K, Denmark. E-mail: dballe23@gmail.com.

Examining the rare-earth elements (REE) supply–demand balance for future global wind power scenarios

Per Kalvig and Erika Machacek

Rare-earth elements (REE) are considered Critical Raw Materials (CRM; EC 2018; US Department of the Interior 2018) and essential in the technological transformation of the energy sector into carbon-free technologies such as wind turbines, electrified transport and LED-lights. The new technologies have led to swiftly expanding markets for REE products, in which China has achieved a monopolistic role in all segments of the REE value chains. Political strategies aimed to establish REE supplies outside China are currently being implemented within the EU and in other Western countries in order to ensure an adequate future REE supply.

However, new REE value chains outside China have not yet materialised.

The aim of this paper is to assess whether the global REE supply from present and potential mines can keep pace with the REE demand for the expanding offshore wind energy sector (Fig. 1). A successful development of this sector outside China relies on an adequate supply of particularly neodymium (Nd) and to some extent praseodymium (Pr), terbium (Tb) and dysprosium (Dy), used in permanent magnets for windmill generators. In 2015, about 82% of the global Nd-oxide production was used in the permanent magnets

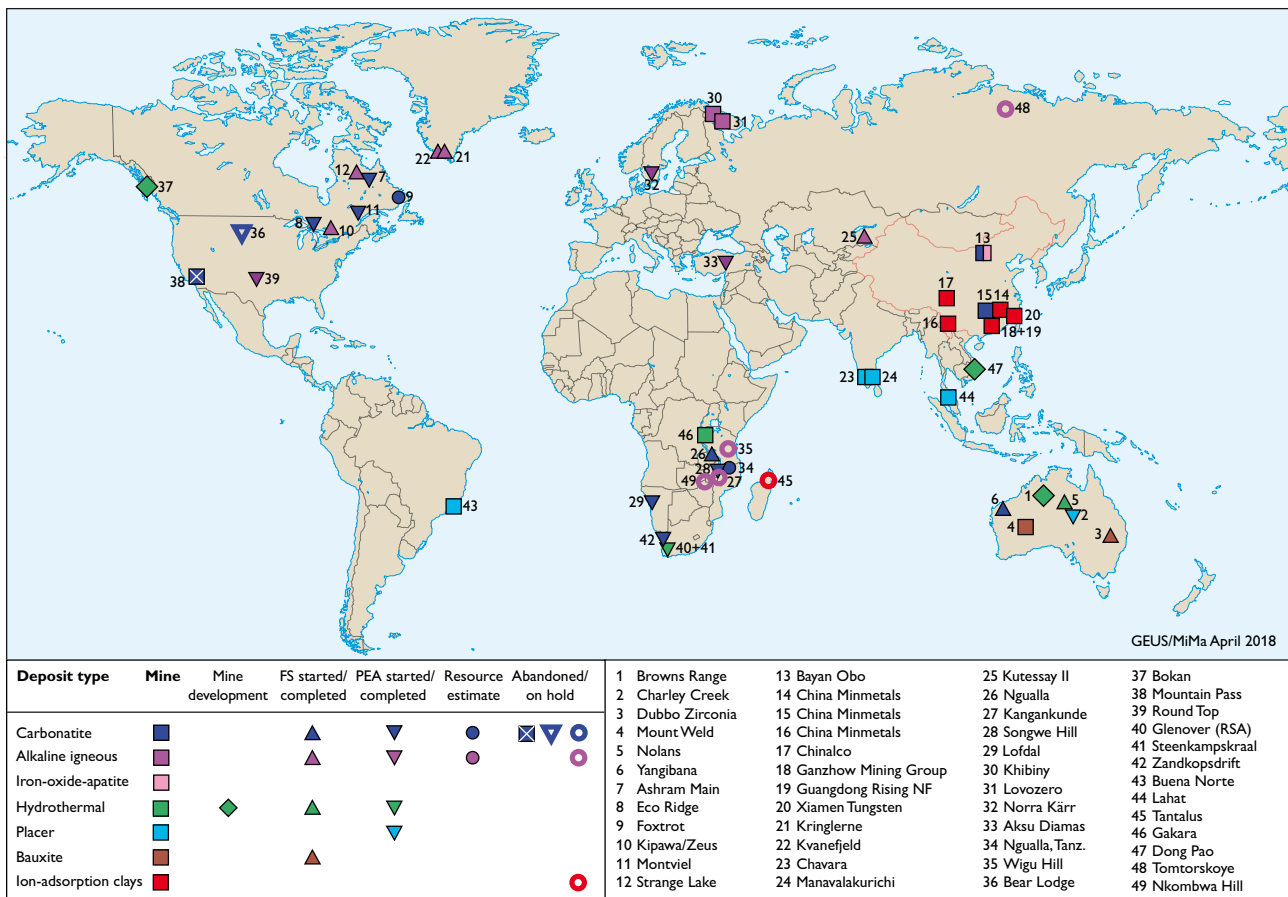


Fig. 1. Global rare-earth element mines and advanced exploration projects. FS: Feasibility study. PEA: Pre-economic assessment.

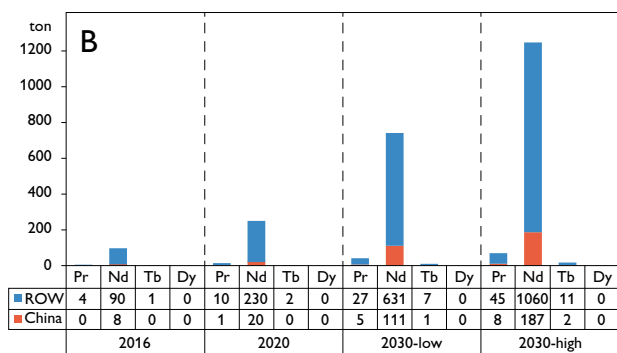
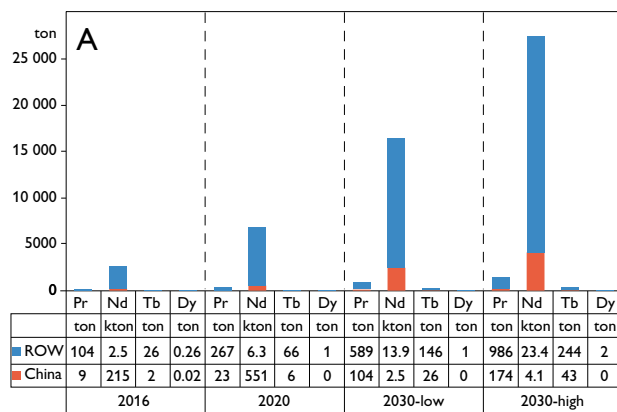


Fig. 2. Rare-earth metal demand by wind energy deployment in China and the ROW in 2016, and forecasts for 2020 and 2030. **A:** assuming that all offshore wind technology is centred on REE-based permanent magnets. **B:** assuming that only a small share of offshore wind technology uses REE-based permanent magnets, and differentiating between varying REE uses per PM generator technology. Note: Both figures show cumulated (forecasted) individual REE use by examined wind energy technology in the respective year. **ROW:** the rest of the world.

production (Adamas 2016). Here we evaluate the future supply and demand situations for Nd, Pr, Tb and Dy in the global wind energy sector in the form of three scenarios, one for 2020 and two for 2030 based on high and low demand. The balance is discussed. Our assessment reflects the challenge caused by limited insight into the REE supply chains inside China, and the figures presented in this paper are therefore only indicative.

Scenarios for future global REE demand of the wind energy sector

In 2016, the Global Wind Energy Council reported a total global wind power capacity of 487 GW (GWEC 2016), of which the offshore capacity amounted to 3% according to the Global Status Report 2017 for Renewables. Due to the

Table 1. Forecast scenarios for installed global offshore wind energy capacity in 2020 and 2030

Wind energy capacity scenarios	Global total From GWEC (2016a)	Global offshore	
		assumptions, this survey	offshore capacity % REE permanent magnets installed capacity
Forecast 2020	739 GW	5% = 37 GW	5% = 1.85 GW
Forecast 2030 low	1260 GW	7% = 88 GW	10% = 8.80 GW
Forecast 2030 high	2110 GW	7% = 148 GW	10% = 14.80 GW

otherwise very high maintenance costs of the offshore wind energy, it depends in part on direct-drive and hybrid wind turbine technologies that use REE-based permanent magnet (PM) or high-temperature superconducting (HTS) generators (Barteková 2016). This is why the offshore wind energy sector is the focus of this study.

Our scenarios solely deal with technologies using permanent magnets in which Nd is vital. Barteková (2016) specifies the consumption of total rare-earth element oxides (TREO) for the individual types of magnets used in wind turbines and indicates the individual REE used. The REO content per magnet varies by generator design between *c.* 23–35%, highest in the permanent magnet of a direct-drive synchronous generator (PMSG-DD), and lowest in hybrid single and multistage synchronous generators (PMSG-SG and PMSG-MG). The relative magnet weight proportions of the four REOs are about 95% Nd, 4% Pr, 0.99% Tb and 0.01% Dy (Barteková 2016).

In order to estimate the future REO-demand of the sector, the following assumptions about the wind energy technology are made based on Barteková (2016, p. 158), who reported that in 2014 the REE-based permanent magnet technology accounted for 4% of the offshore wind technology, equally divided between direct-drive and hybrid generator designs. For our 2016 baseline scenario, we (i) increased this share to 5%, (ii) maintained the equal split between direct-drive and hybrid generator technologies, and (iii) subdivided the hybrid generator designs equally into single and multistage gearbox designs. Further, we assume that in 2016, China held 8% and the rest of the world (ROW) 92% of the global offshore wind capacity.

From the 2016 baseline scenario, we developed three scenarios: (1) the REO use in the total global offshore wind energy capacity in 2020, and (2, 3) low and high forecasts of the same in 2030. We set the regional offshore shares to 85% for ROW and 15% for China. See details in Table 1.

Our scenarios are based on the estimates by GWEC (2016) for 2020, 2030-low, and 2030-high global wind energy capacity. It is important to note the large variability in the underlying assumptions. The most significant parameter is the share of REE-based permanent magnets deployed in offshore installations. For instance, if all offshore technology capacity would employ REE-based permanent magnet technology and 75% of this was installed with the highest REE-using direct-drive design, this would result in the consumption 16 400–27 500 tons Nd-oxide in 2030 (Fig. 2A). In contrast, the wind-turbine sector will demand only about 740–1250 tons Nd-oxide (Fig. 2B) for the alternative technology split-up outlined in Table 1.

Scenarios for the future global REE supply

In 2016, the primary global production of total rare-earth oxides (TREO) amounted to 129 000 tons, of which China produced 83%, Australia 11%, Russia 2%, Brazil 1%, India 1% and Malaysia, Thailand, and Vietnam still less (USGS 2017). Although the TREO supply figures for 2016 reported by different sources are rather similar (USGS 2018: 23 680 tons; Adamas 2016: 24 377 tons), there are major discrepancies at national level. This partly stems from the assumed contributions of the non-reported market which may account for 25–30% (Roskill 2016) and from uncertainties pertaining to production and smelting quota (Adamas, personal communications 2018). This study applies the figures for 2016 from USGS (2018), and contribution from non-reported production is not considered. The 2016 supplies of Pr, Nd, Dy and Tb from China and seven ROW countries are shown in Figs 3A, B. The official Chinese production quota for 2016 was set to 105 000 tons TREO (Machacek & Kalvig 2017); our estimate of the regional REO production is based on Kingsnorth (2016) and shown in Fig. 3A. Given that no scheduled production quotas for 2020 and 2030 are available, our China 2020 and 2030 supply scenarios are arbitrarily set to an increase of 5% p.a., reflecting the anticipated growth in demand (Dutta *et al.* 2016), the potential for higher capacity on existing plants, as well as continued efforts to transform the informal sector into to a formal one.

The ROW supply in the 2020 and 2030 scenarios is developed as follows: of the recorded 320 REE exploration projects outside China, 99 are reported to be active (S&P-database 2017). Our search revealed that 31 of these projects, located in 12 countries, have reached an advanced stage (Fig. 1). These 31 projects are divided into four classes of development, which are in turn translated into expected production start-ups in 2020, 2025, 2030 and 2035.

The estimates of relative REO grades and targeted production of Pr, Nd, Tb and Dy are based on TMR (2015) and company data. Where relative grade data are not available, our estimate is based on the actual REE mineralogy. According to these data, new REO productions in Australia, USA, and Vietnam are expected in 2020. In 2030, REO will also

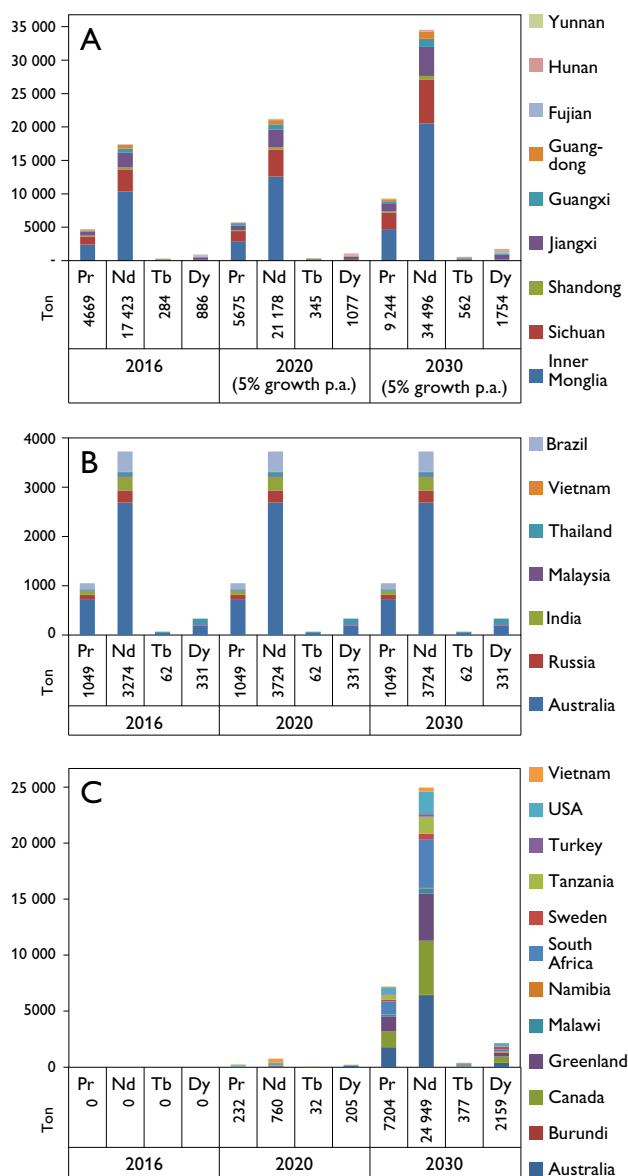


Fig. 3. Current and future REE production scenarios. A: Current and forecasted Chinese production of praseodymium, neodymium, terbium and dysprosium in seven regions. Forecast assumes a general 5% annual increase. B: Current and forecasted production of praseodymium, neodymium, terbium and dysprosium in ROW. Forecast assumes a static production. C: Forecasted production of praseodymium, neodymium, terbium and dysprosium from 31 advanced REE projects outside China.

be supplied by Canada, Greenland, Malawi, Namibia, South Africa, Sweden, Tanzania and Turkey (Figs 1, 3C). The scenarios indicate ROW-TREO productions of 6920 tons in 2020 and 154 075 tons in 2030 (Fig. 3C).

Discussion and summary

We demonstrate here that the level of detail applied to estimates of the future use of different types of generators and their relative shares allow for great variance in the current and forecast REE demand by the wind energy sector. Against this background, our ROW scenario for 2020 points to a Nd demand by the wind energy sector within a wide range of 230–6300 tons (Fig. 2), while our ROW supply forecast for Nd-oxide from both current and new mines is around 4500 tons. A top-down approach indicates that the REE-based permanent magnets for the wind sector absorb 10%, equivalent to about 4000 tons TREO (Lucas *et al.* 2015). Adamas (2016) estimates that Nd-oxide accounts for *c.* 73% of the TREO in the permanent magnets for the wind sector. In effect this means that in 2020, the total Nd-oxide supply for the wind energy sector would be roughly 3000 tons Nd-oxide, i.e. in the middle range of the forecasted global demand for this purpose.

For the 2030 low scenario and with REE technology applied in some but not all offshore technology, the global Nd-oxide demand by the wind sector is forecasted to *c.* 740 tons and for the 2030 high scenario close to 1250 tons. If it is assumed that all offshore technology will draw on REE use, these figures increase to 16 400 and 27 500 tons, respectively. Our global supply forecast of Nd-oxide in 2030 from current operations is about 35 000 tons from China and 3700 tons from ROW, to which advanced ROW REE projects could contribute an additional *c.* 25 000 tons if all projects go into production. If the 10% share of the REE-based permanent magnet sector as well as a stable demand for REE-based permanent magnets from the wind sector are maintained, about 450 tons Nd-oxide could be made available by ROW suppliers in 2020, and 2900 tons in 2030. However, in the scenarios based on generator technologies that consume a higher percentage of REE-based magnets, the estimated ROW sup-

ply is inadequate and an additional Nd-oxide supply will be required, e.g. from Chinese REE operators.

This study shows that there are currently significant uncertainties in trying to determine both the current REE demand and supply in the wind sector and in building scenarios for 2020 and 2030. Given that Nd-Dy permanent magnets represent a fast-growing sector, there is a need to establish a comprehensive, research-based and harmonised framework for precise estimates of the future supply and demand scenarios for REE-based permanent magnets.

References

- Adamas 2016: Rare Earth Market Outlook: supply, demand, and pricing from 2016 through 2025 Report, 822 pp. Adamas Intelligence.
- Barteková, E. 2016: The role of rare earth supply risk in low-carbon technology innovation. In: Borges De Lima, I. & Leal Filho, W. (eds): Rare earths industry: technological, economic, and environmental implications. Amsterdam: Elsevier, 437 pp.
- Dutta, T., Kim, K-H, Uchimiya, M., Kwon, E.E., Jeon, B-H, Deep, A. & Yun, S-T. 2016: Global demand for rare earth resources and strategies for green mining. *Environmental Research* **150**, 182–190.
- EC 2018: Report on Critical Raw Materials and the Circular Economy, 69 pp. Commission Staff Working Document. SWD(2018) 36 final.
- GWEC 2016: Global Wind Energy Outlook 2016. Fried, L. *et al.* (eds), 44 pp. GWEC and Institute for Sustainable Futures, University of Technology Sydney.
- Kingsnorth, D.J. 2016: Curtin University publication on the rare earth industry in 2016.
- Lucas, J., Lucas, P., Le Mercier, T., Rollat, A. & Davenport, W. 2015: Rare-earth-based permanent magnets preparation and uses, 231–249. In: *Rare Earths*. Amsterdam: Elsevier.
- Machacek, E. & Kalvig, P. (eds) 2017: Road map for REE material supply autonomy in Europe. EURARE, European REE market survey (component D1.2). 141 pp + appendix.
- Roskill Informations Services Ltd. 2016: Rare Earths: Global industry, markets and outlook to 2026, 396 pp. Roskill Reports on Metals and Minerals, 16th revised edition.
- S&P-database 2017: S&P Global Market Intelligence Metals & Mining Database 2017.
- Technology Metals Research (TMR) 2015: Advanced Rare-Earth Projects: <http://www.techmetalsresearch.com/metrics-indices/tmr-advanced-rare-earth-projects-index/> (accessed 9 February, 2018).
- US Department of the Interior 2018: Draft List of Critical Minerals. Feb 16, Notices. Federal Register **83**(33), 7065–7068.
- USGS 2018: Mineral Commodity Summaries. US Geological Survey.

Authors' address

Geological Survey of Denmark and Greenland, Øster Voldgade 10, DK-1350 Copenhagen K, Denmark. E-mail: pka@geus.dk.

Analysis of cod otolith microchemistry by continuous line transects using LA-ICP-MS

Simon Hansen Serre, Kristian Ege Nielsen, Peter Fink-Jensen, Tonny Bernt Thomsen and Karin Hüsey

Fish otoliths, also called ear stones or statoliths, are calcified structures functioning as movement and equilibrium indicators in the inner ear of fish (Fig. 1). From hatching to death these structures grow incrementally, with new material accreted daily (Pannella 1971) in successive layers of protein (1–8%, Degens *et al.* 1969) and calcium carbonate. The accretion rate of otoliths varies with fish growth, and in temperate species it is usually lowest during the winter season (Hüsey *et al.* 2010). This results in concentric growth resembling the ringed structure in trees (Fig. 1D), enabling the use of dendrochronological techniques to approximate the age and growth history of fish. During growth, certain elements are incorporated into the otolith structure, some associated with proteins and some with the calcium carbonate component (Thomas *et al.* 2017), supplying a valuable record of different aspects in fish life history and serving as a potential environmental record.

Previous studies show that trace element and isotopic compositions of otoliths can be used as a proxy for reconstructing water chemistry, temperature and salinity (Patterson *et al.* 1993; Thorrold & Shuttleworth 2000). Other studies demonstrate that elemental histories can be used to investigate fish spawning and migration patterns (e.g. Sturrock *et al.* 2012), and more recent studies use elements such as Zn, Cu and Mg as indicators of seasonality (Hüsey *et al.* 2016; Limburg *et al.* 2018). Combining this knowledge of elemental variation with the micro-beam capabilities of laser ablation inductively coupled plasma mass spectrometry (LA-ICPMS) turns otolith microchemistry into a powerful tool for studying important parameters fundamental for establishing modern, sustainable fisheries management policies (e.g. stock identification, migration, pollution indicators, spawning habitats, duration of larval and juvenile stages, and magnitude and timing of spawning).

We present an analytical method developed by the Geological Survey of Denmark and Greenland (GEUS) in collaboration with the National Institute of Aquatic Resources, Technical University of Denmark (DTU Aqua), for element abundance analysis in otoliths. Analyses of otoliths from Baltic Cod (*Gadus morhua*; Fig. 1) are used as an example for its application.

Analytical approach

The microchemical analysis of otoliths focuses on Mg, P, Ca, Mn, Cu, Zn, Sr and Ba, as these elements are typically incorporated into otoliths, and are either subject to environmental control (e.g. Sr and Ba correlate with water salinity) or physiological control (e.g. Zn, Cu and Mg are useful to the interpretation of otolith growth history; Hüsey *et al.* 2016 and references therein; Limburg *et al.* 2018). The LA-ICPMS facility at GEUS employs a NWR213 laser system coupled to an ELEMENT 2 double-focusing, single-collector magnetic sector field ICPMS. Operating conditions, data acquisition and processing parameters are listed in Table 1. LA-ICPMS is often the preferred technique for rapid, *in-situ* analyses of trace elements and isotopes obtained from natural samples,

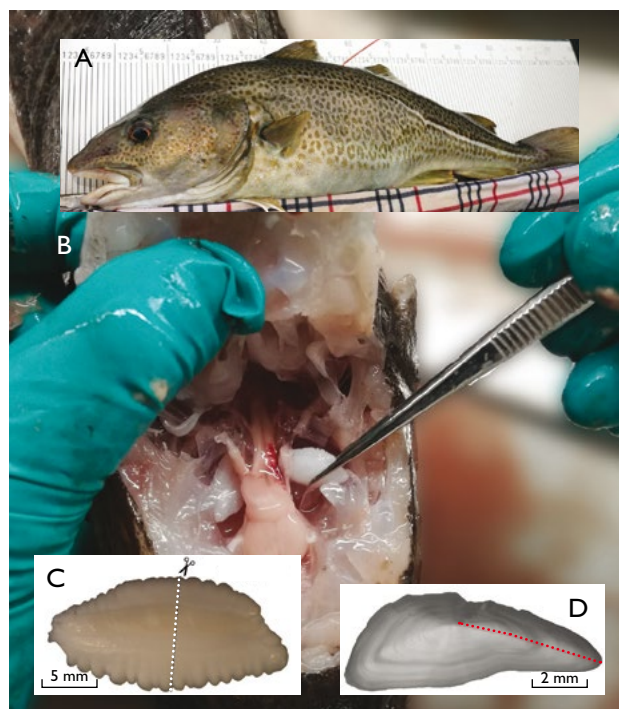


Fig. 1. A: Cod specimen caught in the Baltic Sea. B: Removal of otoliths, the cut is situated just above the eyes. C: Otolith, with dotted line showing the direction of a cross-section. D: Photograph (reflected light) of a polished cross-section of an otolith. The red line shows the position of the laser scan.

Table 1. Instrument operating conditions, data acquisition and processing parameters

<i>Instrumentation:</i>	
Thermo-Fisher Scientific Element 2 double focusing SF-ICP-MS	
Forward power:	1470 W
Cones:	Ni
Plasma gas:	16 l min ⁻¹
Auxiliary gas (He):	0.85 l min ⁻¹
Nebuliser gas (Ar):	0.95 l min ⁻¹
New Wave Research NWR 213 solid state Nd:YAG laser ablation system	
Laser wavelength:	213 nm
Laser fluence:	~ 9.5 J cm ⁻²
Spot size:	40 μm
Repetition rate:	10 Hz
Scan speed:	5 μm s ⁻¹
<i>Data acquisition and processing</i>	
Analyte isotopes: ²⁵ Mg, ³¹ P, ⁴³ Ca, ⁴⁴ Ca, ⁵⁵ Mn, ⁶⁵ Cu, ⁶⁶ Zn, ⁸⁸ Sr, ¹³⁷ Ba	
Sampling time, ms:	10 10 10 10 10 10 10 10 10
Samples per peak:	10 10 10 10 10 10 10 10 10
Acquisition: Time resolved (continuous analysis) along transects	
Mass resolution: 300 (low)	
Oxide production rate tuned to ≤0.3% UO ₂ (²⁵⁴ UO ₂ / ²³⁸ U)	
Single analysis duration and setup: 30 s blank, 2–20 min ablation (sample dependent), 30 s washout	
<i>Software for data reduction:</i>	
Iolite version 2.5 (Paton <i>et al.</i> 2011; Hellstrom <i>et al.</i> 2008)	
<i>Standards:</i>	
Internal standard isotope: ⁴³ Ca	
External standardisation: NIST-612 glass	
Secondary standards: NIST-614 glass, FEBS-1 otolith powder and MACS-3 carbonate powder pressed as tablets	

as it requires little sample preparation and can produce high sample throughput, extracting elemental and isotopic information at a micrometre scale. Most conventional LA-ICPMS analysis is performed by spot analyses, following a bracketing analysis protocol using well-characterised standard materials. This is a powerful method when studying specific areas in solid materials. However, for compositional variations along millimetre- to centimetre-scale transects, the spot approach becomes very time-consuming. For example, a 5 mm long transect requires about one hundred spots 40 μm in diameter, taking 3–4 hours to complete. Spot analysis also introduces difficulties like downhole-element fractionation when the laser drills into the material. Instead, research of fish otolith microchemistry favours faster sampling approaches such as line scans across the sample to acquire continuous time-resolved compositional profiles (a 5 mm long line takes *c.* 17 min, using a fixed scan speed of 5 μm s⁻¹; e.g. Søndergaard *et al.* 2015; Hüseyin *et al.* 2016). This approach is rapid, suppresses depth heterogeneity and avoids downhole elemental fractionation, as it ablates only to a depth of a few microns. The potential interfering effects of varying scan speeds, washout times and debris blanketing from the ablation are not yet

studied, but this is intended in the near future. For ongoing otolith studies, we used a line-scan LA-ICPMS approach to measure 325 cod otoliths (15–30 otoliths per day).

The otoliths were embedded in epoxy resin and cut along the dorsoventral profile to expose the core and annuli. For streamlined, high-throughput analyses, custom-made epoxy mounts 7 × 0.8 × 0.8 cm large were cast, each holding 10 otoliths. A custom-made 10 cm² sample holder with four mounts allows for analysis of 40 otoliths per day. For each otolith, a reflected light optical photo depicting a line from core to edge (Fig. 1D) was imported as an overlay image into the laser ablation software. The image was fitted to the otolith position in the live image, using reference points to facilitate the exact positioning of the line scans.

The ICPMS analysis was optimised for dry plasma conditions through continuous linear ablation of the NIST 612 standard. The signal-to-noise ratios were maximised for the isotopic mass range from Mg to Ba, while opting for low element-oxide production levels by minimising the ²⁵⁴UO₂/²³⁸U ratio. Instrumental drift was minimised by following a standard-sample-standard analysis protocol, bracketing every sample analysis by line analyses of the NIST-612 and NIST-614 glass standards (Jochum *et al.* 2011), while the FEBS-1 otolith (Sturgeon *et al.* 2005) and the MACS-3 carbonate powder tablets (Jochum *et al.* 2012) provided quality control of the NIST-612 standard measurements. The averaged 2σ accuracy and uncertainty of the standards were typically <5% for element abundances >1–3 ppm. Data processing was done with software Iolite v. 2.5 (Hellstrom *et al.* 2008; Paton *et al.* 2011) using the Trace Elements IS data reduction routine. Calculation of abundances were based on ⁴³Ca isotope as the internal standard, assuming 38.3 wt% Ca in all otoliths, comparable to the certified Ca concentration reported for the FEBS-1 otolith standard (Sturgeon *et al.* 2005).

Application of the analytical approach on Baltic cod

The main purpose of the analyses is to answer research questions important to the fisheries management in Denmark and Greenland. The specific approach presented here and modified versions of this method are used in several projects addressing a range of management questions relating to stock structure, migrations and age determination. Here, we highlight some preliminary results of the most advanced project.

The project *Tagging Baltic Cod* (TABACOD) is a joint Baltic collaboration aiming to develop a new age-estimation method based on seasonal variations in element concentrations along a gradient from the core (birth) to the edge (death) of otoliths. Fish age is one of the key variables in stock

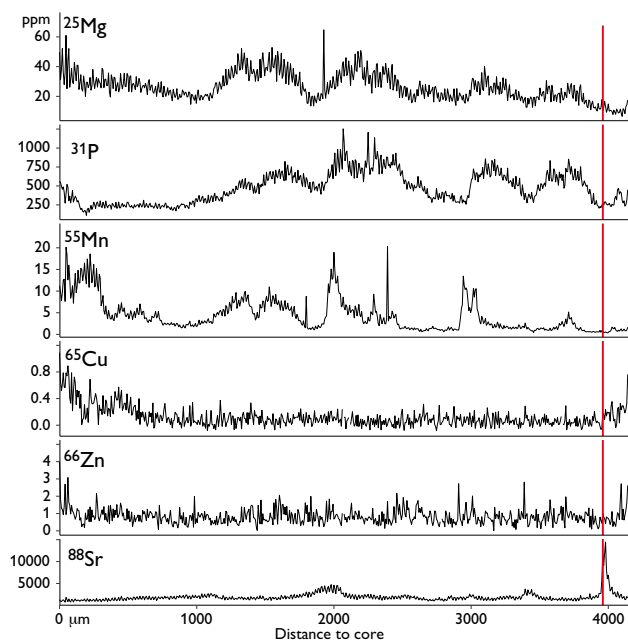


Fig. 2. Trace-element concentration profiles in ppm of the cod otolith shown in Fig. 1D. The x-axis indicates the concentration along the profile from 0 μm , when the fish was born, to 4300 μm , when it died. The red line marks the position of the Sr peak induced by SrCl_2 injection. Data from Nielsen *et al.* (2018). As this cod was tagged in April, the Sr timestamp corresponds to the coldest water temperatures experienced by the cod over a year, where Mg and P concentrations are at a minimum.

assessment and has traditionally been obtained by visual examination of otolith cross-sections, where seasonal fluctuations in growth are visible as optically contrasting growth zones much like the rings in cross-sections of trees. In recent years, this traditional method has failed to provide reliable age information, thus posing severe management problems for the Eastern Baltic cod stock. Initial results from the TABACOD project on the seasonality in the otolith chemical composition are presented as an example of the application of the LA-ICPMS approach. All analysed otoliths were acquired from cod that were subjected to a mark-recapture experiment. A total of *c.* 500 cod specimens were captured, externally marked, injected with SrCl_2 and released again. When the cod were recaptured they were sent to DTU Aqua for analysis. The SrCl_2 is incorporated into the otolith as it grows and acts as an internal timestamp. The chemical signals from timestamp to edge corresponds to the time the fish spent at sea between capture and recapture. Combining information on how many days the fish had been at sea, what time of year it was released/recaptured and how much it had grown since tagging allows us to validate our hypotheses on seasonally varying element concentrations. Concentrations of elements like Mg and Zn vary with season (Hüssy *et al.*

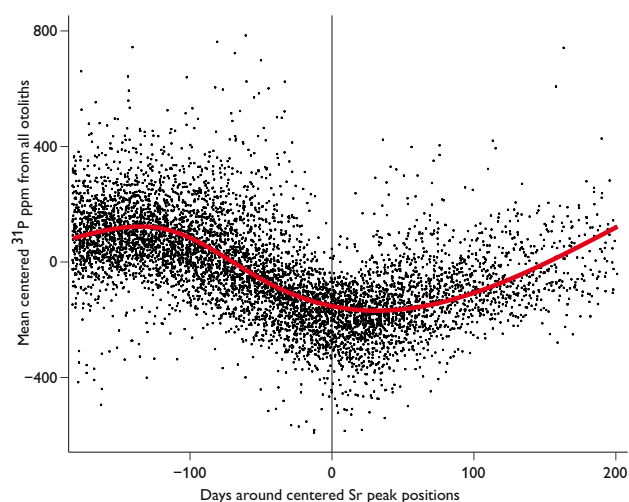


Fig. 3. Variations of phosphorous concentration in all measured otoliths *c.* 200 days before and after the SrCl_2 tagging and release experiment. On the x-axis, measurements are centred on the injection-induced Sr peak. On the y-axis, measurements have been centred on the mean P concentration of each otolith transect. The red line is a Generalised Additive Model smoothed curve.

2016). Figure 2 depicts core-to-edge compositional profiles of Mg, P, Mn, Cu, Zn and Sr from the otolith shown in Fig. 1D, corresponding to the entire life of the fish. The red line in Fig. 2 marks where the Sr concentration dramatically increases, representing the SrCl_2 -tagging event. The Mg, P and Mn concentrations show clear and similar variations throughout the otolith structure on a scale of tens to hundreds of ppm. Zn and Cu concentrations vary around our analytical resolution threshold of *c.* 1–3 ppm and do not show significant systematic variations.

The LA-ICPMS data are currently undergoing statistical analysis to quantitatively identify seasonal variations. However, some analysed elements indicate clear patterns resembling seasonality. If a seasonality in element concentration occurs, superimposing individual transects (like the ones shown in Fig. 2) of all cod in one plot will result in a generic signal. If element signals are random in relation to time, no such signal will be evident. Figure 3 shows P concentrations from all analysed otoliths, standardised by dividing each measured value by the mean profile P concentration to remove the effect of differences in average P levels between individuals. All profiles were centred at the Sr peak, since all cod were tagged during the same season (April to May of the same year). The time scale on the x-axis is estimated, assuming linear growth within years, similar growth in individuals across the year, and that all specimens were tagged and released on the same date of a given year. Although there are individual differences between fish, Fig. 3 indicates a general seasonal variation in

P concentrations. The total number of minima occurring in the profiles from birth to death thus corresponds to the number of winters the fish has experienced and hence its age.

Other ongoing projects

Migration patterns of the Kattegat cod: This project seeks to map migration patterns of cod captured in the Kattegat, which were genetically identified to belong to the North Sea or western Baltic stock. Elemental profiles of 400 cod captured along a geographic gradient covering the entire Kattegat will be compared with baseline samples from adjacent areas. Comparing the results to information about the otoliths' annual growth zones can reveal at what time in its life the cod has migrated to and from the Kattegat.

Stock structure in capelin: With partners from Greenland's fishing industry this project investigates stock structure, migration and natal homing (the return to a birthplace to reproduce) of capelin (*Mallotus villosus*) from 18 areas along the coasts of South and West Greenland. The aim of this project is to provide counsel on sustainable management of a species that plays a vital role in the marine food chain.

Final remarks

A LA-ICPMS approach for quantitative, high-throughput transect measurements of otoliths was successfully set up at GEUS. Data from 325 otoliths are being thoroughly examined, and only an 'appetizer' of the data is presented here. The LA-ICPMS approach is adaptable for most solid carbonate (e.g. bivalves) and phosphate (e.g. teeth, horn) materials showing cross-surface compositional variations. Analyte isotopes include most major, minor and trace elements and acquisition parameters are easily optimised for the specific sample type, thus providing a rapid and extremely versatile *in-situ* analytical approach for comparable natural materials.

Acknowledgements

We thank BalticSea2020 for financial support and Mojagan Alaei, GEUS, for laboratory assistance.

References

Degens, E.T., Deuser, W.G. & Haedrich, R.L. 1969: Molecular structure and composition of fish otoliths. *Marine Biology* **2**, 105–113.

- Hellstrom, J., Paton, C., Woodhead, J. & Hergt, J. 2008: Iolite: software for spatially resolved LA-(quad and MC) ICPMS analysis. *Mineralogical Association of Canada short course series* **40**, 343–348.
- Hüssy, K., Hinrichsen, H.H., Fey, D.P., Walther, Y. & Velasco, A. 2010: The use of otolith microstructure to estimate age in adult Atlantic cod *Gadus morhua*. *Journal of Fish Biology* **76**, 1640–1654.
- Hüssy, K., Gröger, J., Heidemann, F., Hinrichsen, H.H. & Marohn, L. 2016: Slave to the rhythm: seasonal signals in otolith microchemistry reveal age of eastern Baltic cod (*Gadus morhua*). *ICES Journal of Marine Science: Journal du Conseil* **73**, 1019–1032.
- Jochum, K.P. *et al.* 2011: Determination of reference values for NIST SRM 610–617 glasses following ISO guidelines. *Geostandards and Geoanalytical Research* **35**, 397–429.
- Jochum, K.P., Scholz, D., Stoll, B., Weis, U., Wilson, S.A., Yang, Q., Schwalb, A., Börner, N., Jacob, D.E. & Andreae, M.O. 2012: Accurate trace element analysis of speleothems and biogenic calcium carbonates by LA-ICP-MS. *Chemical Geology* **318–319**, 31–44.
- Limburg, K.E., Wuenschel, M.J., Hüssy, K., Heimbrand, Y. & Samson, M. 2018: Making the otolith magnesium chemical calendar-clock tick: Plausible mechanism and empirical evidence. *Reviews in Fisheries Science & Aquaculture* **26**, 1–15.
- Nielsen, K., Serre, S., Thomsen, T. & Hüssy, K. 2018: Using LA-ICPMS to investigate seasonality in cod otolith microchemistry. 33rd Nordic Geological Winter Meeting, DTU, Kongens Lyngby, Denmark. Abstract volume.
- Pannella, G. 1971: Fish otoliths: daily growth layers and periodical patterns. *Science* **173**, 1124–1127.
- Paton, C., Hellstrom, J., Paul, B., Woodhead, J. & Hergt, J. 2011: Iolite: Freeware for the visualisation and processing of mass spectrometric data. *Journal of Analytical Atomic Spectrometry* **26**, 2508–2518.
- Patterson, W.P., Smith, G.R. & Lohmann, K.C. 1993: Continental paleothermometry and seasonality using the isotopic composition of aragonitic otoliths of freshwater fishes. In: Swart, P.K. *et al.* (eds): *Climate Change in Continental Isotopic Records*. American Geophysical Union Monograph (1993), 191–202.
- Søndergaard, J., Halden, N., Bach, L., Gustavson, K., Sonne, C. & Mosbech, A. 2015: Otolith chemistry of common sculpins (*Myoxocephalus scorpius*) in a mining polluted greenlandic fjord (Black Angel Lead-Zinc Mine, West Greenland). *Water, Air and Soil Pollution* **226**(10) 336, 12 pp.
- Sturgeon, R.E., Willie, S.N., Yang, L., Greenberg, R., Spatz, R.O., Chen, Z., Scriver, C., Clancy, V., Lam, J.W. & Thorrold, S. 2005: Certification of a fish otolith reference material in support of quality assurance for trace element analysis. *Journal of Analytical Atomic Spectrometry* **20**, 1067–1071.
- Sturrock, A.M., Trueman, C.N., Darnaude, A.M. & Hunter, E. 2012: Can otolith elemental chemistry retrospectively track migrations in fully marine fishes? *Journal of Fish Biology* **81**, 766–795.
- Thomas, O.R.B., Ganio, K., Roberts, B.R. & Swearer, S.E. 2017: Trace element–protein interactions in endolymph from the inner ear of fish: implications for environmental reconstructions using fish otolith chemistry. *Metallomics* **9**, 239–249.
- Thorrold, S.R. & Shuttleworth, S. 2000: In situ analysis of trace elements and isotope ratios in fish otoliths using laser ablation sector field inductively coupled plasma mass spectrometry. *Canada Journal of Fisheries and Aquatic Sciences* **57**, 1232–1242.

Authors' addresses

S.H.S. & T.B.T., *Geological Survey of Denmark and Greenland, Øster Voldgade 10, DK-1350 Copenhagen K., Denmark*. E-mail: shs@geus.dk.

K.E.N., P.F.J. & K.H., *National Institute of Aquatic Resources, Technical University of Denmark, Kemitorvet, Building 202, DK-2800 Kgs. Lyngby, Denmark*.

Towards a common geological data infrastructure for Europe

Jørgen Tulstrup and Mikael Pedersen

Geology does not respect national borders. Hence, in order to get geological overviews of Europe, input from geological surveys in more than 35 countries is required. European policy makers have several times been forced to rely on the US Geological Survey to provide e.g. resource estimates from the European continent, but for obvious reasons there is a wish to base European decision making on European knowledge. Consequently, the European Commission and the European Parliament have formulated a request for the establishment of a 'Geological Service for Europe'. In its strategy towards 2020, EuroGeoSurveys (EGS) addresses the creation of such a service through three pillars. EGS is an umbrella organisation through which national geological survey organisations of 36 European countries cooperate, referred to below as national surveys. The three pillars are designed to integrate input from all national surveys into a system that can swiftly act on urgent needs for knowledge-based decision support. The three pillars relate to joint research, data integration and sharing of facilities (Fig. 1). Whilst the third pillar has only recently been dealt with, the two first have already advanced through a number of recent initiatives. Having been a key player in numerous EU projects for many years, the Geological Survey of Denmark and Greenland (GEUS) has attained a central role in the implementation of these two pillars of the strategy, both as coordinator of the European Geological Data Infrastructure (EGDI, www.europe-geology.eu) and as one of the biggest players in the so-called GeoERA programme. GEUS participates in ten projects and is a partner in the secretariat and the coordinator of the GeoERA Information Platform. The present paper outlines the main steps towards the current situation and provides a background for GEUS' role in this.

Towards a EU geological knowledge base

The European Commission has contributed financially through several framework programmes to increase knowledge sharing, capacity building as well as cross-border and pan-European research within different geoscience domains. In most cases, data play a central role, and EGS members have many years of experience in working together with the purpose of making geological data FAIR (Findable, Accessible, Interoperable and Reusable). In many cases, Euro-

pean projects have historically only had the participation of a limited number of national surveys, but in 2008 a flagship project funded by the EU was launched with the participation of 20 national surveys as a logical follow-up of the global OneGeology initiative (www.onegeology.org). OneGeology aimed at assembling a geological map of the world on a scale of 1:1 000 000 by piecing together national contributions in whatever format they had, using distributed web services. The OneGeologyEurope project went a step further. GEUS and the 19 other European national surveys worked together for two years to produce a distributed, web-based surface geological map of Europe on a scale of c. 1:1 000 000 that was harmonised with a common data structure and agreed geological classifications. At that time, the project represented a leading edge activity, as it demonstrated the power of national organisations working together around a common data structure and nomenclature for geological units (geochronology and lithology). Importantly, the project built on principles and rules from the INSPIRE directive from 2007 and was thus not only a step on the way for the national sur-

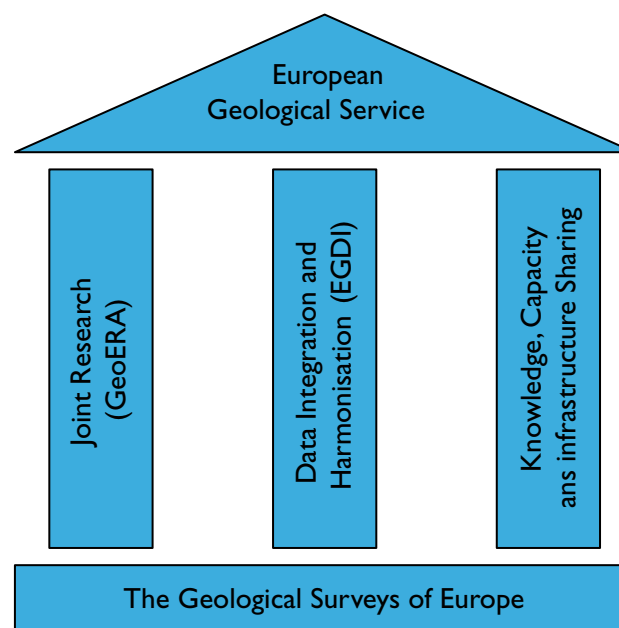


Fig. 1. The three pillars of the EGS strategy for the establishment of a European Geological Service.

veys to fulfil their obligations towards the directive, but also served to demonstrate the feasibility of making geological data interoperable for Europe and beyond. The results of the project were fed into the legal process to define the EU-wide INSPIRE geological data specification, which since 2014 constitutes the implementing rules.

Upon the success of OneGeologyEurope, a natural extension came with the increased attention on securing the supply of critical raw materials for European industry. This was partly based on the rare-earth element trade dispute that began in 2010 when China imposed strict export quotas for rare-earth elements. Such elements are used in a number of high-technology industries, and since China accounts for 97% of the world production, the situation was considered critical (Kalvig & Machacek 2018, this volume). Consequently, the European Commission urgently needed an overview of raw materials resources in Europe. This led to a number of EU projects. Especially one of them had strategic importance for the EGS, namely the Minerals4EU project. GEUS cooperated with 27 other national surveys and other EU organisations to build the foundation for a European raw materials knowledge base, by extending the OneGeologyEurope philosophy and by complying with and contributing to INSPIRE. Subsequently, other EU projects like EURare, ProSUM, MICA and the recently launched ORAMA project have extended and/or improved this common knowledge base. At the same time GEUS also participates in the Knowledge and Innovation Community (KIC) for Raw Materials, through which a number of complementary projects are run in cooperation with universities and industrial partners.

Simultaneously with these raw materials projects, a number of other European data harmonisation projects were

carried out within other EGS research areas such as groundwater, energy, geohazards and soil. However, it became increasingly clear along the way that there was a need for co-ordination in order to increase the efficiency, reusability and sustainability – not only to meet European expectation, but also for the sake of geoscientists. This was addressed in the EGS strategy that was published in 2014 and laid the foundation for the European Geological Data Infrastructure.

The European Geological Data Infrastructure

In 2012, EGS' members were granted a two-year EU project called EGDI-Scope, aiming to assess the possibilities of setting up a long-term sustainable European geological data infrastructure in line with the second pillar of the EGS strategy. The initiative addressed the fact that almost all previous common European geoscience projects had succeeded in producing good European datasets and commonly also web-based dissemination platforms, but that such systems would typically disappear after a certain period because of lack of financial support for basic operation and maintenance. The EGDI-Scope project revealed that data from more than 80 past European projects, worth 400–700 million Euro, could potentially be 'saved' and made available through a common data infrastructure which should also be the natural dissemination platform for future projects. GEUS was part of the EGDI-Scope core team and was in charge of stakeholder consultation, thereby analysing both end-user needs and interfaces to other large European earth science projects and initiatives.

An important goal of EGDI-Scope was to pave the way for a larger EU project, whereby EGDI could be implemented.

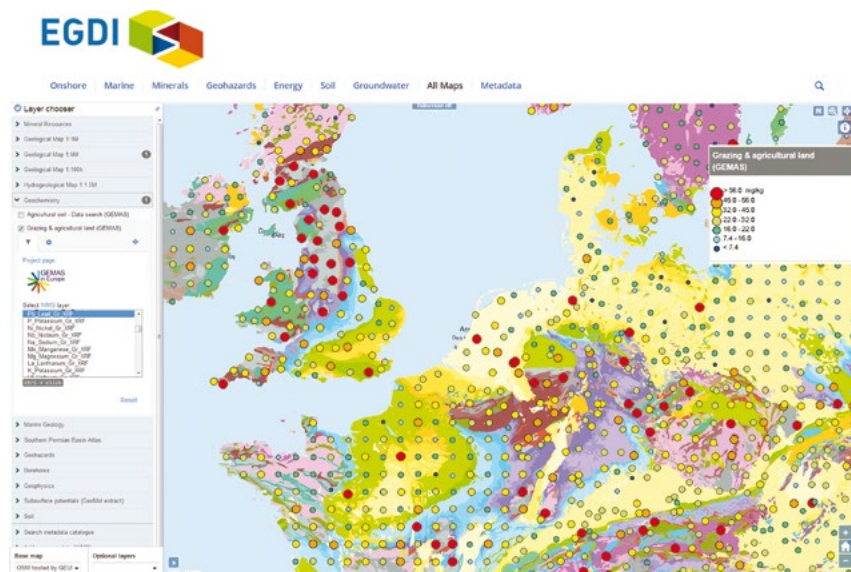


Fig. 2. The interactive map viewer of the European Geological Data Infrastructure (EGDI) portal through which hundreds of different data themes can be viewed in combination. The map shown here illustrates the concentration of lead in grazing land (coloured dots) on top of a geological map of Europe.

Unfortunately no appropriate Horizon 2020 (EU's framework programme) calls were launched, and two proposals targeting some generic electronic infrastructure calls were rejected. However, the concept of EGDI was widely used in strategic communication, and eventually the situation became critical: everybody talked about EGDI, but it did not exist. Consequently, GEUS mobilised the so-called 'Spatial Information Expert Group' of the EGS, and after a long process of argumentation and communication the EGS General Assembly accepted to provide in-kind resources from the national surveys to establish a first basic implementation of the EGDI.

EGDI version 1

On 14 June 2016, the first version of EGDI was launched at the premises of the EGS secretariat in Brussels. Besides directors and other EGS key persons, the audience comprised a number of distinguished EU commissioners representing different parts of the commission, including DG GROW (raw materials), DG MARE (maritime affairs), DG ENER (geoenergy), DG RTD (research) and DG JRC (joint research and INSPIRE). The participants were very happy with what they saw. Even though it is not fully-fledged, EGDI V.1 contains most parts of the system that was identified under the EGDI-Scope project. A number of datasets from past European projects are included and made available through a common web portal (www.europe-geology.eu; Fig. 2), which was to a large extent developed by GEUS. However, the portal is only a small part of EGDI. The infrastructure itself consists of a complex of central databases, a metadata catalogue and distributed web services that all conform to the same standards. Roles and responsibilities are agreed internally in EGS, and work is in progress to establish a more permanent governance structure.

EGDI in the European landscape of electronic infrastructure

EGDI is not alone! There are many other related European initiatives (Fig. 3) and a few will be mentioned here. The European Plate Observing System (EPOS) is a research infrastructure for solid-earth sciences in Europe and is of strategic importance to the EU. It aims to facilitate research into natural disasters such as earthquakes and volcanic eruptions through the integration of geoscience data from a number of different research communities. Geological data represent one of the domains that EPOS will integrate; the EGS community is the main provider of such data. GEUS has a role in the implementation project EPOS-IP and actively uses this position together with other participating national surveys to ensure the complementarity between EGDI and EPOS through various coordination activities.

The European Marine Observation and Data Network (EMODnet) is a large programme aiming at providing uniform access to marine data from Europe's coastal states. EMODnet is divided into seven discipline-based themes, one of which deals with geological data. The EMODnet-geology project has been running in several phases since it started in 2008. In the current third phase, GEUS has leading role in the work package dealing with data management and web portal development – again a strong position that GEUS uses to strengthen the coherence of the European e-Infrastructure landscape through technical coordination with EGDI, EPOS and other large initiatives.

The role of EGDI as a central data-bearing component in European geoscience research is continuously being strengthened through coordination with other European projects and programmes. One of these is GeoERA.

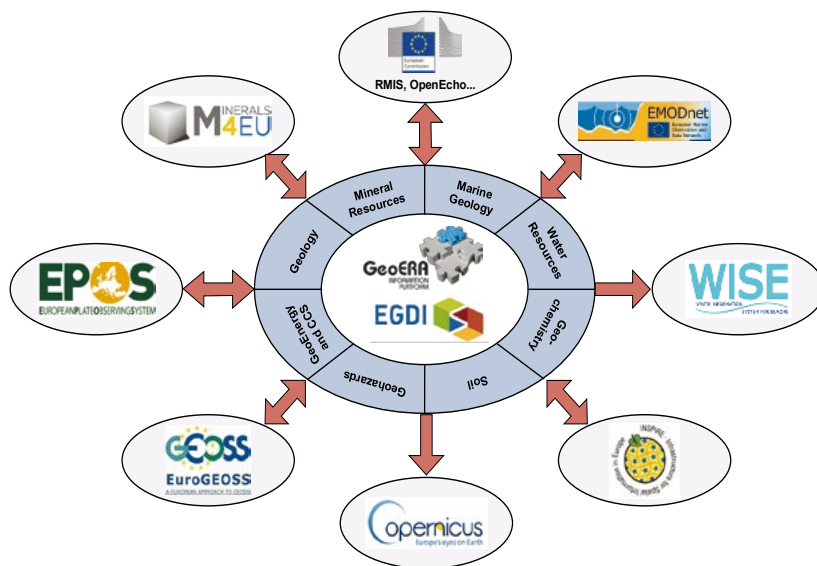


Fig. 3. The central position of the EGDI in the European e-Infrastructure landscape. EGDI serves geological data from a lot of different geological research areas and thereby contributes geological data to numerous European information systems through interoperable web services.

GeoERA

The first pillar of the EGS strategy, the joint research pillar, is on its way to be implemented through an ERA-NET on 'Establishing the European Geological Surveys Research Area to deliver a Geological Service for Europe (GeoERA)'. The main objective of GeoERA (<http://geoera.eu>) is to contribute to the optimal use and management of the subsurface. Forty-eight national surveys from 33 European countries will participate in research projects under GeoERA with the purpose of supporting a more integrated and efficient management as well as a more responsible and publicly acceptable exploitation and use of the subsurface. GeoERA covers the three geoscientific themes of geo-energy, groundwater and raw materials; the projects will run for three years starting in July 2018.

The three geoscientific themes share the objective of organising and disseminating a large amount of results in the form of digital maps and other data. Furthermore, cross-thematic integration of information is an important aspect of GeoERA. It has therefore been decided to establish a common 'Information Platform' for the efficient integration of all IT-related and technical issues (database and dissemination) from all GeoERA projects. The platform will be capable of integrating up-to-date data, interpretations and models from different and distributed sources, both within and across the three main geoscientific themes of GeoERA.

The platform will be based on EGDI which contains some of the functionality foreseen to be required by the GeoERA projects. EGDI will, however, have to be extended in order to handle and disseminate for instance 3D/4D geological models.

In addition to organising the geoscientific projects, GeoERA also carries out 'foresight activities' with the purpose of assessing how longer-term funding of the activities can be obtained and eventually lead to a 'Geological Service for Europe'. The safeguarding of the GeoERA results through the information platform and the long-term operation and maintenance of the entire EGDI should be seen in this context.

The future

One of the main challenges for all these European initiatives, including EGDI, is to make them sustainable. All EU projects are run for a limited period after which the funding

ends, and due to budget mechanisms, the European Commission is not in a position to fund permanent maintenance of any system. EGS has therefore continuously tried to find sustainable funding models to keep EGDI alive in a technical and organisational sense. Currently the EGS members are able to finance the very basic operation of EGDI. From 2018–2021 work within the GeoERA projects will ensure that EGDI will be significantly upgraded with much more data and functionality. With EGDI becoming a continuously bigger and more integrated piece in the European puzzle, the chances of finding a long-term solution are on the increase, but a sustainable solution will probably have to be connected to the establishment of the 'Geological Service for Europe' at least partly funded by EU.

Other challenges facing the generation of truly pan-European harmonised geological datasets are that some of the most relevant data are considered confidential in some countries. This is for instance the case for some data about mineral occurrences in certain East European countries. In other countries the organisation and provision of data are the responsibility of regional authorities instead of national surveys, who are less committed to the European viewpoint on data than EGS.

Finally, it has turned out that it is difficult to convert national geological databases and make them interoperable according to the requirements in the INSPIRE implementing rules. Many of these rules are very complicated, and many resources have been allocated to the database administrators at the national surveys in order to make their data compliant with the standards.

References

- An effective raw materials strategy for Europe. European Parliament resolution of 13 September 2011 on an effective raw materials strategy for Europe. <https://eur-lex.europa.eu> (2011/2056(INI)).
- Communication from the Commission to the European Parliament, the Council, The European Economic and Social Committee and the Committee of the Regions. Making raw materials available for Europe's future wellbeing. Proposal for a European Innovation Partnership on raw materials. <https://eur-lex.europa.eu> (Com(2012) 82).
- Kalvig, P. & Machacek, E. 2018: Examining the rare-earth elements (REE) supply-demand balance for future global wind power scenarios. Geological Survey of Denmark and Greenland Bulletin 41, 87–90 (this volume).
- The EuroGeoSurveys vision towards a Geological Service for Europe. <http://www.eurogeosurveys.org/wp-content/uploads/2014/08/EGS-Strategy-Document-2014-A4.pdf>.

Authors' address

Geological Survey of Denmark and Greenland, Øster Voldgade 10, 1350 Copenhagen K, Denmark. E-mail: jtu@geus.dk.

Analytical procedures for 3D mapping at the Photogeological Laboratory of the Geological Survey of Denmark and Greenland

Erik Vest Sørensen and Mads Dueholm

Photogrammetry is a classical remote sensing technique dating back to the 19th century that allows geologists to make three-dimensional observations in two-dimensional images using human stereopsis. Pioneering work in the 1980s and 1990s (Dueholm 1992) combined the use of vertical (nadir-looking) aerial photographs with oblique stereo images from handheld small-frame cameras into so-called multi-model photogrammetry. This was a huge technological step forward that made it possible to map, in three dimensions, steep terrain that would otherwise be inaccessible or poorly resolved in conventional nadir-looking imagery. The development was fundamental to the mapping and investigation

of e.g. the Nuussuaq basin (Pedersen *et al.* 2006). Digital photogrammetry, the all-digital version of multi-model photogrammetry, is nowadays an efficient and powerful geological tool that is used by the Photogeological Laboratory at the Geological Survey of Denmark and Greenland (GEUS) to address geological problems in a range of projects from 3D mapping to image-based surface reconstruction and orthophoto production. Here we present an updated description (complementary to Dueholm 1992) of the analytical procedures in the typical digital workflow used in current 3D-mapping projects at GEUS.



Fig. 1. During field work new stereo imagery is normally collected from helicopters or boats, but could also be collected from smaller fixed-wing aircraft, drones or while walking.

Multi-model photogrammetry in its present form is essentially a technique that allows geologists to combine stereo images of different origin e.g. from satellite, aerial or hand-held cameras, and with different resolutions and viewing angles in their geological interpretations (Fig.1), using a digital photogrammetric workstation. Examples are plentiful with scales ranging from metres (Vosgerau *et al.* 2010, 2016) to kilometres (Svennevig *et al.* 2015; Sørensen & Guarnieri 2018, this volume) or even hundreds of kilometres (Sørensen *et al.* 2017).

The strength of the methodology lies in the ability to combine stereo images with different viewing angles. Regional geological structures are e.g. typically well resolved in nadir-looking aerial or satellite images, while steep cliffs are better resolved from closer range images acquired perpendicularly to the slope of the outcrop. Essentially, digital photogrammetry allows the user to map and quantify in three dimensions whatever can be seen in the stereo images across different scales and resolutions.

The digital photogrammetric workstation described here is the modern equivalent to the analytical setup previously used at GEUS (Hougaard *et al.* 1991) and at the Institute of Surveying and Photogrammetry, Technical University of Denmark (Dueholm 1992). The workstation consists of a Windows-based computer and a split-screen 3D monitor system (Fig. 2). Technically, the monitor system displays an image of an object in one screen and an overlapping image of the same object but from a slightly different position on a second screen. A beam splitter mirror splits the polarisation direction of the two screens into separate horizontal and vertical directions. Polarising glasses used by the viewer then filter the signals so that the top screen is solely presented to

the right eye and the bottom screen is solely presented to the left eye. This allows the human visual system to merge the two images, whereby a stereoscopic model is created in front of the user.

The central part of the workstation is the photogrammetric software, which is essentially a computer-controlled set of algorithms that controls the viewing of the stereoscopic model as well as the collection and manipulation of three-dimensional data within the model. This allows for seamless movement and data capture between different stereoscopic models regardless of scale, origin and viewing angle, which highly increases the speed and efficiency of geological mapping, especially in steep and inaccessible terrains.

At present, the Photogeological Laboratory uses two commercial photogrammetric 3D-mapping software solutions (*Socet GXP* from BAE Systems and *3D Stereo Blend*) that are complementary to each other in terms of technical capabilities. In the following, we describe the typical workflow used with *3D Stereo Blend*: 1) data acquisition during field work, 2) data preparation of the images, 3) data interpretation (Fig. 3). This description, however, should not be viewed as a complete manual to the software. *3D Stereo Blend* is developed by Anchor Lab in close collaboration with GEUS' Photogeological Laboratory. The software is optimised to 3D-mapping and structural interpretation using oblique stereo images collected with calibrated hand-held digital cameras. It is an essential part of the overall strategy of the Photogeological Laboratory to increase the efficiency and usability of digital photogrammetry from data acquisition to end-product, so that the method becomes a geological tool routinely used by geologists also without prior expert knowledge.

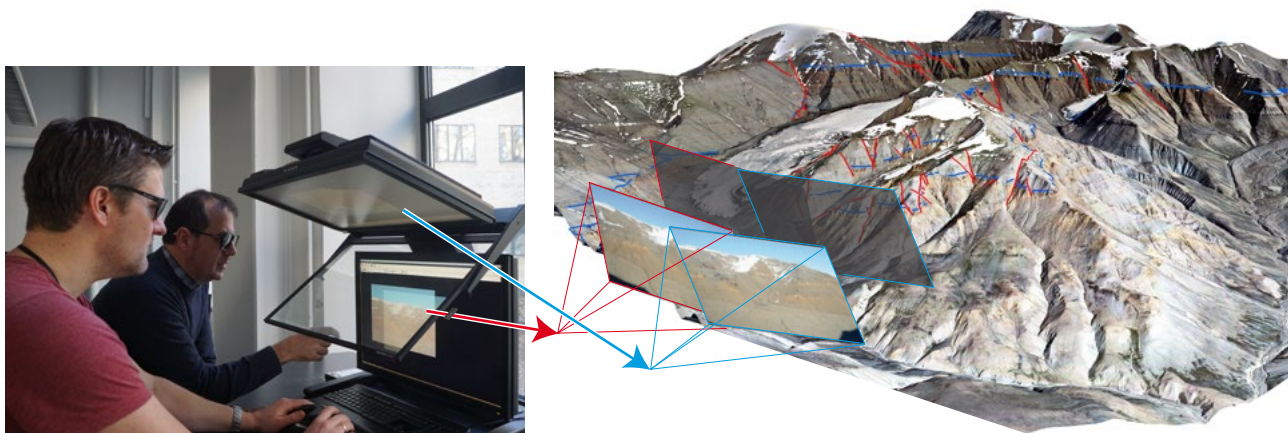


Fig. 2. The geologist at work in the Photogeological Laboratory. The stereoscopic model is displayed on a 3D monitor system that is well suited for full-day working. The stereoscopic model can be observed simultaneously by several viewers; this makes it easy to illustrate and discuss geological observations and ideas, which is beneficial for the geological interpretation.

Data acquisition – field photography

Field work provides the geologist with important first order observations of the bedrock. Working in remote and mountainous areas such as Greenland is often challenging because of inaccessible outcrops (steep cliffs) and time constraints (short field seasons). The result is spatially scattered outcrop observations that can be difficult to correlate or relate to overall regional structures. To overcome this problem, stereo images, i.e. strips of overlapping images taken from different positions and covering the geological outcrops of interest are collected on a routine basis using hand-held digital cameras, commonly deployed from helicopters (Fig. 4). The simplicity of using a hand-held digital camera makes the data acquisition extremely mobile and fast. Furthermore, the quality, resolution and storage capacity of modern digital cameras have led to a huge increase in efficiency and capacity during data acquisition compared to the earlier days of 3D mapping. As an example, overview images of a small outcrop were collected within minutes using a helicopter, while on a more regional scale, a 100 km cliff section was photographed within less than one hour (Sørensen *et al.* 2015a). Depending on the logistic setup, the images could equally well be collected by other means (Fig. 1), as long as sufficient overlap between the images is ensured. As a rule of thumb, 60–80% overlap is needed to obtain continuous overlap and good stereoscopic measurement accuracy (Dueholm 1992). However, it is now recommended that images are taken with up to 90% overlap because this results in a more successful automatic generation of common points (so-called tie points) between different images. It will also, at a later stage, make it possible to use the images for surface reconstruction using dense image matching routines (Sørensen *et al.* 2015b). The cameras are full-frame, digital single-lens reflex with high-quality 35 mm prime lenses that are fixed and focused at infinity. However, essentially any camera can be used as long as the camera parameters (lens distortion, focal length and principal point) of the camera can be modelled. The cameras are calibrated prior to field work using a test field consisting of a steel grid with *c.* 100 points. We recommend that the images are acquired in the raw image format of the camera and that the location of the camera is registered with Global Navigation Satellite Systems (GNSS). Depending on the requirements for absolute accuracy, different GNSS equipment can be used, from simple geotagging devices to more advanced differential GNSS systems.

Data preparation

Setting up the images essentially consists of two steps. First, a relative model is constructed by identifying common points

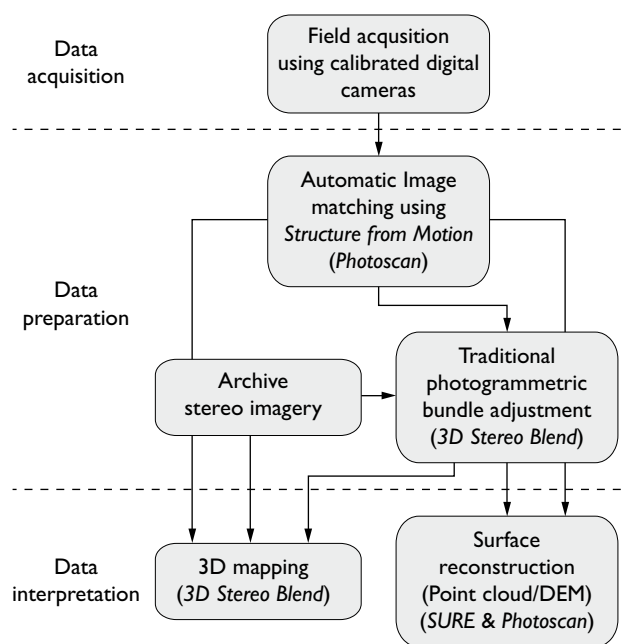


Fig. 3. Schematic flow diagram summarising the typical 3D-mapping workflow from data acquisition to photogrammetric data preparation and interpretation.

(tie points) between overlapping images. Secondly, this model is transformed into absolute, ‘real-world’ coordinates by combining camera location data and control points.

Relative orientation

The relative connectivity between images in object space is established by automatic tie point measurement using ‘Structure from Motion’ (SfM) image-matching algorithms (Lowe 2004; Snavely *et al.* 2008), with possible manual editing or addition of tie points by stereoscopic measurement within *3D Stereo Blend*. The commercial software *Photoscan Professional (PS)* from Agisoft is used for the image matching, but other software solutions can also be used. The raw image-matches (tie points) are subsequently exported to *3D Stereo Blend*. *3D Stereo Blend* uses the imported tie point file as a block definition and set-up file as well as for preliminary triangulation. The file is typically thinned when imported using an area-based thinning technique to give an even distribution of tie points across the images. The next step is to make a preliminary so-called bundle adjustment or triangulation, including error detection and elimination of erroneous tie points from the imported data. The images can subsequently be viewed in 3D with the orientation of that exported from *PS*. If positional data, such as e.g. GNSS camera positions, are included in the export from *PS*, the stereo-



Fig. 4. Stereo images collected from helicopter using a hand-held digital camera. This method makes the data acquisition very mobile and fast. The location of the camera is registered with Global Navigation Satellite Systems. Photo: Jonas Petersen.

stereoscopic model will be placed in absolute coordinates within *3D Stereo Blend*. Depending on the project requirements, one could move directly on to the 3D-mapping stage for rapid results or if absolute accuracy is of minor importance. However, requirements for absolute accuracy often mean that additional control data must be added.

Absolute orientation

The absolute orientation relates the photogrammetric models in object space to absolute coordinates through a proper bundle adjustment process, whereby the stereoscopic model gets the correct scale and levelling. When solving the bundle adjustment, all provided control information is weighted according to an *a priori* estimated error. Different sources of control data can be used in this process, including surveyed control points, pass-points, camera GNSS-data, planar levelling points and distances. Surveyed ground-control points generally give the best positional accuracy. However, considering the regional scale of many 3D-mapping projects, this approach is often not viable from a practical point of view. Instead, pass-points from already aerotriangulated aerial photographs can be used as control-point source, which eliminates the need for ground-control-point collection during field work. This is done by identifying common points between for example a set of vertical aerial photographs and local oblique-view images. This process is sensitive due to the different perspectives of the image data sets as well as the different resolutions, and takes some practical experience to carry out. However, workflows implemented within *3D Stereo Blend* have significantly improved the efficiency of the identification process. GNSS data collected with the camera

yield the position of the camera at the time of acquisition that is important for setting up the images. Simple geotagging equipment typically yields a camera position accuracy of around 5–10 m. However, more advanced differential GNSS set-ups could result in a positional accuracy at the sub-metre level, which might minimise or completely eliminate the need for surveyed ground- control points or measured pass-points.

The overall time consumption in the preparation of the images has significantly decreased compared to the early days of analytical 3D mapping. This is largely a consequence of computer hardware and digital camera development, but also of software improvements including better image-matching algorithms and improved photogrammetric workflows in the *3D Stereo Blend* software. Consequently, small blocks of stereo images can be prepared for geological interpretation within a day. This opens up for e.g. using digital photogrammetry as an active tool during field work.

Stereoscopic image interpretation – 3D mapping

Once the images are properly prepared, or if archive data are available, the geologist can commence the geological photointerpretation in three dimensions. This is done by tracing geological features of interest in the stereoscopic models. The change between neighbouring stereo models takes place automatically, so that important horizons can be traced seamlessly for kilometres. Several views can be opened simultaneously, whereby an outcrop can be seen from different perspectives and at different resolutions, which is important for the geological interpretation. The different views can fur-

thermore be linked, so that a movement in one window is also updated in the linked window. Changing the displayed stereo block is either done by selecting from a pull-down window or by selecting the cameras in perspective view interactively. All images from the cameras within a project can be shown in the perspective view. This makes it easy to manage and move around in large regional data sets with thousands of images. The outcome of the drawing is a number of vectorised lines in 3D with many nodes (so-called polylines) superimposed on the stereoscopic model (Fig. 2). The polylines can be labelled and grouped according to the user's need, and subsequently exported to GIS packages for GIS analysis or to 3D-modelling software. The software automatically registers the original stereo model in which each node of a given polyline was drawn. This makes it possible to automatically adjust the images if their orientation is changed at some point. This is helpful e.g. if an initial interpretation of the images is done on a preliminary set-up of the images without proper ground control.

A central part of the *3D Stereo Blend* software is a set of structural tools that enables the viewer to evaluate structural parameters such as strike and dip of bedding, plunge and direction of fold axes and stratigraphic thickness of beds. This allows the geologist for instance to populate a geological map with many structural observations from areas that could not be visited in the field, to correlate bedding from one side of a fjord to the other or to measure true thicknesses. The structural tool-set consists of selected routines from the *Geoprogram* software (Dueholm & Coe 1989) and works by fitting planes by least-squares adjustment of captured data points. Of special importance is the possibility to project captured data into geological sections which can have arbitrary orientations and also be inclined to better reflect e.g. true thicknesses.

In summary, with the present set-up, 3D mapping has become much more effective and user-friendly than previously, which is largely due to the improved photogrammetric workflows in the *3D Stereo Blend* software. For instance, it is now possible for the untrained geologist to engage in 3D mapping with only 1–2 days of training.

Resolution and accuracy

The resolution of the stereoscopic models depends on the distance between the camera and outcrop, the camera focal length and the pixel size (pixel pitch) of the sensor of the digital camera. As an example, photographing an outcrop at a distance of 100 m gives a ground sampling distance (GSD) of 14 mm using e.g. a 36 megapixel *Nikon D800E* camera with a calibrated sensor pixel pitch of $4.89 \mu\text{m}$ and a focal length of 36 mm, or a scale of *c.* 1:3000, while increasing the dis-

tance to 1000 m will give images with GSD of 0.14 m (scale 1:30 000).

The photogrammetric or geometric accuracy in the image plane on the ground (the *x* and *y* axes perpendicular to the direction of view) relates to the distance between the camera and outcrop, the camera focal length and how accurately a point can be determined in the stereoscopic model. The latter is a function of the accuracy of the triangulation, the camera calibration and on how well the user can place a point in the stereoscopic model. In addition, the photogrammetric accuracy in depth (the *z* axis, in the direction of view) also depends on the ratio between the distance between the camera and the object and the distance between the camera stations (also called the baseline). A typical value for the point determination is around one pixel, which leads to an accuracy of *c.* 14 mm in the image plane, while the accuracy in depth is *c.* 35 mm with a distance to the outcrop of 100 m and a baseline of 40 m (corresponding to 60% overlap). If the camera-to-object distance is increased to 1000 m, the accuracy in the image plane decreases to 0.14 m, while the accuracy in depth will decrease to 0.35 m, assuming that the baseline is increased to 400 m to maintain a 60% image overlap. However, if the baseline remains 40 m long there is a significant decrease in the depth accuracy to *c.* 3.5 m. This illustrates the importance of having an appropriate image overlap.

The absolute accuracy of the stereoscopic model relates to that of the control source. In Greenland, pass-points are commonly acquired from the monochrome vertical aerial photographs on a scale of 1:150 000 that cover most ice-free areas. Typical achievable accuracies on the point transfer from these photographs is around 3–5 m. Using high-precision differential GNSS setup it should be possible to obtain accuracies of less than 1 m, whereby the absolute accuracy approaches the photogrammetric accuracy.

Although the absolute accuracy generally exceeds that of the photogrammetric accuracy, the relative accuracy between models remains equal to the photogrammetric accuracy, because the ground-control data is weighted during the bundle adjustment. This means that when calculating e.g. thicknesses or structural parameters such as strike and dip, the accuracy is determined from the photogrammetric accuracy. In practice, this is all handled automatically within the *3D Stereo Blend* software.

Other derived products

In addition to the 3D geological mapping workflow, the technical development of automatic multi-view- stereo-matching routines (Rothermel *et al.* 2012) has facilitated the extraction of digital outcrop models from stereo imagery (Sørensen

et al. 2015b). The digital outcrop model is a 3D representation of the outcrop surface. This type of routine utilises the redundancy of high image overlap to produce a set of high-resolution data points in space (so-called point clouds) that need little manual editing. Although a high image overlap (i.e. a small baseline) reduces the precision of individually matched pixels, this is compensated by determining the same point in multiple images, which leads to effective automatic elimination of erroneous points. The point cloud is used e.g. for visualisation purposes where it can be integrated with the results of the 3D geological mapping, but it can also be further processed into 3D mesh representations of the terrain, or production of digital terrain models and orthophotos. GEUS' Photogeological Laboratory is currently using a suite of software solutions for terrain extraction. Software such as *Photoscan Professional* from Agisoft and *SURE* from Nframes is typically used in the digital outcrop model workflow, while more conventional aerial and satellite imagery is processed using *Socet GXP*.

Summary

The all-digital version of multi-model photogrammetry, now referred to as digital photogrammetry or just 3D mapping, has brought the geological outcrop into GEUS' Photogeological Laboratory. The recent increases in efficiency all the way from data acquisition to the geological interpretation makes 3D mapping an attractive geological tool available to the geologist. With a digital photogrammetric workstation, the users can view, map and explore any geological feature in three dimensions, following the principle that whatever can be seen in the images can also be mapped and quantified in 3D.

Acknowledgments

The authors would like to thank Max Strunck and Birgir Óskarsson for reviewing the manuscript as well as Asger Ken Pedersen and Lotte Melchior Larsen for helpful comments and suggestions.

References

- Dueholm, K.S. & Coe, J.A. 1989: Geoprogram. Program for geological photogrammetry. *The Compass* **66**, 59–64.
- Dueholm, K.S. 1992: Geologic photogrammetry using standard small-frame cameras. In: Dueholm, K.S. & Pedersen, A.K. (eds): Geological analysis and mapping using multi-model photogrammetry. *Rapport Grønlands Geologiske Undersøgelse* **156**, 7–17.
- Hougaard, G., Jepsen, H.F. & Neve, J.K. 1991: GGU's photogeological laboratory: aerial photogrammetry – a valuable geological mapping tool in Greenland. *Grønlands Geologiske Undersøgelse Rapport* **152**, 32–35.
- Lowe, D.G. 2004: Distinctive image features from scale-invariant key points. *International Journal of Computer Vision* **60**, 91–110.
- Pedersen, A.K., Larsen, L.M., Pedersen, G.K. & Dueholm, K.S. 2006: Five slices through the Nuussuaq Basin, West Greenland. *Geological Survey of Denmark and Greenland Bulletin* **10**, 53–56.
- Rothermel M., Wenzel, K., Fritsch, D. & Haala, N. 2012: SURE: photogrammetric surface reconstruction from imagery. In: *Proceedings, LC3D Workshop, Berlin, 4–5 December 2012*, 9 pp.
- Snavely, N., Seitz, S. & Szeliski, R. 2008: Modeling the World from internet photo collections. *International Journal of Computer Vision* **80**, 189–210.
- Sørensen, E.V., Pedersen, A.K., Garcia-Sellés, D. & Strunck, M.N. 2015a: Point cloud from oblique stereo-imagery: an outcrop case study across scales and accessibility. *European Journal of Remote Sensing* **48**, 593–614.
- Sørensen, E.V., Bjerager, M. & Citterio, M. 2015b: Digital models based on images taken with handheld cameras – examples on land, from the sea and on ice. *Geological Survey of Denmark and Greenland Bulletin* **33**, 73–76.
- Sørensen, E.V., Baker, N.G. & Guarnieri, P. 2017: Three years of photogrammetry – extreme 3D mapping. Abstract, GRSG 28th International Annual Conference – Applied Geological Remote Sensing. <https://www.grsg.org.uk/wp-content/uploads/2017/12/GRSG-AGM-and-Conference-Abstract-Book-2017.pdf>
- Sørensen, E. V. & Guarnieri, P. 2018: Remote geological mapping using 3D photogrammetry: an example from Karrat, West Greenland. *Geological Survey of Denmark and Greenland Bulletin* **41**, 63–66 (this volume).
- Svennevig, K., Guarnieri, P. & Stemmerik, L. 2015: From oblique photogrammetry to a 3D model – Structural modeling of Kilen, eastern North Greenland. *Computers & Geosciences* **83**, 120–126.
- Vosgerau, H., Guarnieri, P., Weibel, R., Larsen, M., Dennehy, C., Sørensen, E.V. & Knudsen, C. 2010: Study of a Palaeogene interbasaltic sedimentary unit in southern East Greenland: from 3-D photogeology to micropetrography. *Geological Survey of Denmark and Greenland Bulletin* **20**, 75–78.
- Vosgerau, H., Passey, S. R., Svennevig, K., Strunck, M. N. & Jolley, D.W. 2016: Reservoir architectures of interlava systems: a 3D-photogrammetrical study of Eocene cliff sections, Faroe Islands. *Geological Society, London, Special Publications* **436**, 55–73.

Authors' addresses

E.V.S., *Geological Survey of Denmark and Greenland, Øster Voldgade 10, DK-1350 Copenhagen K, Denmark*. E-mail: evs@geus.dk.

M.D., *Anchor Lab K/S, H.C. Andersens Boulevard 37, 5. MF, DK-1553 Copenhagen V, Denmark*.